INVESTIGATION OF TISSUE MICROENVIRONMENTS USING DIFFUSION MAGNETIC RESONANCE IMAGING

by

Emma Maria Meeus

A thesis submitted to the University of Birmingham
for the degree of DOCTOR OF PHILOSOPHY

Physical Sciences of Imaging in the Biomedical Sciences
School of Chemistry
College of Engineering and Physical Sciences
University of Birmingham
November 2017

Abstract

Diffusion-weighted magnetic resonance imaging (DW-MRI) has rapidly become an important part of cancer patient management. In this thesis, challenges in the analysis and interpretation of DW-MRI data are investigated with focus on the intravoxel incoherent motion (IVIM) model, and its applications to childhood cancers. Using guidelines for validation of potential imaging biomarkers, technical and biological investigation of IVIM was undertaken using a combination of model simulations and in vivo data. To reduce the translational gap between the research and clinical use of IVIM, the model was implemented into an in-house built clinical decision support system. Technical validation was performed with assessment of accuracy, precision and bias of the estimated IVIM parameters. Best performance was achieved with a constrained IVIM fitting approach. The optimal use of *b*-values was dependent on the tissue characteristics and a compromise between bias and variability. Reliable data analysis was strongly dependent on the data quality and particularly the signal-to-noise ratio. IVIM perfusion fraction (*f*) was generally found to correlate with dynamic susceptibility contrast imaging derived cerebral blood volume. IVIM-*f* also presented as a potential diagnostic biomarker in discriminating between malignant retroperitoneal tumour types. Overall, the results encourage the use of IVIM parameters as potential imaging biomarkers.

To my husband Yannick,

For your Patience, Love & Support

Declaration

I declare that the work presented in this thesis is entirely my own.

The work presented (including data acquisition and analysis) was carried out by myself, except in the cases listed below:

- Patient MRI data was collected by radiographers, part of the Radiology Department at Birmingham Children's Hospital.
- Informed parental consent was obtained for all subjects and multicentre ethical approval was given by the East Midlands – Derby Research Ethics Committee (REC/HRA ref: 04/MRE04/41) to the study: Functional Imaging of Tumours (CNS 2004 10); under the rules of Declaration of Helsinki 1975 (and as revised in 1983). The data was downloaded from the Children's Cancer and Leukaemia Group (CCLG) Functional Imaging Group e-repository.
- Perfusion MRI post-processing was performed using an in-house tool developed by Dr. Stephanie Withey.
- The MIROR study was part of a larger collaborative project. Tumour regions-of-interest were drawn by Dr. Karen Manias and refined by consultant radiologist Dr. Katharine Foster. The graphical user interface (GUI) was implemented by Dr. Niloufar Zarinabad, who also aided in aspects of module development and connecting the diffusion algorithms to the user interface.

Acknowledgements

First and foremost, I would like to thank my supervisors Andrew Peet, Jan Novak, and Hamid Dehghani for their guidance and support throughout this Ph.D. I am grateful for having the chance to do research in such an exciting field of study, and the opportunity to widen my horizons into new disciplines.

I want to thank everyone of the Children's Brain Tumour Research Team (past and present) for providing a welcoming place to work at. Becky Sawbridge, Dom Carlin and Emma Metcalfe-Smith, for sharing the journey of Ph.D., the good and the bad, and for providing an invaluable support system. Heather Rose and Chris Bennett, for all the coffee breaks and the discussions about the most random of things, I'll be missing those. Niloufar Zarinabad, for being my mentor and most of all for being my friend, I've learned so much from you.

I also want to thank everyone at the PSIBS doctoral training centre for creating a community of enthusiastic scientists. Thank you for your inspiration and motivation. Thanks to Engineering and Physical Sciences Research Council (EPSRC, EP/F50053X/1) for funding this project. I also acknowledge support from the National Institute for Health Research (NIHR, 13-0053), the Birmingham Children's Hospital Research Foundation and Help Harry Help Others in conjunction with Free Radio. MR imaging was performed in the NIHR 3T MRI Research Centre at Birmingham Children's Hospital.

Finally, I am the most grateful to my husband and my family for their encouragement, love and never-ending support. Yannick, thank you for bearing with me on the late nights and reminding me that there is life outside the Ph.D. My parents, thank you for being supportive of the choices I've made throughout these years, I wouldn't be here without you.

Publications

Journal publications:

- [**P01**] **E.M. Meeus**, J. Novak, S.B. Withey, N. Zarinabad, H. Dehghani and A.C. Peet, "Evaluation of intravoxel incoherent motion fitting methods in low-perfused tissue", *Journal of Magnetic Resonance Imaging*, 2017;45:1325-1334.
- [**P02**] **E.M. Meeus**, J. Novak, H. Dehghani and A.C. Peet, "Rapid Measurement of Intravoxel Incoherent Motion Derived Perfusion Fraction for Clinical Magnetic Resonance Imaging", *Magnetic Resonance Materials in Physics, Biology and Medicine*, 2017, DOI: 10.1007/s10334-017-0656-6
- [**P03**] **E.M. Meeus**, N. Zarinabad, K.A. Manias, J. Novak, H. Rose, H. Dehghani, K. Foster, B. Morland and A.C. Peet, "Diffusion-Weighted MRI and Intravoxel Incoherent Motion Model for Diagnosis of Pediatric Solid Abdominal Tumors", *Journal of Magnetic Resonance Imaging*, 2017, DOI: 10.1002/jmri.25901
- [**P04**] N. Zarinabad, K.A. Manias, **E.M. Meeus**, K. Foster and A.C. Peet, "MIROR, An automated modular MRI clinical decision support system: an application in paediatric cancer diagnosis", *JMIR Medical Informatics*, 2017, DOI: 10.2196/medinform.9171

Conference presentations:

- [**P05**] **E.M. Meeus**, J. Novak, S.B. Withey, N. Zarinabad, L. MacPherson, H. Dehghani and A.C. Peet, "Evaluation of IVIM Perfusion Parameters as Biomarkers for Paediatric Brain Tumours", *International Society of Magnetic Resonance in Medicine (ISMRM) Annual Scientific Meeting*, Singapore, Singapore. 2016: 2047.
- [**P06**] **E.M. Meeus**, J. Novak, H. Dehghani and A.C. Peet, "Rapid Measurement of Perfusion Fraction in Clinical Neuroimaging", *International Society of Magnetic Resonance in Medicine (ISMRM) Annual Scientific Meeting*, Honolulu, Hawaii USA. 2017: 1806.
- [**P07**] K.A. Manias, N. Zarinabad, K. Foster, P. Davies, **E.M. Meeus (presenter)** and A.C. Peet, "The role of ADC histogram analysis in discriminating between benign and malignant tumours in children", *International Society of Magnetic Resonance in Medicine (ISMRM) Annual Scientific Meeting*, Honolulu, Hawaii USA. 2017: 2910.
- [**P08**] **E.M. Meeus,** J. Novak, H. Dehghani and A.C. Peet, "Investigation of Tissue Microenvironments using Diffusion MRI and its Applications in Childhood Cancers", *Research Poster Conference*, University of Birmingham, UK. 2017.

Table of Contents

List of Illustrations

List of Tables

Abbreviations

ADC = Apparent diffusion coefficient

ANOVA = Analysis of variance

AUC = Area under the ROC curve

CBV = Cerebral blood volume

CBF = Cerebral blood flow

CDSS = Clinical decision support system

CSF = Cerebrospinal fluid

CV = Coefficient of variation

DICOM = Digital imaging and communications in medicine

DWI = Diffusion-weighted imaging

DSC = Dynamic susceptibility contrast

GM = Grey matter

IVIM = Intravoxel incoherent motion

MIROR = Medical image region-of-interest analysis tool and repository

MRI = Magnetic resonance imaging

MTT = Mean transit time

ROC = Receiver operating characteristic

ROI = Region-of-interest

SNR = Signal-to-noise ratio

WM = White matter

Chapter 1

Introduction

1. Introduction

This Chapter introduces the role of non-invasive imaging in the clinical management of childhood cancers. The focus is on magnetic resonance imaging (MRI), how it has contributed towards the improvements seen in patient care and what challenges remain today. The concept of imaging biomarkers is then introduced and tied to the aims and objectives of this thesis.

1.1 Importance of MR Imaging in Childhood Cancers

More than 1,800 new cases of childhood cancers are diagnosed every year in the United Kingdom (1). Cancer is the leading cause of disease related deaths in children aged 1-14, and the highest incidence rates are observed for ages 0-4. Brain and other central nervous system (CNS) tumours (Figure 1.1) are the principal cause of children's cancer death, accounting for 32 % of cases (2). However, with improvements made in the last 50 years, the survival rates for CNS tumours have doubled to 70 % at five years. Nevertheless, brain tumours present a diverse group of tumours, and the survival rates remain very tumour specific. Overall, the survival rates for childhood cancers stand at approximately 82 % over five or more years (1).

MR imaging is a non-invasive imaging method, which is increasingly used and has led to improvements in clinical management of childhood cancers (3, 4). Depending on the location and type of tumour, MR imaging is performed at diagnosis, prior to and after surgery, during treatment and at the end of the treatment for tumour surveillance (5). The standard clinical imaging includes conventional MR imaging protocols, which provide excellent structural detail in millimetre resolution, but are limited in measuring quantitative tissue properties.

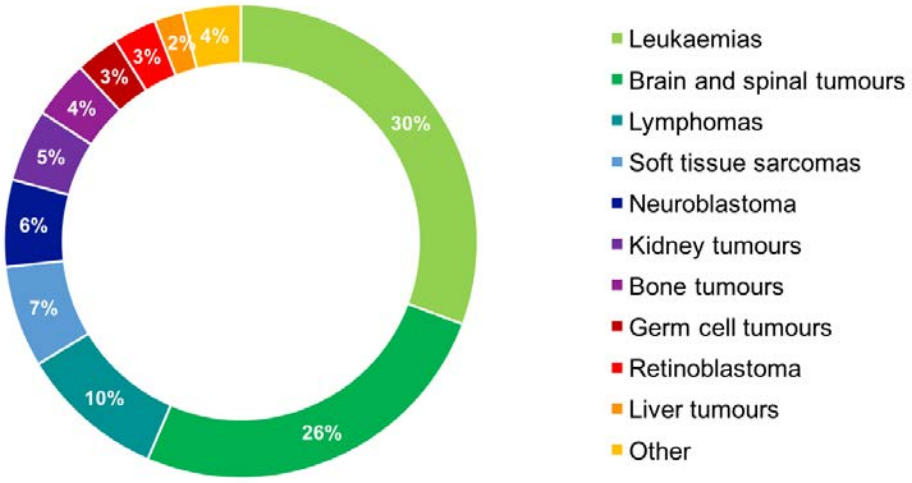

Figure 1.1 Childhood cancer types. A chart demonstrating the incidence of childhood cancers in the UK and Ireland (source: CCLG, 2017 (6)).

MR imaging is used in the diagnosis of both brain and body tumours, although histopathological diagnosis following biopsy or surgical resection remains the gold standard. Diagnosis based on MR imaging involves the qualitative assessment of the appearance of the tumour on the resulting MR images. However, some childhood tumours, such as CNS tumours, are very diverse in their pathology (Figure 1.2) and some tumour types, in both the brain and abdomen, are known to have overlapping imaging characteristics (4, 7). Therefore, diagnosis of tumours is often not possible and thus rarely based on conventional MR imaging alone.

Based on the most recent World Health Organization (WHO) classification (2016), there are now more than 50 different brain tumour types and subtypes (8). Previous brain studies have demonstrated that conventional MR imaging alone is not tumour grade or type specific (9, 10), while separate challenges remain with procedures required for histopathological diagnosis. For example, some brain tumours occur in regions that are not surgically accessible, which means that the diagnosis and choice of treatment will be based solely on the qualitative inspection of images. In the abdomen, tumours are often large and heterogeneous in nature, which means that the biopsy might not be obtained

from a region that is very characteristic of the tumour type. These challenges highlight the need for more advanced quantitative imaging methods, in particular for cases where biopsy might not be possible.

Conventional MR imaging has also been used for the assessment of treatment response. This relies on the measurement of tumour volume changes, often only based on the largest tumour diameter on a single image slice. However, with the low specificity of MR imaging in biological tissue, the differentiation of tumours from pseudoprogression or pseudoresponse can be difficult (11). Pseudoprogression and pseudoresponse correspond to an apparent false increase and decrease in tumour size, respectively, assuming a contrast agent is used for an enhancement. For example, differentiation of pseudoresponse from true tumour response can be difficult, when a decrease in the enhancement indicates a response to a treatment, but could result from changes in the vascular permeability. Changes in the vascular permeability are often a result of certain chemotherapy drugs, and the effect may be readily reversible when the drug is stopped. Therefore, while conventional MR imaging has become an important technique in the assessment of tumours, new quantitative MR imaging methods are required to improve its specificity in characterising tissues.

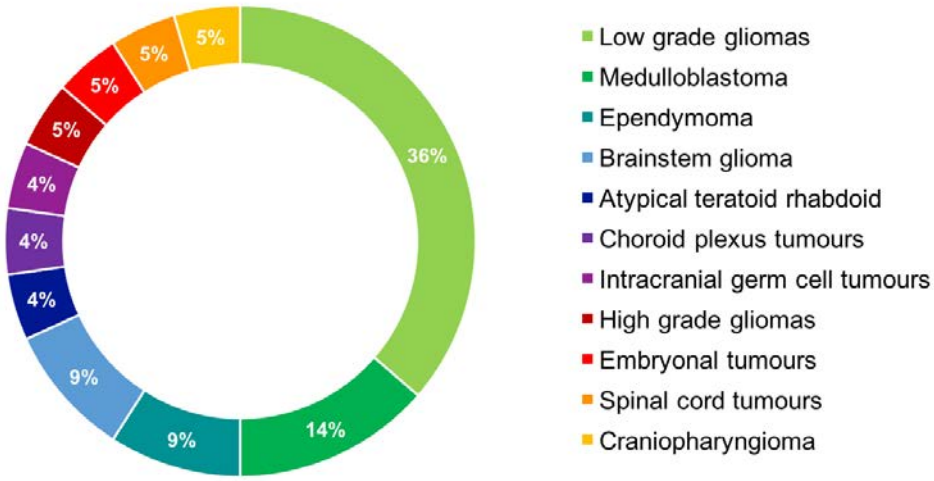

Figure 1.2 Childhood brain cancer types. A chart demonstrating the incidence of different childhood brain cancers in the UK and Ireland (source: CCLG, 2017 (6)).

1.2 Diffusion-weighted MR Imaging of Childhood Cancers

The development of new MR imaging techniques, such as diffusion- and perfusion-weighted imaging and MR spectroscopy, has made it possible to probe the underlying tissue properties and characteristics. These methods have the potential to provide clinically relevant and complementary information, far extending the information provided by conventional MR imaging. A range of these advanced imaging methods are already being implemented in clinical practice, further increasing the role of MR imaging in clinical management of childhood cancers (3, 12).

Diffusion-weighted MR imaging (DW-MRI) is one of the most widely accepted non-conventional MR imaging methods, where the MR signal is attenuated by the movement of water molecules. DW-MRI initially gained a lot of attention in the imaging of acute stroke, where it was able to detect a 30-50 % decrease in the water signal during the very early phase of acute brain ischemia (13). Conventional MR imaging on the same cases showed no apparent differences. These observations led to the development of DW-MRI as a clinical tool, formally only considered a pure research tool, and to its implementation on most clinical systems today as a standard protocol.

DW-MRI has been applied as both a diagnostic and prognostic technique. The commonly derived quantitative parameter from DW-MRI is the apparent diffusion coefficient (ADC), which measures the apparent magnitude of diffusion within tissue. In clinical practice, the ADC is often determined using two *b*-values, which correspond to the degree of diffusion-weighting applied in the MR imaging. The ADC (in units of mm^2/s) can then be calculated from the fitting gradient of the diffusion-weighted signal measured at the corresponding *b*-values. Although ADC provides a quantitative measure, it is generally only used by qualitative review of the ADC maps in clinical practice. ADC has been associated with an inverse relationship to extracellular density in many previous studies, including paediatric studies (14-20). However, other biophysical processes relating to the different environments of the water molecules have the potential to increase the apparent water diffusion, including perfusion, bulk movement such as cardiac and respiratory motion, necrosis and nuclei to cytoplasm ratio (19, 21-23).

The effect of perfusion on ADC and the diffusion signal attenuation has been demonstrated in previous studies using multiple *b*-values (23-26). The use of multiple *b*-values allows the detection of faster and slower diffusion components at low and high *b*-values, respectively. Using this concept, Le Bihan et al. (24, 25) proposed the intravoxel incoherent motion (IVIM) model, which accounts for the perfusion effect in the modelling of diffusion-weighted MR signal. The model has been applied in an increasing number of adult studies (27-30), but only a few studies have reported its use in paediatrics (31-34). A more thorough introduction to the IVIM model is given in the following Chapter.

A large number of studies have been reported on paediatric brain tumours and their characterisation with ADC (35-40). These include classification of cerebellar tumours and tumour grading, although overlapping ADC values of some of these tumours limit

its diagnostic performance (35-38, 40). Some of the most cited articles include a study by Bull et al. (35), who showed a 74.1 % success rate in discrimination of paediatric brain tumours, and a study by Rodriguez et al. (39), who reported a 91.4 % success rate for posterior fossa tumours. Both studies used a histogram analysis, which accounted for the tumour heterogeneity.

Only a few studies have reported the characterisation of childhood abdominal tumours with ADC (32, 41-43) and most of these studies focused on discriminating between benign and malignant abdominal lesions. For example, a study by Kocaoglu et al. (41) demonstrated a significantly lower ADC for malignant tumours compared to benign cases, and a cut-off value 1.11×10^{-3} mm^2/s was determined. However, in some cases, ADC was not predictive of the benign nature of lesions, possibly due to the influence from other underlying tissue properties such as vascularity, which is not accounted for by the ADC.

Although promising results have been reported for the use of ADC in the characterisation of paediatric tumours, limitations exist in its methodology. The qualitative use of ADC in clinical practice restricts its potential, though slow movement towards using quantitative information as part of clinical management is taking place. Some of these methodological limitations are discussed in the following Chapter 2, together with alternative approaches and models for the diffusion-weighted signal.

1.3 Imaging Biomarkers

A biomarker is defined as "a characteristic that is measured as an indicator of normal biological processes, pathogenic processes or responses to an exposure or intervention, including therapeutic interventions" (44). According to the most recent consensus statement from the FDA-NIH Biomarker Working Group, a biomarker can be a molecular, histologic, radiographic or physiologic characteristic (45). Both imaging and biospecimen-derived biomarkers have been widely studied in oncology, and include biomarkers for many different purposes. For example, biomarkers have been used in the diagnosis and prognosis of cancer, staging of cancer, and assessment of therapeutic efficacy or toxicity (46).

New imaging biomarkers are increasingly needed to test research hypotheses in clinical trials and research studies, and to utilise them as clinical decision-making tools. To accelerate this process, a recent consensus paper for cancer studies introduced guidelines for the clinical translation of imaging biomarkers (47). The process requires validation and quantification by crossing the two translational gaps, as described in Figure 1.3. These gaps represent the key points in the evaluation of biomarkers, and are defined as the stage when the imaging biomarker can be reliably used to test medical hypotheses, and the final stage, when it can be used as a tool for clinical-decision making.

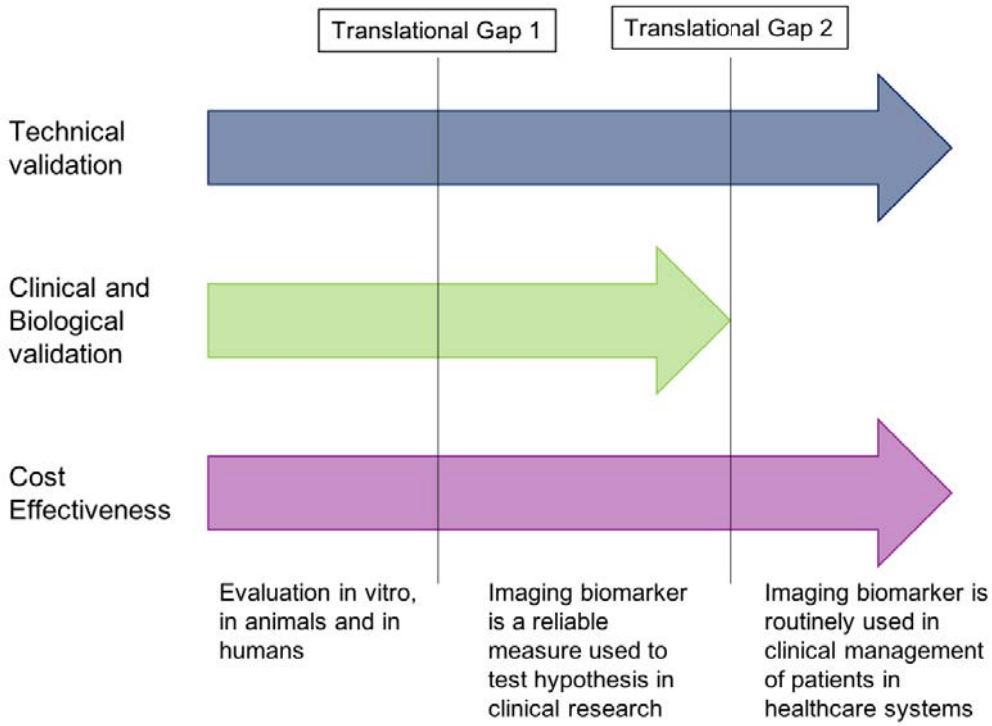

Figure 1.3 Summary of the imaging biomarker evaluation and development. The development of imaging biomarkers includes two key translational gaps. Gap 1: to become a robust medical research tool, and Gap 2: to be integrated into a routine patient care. The figure is adapted from the consensus study by Cancer Research UK (CRUK) and the European Organisation for Research and Treatment of Cancer (EORTC) (47).

The technical and biological validation of imaging biomarkers run in a parallel fashion, together with considerations for the cost effectiveness. The technical validation of imaging biomarkers involves the assessment of precision and accuracy, and whether the biomarker (and hence imaging method) is accessible in different geographical locations. The biological and clinical validation determines whether the biomarker can measure a relevant biological property or predict a clinical outcome. The processes also include an assessment of uncertainty and risk in using the biomarker for clinical-decision making. Finally, cost effectiveness has a key role in later aspects such as large multi-centre reproducibility studies and clinical trials.

As part of the consensus study (47), four key attributes were suggested for all imaging biomarkers:

I. The imaging biomarker is a subset of all biomarkers
II. The imaging biomarker is either quantitative or qualitative (categorical)
III. The imaging biomarker is derived from imaging modality, technique or signal, but is a distinct entity
IV. One imaging measurement can support multiple distinct imaging biomarkers.

Imaging biomarkers also have some additional considerations in comparison to biospecimen-derived biomarkers. These include the performance of the imaging device, which might vary across different clinical centres and manufacturers. Innovation in manufacturing tends to focus on the image quality and user interface, while the effects of quantification of imaging biomarkers remain secondary. Furthermore, the validation of imaging biomarkers is not aligned with biospecimen-derived biomarkers. An important part of biospecimen-derived biomarker validation is to assess the biophysical stability and reliability of the analytes. However, this is not possible with image analysis and the validity of the measurement mainly remains at the point of patient imaging. A detailed roadmap proposed for the development of imaging biomarkers is presented in Figure 1.4 (47).

The current practice of medicine has transformed with the introduction and development of new imaging methods (48). Imaging biomarkers have an immense potential in further improving the clinical management of cancer by addressing different clinical questions from diagnosis to assessing treatment effects. However, as suggested by the guidelines, careful validation and quantification is essential to ensure that informed decisions can be made based on the imaging biomarkers.

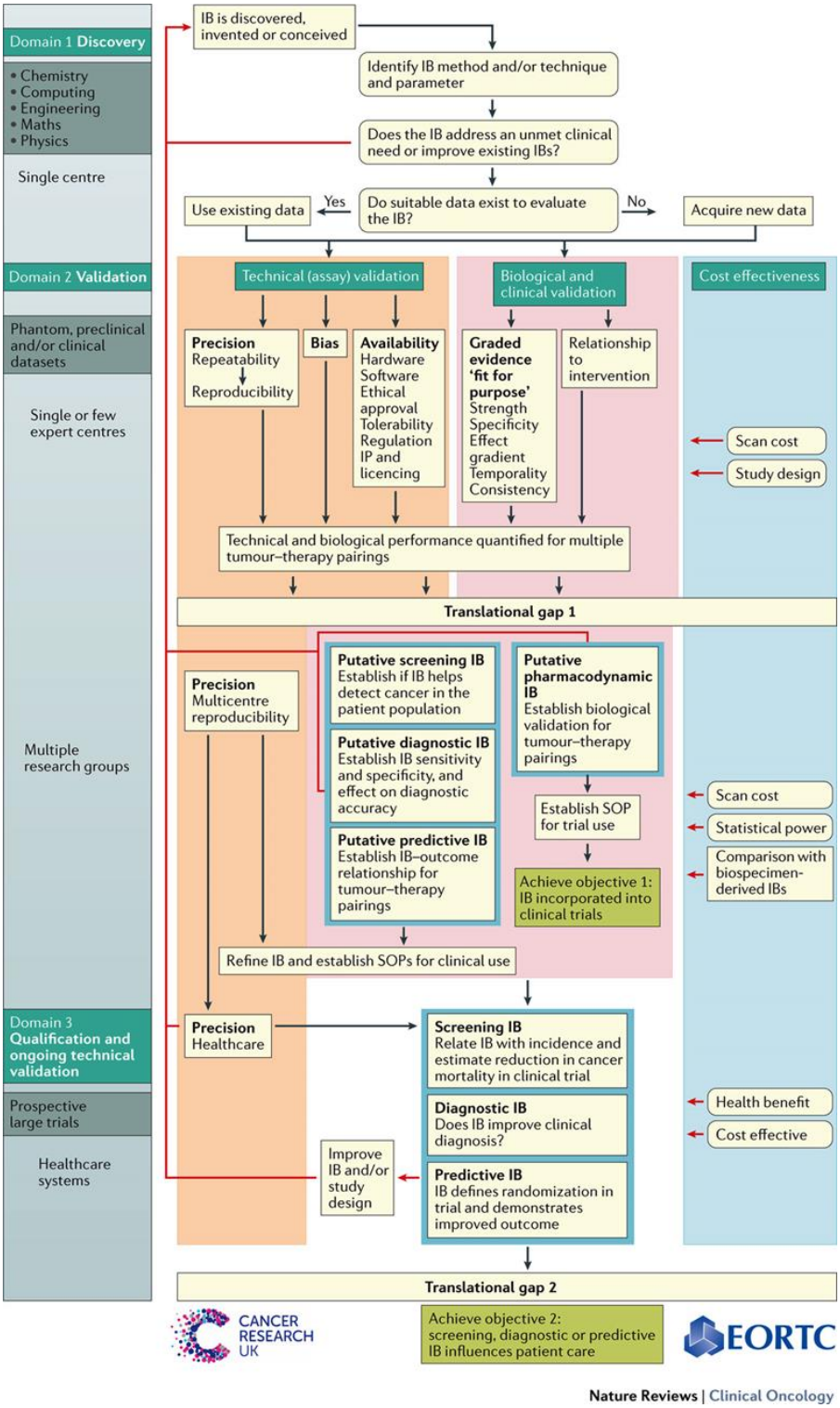

Figure 1.4 The imaging biomarker roadmap. A schematic roadmap produced for imaging biomarker evaluation in cancer studies. Technical and clinical validation run parallel, and important technical validation e.g. multicentre reproducibility occurs later in the evaluation after which definitive clinical validation in terms of clinical trials can take place. At each stage, cost effectiveness impacts the roadmap. (source: O'Connor, JPB. et al. (2016) Imaging biomarker roadmap for cancer studies *Nat. Rev. Clin. Oncol.* doi:10.1038/nrclinonc.2016.162, ref (47), under Creative Commons licence v.4.0)

1.4 Aims and Objectives

The overall aim of this work was to investigate diffusion-weighted MR imaging and the application of intravoxel incoherent motion (IVIM) model in childhood cancers. The study focuses on the post-processing aspects of IVIM and its technical and biological validation as a potential imaging biomarker.

Objectives:

I. To investigate the robustness of IVIM fitting methods and parameters in low-perfused tissues observed in the brain and childhood brain tumours

II. To establish the reliability of IVIM parameters based on a rapid MR imaging protocol for tissues in the brain and abdomen

III. To investigate the biophysical origin of IVIM perfusion fraction parameter by comparison to dynamic susceptibility contrast (DSC) MR imaging derived cerebral blood volume parameter, in healthy and pathological brain tissue

IV. To integrate the IVIM application into an in-house built clinical decision support system, MIROR.

V. To evaluate the use of IVIM as potential diagnostic biomarker in a cohort of childhood abdominal lesions

1.5 Thesis Structure

This Chapter provided background to the clinical motivation behind the presented work and introduced the concept of imaging biomarkers. The content of the following Chapters is summarised below:

Chapter 2: Diffusion-Weighted MR Imaging and Modelling of the Diffusion Signal

Chapter 2 provides the theoretical background on the principles of MR imaging, with focus on diffusion-weighted MRI (DW-MRI). The physical phenomenon of apparent diffusion, how it appears in biological tissues, how it can be measured and modelled are discussed. A more thorough review is given on the concepts of intravoxel incoherent motion (IVIM) model, its implementation, biophysical origins and clinical applications.

Chapter 3: Investigation of IVIM Fitting Methods in Low-Perfused Tissues

In this Chapter, the robustness of constrained and simultaneous IVIM fitting methods are investigated using model simulations based on low-perfused tissues as part of the technical validation of IVIM. Previous simulation studies have included higher perfusion scenarios, which differ from what is observed in many of the childhood brain tumours. Evaluation of the uniqueness of IVIM parameters is also performed to assess their clinical reliability.

Chapter 4: Rapid Measurement of IVIM Perfusion Fraction for use in Clinical MR Imaging

Chapter 4 continues with the technical validation of IVIM and investigates the dependency between estimated IVIM parameters and the acquired data i.e. *b*-values. While many studies have focused on increasing the number of *b*-values, here we assess the use of simple three *b*-value acquisition to determine the IVIM diffusion coefficient and perfusion fraction, which have previously shown promising clinical value. The reliability of the IVIM parameters is assessed in terms of bias, accuracy and

reproducibility for different perfusion scenarios, including tissue models relevant to brain, kidney and liver. Based on the model simulations, the optimal use of *b*-values is suggested for different tissue types, including discussion on common pathologies and interpretation of differences seen between IVIM parameters from previous studies. A comparison of the model data to in vivo brain DW-MRI data is used to validate the results.

Chapter 5: Comparison Study of IVIM and DSC Perfusion Parameters in Childhood Brain Tumours

In Chapter 5, the focus is on the biological validation of the IVIM perfusion fraction parameter. The physical origins of the perfusion fraction are investigated with comparison to the "gold standard" dynamic susceptibility contrast (DSC) derived cerebral blood volume (CBV). Although this comparison has been performed previously in adult brain tumours, here we look at childhood low-grade gliomas, which commonly have low perfusion, to assess whether IVIM could provide an alternative non-invasive measure of vascularity. The similarities and differences of IVIM perfusion fraction and DSC-CBV parameters are discussed.

Chapter 6: MIROR Clinical Decision Support System: Implementation of Diffusion Module and Investigation of Childhood Solid Tumours

Chapter 6 describes the implementation of a diffusion module, including ADC and IVIM modules, to an in-house built clinical decision support system, MIROR. The implemented diffusion module is applied to a cohort of childhood abdominal lesions to validate its use and to evaluate the potential of IVIM parameters as diagnostic biomarkers. The purpose of the module was to develop an adaptable MR analysis tool for clinicians, and to provide a framework for its use as part of the evidence-adaptive clinical decision support system at a later stage.

Chapter 7: Conclusions and Further Work

The final Chapter provides a summary of the results presented in this thesis and the conclusion drawn from this study. Suggestions for future work and directions are also proposed.

Chapter 2

Diffusion-Weighted MR Imaging and Modelling of the Diffusion Signal

2. Diffusion-Weighted MR Imaging and Modelling of the Diffusion Signal

This Chapter provides a background to MR imaging. The focus is on diffusion-weighted MR imaging and how it can be modelled to provide information about the underlying tissue microstructure and microenvironment. For a more in-depth description of MR imaging, please refer to textbooks by Brown et al. (49) and Freeman (50).

2.1 MR Imaging

MR imaging is derived from the physical phenomenon known as nuclear magnetic resonance (NMR). Here the principles of NMR and the idea of nuclear spin are introduced using the classical physics and the quantum mechanical models, respectively. The focus in this section is on the ^{1}H protons of water, which constitutes approximately 70 % (51) of the adult human body. Because of this, the protons are the most commonly used nuclei in clinical MR imaging.

2.1.1 Nuclear Magnetic Resonance

Nuclei that possess nuclear spin are said to be NMR active. Nuclear spin is a property of a nucleus, which contains unpaired nucleons comprising of neutrons and protons, each with a nuclear spin of a half. Therefore, an NMR active nucleus always has a non-zero spin quantum number, $\boldsymbol{I}$, and for the case of ^{1}H, $\boldsymbol{I} = ½$, corresponding to the single proton in the nucleus. Another property of a nucleus possessing a nuclear spin is the spin angular momentum, $\boldsymbol{P}$, which is defined as $2\,\boldsymbol{I} + 1$. This defines the number of possible orientations of the spin along a given axis. For the ^{1}H nucleus, this results in two possible spin states, + ½ and - ½. The two spin states (m = + ½ and m = - ½) are degenerate in the absence of an external magnetic field (Figure 2.1). However, when the nucleus is placed in a magnetic field, the interactions between the magnetic moment and

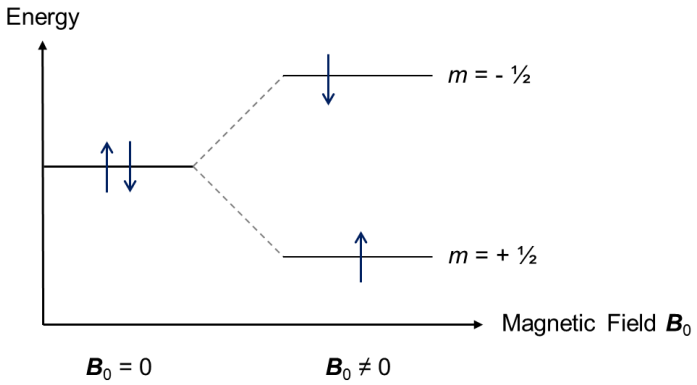

Figure 2.1 Energy levels of a proton nucleus. Diagram of the energy levels of a proton nucleus in the absence of a magnetic field ($\boldsymbol{B}_0 = 0$) and the splitting of the spin states in an applied magnetic field ($\boldsymbol{B}_0 \neq 0$).

the static magnetic field result in splitting of the spin states. The magnetic moment of a nucleus is related to its spin angular momentum with a proportionality constant γ, the gyromagnetic ratio:

$$\boldsymbol{\mu} = \gamma \boldsymbol{P} \qquad [2.1]$$

The gyromagnetic ratio for a ^{1}H nucleus is $\gamma = 2.68 \times 10^8$ rad s^{-1} T^{-1}, which is defined as the ratio of its magnetic moment to its angular momentum.

The precession of spins is often described using classical physics. The nuclear spins start to precess due to torque imposed on the magnetic moments by the applied magnetic field (Figure 2.2). The precession occurs in the direction of $\boldsymbol{B}_0$ and the rate of this precession is called the Larmor frequency (in s^{-1}). The precession is proportional to γ and the strength of the magnetic field:

$$\omega = \frac{\gamma \boldsymbol{B_0}}{2\pi} \qquad [2.2]$$

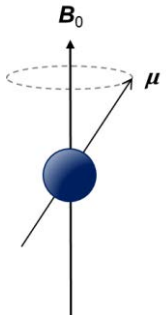

Figure 2.2 Precession of a nucleus. Diagram of the precession of a nucleus in an applied magnetic field.

The nuclear spins that align parallel (+ ½) to the external field are in a lower energy state compared to those that align anti-parallel (- ½) (Figure 2.1). The energy gap between the two states can be defined as:

$$\Delta E = \mathrm{h}\upsilon = \frac{\mathrm{h}\gamma \boldsymbol{B}_0}{2\pi} \qquad [2.3]$$

where h is the Planck's constant and υ is the frequency.

In NMR experiments, the focus is on the ensemble of spins, rather than the behaviour of the individual spins. This is described by the macroscopic magnetisation vector, $\boldsymbol{M}_0$ (Figure 2.3), which is the sum of all the individual spin vectors. At the thermal equilibrium, the spins are distributed per the Boltzmann distribution and the difference between the spin populations is extremely small, with a small excess in the lower energy state. This means that at the equilibrium, the macroscopic magnetisation vector $\boldsymbol{M}_0$ aligns along the direction of the applied field. The ratio of the spin populations is governed by the Boltzmann equation:

$$\frac{N_+}{N_-} = \exp\left(\frac{-\Delta E}{\mathrm{k}_B T}\right) \qquad [2.4]$$

where N_+ and N_- are the number of spins aligning parallel and anti-parallel to the field, respectively, $\mathrm{k_B}$ is the Boltzmann constant and T is the temperature.

The magnetisation vector, $\boldsymbol{M}_0$, is what is being manipulated in MR imaging and forms the basis of all experiments.

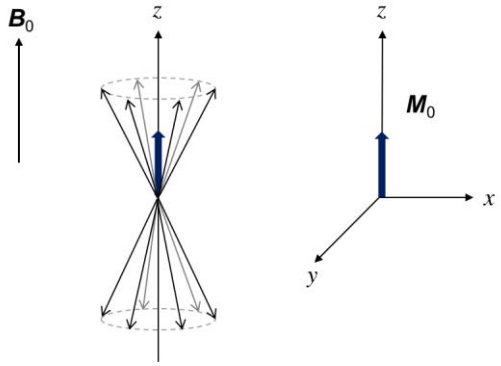

Figure 2.3 Macroscopic magnetisation vector, M_0. Diagram of the vector presentation of the spin ensemble and the resulting macroscopic magnetisation vector, $\boldsymbol{M}_0$ aligning along the direction of the applied magnetic field.

2.1.2 Radio frequency Pulses

Radio frequency (rf) pulses can be used to manipulate the $\boldsymbol{M}_0$ vector. This results in transitions between the spin-states, when the energy of radiation is equal to ΔE and matches the Larmor frequency. The NMR signal may be measured when the $\boldsymbol{M}_0$ vector precesses orthogonally to the applied field and the precession induces an oscillating current within the receiver coil. The maximum NMR signal can be produced by an rf pulse that brings the $\boldsymbol{M}_0$ vector to the *xy* transverse plane (Figure 2.4). This corresponds to an rf pulse with an intensity and duration that result in a rotation of 90 degrees. The angle of rotation is called the flip angle (θ), which can be calculated using:

$$\theta = \gamma \boldsymbol{B}_1 t_p \qquad [2.5]$$

where $\boldsymbol{B}_1$ is the generated rf field and t_p is the time duration of the applied pulse.

After an rf pulse, the magnetisation vector will return to its thermal equilibrium over time due to two relaxation processes, the longitudinal and transverse relaxation. The signal decay over time is called the free induction decay (FID). The combination of measured MR signals (a series of damped sine waves) can be separated by a Fourier transformation, which converts the time domain signal to a frequency domain (Figure 2.5).

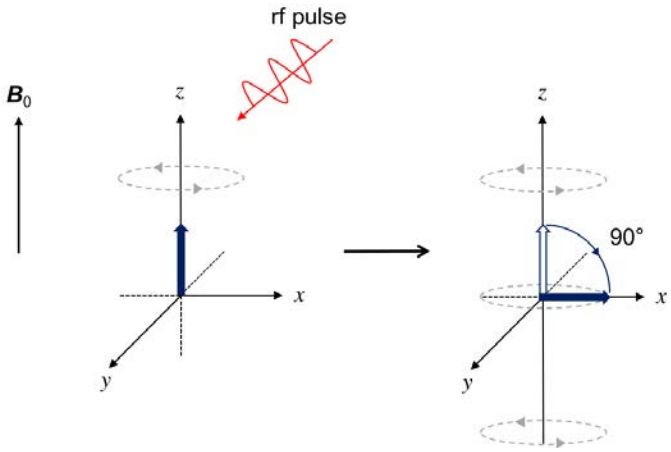

Figure 2.4 Application of a radio frequency pulse. Diagram of the application of a 90-degree pulse to bring the magnetisation vector, $\boldsymbol{M}_0$, to the *xy* transverse plane, where it can produce the maximum NMR signal.

The complex motion of spins is often simplified by using a rotating frame of reference. This means that the *xy* plane (the reference frame) is assumed to rotate around the *z*-axis at the Larmor frequency. After a 90 degree rf pulse, the magnetisation vector and the applied field will then appear stationary and the system can be referred to as on-resonance. This simplifies the description of any deviations from the Larmor frequency.

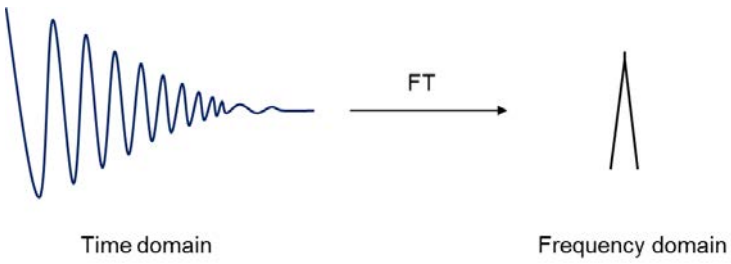

Figure 2.5 Free induction decay (FID). Diagram of the acquired free induction decay signal in the time domain, and the conversion to frequency domain by application of a Fourier transformation.

2.1.3 Relaxation Processes

The return of the spins to thermal equilibrium after an rf pulse happens via spin-lattice (T_1) and spin-spin (T_2) relaxation processes (Figure 2.6). The T_1 relaxation, also known as longitudinal relaxation, corresponds to the process of spins moving between the energy levels to restore the thermal equilibrium. This causes the release of energy from spins to the surrounding environment, the lattice. The T_1 is the time constant defined as the time it takes for a signal to recover back to 63 % of its original value and is described by (52):

$$\boldsymbol{M}_z = \boldsymbol{M}_0(1 - \exp^{-t/T_1}) \quad [2.6]$$

where $\boldsymbol{M}_z$ is the component of the bulk magnetisation vector in the z-direction, and t is the time delay allowed for longitudinal relaxation ($\boldsymbol{M}_z = 0$ at $t = 0$ returns to $\boldsymbol{M}_z \neq 0$).

The T_2 relaxation, also known as transverse relaxation, is the time it takes for a system to lose its phase coherence on the xy plane. After a 90-degree rf pulse, the spins have phase coherence by alignment in the transverse plane, but due to inter-and intra-molecular interactions, the phase coherence is lost. The T_2 relaxation can be described by (52):

$$\boldsymbol{M}_z = \boldsymbol{M}_0 \cdot \exp^{-t/T_2} \quad [2.7]$$

where t is the time delay.

The measurement of T_2 relaxation is sensitive to any microscopic diffusion taking place during the MR acquisition and the presence of inhomogeneities in the applied magnetic field ($\boldsymbol{B}_0$). This causes the incomplete refocusing of the magnetisation vector (in gradient-echo imaging), which results in a significantly shorter T_2 compared to the real T_2 relaxation time. The measured T_2 is then referred to as the T_2* relaxation time. However, the real T_2 relaxation time can be measured with spin-echo imaging, which eliminates the field inhomogeneity and diffusion effects by an application of a 180-degree

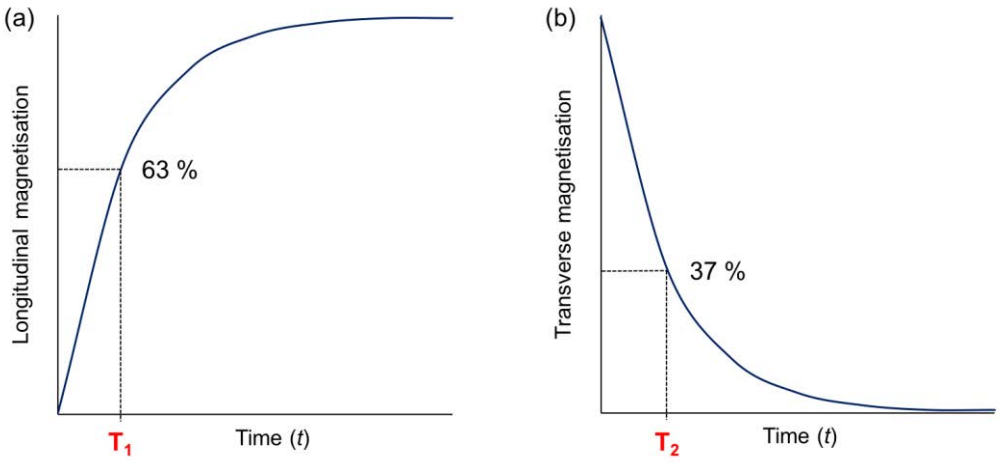

Figure 2.6 Return of the system back to thermal equilibrium via relaxation processes. Recovery of the magnetisation vector, $\boldsymbol{M}_0$, with (a) longitudinal relaxation and (b) transverse relaxation over time. The T_1 relaxation time is defined as the 63 % ($1 \times T_1$) recovery of the maximum value of $\boldsymbol{M}_0$, with full recovery reached at approximately $5 \times T_1$. Similarly, the T_2 relaxation is the time defined as reduction of the $\boldsymbol{M}_{xy}$ to 37 % of its initial value after rf excitation.

rf pulse, and refocuses the signal on a timescale, where the diffusion effects are kept minimal.

2.1.4 Magnetic Field Gradients and Image Acquisition

Magnetic field gradients are used in MR imaging to localise the MR signal. The gradients are applied in a controlled manner and are used to construct pulse sequences together with rf pulses and the constantly present static magnetic field, $\boldsymbol{B}_0$. Gradients apply spatially linear variation to the static magnetic field, e.g. a gradient $\boldsymbol{G}_x$ will add or subtract from the magnitude of $\boldsymbol{B}_0$ in different points along the x-direction, as described in Figure 2.7. The precession of the spins will linearly decrease or increase depending on their position. At the centre ($x = 0$) the spins will precess at the Larmor frequency as the total magnetic field equals $\boldsymbol{B}_0$.

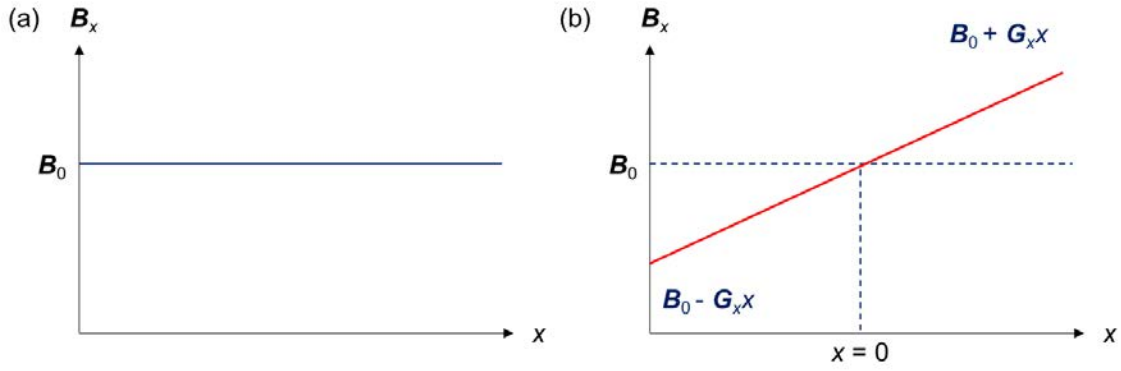

Figure 2.7 Application of magnetic field gradients. (a) No gradients are applied and the spins precess at the same frequency and (b) application of a magnetic field gradient $\boldsymbol{G}_x$ in x direction, introducing spatial dependency to the magnetic field (in z direction) with position along x.

An example of a basic gradient-echo (GRE) pulse sequence is shown in Figure 2.8, which describes how the MR signal is encoded for position using three orthogonal magnetic field gradients. The sequence starts with a slice selection by simultaneous application of a frequency selective rf pulse, containing a narrow band of frequencies and a linear slice selective gradient $\boldsymbol{G}_{ss}$ gradient (also known as $\boldsymbol{G}_z$), applied along the direction of the selected slice. This results in an excitation of a thin section, where the object has a resonance frequency (or Larmor frequency) within the bandwidth of the applied rf pulse. The thickness of the slice is determined by the effective bandwidth of the rf pulse and the magnitude of the applied gradient. The application of a negative $\boldsymbol{G}_{ss}$ gradient after the slice selection is to re-focus the spins within the selected slice in preparation for the following gradients.

The next part of the GRE sequence involves the application of phase (PE) and frequency (FE) encoding gradients to determine the spin density within the selected slice. The PE gradient is applied for a fixed time period prior to signal acquisition and affects the phase of the spins. After the gradient is switched off, the frequencies of the spins become similar, but with a phase difference dependent on their position. This is repeated until all possible spatial frequencies are interrogated in the phase-encoding direction.

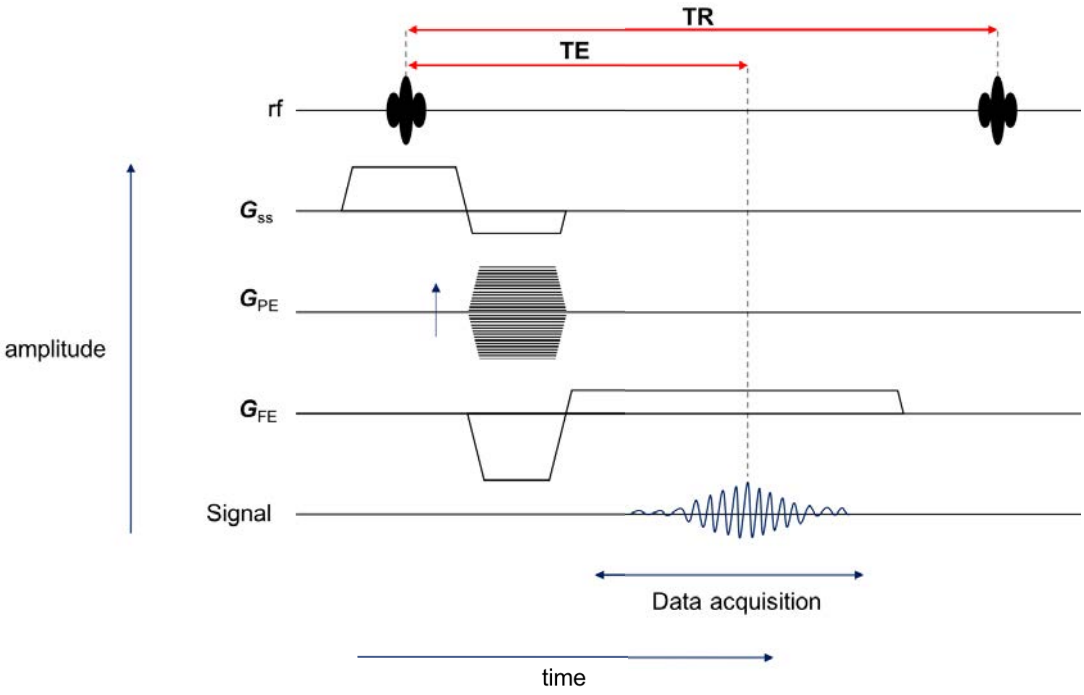

Figure 2.8 Gradient-echo MR imaging pulse sequence. Diagram of a basic gradient-echo MR imaging pulse sequence, which includes the simultaneous application of an rf pulse and a slice selective gradient ($\boldsymbol{G}_{ss}$), followed by the application of phase and frequency encoding ($\boldsymbol{G}_{PE}$ and $\boldsymbol{G}_{FE}$) gradients and the signal acquisition. TE and TR correspond to the sequence echo time and repetition time.

The FE gradient consists of bipolar gradient pulses to generate a gradient echo, which is required for the data sampling as there are no refocusing rf pulses. A negative FE gradient is first applied to dephase the signal, after which the positive FE gradient is used as a readout gradient during the acquisition. The signal is acquired at fixed time intervals, encoding the signal for position in terms of the frequency. The pulse sequence is then repeated to collect all the data within the user-defined region.

The GRE pulse sequence in Figure 2.8 also features the basic pulse sequence parameters: echo time (TE) and repetition time (TR). The TE defines the time between the excitation rf pulse and the maximum of the signal echo, and TR the time between the consecutive excitation rf pulses. Both parameters are typically measured in milliseconds.

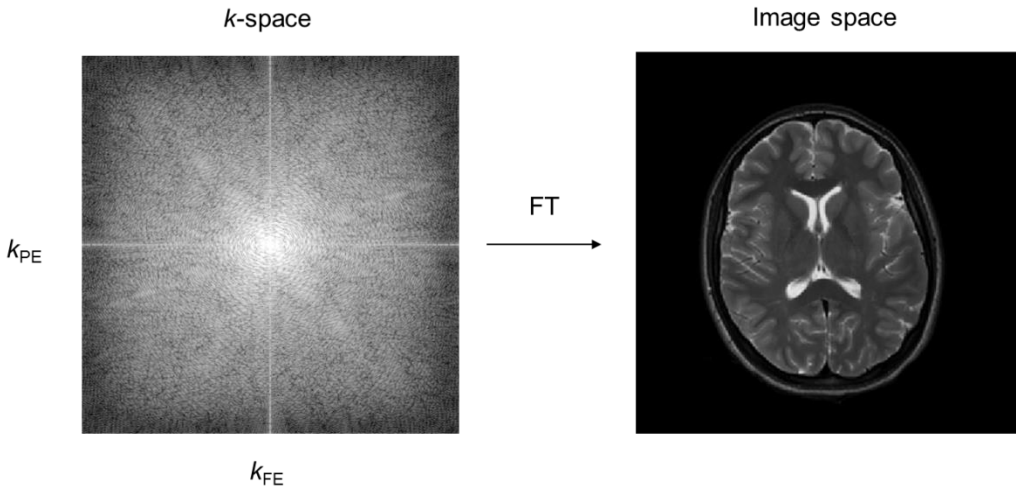

Figure 2.9 Generating the MR image. Conversion of raw *k*-space data to image space data by a 2D Fourier transform. The presented example is from a T_2-weighted imaging sequence with a Cartesian *k*-space trajectory.

The collected raw data is stored as a matrix called the *k*-space, where k_{PE} and k_{FE} represent the signal from the phase and frequency encoding directions. Each point in *k*-space determines a single measurement of the entire MR signal, and therefore each point in *k*-space contributes information to all pixels in the image space (Figure 2.9). The *k*-space data is converted to image space using a two-dimensional Fourier transform.

Different anatomical planes can be studied with MR imaging by acquisition of data in different imaging planes. This does not involve the moving of a patient, but can be performed by simply changing the magnetic field gradients. The commonly used imaging planes include axial, sagittal and coronal, as presented in Figure 2.10.

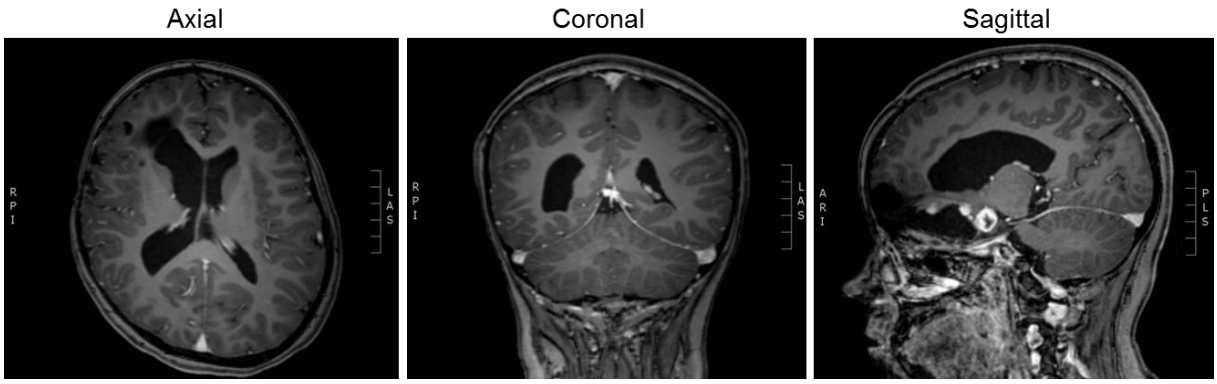

Figure 2.10 Common imaging planes used in clinical MR imaging. The imaging planes from left: axial, coronal and sagittal. The post-contrast T_1-weighted images are from a patient with optic pathway glioma.

2.1.5 Image Quality

Image quality is an important factor for any quantitative analysis based on the image data. Random or systematic noise is included in all physical measurements, which affects the accuracy of the quantitative analysis (49). Generally, the noise in MR imaging arises from random thermal fluctuations of the voltage in the receiver coil and the patient. The fluctuations in the measured signal are "white", meaning the noise is characterised by equal intensities at different frequencies and can be described as Gaussian.

The construction of the magnitude images from the complex raw data is performed using non-linear mapping, which means that the noise distribution is no longer Gaussian (53). The noise in MR magnitude images can be modelled by the Rician distribution, which has a non-zero mean. However, at signal-to-noise ratio (SNR) levels > 3, the Rician distribution approximates to a Gaussian (53, 54). In regions where there is only noise and no signal, the Rician distribution approximates to a Rayleigh distribution.

The differentiation of structures and tissue types from MR images depends on three key factors: the spatial resolution, image contrast and SNR. The spatial resolution of the resulting MR image is determined by the matrix size, field-of-view (FOV) and slice

thickness. The matrix size is controlled by the number of frequency and phase encoding steps. However, only the increase in PE matrix size results in a direct increase in the scan time for most practical applications. This is due to the phase relationships requiring multiple signals, each with a different phase-encoding step. In most cases the matrix size is kept equal in both directions as the formation of non-isotropic voxels within a plane is not preferable.

The SNR and contrast are both affected by the voxel size. A larger voxel results in a higher SNR level, but poorer contrast due to reduction in the spatial resolution. The larger voxel size results in partial volume effects, where a combination of signal from different tissues such as a lesion and healthy tissues are mixed. In order to improve contrast yet acquire sufficient SNR level, a smaller voxel size can be used with a higher number of signal averages (NSA or NEX). The signal increases in proportion to $\sqrt{\mathrm{NSA}}$ due to the randomness of noise, meaning that if the NSA is doubled, the SNR is increased by a factor of $\sqrt{2}$. However, the use of higher NSA leads to longer acquisition times, and therefore there is often a need to decide on the trade-off between SNR and the acquisition duration.

2.1.6 Basic Brain and Body Anatomy with MR Imaging

This section briefly outlines the basic anatomy seen on MR images of both brain and the abdomen.

2.1.6.1 Central Nervous System

The nervous system of the body is composed of central and peripheral systems. The central nervous system (CNS) is formed of two components: the brain and the spinal cord, with its main purpose to receive, process and store information, and to direct any activity of the body. Three main parts compose the brain, including the cerebrum, cerebellum and brainstem, which are protected within the skull, as shown in Figure

2.11a. The cerebrum is divided into four lobes: frontal, parietal, temporal and occipital, forming the largest part of the brain. Higher functions such as vision, hearing, reasoning and learning originate from the cerebrum. The cerebellum is located underneath the cerebrum, and is responsible for functions such as muscle movement and balance. Finally, the cerebrum and cerebellum are connected to the spinal cord via the brainstem, which acts as a relay centre. The functions of the brainstem include many automatic processes such as breathing, body temperature, digestion and heart rate.

The surface of the cerebrum has a folded appearance, called the cortex. The cortex contains about 70 % of the 100 billion nerve cells in the human brain and appears grey-brown in colour, lending to its name the grey matter. Beneath the grey matter, long connecting fibres between neurons form the white matter. Fluid-filled cavities in the brain are called ventricles, which are filled with cerebrospinal fluid (CSF). The CSF is made in the choroid plexus, and is responsible for cushioning the brain and spinal cord from injury. The CSF flows within and around the brain, and the circulating fluid is constantly absorbed and replenished. Segmented regions of CSF, cortical grey matter and white matter are presented in Figure 2.11.

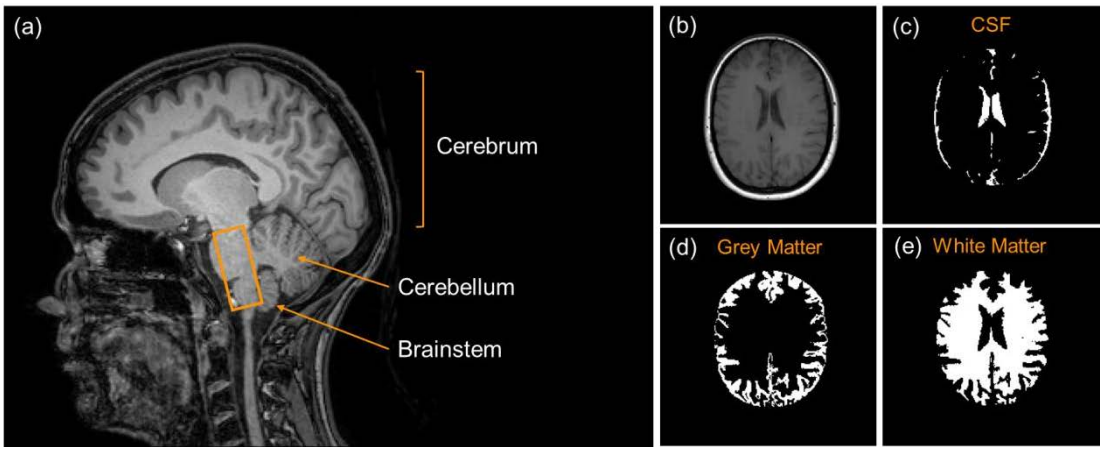

Figure 2.11 The main brain structures and regions. MR images of the brain (a) main structures: cerebrum, cerebellum and brainstem and regions of the brain on (b) T_2-weighted image and the segmented regions of (c) cerebrospinal fluid, (d) grey matter and (e) white matter.

2.1.6.2 Abdominal Organs

MR imaging of the body is an important part of clinical practice for many abdominal diseases. Here, the locations of the organs in MR images are briefly familiarised with. MR images of the abdominal region are shown in Figure 2.12 for coronal and axial planes. Looking at the coronal image (Figure 2.12a), the liver and spleen are located on the top, with kidneys directly below. The same organs can be observed in the axial MR image (Figure 2.12b), which also shows the location of the gall bladder and the bowel at the top right of the image.

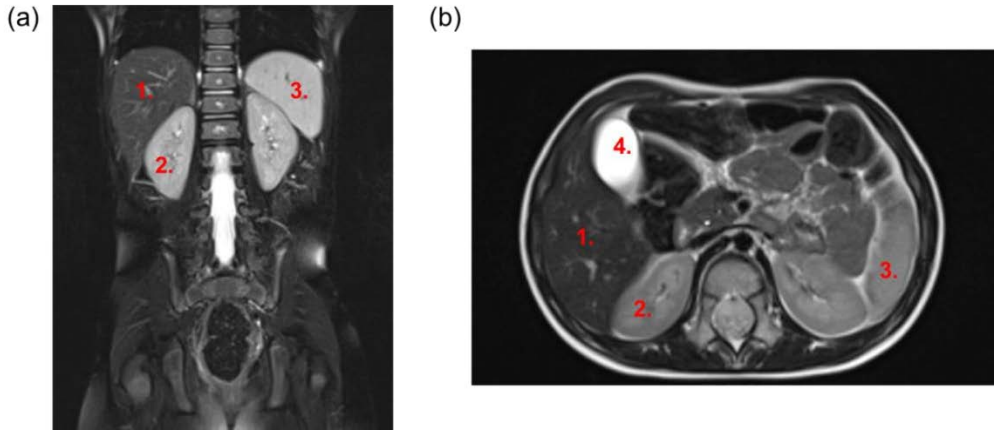

Figure 2.12 Abdominal MR imaging. Abdominal MR T_2-weighted images in (a) coronal and (b) axial planes. Locations of the large abdominal organs are indicated with numbers: 1. liver, 2. kidney, 3. spleen, and 4. gall bladder.

2.2 Diffusion MR Imaging

Many areas of research have contributed towards the success of diffusion-weighted MR imaging (DW-MRI) (13, 55, 56). In clinical applications, the technique has resulted in significant improvements in stroke patient management from diagnosis (57) to predicting clinical outcome (58). Following on, the technique has rapidly become an important part of cancer patient management (59). In this section, the underlying principles of the diffusion phenomenon and the measurement of diffusion with MR imaging are described.

2.2.1 Physical and Biological Origins of Diffusion

The diffusion phenomenon arises from the random translational motion of molecules within a fluid suspension (60). It is caused by the thermal energy possessed by the molecules and results in molecular or particle mixing. Unlike other transport mechanisms, diffusion does not require bulk motion. The mixing process was first explained by Fick's first law (61), which related the diffusive flux to particle concentration and the diffusion coefficient. It embodied the idea that the diffusion coefficient is an intrinsic property of the medium, depending on the size of molecules, temperature and microstructure. Although the work by Fick suggested that no net flux occurs at thermodynamic equilibrium, it was later discovered that microscopic random motion still exists. This is now commonly known as Brownian motion, named after Robert Brown (62).

Later on, a displacement distribution function was introduced by Albert Einstein (63), quantifying the fraction of particles that traverse a certain distance within a time frame. He derived that motion can be quantitatively defined as the diffusion coefficient, *D*, given in units of mm^2/s as the mean displacement, *d* within a time *τ:*

$$\langle d^2 \rangle = 6 \cdot D \cdot \tau \qquad [2.8]$$

The Einstein equation (Eq. 2.8) describes diffusion as a Gaussian function, where the width of the distribution is determined by the diffusion coefficient. It assumes that diffusion is free, with the self-diffusion coefficient of free water approximately measured at 3.0×10^{-3} mm^2/s (37 °C). However, diffusion in biological tissue is rarely free due to the presence of different barriers and obstacles including macromolecules, cell membranes and fibres. Therefore, deviation occurs from the Gaussian behaviour and the molecular displacement distribution becomes sharper, as described in Figure 2.13 (64).

Water molecules within tissues are often considered to be in intracellular and extracellular compartments (65). Those found in the extracellular compartment are hindered by cell membranes, but can travel longer distances compared to water molecules within the intracellular compartment. Depending on the cell shape, the intracellular water diffusion might be restricted to a different extent in different directions. For example, in elongated cells such as axons and dendrites, the water is more restricted in the perpendicular direction. Cell permeability is another important factor, usually determined by the cell type. Cells such as astrocytes can facilitate water transfer between the intra- and extracellular compartments, whereas myelinated axonal membranes are practically impermeable (66). These structural restrictions mean that the diffusion distance of water in biological tissues is in the range of micrometres, in the period of typically applied diffusion times (tens of milliseconds) (64). Therefore, within any voxel (mm) measured with diffusion-weighted MR imaging, there will be multiple

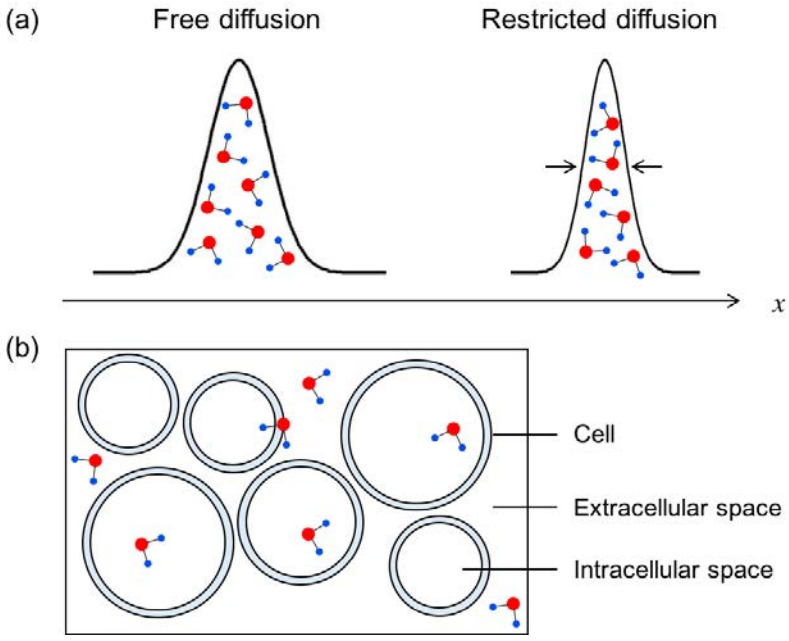

Figure 2.13 Diffusion of water in tissue. Diagram of (a) water displacement function when diffusion is free (described by a Gaussian) and restricted as observed in biological tissues, (b) depiction of diffusion at the cellular level with water restricted within cells, crossing cell membranes and hindered in the extracellular space.

complex water environments, each with their own apparent water diffusion coefficients.

2.2.2 Measurement of Diffusion with MR Imaging

Diffusion MR imaging is based on the concept that molecular diffusion can probe the underlying tissue structure on a micrometre scale. It provides a non-invasive measure of diffusion in vivo, which can describe changes to tissues due to physiological or pathological reasons (67). Other conventional MRI techniques are unable to resolve the micrometre detail that characterises diffusion in biological systems.

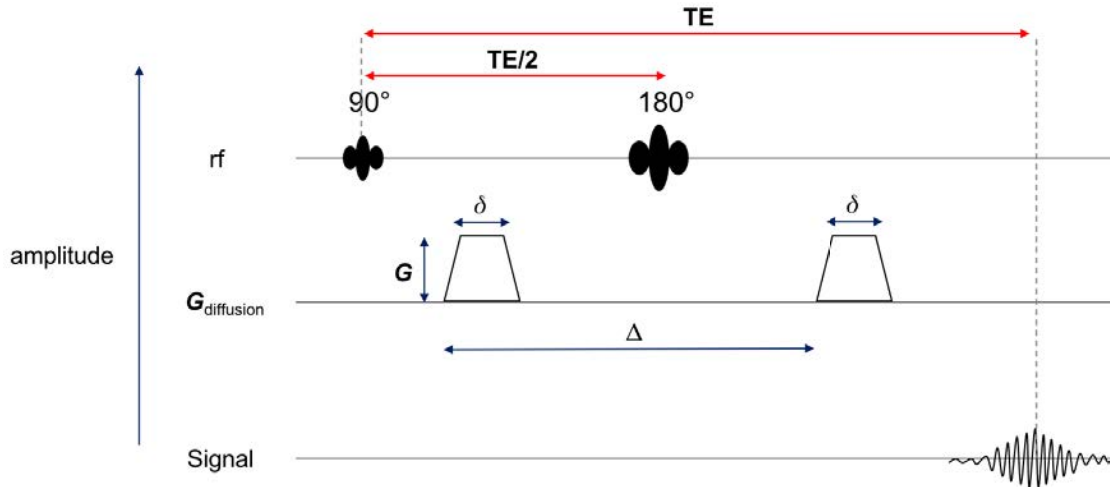

Figure 2.14 PGSE pulse sequence for diffusion-weighted MR imaging. Schematic of the pulsed field gradient spin-echo (PGSE) sequence. After a 90-degree pulse, the first $\boldsymbol{G}_{\text{diffusion}}$ gradient acts to label the space along one direction for a finite time interval (δ). The 180-degree pulse then inverts the phase prior to the second gradient, which encodes any displacement of water molecules in that direction, and the diffusion-weighted signal is acquired. TE indicates the echo time of the sequence, with the application of the 180-degree rf pulse at TE/2. The slice selection and spatial encoding gradients are not included in the diagram.

Many of the diffusion-weighted MR imaging protocols today are based on a sequence introduced by Stejskal and Tanner in 1965 (68). The pulsed gradient spin-echo (PGSE) sequence is described in Figure 2.14, which shows how the MR signal is sensitised to diffusion by additional magnetic field gradients (sometimes known as diffusion gradients). The sequence begins with a 90-degree pulse, after which the first gradient (duration, δ and strength, $\boldsymbol{G}$) imposes a spatially dependent phase on the magnetisation vectors, encoding them for position. The 180-degree pulse at TE/2 then inverts the phase and after a time Δ, the second gradient acts to re-focus the magnetisation vectors. Finally, the signal is acquired. If any incoherent motion occurs during the diffusion time (Δ), the magnetisation vector will not be fully re-focused and results in an attenuation of the signal.

The diffusion gradient parameters (δ, Δ and $\boldsymbol{G}$) have an important role in determining the applied diffusion-weighting on the signal. The strength ($\boldsymbol{G}$) and duration (δ) of the

gradient pulse affect the amount of spin dephasing. Therefore, a larger or longer gradient leads to a greater signal loss. The time between the pulses (Δ) determines how long the molecules can diffuse, and longer times lead to a greater mean displacement (Eq. 2.8). In clinical practice, these factors are combined into a single value called the *b*-value, which determines the diffusion-weighting of the observed signal:

$$b = \gamma^2 \boldsymbol{G}^2 \delta^2 \left(\Delta - \frac{\delta}{3}\right) \quad [2.9]$$

Most importantly, the diffusion signal attenuation is material or tissue dependent. This can be characterised by the diffusion coefficient, D (in mm²/s), with large and small D corresponding to faster and slower diffusion, respectively. The relationship between the signal and the diffusion coefficient is given by:

$$\frac{S(b)}{S(0)} = \exp^{-b \cdot D} \quad [2.10]$$

where $S(b)$ is the signal at the applied diffusion weighting (determined by the *b*-value) and $S(0)$ the signal with no diffusion weighting (or $b = 0$). The quantity $S(b)/S(0)$ is called the MR signal attenuation, which is solely dependent on diffusion. Any relaxation effects are removed by dividing the diffusion-attenuated signal $S(b)$ with signal in the absence of gradients $S(0)$. This is based on the relaxation-related signal attenuation being approximately independent of the diffusion gradients (60).

2.3 Modelling of Diffusion-weighted MR Imaging

The observed DW-MRI signal in complex multi-component systems such as the brain has posed a significant challenge for the analysis and interpretation of the data (65). The previously introduced idea of two water compartments, extra- and intracellular, in biological tissue has been one of the more controversial topics in diffusion MR imaging (69). The diffusion MR signal curve is characterised by a faster decay at lower *b*-values (≤ 2000 s/mm²) and slower decay at higher *b*-values (≥ 2000 s/mm²). The relative

fractions of these diffusion components in the brain have been found to be around 0.7 and 0.3, corresponding to the fast and slow components, respectively (70, 71). As a result, some studies have considered the fast and slow components to relate to the extracellular and intracellular compartments, respectively (72, 73). However, the measured water fractions in typical brain tissue have been measured at 0.2 for extracellular and 0.8 for intracellular compartments (74), and thus approximately the opposite of what is expected.

Different solutions have been suggested to account for the above behaviour, including a difference in T_2 values of the intracellular and extracellular compartments (69). However, no distinction between water T_2 values of the two compartments have been inferred from T_2 measurements to date (75, 76). A different approach was taken by Jespersen et al. (77), who suggested a model based on neural cytoarchitecture. In this model, the two diffusion components arise from dendrites and axons (modelled as long cylinders) and the isotropic component of water within and across other structures e.g. extracellular space and non-cylindrical cells. Physiologically reasonable estimates were derived in this study for both white and grey matter (77). These studies suggest that the interpretation of extracellular and intracellular compartments is unlikely to fully account for the observed behaviour in diffusion measurements. Therefore, models including geometrical features of tissue microstructure might provide a reasonable compromise for the interpretation of the MR signal at the higher *b*-values.

The focus in this thesis is at the lower *b*-value region (0 - 1000 s/mm^2), where two distinct diffusion components can also be observed. The very fast diffusion signal decay ($b \leq 200$ s/mm^2) is often thought to be influenced by perfusion (24, 25), which is described by the intravoxel incoherent motion (IVIM) model, introduced in the following section. Other models used to interpret the diffusion-weighted signal are also briefly introduced,

including the simplistic ADC model, and the kurtosis, Gaussian and stretched-exponential models.

2.3.1 Apparent Diffusion Coefficient (ADC)

The first diffusion-weighted images of the human brain were introduced in 1985 by Le Bihan et al. (25) together with the idea of apparent diffusion coefficient (ADC). ADC was proposed to avoid the challenges of non-Gaussian diffusion and to promote the technique as a clinical application (78). The ADC concept utilises the previously introduced Gaussian diffusion (Eq. 2.10), but underlines the differences to free water diffusion, and is hence called the "apparent" diffusion coefficient:

$$\frac{S(b)}{S(0)} = \exp^{-b \cdot ADC} \qquad [2.11]$$

Diffusion-weighted MR imaging is commonly performed with diffusion gradients applied in three orthogonal directions. The diffusion-weighted images from these directions are averaged (known as geometrical average or trace) and the resultant diffusion-weighted images are then used to compute the ADC map. This is to minimise any anisotropic tissues producing artificially low or high ADC values, which might present if a diffusion gradient is only applied in one direction. The ADC can be calculated from at least two b-values, where one of them is commonly $b = 0$ (Figure 2.15). The mono-exponential relationship (Eq. 2.11) is used in a voxel-by-voxel basis, and the resulting ADC parameter is often reported in units of $\times 10^{-3}$ mm^2/s or $\times 10^{-6}$ mm^2/s in clinical practice. Most scanner software packages now provide ADC maps as an automatic output for diffusion-weighted MR imaging.

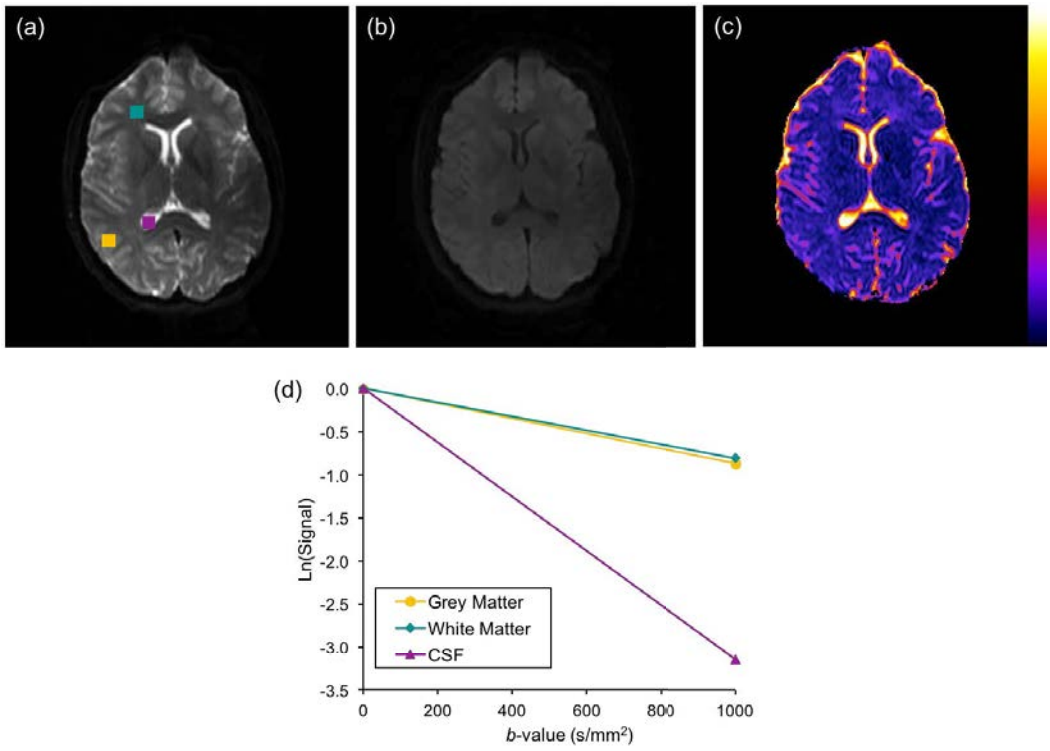

Figure 2.15 Diffusion-weighted MR imaging in clinical practice. DW-MRI mages at *b*-values (a) $b = 0$ and (b) $b = 1000$ s/mm^2 and (c) the resulting ADC map (in mm^2/s). The diffusion signal decay plots shown in (d), correspond to the regions-of-interest shown on the $b = 0$ image for grey matter (yellow), white matter (green) and cerebrospinal fluid (purple).

The interactions of water molecules within tissue are reflected in the magnitude of ADC, and it is highly sensitive to physiologic and pathologic conditions. The ADC values of grey and white matter are similar, as shown in Figure 2.15d, and a previous multi-centre study reported these to be 0.83 ± 0.02 and 0.70 ± 0.02 ($\times 10^{-3}$ mm^2/s), respectively (79). Areas of fluid, e.g. cerebrospinal fluid (CSF) and cysts, present highly diffused areas in the ADC map due to the greater mean displacement of water. This results in greater dephasing of the magnetisation vector during acquisition and causes the fluid to appear dark (e.g. CSF in Figure 2.15b). The ADC of CSF in the lateral ventricles has been reported to be in the range of $2.73 – 3.02$ ($\times 10^{-3}$ mm^2/s) for a healthy adult brain (80).

Although simplistic, ADC remains the most used diffusion model in clinical practice. However, the quantitative information is still often overlooked in preference to visual inspection of the parametric maps

2.3.2 Intravoxel Incoherent Motion (IVIM) Model

The intravoxel incoherent motion (IVIM) model was introduced in 1986 by Le Bihan et al. (25) to describe the multi-exponential diffusion signal decay observed with the acquisition of multiple *b*-values. The model has gained more interest in the recent years, with its idea that diffusion-weighted MR imaging can also provide information about tissue perfusion, and thus vascularity.

The IVIM model considers perfusion as a form of incoherent motion, which contributes towards the observed diffusion signal attenuation (81). The incoherent motion is thought to arise from the microcirculation of blood in the capillary network, with its magnitude depicted by the volume fraction (IVIM-*f* parameter). The flow of blood water (IVIM-*D** parameter) in the randomly oriented capillaries mimics a random walk, and contributes to the signal attenuation during the application of diffusion gradients. This can only be observed at low *b*-values, as the pseudodiffusion coefficient, *D**, is greater than the tissue water diffusion coefficient, *D*. The difference of the diffusion coefficients is approximately an order of a magnitude, allowing the separation of the two effects. The multi *b*-value DW-MRI and the fitting of the diffusion signal with IVIM is described in Figure 2.16, which also shows how the fitting with the ADC model is unable to account for the multi-exponential diffusion signal decay.

The IVIM model uses a bi-exponential approach to derive the two diffusion coefficients and their relative fractions:

$$\frac{S(b)}{S(0)} = f \cdot \exp^{-b \cdot D^*} + (1 - f) \cdot \exp^{-b \cdot D} \qquad [2.12]$$

where *f* is the perfusion fraction, *D** the pseudodiffusion coefficient and *D* the tissue diffusion coefficient. These parameters can be derived on a voxel-by-voxel basis and presented as quantitative parameter maps (Figure 2.17).

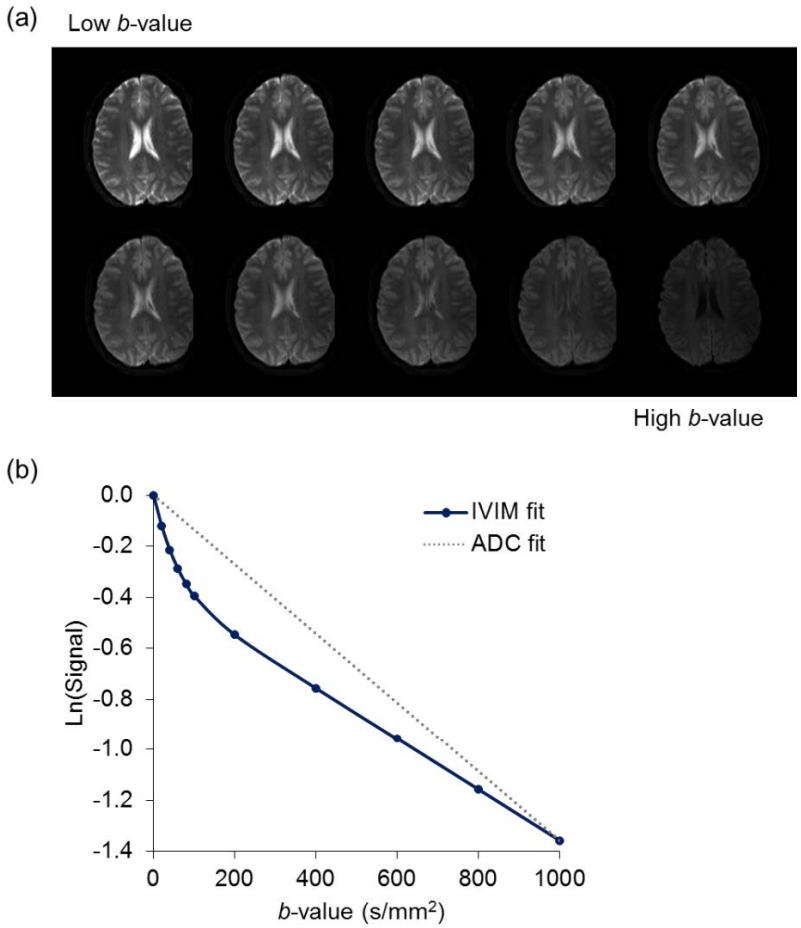

Figure 2.16 Multi *b*-value diffusion-weighted MR imaging. (a) DW-MR images showing the attenuation of signal towards high *b*-values and (b) fitting of the multi *b*-value diffusion-weighted signal with ADC and IVIM models.

2.3.2.1 Implementation of IVIM

The use of IVIM or any quantitative technique as a clinical application requires it to be sufficiently robust in the process of image acquisition, image processing, data fitting and analysis of the resulting parametric maps (82). Such technical challenges also form an important part of the validation process for potential imaging biomarkers (47). Previous studies have investigated the optimisation and effect of *b*-values and the use of different fitting algorithms on the estimated IVIM parameters (83-88). These studies have clearly demonstrated that the reliable derivation of IVIM parameters depends on the chosen DW-MRI protocol and the subsequent post-processing of the image data.

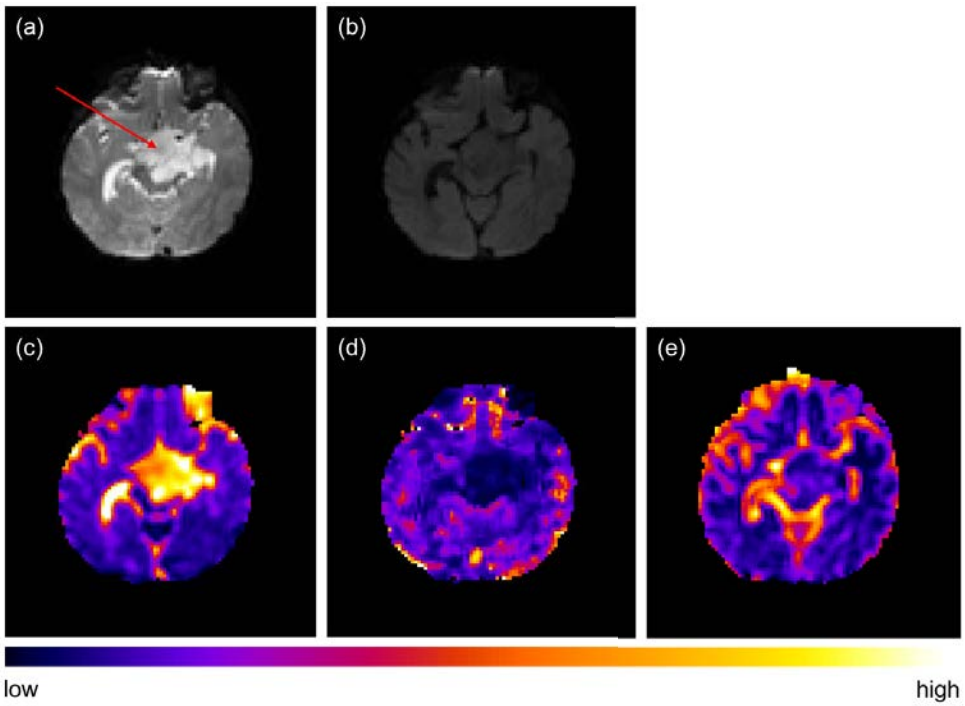

Figure 2.17 Intravoxel incoherent motion (IVIM) parameter maps. Diffusion-weighted MR images of (a) b = 0, (b) b = 1000 s/mm^2 and the IVIM parameter maps of (c) D, (d) D^* and (e) f presented for a case of optic pathway glioma (indicated by the arrow on b_0 image).

The most commonly used IVIM fitting algorithms include the non-linear least-squares, and more recently the Bayesian probability methods (85, 88). The least-squares fitting can be constrained to different extents, as described in Figure 2.18. In a non-constrained approach, the fitting can be performed simultaneously and all three parameters are fitted at once. However, as most image data is influenced by noise, this approach is rarely feasible due to its high degree of freedom in the fitting algorithm. Therefore, and to overcome this mathematical instability, constrained least-squares fitting approaches have been introduced.

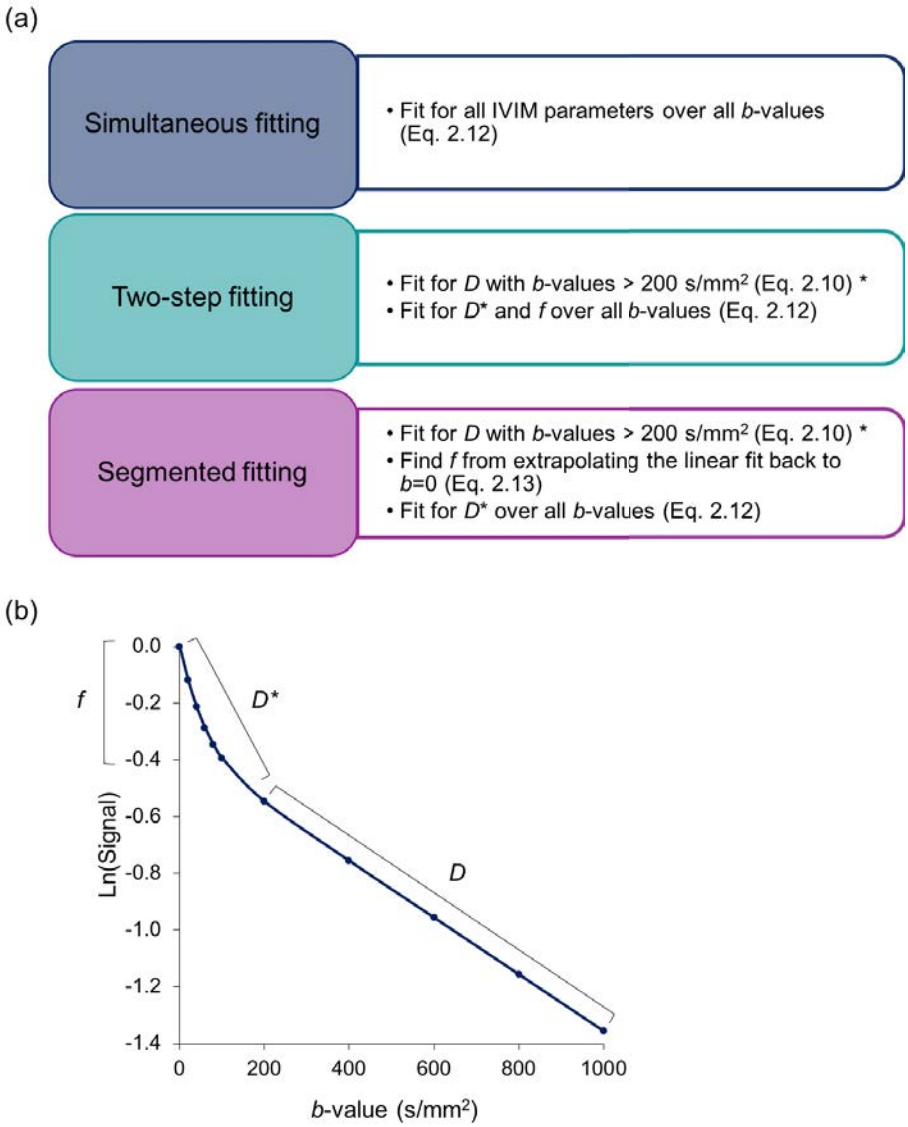

Figure 2.18 IVIM least-squares fitting algorithms. (a) Descriptions of the commonly used IVIM fitting methods. * indicates a step in the method, where the commonly proposed threshold is b = 200 s/mm^2; however this is user and sometimes tissue dependent. (b) Visualisation of the regions of signal where the IVIM parameters are derived.

Two constrained approaches have been previously reported: the so-called segmented method (88, 89) and its less constrained variant the two-step method (28). In all cases, the $S(0)$ is set to the b = 0 image. Both approaches assume that at the higher b-values, the effect of pseudodiffusion can be neglected ($D^* \gg D$) and the tissue coefficient, D, can be estimated by linear fitting to the log of the high b-value data, normalised to the $S(0)$ (Eq. 2.10). In the segmented method, the f parameter is approximated from the y-

intercept of the same linear fit (Eq. 2.13), after which the D^* parameter is estimated by non-linear fitting with the bi-exponential equation over all b-values (Eq. 2.12), again normalised to the $S(0)$. In the two-step model, both f and D^* parameters are estimated from the previously described non-linear fitting over all b-values.

$$f = \frac{(S(0) - S(int))}{S(0)} \quad [2.13]$$

The constrained methods have been shown to produce more robust IVIM parameters with higher accuracy and reproducibility, although previous studies have mostly focused on the abdominal organs (88, 90, 91). Perfusion in the abdomen is relatively higher compared to the brain (92). This results in a more challenging scenario for the IVIM fitting in the brain, which assumes that the given signal data is bi-exponential (24, 25). A few studies have reported simulations based on a healthy brain (87, 92), however these studies did not consider regions of very low perfusion, such as observed in acute ischemic stroke (28, 93), brain injury (94) and some of the low-grade brain tumours (27, 95). The previous brain studies have also only focused on single fitting methods, not accounting for the differences that might arise due to the use of fitting constraints.

Recently, the Bayesian probability method for estimation of IVIM parameters has also been of interest (85, 96). This approach does not require the user to define parameters or their variability, but they can be derived from the data itself. The Bayesian studies have shown cleaner and more visually pleasing IVIM parameter maps due to smaller estimation uncertainties in heterogeneous tissue regions. However, a recent study suggested that some of the features in heterogeneous tissue regions were masked completely (97). Therefore, the implementation of Bayesian method, although more visually pleasing, might lead to underestimation of the heterogeneity of tumours, which can be vital in clinical applications.

The other challenge with the use of IVIM is the number and magnitude of *b*-values used in the data acquisition, which have a direct impact on the computation of IVIM parameters (83, 88, 90). For IVIM, the low *b*-value region (0 – 200 s/mm^2) is critical for the evaluation of the perfusion characteristics. However, most studies to date have utilised different sets of *b*-values, although a recent consensus study was reported for IVIM in the body (98). The use of a larger number of *b*-values can aid to stabilise the data fitting, but becomes clinically less appealing due to longer acquisition times. Therefore, a common theme in the clinical research studies has been to utilise a set of *b*-values (often between six to ten) and introduce a higher number of signal averages. This results in improvement of the image SNR, which has been shown to be more important than the use of additional *b*-values for accurate data fitting (92).

Optimisation of *b*-values for IVIM has been reported in many previous studies (83, 92, 99, 100). However, these studies report optimisation for specific organs or tissue types and therefore one cannot generalise their use for standard clinical imaging. The choice of *b*-values is important for data fitting, especially when a pre-defined threshold is chosen to separate the perfusion and diffusion components (constrained fitting). For this purpose, thresholds of b = 100 and 200 s/mm^2 have been suggested for body (101) and brain (102), respectively. The effect of the threshold *b*-value was also reported in an abdominal study by Wurnig et al. (103). Their study showed that the estimated IVIM parameters were dependent on the chosen threshold, which also varied depending on the region of abdomen. Therefore, for the implementation of IVIM, it is vital to consider and assess the choice of *b*-values, the fitting algorithm and the data quality (SNR), to ensure the best yield of clinically meaningful results.

2.3.2.2 IVIM Parameter Reproducibility

Reproducibility of IVIM parameters is particularly important for the clinical uptake of the method for practice. It describes the ability of a method to give similar results from repeated measurements, and the variability between them. It is not to be confused with the term repeatability, which describes the consistency of the quantitative parameter of the same imaging test on the same object, performed at short intervals on the same scanner and the same operator.

Multiple sources of variance can influence the overall reproducibility. These include biological properties (e.g. heterogeneity of tissue, patient size), hardware (e.g. MRI system, pulse sequence), MR operator and data analysis (e.g. algorithms for quantitative analysis). Only one multi-centre, multi-scanner brain study on reproducibility of IVIM has been reported (79), while other multi-centre studies have covered the use of ADC (79, 104) and diffusion tensor imaging (DTI) derived parameters (105-107). The IVIM-D parameter was reported to have good reproducibility with coefficient of variation (CV) < 4 % for grey and white matter (accounts for inter-scanner, inter-volunteer and intra-scanner reproducibility). The f parameter had a good overall reproducibility with CV = 5.3 and 8.5 % in grey and white matter, respectively. No values were reported for the D^* parameter. Interestingly, the protocols used across the different centres were not precisely matched, which suggests that IVIM parameters D and f are quantitatively robust.

Reproducibility has also been examined in previous single-centre liver (84, 99, 108, 109), and simulation based studies including various tissue types (85, 88, 92). For example, in a study by Kakite et al. (110), the reproducibility (CV) in healthy liver was reported to be 13.2 % (range: 1.2-28.5 %) for D, 25.3 % (range: 9.3-84.9 %) for f, and 59.0 % (range: 2.4-121.3 %) for D^*. Another study by Andreou et al. (108) reported the 95 % confidence

intervals of the percentage difference between paired measurements in the liver to be -5.12 to 8.09 % for D, -24.3 to 25.1 % for f and -31.2 to 59.1 % for D^*. The overall findings suggest that while D and f are sufficiently reproducible for clinical use, the reproducibility of D^* parameter is relatively poor. However, the use of D^* has shown potential in clinical diagnosis, e.g. for liver cirrhosis (89, 111). Therefore, further studies are needed to improve the robustness of D^* parameter to justify its use for clinical applications.

2.3.2.3 Biophysical Origins of IVIM Parameters and Perfusion

The idea of using diffusion-weighted MR imaging for derivation of quantitative parameters of both diffusion and perfusion has its advantages. The gold standard MR perfusion imaging method: dynamic susceptibility contrast (DSC) requires the use of a contrast agent, which is often not possible in patients with renal failure and can be difficult in younger patients. Recent reports of gadolinium deposits in the brain, from DSC contrast agents, have also posed questions on the safety of the agents (112, 113).

Measurement of perfusion has shown promise in various aspects of clinical management of cancer, including tumour grading (114, 115), differentiation (116), treatment planning (117) and predicting long-term outcome (118). Perfusion of blood in tissue is responsible for the delivery of oxygen and nutrients to cells (119). This occurs via a capillary network that allows blood-tissue exchange through the capillary walls. Similarly, the waste products of tissue metabolism are transported through the capillary network. The overall process is affected by many physiological parameters such as blood pressure, velocity and microstructure. In clinical environment, the term perfusion is often loosely described as the degree of microvasculature of a tissue.

Measurement of perfusion with DSC-MRI relies on the regional susceptibility induced signal loss caused by the first passing of paramagnetic contrast bolus (120). The contrast

is injected intravenously, after which imaging is performed rapidly and repeatedly to acquire the MR signal, which relates to the concentration of the contrast agent in tissue. A curve of the signal intensity as a function of time for each voxel can be converted to tracer tissue concentration-time data using a well-known relationship between T_2 or T_2* signal intensity and tracer tissue concentration. The principles of a kinetic model can be used to estimate the perfusion parameters: cerebral blood volume (CBV), cerebral blood flow (CBF) and mean transit time (MTT), as described in Figure 2.19. More information on DSC-MRI can be found on references (120, 121).

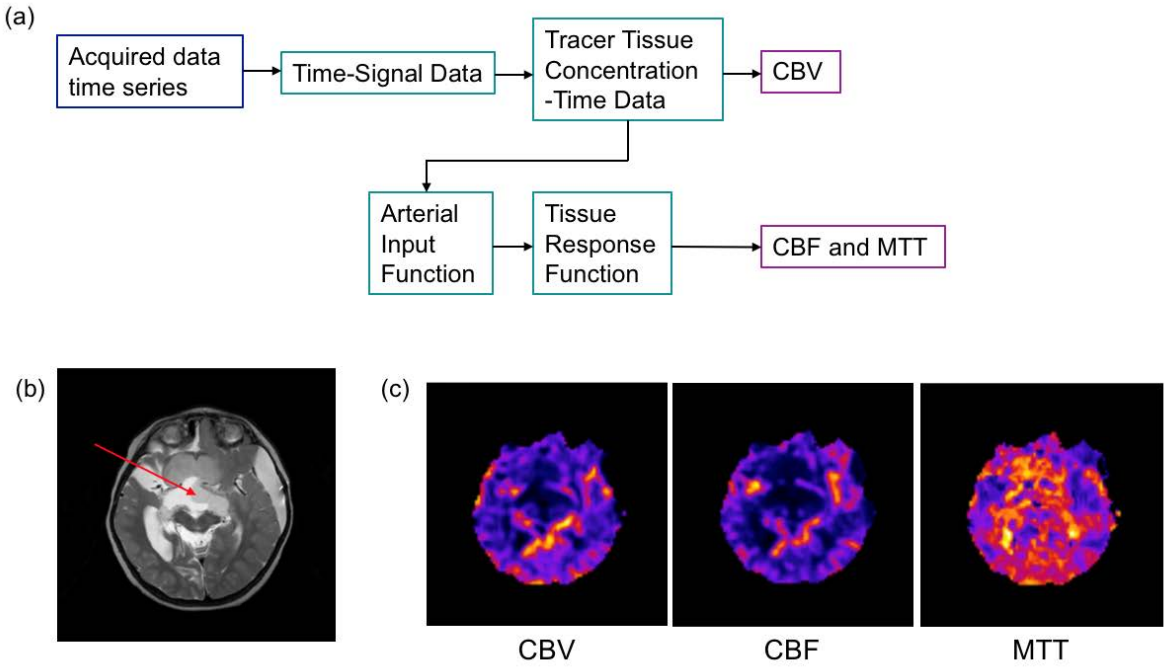

Figure 2.19 DSC-MR imaging and the computation of DSC perfusion parameters. (a) Diagram showing the processing required to estimate the DSC parameters. This involves signal data conversion to tracer tissue concentration, from which CBV can be determined. An arterial input function (AIF) can be determined from the image data and is a function describing the time-dependent concentration input to tissue. The AIF is deconvolved from the tissue concentration-time curve resulting in the tissue response function. From this, parameters of CBF and MTT can be determined. An example case of optic pathway glioma shown on (b) T_2-weighted image (tumour indicated by the arrow) and (c) the DSC parameter maps.

A study linking the DSC parameters to the IVIM parameters was reported by Le Bihan and Turner (119). The IVIM perfusion fraction, *f*, or the fractional volume (%) of capillary blood can be thought as the ratio of the volume of water flowing in the capillary compartment (V_d) to the total water volume (V_{H2O}) within a voxel. This can be converted to the volume of capillary blood per 100 g of tissue (DSC-CBV), if the water content fraction ($f_w = V_{H2O}/ V_d$) is known and assuming tissue density unity:

$$f = \frac{V_d}{V_{H2O}} = \frac{V_d}{f_w V} = \frac{CBV}{f_w} \qquad [2.14]$$

The study also suggested the relation of IVIM *D** parameter to the average blood velocity and the mean capillary segment length. This results in an inverse relationship of *D** to the DSC-MTT parameter. The product of *fD** was related to the measure of CBF on the basis that the link between the IVIM and classical perfusion is in the capillary geometry.

The idea of a link between the IVIM and DSC perfusion parameters has been investigated in previous correlation studies (Table 2.1). Moderate to strong correlation between IVIM-*f* and DSC-CBV has been demonstrated in healthy grey matter (87) and pathological tissues including low- and high-grade gliomas (27, 28, 93) and glioblastomas (122, 123). The comparison of *D** and *fD** to perfusion parameters has been more inconclusive. Only one study reported the comparison of IVIM-*D** and DSC-MTT, which did not demonstrate significant correlation but indicated negative association of the parameters (28). The same study also reported comparison of *fD** to DSC-CBF, which showed moderately positive correlation. Although a mixture of different tumours has been studied, the correlation has not been assessed in low-perfused tumours, such as presented in some paediatric brain tumours (124).

The comparison of IVIM and DSC parameters is difficult, as both methods provide separate challenges in the acquisition and analysis of the data, as well as some inherent

differences in what they are able to measure. The IVIM-*f* parameter has previously been reported to be approximately 0.10 and 0.08 in grey and white matter, respectively (79, 125), whereas the CBV fractions have been reported to be approximately 5.2 % in grey matter and 2.7 % in white matter (126). Although these *f* values have not been converted to the CBV equivalent values using Eq. 2.14, it is unlikely that IVIM-*f* provides a direct measure of CBV. The IVIM has been shown to be more sensitive to the perfusion in the microcapillary network (127, 128), with a smaller contribution, if any, resulting from the larger arteries containing faster blood flow. This contrasts with DSC, where larger arteries provide a major contribution to the DSC signal (27, 28, 93).

For the other DSC parameters CBF and MTT, the measurement of the arterial input function (AIF) can be difficult and is often not even performed in clinical practice (121). The AIF is required to remove variations in the supply of the contrast agent to the tissue, because of changes in the physiology and the administration of the contrast agent (129). The measurement of AIF is optimally performed using a vessel close to the tissue of interest, which needs to be included within the MR field-of-view. Conversely, the AIF is often measured using larger feeding vessels rather than direct smaller vessels. This is due to the tumour potentially influencing the blood supply of the nearby vessels, as well as possible issues with partial volume effects. However, the use of larger vessels can also lead to erroneous measures of AIF due to dispersion of the bolus, thereby leading to inaccuracies in the estimation of the CBF and MTT parameters.

Evidence of tissue perfusion detected with IVIM has been provided from a few studies using purpose-built model phantoms. The first IVIM phantom was introduced together with the IVIM model by Le Bihan et al. (24). This involved a chromatographic column packed with resin microspheres, through which water drains under gravity (replicating microcapillary perfusion). In their experiments, a series of water flow rates were applied

and a reduced flow rate was observed as a decrease in the perfusion fraction. Another phantom study using different area fractions of flowing water compartments reported significant positive correlation between the flow rate and *f* and *D** (91). Similar findings were reported by Cho et al. (130), who used a complex flow phantom mimicking tumour microenvironment. These studies suggest that the DW-MRI is sensitive to flow effects and support the IVIM model. However, further evaluation of the underlying principles and the association of these parameters with the tissue microstructure would be beneficial to demonstrate the full potential of IVIM for clinical applications.

Table 2.1 Previous literature on comparison of IVIM and DSC-MRI perfusion parameters.

Author	**Year**	**Study region**	**Parameters compared**	**Correlation coefficient**	***P*-value**
Wirestam (125)	2001	Grey matter	IVIM-f - DSC-CBV	$r = 0.44$	0.001
		White matter	IVIM-f - DSC-CBV	$r = 0.44$	0.001
Federau (27)	2014	Glioma	IVIM-f - DSC-rCBV*	$r = 0.59$	-
Federau (28)	2014	Mixture of brain pathologies	IVIM-f_r - DSC-rCBV, IVIM-D^*_r - DSC-rMTT^{-1}, IVIM-fD^*_r - DSC-rCBF*	$r = 0.75$, $r = -0.27$, $r = 0.65$	-, -, -
Kim (122)	2014	Glioblastoma	IVIM-f - DSC-rCBV*	$r = 0.674$	< 0.001
Puig (123)	2016	Glioblastoma	IVIM-f - DSC-rCBV* IVIM-D* - DSC-rCBF*	$r = 0.49$ $r = 0.71$	0.04 < 0.001
Wu (87)	2015	Grey matter	IVIM-f - DSC-CBV†	$r = 0.48$	< 0.001
		White matter	IVIM-f - DSC-CBV†	$r = 0.02$	0.58
Conklin (93)	2016	Glioma	IVIM-f - DSC-rCBV	$r = 0.49$	-

*rCBV, rCBF and rMTT are relative values calculated by dividing the mean tumour perfusion value by normal appearing white matter perfusion value. Similarly, f_r, D^*_r and fD^*_r are relative values (tumour region/white matter region).
† value in units of ml/100 ml

2.3.2.4 IVIM in Clinical Studies

Despite the uncertainties with regards to the biophysical origins of the IVIM parameters, an increasing number of studies have investigated the use of IVIM for clinical applications. A summary of some of these studies can be found in Table 2.2, including the type of pathology and the derived IVIM parameters.

A study that led to a surge of studies exploring IVIM in clinical applications was by Luciani et al. (81), who investigated the use of IVIM for diagnosis of cirrhotic liver (111). Their study showed that the pseudodiffusion coefficient was lower in cirrhotic liver compared to normal healthy liver, and thereby likely contributing towards the restricted diffusion seen in cirrhosis. Following this, many studies in the intra-abdominal organs (liver, spleen, kidneys, pancreas) have revealed the presence of a strong bi-exponential diffusion signal attenuation (82, 131). This has allowed the utilisation of the perfusion-sensitive diffusion component, in particularly for the abdomen.

Interesting abdominal studies have included types of liver and pancreatic cancers (30, 132-135). A study looking at differentiation of low- and high-grade hepatocellular carcinoma found that the D parameter had significantly better diagnostic performance compared to ADC (30). This study also reported significant correlation of f to the percentage of arterial enhancement. Another study including common pancreatic tumours and chronic pancreatitis, demonstrated that D^* and f were more valuable than ADC or D in their differentiation (132).

Table 2.2 Previously reported examples of IVIM parameters in different pathologies (no studies of healthy tissues are included).

Author et al.	Year	Pathology	Cases	*D*	*D**	*f*
Bisdas (136)	2013	Low-grade glioma	7	0.52	10.8	0.06
		High-grade glioma	15	0.76	41.6	0.11
Federau (27)	2014	Low-grade glioma	5	1.00	11.4	0.08
		High-grade glioma	16	2.00	11.7	0.13
Hu (137)	2014	Low-grade glioma	13	0.76	2.15	0.48
		High-grade glioma	29	0.51	2.71	0.29
Lin (138)	2015	Low-grade glioma	13	0.81	2.77	0.49
		High-grade glioma	11	0.69	5.10	0.40
Freiman (31)	2013	Crohn's disease non-enhancing	13	1.70	18.5	0.59
		Crohn's disease enhancing	11	1.30	51.9	0.27
Suo (139)	2016	Ischemic stroke	101	0.42	10.2	0.04
Cho (90)	2015	Breast cancer	14	1.40	15.0	0.13
Sigmund (140)	2015	Breast cancer	27	2.36	15.1	0.10
Hayashi (141)	2013	Cirrhotic liver	29	0.87	25.0	0.24
Luciani (111)	2008	Cirrhotic liver	12	1.19	61.0	0.30
Patel (89)	2010	Cirrhotic liver	14	1.04	27.9	0.25
Shinmoto (142)	2008	Prostate cancer	12	0.30	1.70	0.50
Kuru (143)	2014	Prostate cancer	27	1.04	31.1	0.10
Ueda (144)	2016	Prostate cancer	63	0.65	7.48	0.23
Hectors (133)	2015	Hepatocellular carcinoma	25	1.36	64.1	0.18
Woo (30)	2014	Low-grade hepatocellular carcinoma	24	1.18	36.8	0.22
		High-grade hepatocellular carcinoma	18	0.99	32.2	0.19
Lemke (135)	2009	Pancreatic adenocarcinoma	23	1.15	20.0†	0.09
Kang (132)	2014	Chronic pancreatitis	7	1.41	40.8	0.19
		Neuroendocrine tumour	17	1.11	43.7	0.30
		Pancreatic adenocarcinoma	39	1.14	22.3	0.12
		Intraductal papillary mucinous neoplasm	37	2.84	15.6	0.10
Klauss (134)	2011	Chronic pancreatitis	9	1.07	20.0†	0.16
		Pancreatic adenocarcinoma	15	1.09	20.0†	0.08

† *D** fixed in fitting. *D* and *D** values are reported in units of $\times 10^{-3}$ mm²/s.

More recently, IVIM brain applications have been reported for the differentiation of low- and high-grade gliomas (27, 136-138) and the assessment of stroke (139). The glioma studies have showed promising results for the use of perfusion fraction, f, in the grading of tumours. However, the agreement of the perfusion fraction values has been poor. A range of values for low- (f = 0.06 – 0.49) and high-grade (f = 0.11 – 0.40) gliomas have been reported. Higher f values (> 0.29) were reported in studies, which included b-values ≥ 1500 s/mm^2 (137, 138), compared to studies with lower b-values ≤ 1300 s/mm^2 (f ≤ 0.13).

Previous simulation studies have indicated that the IVIM analysis in the brain is much more demanding in terms of the data quality and SNR level (87, 92). This is partially due to the relatively low perfusion in the brain compared to the abdomen, leading to a lower degree or subtler bi-exponential signal behaviour. The low-perfused scenario is more challenging for the IVIM model, in particular with regards to data fitting. Therefore, consideration of factors such as the choice of b-values, pre-defined thresholds and fitting algorithms (section 2.3.2.1) becomes even more essential for IVIM analysis in the brain.

The previous IVIM studies have shown interesting and promising results for its use in clinical applications, although challenges remain with its methodology. The discrepancies seen in the previous glioma studies make it difficult to assess the accuracy of the IVIM parameters, and raise the need for guidelines to aid in interpretation of these differences. Further technical validation in terms of the assessment of data quality and the reliability of the IVIM parameters, need addressing before the method can be truly applied in clinical practice.

2.3.3 Other Mathematical Models for Diffusion MR Imaging

Other mathematical models have been proposed to describe the attenuation of diffusion signal at multiple *b*-values. These include the stretched exponential (145), Gaussian or statistical (146) and kurtosis (147) models. These models introduce additional parameters, which are not of specific physiologic basis. They do however consider the non-mono-exponential behaviour of diffusion signal seen in tissues. Here, a brief summary is given of these models.

The stretched-exponential model was introduced by Bennett et al. (145) to account for the microscopic heterogeneity seen in cerebral cortex, with no assumptions made on the number of diffusing components:

$$\frac{S(b)}{S(0)} = \exp[(-b \cdot D)^{\alpha}] \qquad [2.15]$$

where D (in mm²/s) is the distributed diffusion coefficient and α (no units) the heterogeneity index between 0 and 1. The D can be simply interpreted as the diffusion coefficient, but the interpretation of α is more challenging with no clear link between the parameter and a physiological origin. In the original study, the model was found to provide a better fit for 20 % of the voxels in comparison to the IVIM model. However, only voxels from the cerebral cortex were included and therefore its use for other brain tissues was not justified.

Another mathematical model, the Gaussian model, was proposed by Yablonskiy et al. (146). The model accounts for within-voxel heterogeneity and assumes a Gaussian distribution of diffusion coefficients, $P(D)$.

$$\frac{S(b)}{S(0)} = \int_0^{\infty} dDP(D)\exp(-bD) \qquad [2.16]$$

The fitting with this model provides a truncated Gaussian distribution with mode Δ (mm²/s) and spread σ (mm²/s). The proposed model provides a framework for analysis of

complex diffusion, although the use of such a complex model itself can be rather slow and complicated for clinical use.

Finally, the kurtosis model was introduced by Jensen et al. (147) to quantify the degree of non-Gaussian water diffusion (Eq. 2.17). This is measured by the kurtosis term, K, which estimates the excess kurtosis of the diffusion displacement probability distribution. The method uses a quadratic function, therefore allowing the estimation of both diffusion coefficient and diffusional kurtosis:

$$\frac{S(b)}{S(0)} = \exp(-b \cdot D + b^2 D^2 K/6) \qquad [2.17]$$

Promising results were reported in the original kurtosis study, which demonstrated a significantly higher kurtosis in white matter compared to grey matter, potentially reflecting the structural differences between these tissues. While the kurtosis model is relatively simple to apply, it does require the acquisition of higher b-values (> 1000), currently not part of most clinical protocols.

The mathematical models described here can provide additional parameters as potential statistical biomarkers of disease. They might also provide better mathematical fits compared to models such as IVIM (148). However, the biological basis of these parameters remains uncertain and therefore the clinical value of these models is yet to be established.

2.4 Summary

This chapter introduced the basic principles and theory behind MR imaging. This was followed by background on the physical phenomenon of diffusion, how it can be measured, and what it can tell us about the underlying tissue microenvironment. Consideration of these aspects is important to understand the challenges and restrictions posed for acquisition of high quality data, a necessity for robust data analysis, and the interpretation of results based on phenomenological models such as the IVIM.

The second part of this chapter introduced the models used to describe the diffusion-weighted MR signal. Focus was on the IVIM model, which includes the perfusion component into the modelling of the diffusion signal. The technical challenges in the implementation of IVIM in low-perfused tissues and the lack of studies thereof in assessing its reliability for such regions was covered to highlight the need for validation for its potential clinical use. A second limitation in the current literature is the continuous drive for increasing the number of b-values, rather than the use of higher NSA to improve the data quality and hence the IVIM parameter estimation. Therefore, the importance of data quality for reliable IVIM analysis should be further assessed. In this thesis, these limitations are addressed to advance the technical and clinical validation of IVIM, and to reduce the translational gap between its research and clinical use.

Chapter 3

Investigation of IVIM Fitting Methods in Low-Perfused Tissues

3. Investigation of IVIM Fitting Methods in Low-Perfused Tissues

Some aspects of the work presented here were published in [**P01**] and [**P05**].

3.1 Introduction

The intravoxel incoherent motion (IVIM) model is based on the estimation of two diffusion components in tissue. One from the molecular diffusion of water and one from the blood perfusion in the microcapillary network (24, 25). Promising results have been reported for its use in clinical applications, yet challenges remain with its data acquisition and analysis, which have a direct effect on whether the IVIM parameters can be derived reliably (84, 85, 88, 92).

The image quality, and the number and magnitude of *b*-values (Chapter 4) are important considerations for IVIM data acquisition. The data quality is often assessed in terms of signal-to-noise ratio (SNR), which determines the ratio of level of signal to the level of background noise. Requirements for sufficient SNR levels for different tissue types have been reported in previous IVIM studies (87, 88, 92). For the brain, a requirement of at least SNR = 30 or 50 has been proposed, with lower requirements suggested for the abdominal organs (87, 92). Although these studies provided recommendations for the sufficient SNR levels for IVIM, the in vivo SNR measurements were most commonly performed with the b = 0 images, apart from Wu et al. (87) who reported SNR ≈ 30 in the brain for b = 1000 s/mm^2. However, the SNR at b = 0 might not correctly reflect the SNR at the higher *b*-values with lower signal intensities, and hence the data quality. Therefore, it is important to consider the SNR at the higher *b*-values to determine whether the IVIM parameters can be estimated in a robust manner.

Previous IVIM data fitting studies have mainly focused on the abdominal regions, which are relatively high perfused compared to the brain (84, 85, 88). In a comprehensive study by Barbieri et al. (85), variability was shown between the fitting algorithms depending on the abdominal region alone. This suggests that the performance of the fitting methods is highly dependent on the underlying tissue perfusion characteristics, and thus the degree of bi-exponential behaviour of the diffusion signal.

As mentioned above, the application of IVIM in the brain differs from the abdominal organs in terms of the degree of perfusion (28). Perfusion in the brain is generally lower, which poses a greater challenge for the IVIM fitting, which assumes a bi-exponential signal (92). The brain also includes regions that exhibit mono-exponential signal behaviour e.g. cerebrospinal fluid (CSF), although this might not be the case for CSF in lateral ventricles due to pulsatile flow (149). While the use of IVIM in such regions is generally not problematic, the regions around the edges of CSF can produce artificially high degrees of bi-exponential or multi-exponential behaviour due to partial volume effects. This is picked up by the IVIM model, resulting in particularly high values for IVIM perfusion fraction. Thresholding methods have been commonly applied to remove such values (27, 28, 87, 93).

Although the brain provides a relatively low-perfused region itself, even lower perfused tissues can exist in acute ischemic stroke (28), traumatic brain injury (94) and both adult and paediatric low-grade brain tumours (27, 95). As shown in previous studies, tissue characteristics are important for the evaluation of IVIM fitting methods, yet low-perfused pathological brain tissues have not been reported to date. Therefore, this Chapter aims to assess and compare the constrained and simultaneous IVIM fitting methods in low-perfused tissues to evaluate its use for clinical applications in such regions.

3.2 Methods

3.2.1 Data Simulations

Model simulations were performed to investigate the influence of constraints on fitting algorithms and the resulting accuracy and precision (or reproducibility) of the estimated IVIM parameters. All simulations and data analysis were implemented using in-house Python software (Anaconda, Continuum Analytics, v. 2.7.1.0) with the LmFit library (150) and MATLAB (MathWorks, Natick, MA, v.2016b). The model data signal values were generated with Eq. 2.12 (Chapter 2) using b-value distribution: 0, 20, 40, 80, 110, 140, 170, 200, 300, 500, 1000 s/mm^2. The distribution was chosen based on the MR protocol used in the local institution. The IVIM parameters used for the grey matter (GM) and low-grade glioma tumour models were based on preliminary measurements performed with a paediatric brain tumour patient cohort (Table 3.1), presented in Chapter 5.

Table 3.1 Tissue models and IVIM parameters used in the simulations.

Tissue Model	D (× 10^{-3} mm^2/s)	D^* (× 10^{-3} mm^2/s)	f
Grey Matter	0.83	20.8	0.115
Tumour	1.63	7.23	0.095

Random white Gaussian noise was introduced to the modelled data to simulate the Rician distribution of noise found in MR images using the in-built MATLAB function (Communications System toolbox, awgn() function). This was based on the Rician distribution equalling to Gaussian distribution for SNR levels > 3 (53). SNR levels of 20, 30, 40, 50, 60 and 70, simulated with Gaussian noise, were used to study the influence of noise on the estimated parameters. SNR levels were selected based on previous brain DW-MRI publications (87, 151, 152) and SNR measurements performed with the DW-MRI data from the local institution at b = 1000 s/mm^2 (Chapter 4).

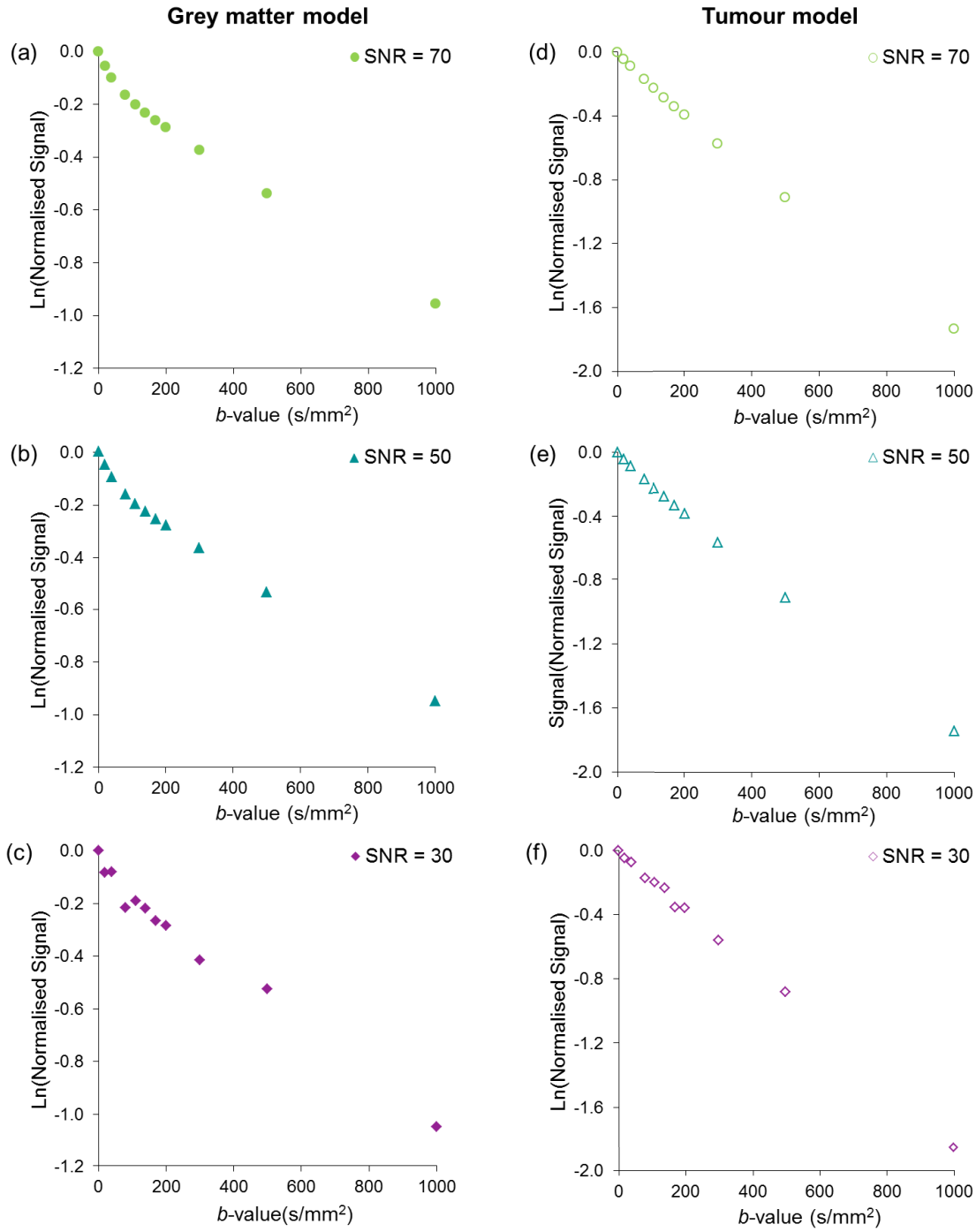

Figure 3.1 Simulated diffusion signal data for grey matter and low-perfused tumour models. Examples of grey matter (a-c) and tumour (d-f) diffusion signals generated at SNR = 70 (a,d), 50 (b,e) and 30 (c,f).

Examples of grey matter and tumour diffusion signal data generated based on in vivo DWI data are presented in Figure 3.1.

Data simulations were performed using 1,000 random data iterations for each model and SNR level. Data iterations were defined as outliers if the standard error of the individual parameters was higher than 30 % for the bi-exponential fitting step. The standard errors for each parameter were determined by taking the square root of the diagonal elements in the variance-covariance matrix.

3.2.2 Data Analysis

Non-linear least-squares minimisation was performed with the Levenberg-Marquardt (153) algorithm for the IVIM fitting. The fitting was performed on a voxel-by-voxel basis using the bi-exponential methods outlined in Figure 2.18 and section 2.3.2.1. The fitting methods varied from a non-constrained simultaneous fitting to a more constrained step-wise fitting with fixed IVIM parameters.

For the two-step and segmented fitting methods, an assumption was made that the perfusion effects are negligible at high b-values > 200 s/mm^2 (27, 28, 154). Based on this assumption, the mono-exponential relationship (linear fitting) was applied to the log of the high b-value data to define the diffusion coefficient D (Eq. 2.10). The segmented fitting includes an additional constraint with the derivation of perfusion fraction f from the same linear fit (Eq. 2.13), by extrapolating the fit to the y-intercept, S(int). If no vascular component is present, S(int) = S(0), where S(0) is the image data at b = 0. The final fitting step was performed with the non-linear bi-exponential fitting (Eq. 2.12), which for the case of simultaneous fitting was the only fitting step.

A few constraints were used in the data fitting. The following boundaries were applied to the IVIM parameters: $0 < D < 0.1$ mm^2/s, $0 < D^*$ 1 mm^2/s and $0 < f < 1$. These boundaries were chosen to eliminate any non-physiological results (88).

3.2.3 Statistical Analysis

Statistical analysis was performed in SPSS Statistics (IBM, Chicago, IL, v.22), unless stated otherwise.

The following statistics were calculated for the estimated parameters D, D^* and f. Accuracy was determined using the true IVIM values (used in signal data generation) and the measured mean values estimated from fitting of the simulated data. The reproducibility of the estimated parameters was determined as a coefficient of variation (CV%), expressed as the percentage of the ratio of the standard deviation to the mean. Additionally, confidence intervals and 2D error norm plots (LmFit library (150)) were used to analyse the estimation of IVIM parameters for data with a great amount of random noise and where data fitting was poor. The method used an F-test to compare the null model (best fit) with an alternate model where one parameter was fixed.

Analysis of variance (ANOVA) was performed for the repeated IVIM model data simulations and the estimated parameters derived using the different fitting methods. This was to test if the estimated parameters differed significantly between the fitting algorithms. The Tukey *post-hoc* analysis was used to define which algorithms differed significantly. P-value < 0.05 was considered to indicate significant difference.

3.3 Results

3.3.1 Model Data Simulations

The accuracy of the fitting methods and hence the estimated IVIM parameters are described in Figures 3.2 and 3.3 for grey matter and tumour models, respectively. The estimation of *D* was robust for both the constrained and simultaneous fitting methods. At lower SNR levels, the mean *D* value decreased, which led to an increase in both *f* and *D** mean values. While an increasing variance was observed for all the IVIM parameters at decreasing SNR levels, the variance was comparatively reduced for *D* and *f*.

Significant differences between the fitting algorithms were observed for the grey matter model (Table 3.2) and the estimation of *D* (SNR 20-40; *P* 0.001 – 0.007), *D** (SNR 20-70; $P < 0.001 – 0.005$) and *f* (SNR 20-40; *P* 0.001 – 0.013). The post-hoc test attributed this to the differences between the constrained fitting methods and the simultaneous fitting. Differences between the two constrained fitting methods were observed for *D** and *f* at SNR 20-40.

For the tumour model (Table 3.3), significant differences were observed for the estimation of *D* (SNR 20-60; $P < 0.001 – 0.046$), *D** (SNR 20-50; $P < 0.001 – 0.001$) and *f* (SNR 20-60; $P < 0.001 – 0.008$). Similarly to the grey matter model, the differences were found to be between the constrained and simultaneous fitting methods.

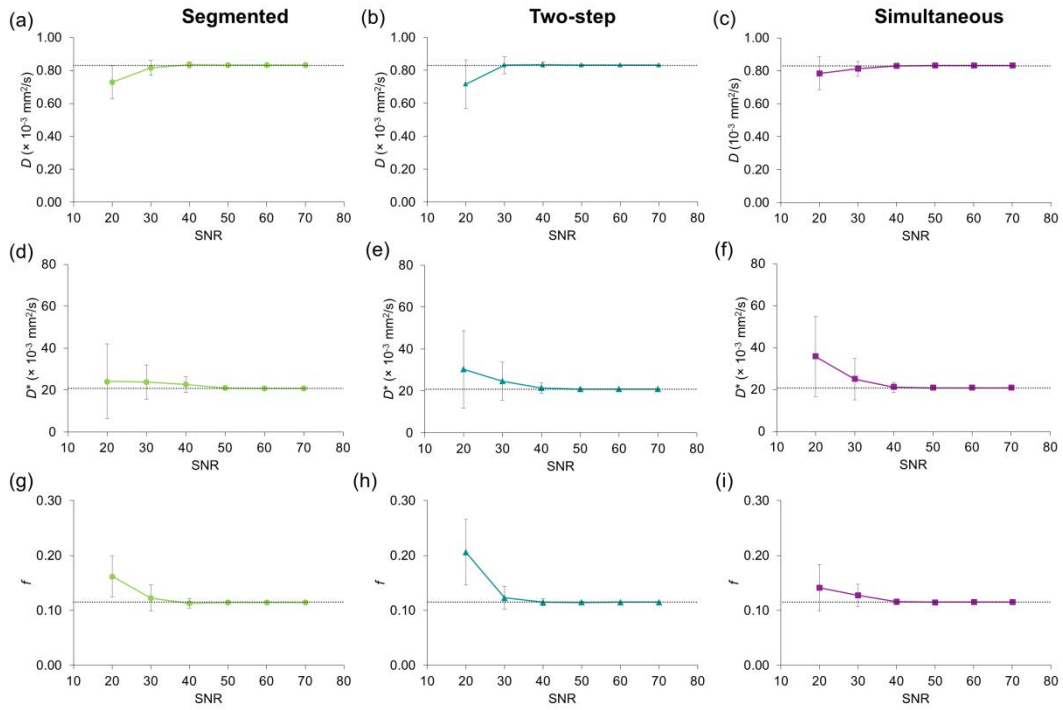

Figure 3.2 The accuracy results for IVIM fitting methods using the grey matter model. Data simulation results for IVIM *D* (a-c), *D** (d-f) and *f* (g-i) using the segmented, two-step and simultaneous fitting.

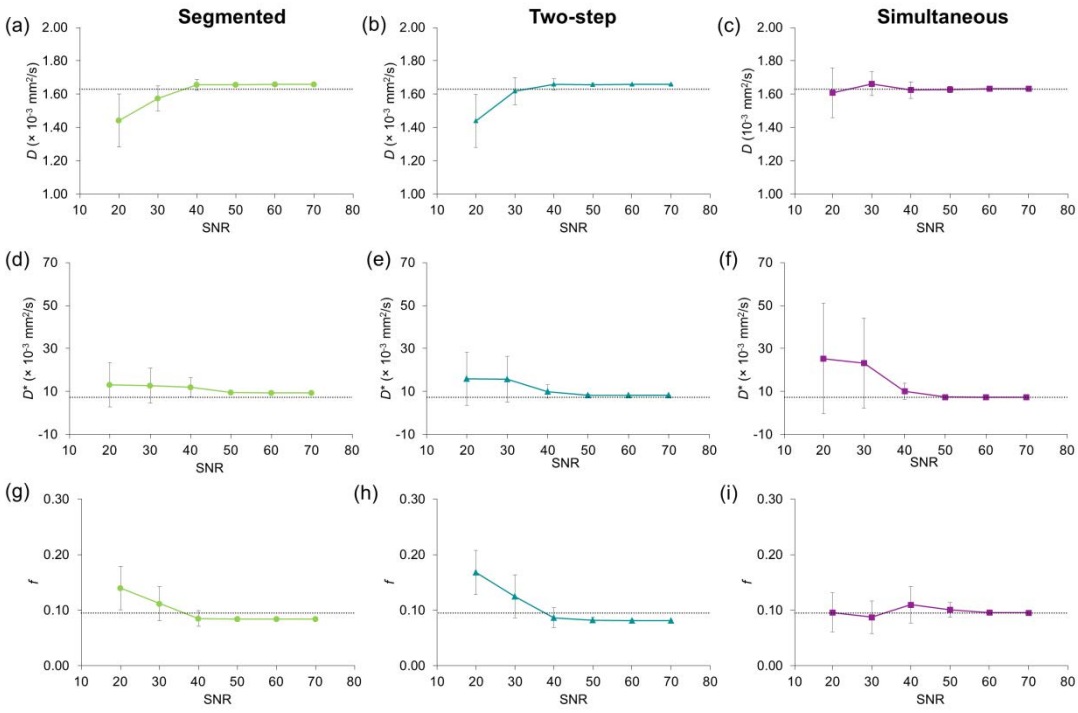

Figure 3.3 The accuracy results for IVIM fitting methods using the tumour model. Data simulation results for IVIM *D* (a-c), *D** (d-f) and *f* (g-i) using the segmented, two-step and simultaneous fitting.

Table 3.2 ANOVA results for the comparison of the estimated IVIM parameters among the different fitting algorithms for the grey matter model.

	***P*-value**			**Tukey *post-hoc* (*P*-value)**		
SNR	***D***	***D****	***f***	***D***	***D****	***f***
70	0.944	0.100	0.735	-	-	-
60	0.089	< 0.001	0.211	-	Seg-Sim < 0.001	-
50	0.400	< 0.001	0.147	-	Seg-Sim 0.02	-
40	0.007	< 0.001	0.001	Seg-Sim 0.018	Seg-Sim < 0.001	Seg-Sim < 0.001
				2Step-Sim 0.018		Seg-2Step 0.014
30	< 0.001	< 0.001	0.001	Seg-Sim < 0.001	Seg-Sim < 0.001	Seg-Sim < 0.001
				2Step-Sim < 0.001	Seg-2Step < 0.001	Seg-2Step 0.002
						2Step-Sim <0.001
20	< 0.001	0.005	0.013	Seg-Sim < 0.001	Seg-Sim < 0.001	Seg-2Step <0.001
				2Step-Sim < 0.001	Seg-2Step < 0.001	2Step-Sim <0.001

* Seg = segmented, 2Step = two-step, Sim = simultaneous fitting.

Table 3.3 ANOVA results for the comparison of the estimated IVIM parameters among the different fitting algorithms for the simulated tumour model.

	***P*-value**			**Tukey *post-hoc* (*P*-value)**		
SNR	***D***	***D****	***f***	***D***	***D****	***f***
70	0.132	0.374	0.121	-	-	-
60	0.004	0.785	< 0.001	Seg-Sim 0.006	-	Seg-Sim < 0.001
				2Step-Sim 0.017		2Step-Sim < 0.001
50	< 0.001	< 0.001	< 0.001	Seg-Sim < 0.001	Seg-2Step 0.006	Seg-Sim < 0.001
				2Step-Sim < 0.001	Seg-Sim < 0.001	2Step-Sim < 0.001
40	0.046	0.067	0.008	Seg-Sim 0.07	-	Seg-Sim < 0.001
				2Step-Sim 0.067		2Step-Sim < 0.001
30	< 0.001	0.001	0.005	Seg-Sim 0.001	Seg-Sim 0.001	Seg-2Step < 0.001
				2Step-Sim < 0.001	2Step-Sim 0.018	Seg-Sim < 0.001
						2Step-Sim < 0.001
20	< 0.001	< 0.001	0.001	Seg-Sim <0.001	Seg-Sim < 0.001	Seg-2Step < 0.001
				2Step-Sim 0.001		Seg-Sim < 0.001
						2Step-Sim < 0.001

* Seg = segmented, 2Step = two-step, Sim = simultaneous fitting.

The IVIM parameter precision (or reproducibility) in terms of coefficient of variation (CV%) are reported in Tables 3.4 and 3.5 for the fitting of grey matter and tumour models, respectively. The number of outliers from the fittings methods are reported in Table 3.6.

The grey matter model resulted in better precision and a smaller number of outliers compared to the tumour model. The simultaneous fitting was the most reproducible for the grey matter model, although not to a great extent. However, the simultaneous fitting was found to result in a large number of outliers.

The precision of the tumour model was found to be poor especially at low SNR levels for the IVIM perfusion parameters D^* and f. The precision of D was similar for both models. The estimation of D^* and f was more variable across all SNR levels, and in particular at SNR 20-40. The more constrained fitting methods improved the precision compared to the simultaneous fitting. The segmented fitting of the constrained methods was found to be the most reproducible with the lowest number of outliers.

Overall, the segmented fitting approach estimated the most accurate and precise D, D^* and f values, without excluding a great amount of the data. This was more pronounced for the low-perfused tumour model. At SNR 40, the mean error % / precision (CV%) for D, D^* and f were -0.30/4.23, 8.91/32.8, and 1.68/15.6 for the grey matter model, and -1.57/3.95, 64.9/64.2, and 10.4/33.4 for the tumour model, respectively.

Table 3.4 Reproducibility (CV%) results of the grey matter model.

	Segmented			Two-step			Simultaneous		
SNR	***D***	***D****	***f***	***D***	***D****	***f***	***D***	***D****	***f***
70	0.13	0.98	0.49	0.13	0.73	0.36	0.10	0.67	0.29
60	0.41	3.20	1.54	0.41	2.37	1.12	0.31	2.21	0.90
50	1.37	10.3	5.07	1.37	7.54	3.66	0.99	7.04	2.91
40	4.23	32.8	15.6	4.23	23.2	11.4	3.31	21.8	9.21
30	11.3	68.7	38.3	12.4	73.9	34.2	12.6	80.0	31.4
20	27.9	147	45.8	41.5	122	58.1	39.5	112	59.3

Table 3.5 Reproducibility (CV%) results of the tumour model.

	Segmented			Two-step			Simultaneous		
SNR	**D**	**D***	**f**	**D**	**D***	**f**	**D**	**D***	**f**
70	0.13	1.04	1.08	0.13	1.39	1.41	0.21	2.04	2.24
60	0.40	3.29	3.33	0.40	4.45	4.38	0.68	6.59	7.23
50	1.26	11.8	10.6	1.26	14.3	13.6	2.29	20.7	25.5
40	3.95	64.2	33.4	4.11	60.6	41.6	6.00	74.8	60.2
30	9.51	128	55.2	10.1	136	61.8	8.47	181	66.9
20	22.1	158	56.3	22.2	155	65.5	18.6	204	73.8

Table 3.6 Number of outliers (%) from the data fitting.

	Grey Matter			Tumour		
SNR	**Seg**	**Two-step**	**Sim**	**Seg**	**Two-step**	**Sim**
70	9.10	10.2	19.6	11.3	21.7	30.1
60	11.5	12.6	22.4	12.9	23.6	49.2
50	18.5	24.5	35.7	20.5	29.9	54.9
40	23.3	28.7	43.7	26.7	42.0	65.6
30	27.7	31.5	54.6	28.4	49.9	70.1
20	31.8	37.3	55.7	34.2	54.7	73.0

3.3.2 Uniqueness of IVIM Parameters

Confidence intervals were computed for the IVIM parameters at different SNR levels to investigate their uniqueness, focusing on cases that resulted in ill-conditioned data fitting. In this context, uniqueness was used to describe whether the IVIM parameters are unique of one another in their estimation.

Example cases of 2D-confidence interval or error-norm plots at SNR = 40 and 20 with grey matter and tumour models are shown in Figure 3.4 and 3.5, respectively. The plots represent signal data, where data fitting was starting to fail due to a greater amount of random noise or at the so-called "worst case scenario". The D and f were the most robust parameters, varying little within the 95 % confidence regions. The D^* was increasingly overestimated at decreasing f or increasing D values, which corresponded to decreasing bi-exponential behaviour of the signal. Similar behaviour was observed across all three bi-exponential fitting methods, whether constrained or not, although slightly more elongated confidence regions were observed for the simultaneous fitting.

The error norm plots for the tumour model showed similar behaviour to the grey matter model, although the 95 % confidence regions appeared relatively more elongated for each IVIM parameter (Figure 3.5). No multiple minima were observed for either of the tissue models, meaning that the Levenberg-Marquardt fitting algorithm was appropriate for the use of IVIM in the brain, as only a global minimum was observed.

The distributions of the estimated IVIM parameters at increasing SNR levels are shown for segmented and simultaneous fitting methods in Figure 3.6. The estimation of D values was robust with a few outliers, while a wider spread of values was observed for both D^* and f. The f value distributions were found positively skewed towards the higher values at the reducing SNR levels, and the median gave a better measure of the central tendency. This was also seen in Figure 3.4 as the elongation of the confidence levels

towards greater *f* values. The estimation of *D** had limited robustness even at the higher SNR levels.

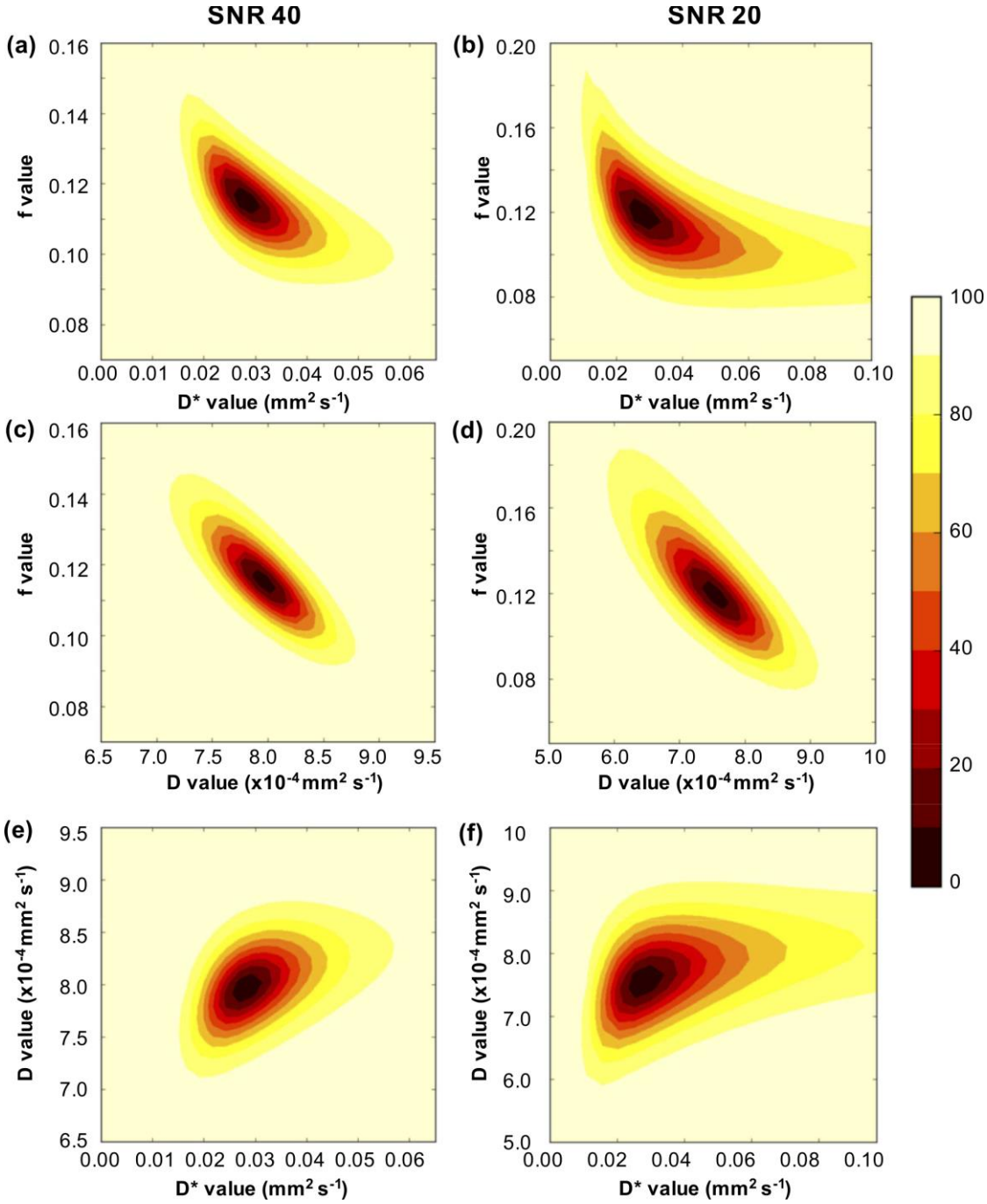

Figure 3.4 Error norm plots for the grey matter model. Examples of segmented fitting and the resulting error normal plots at SNR = 40 (left) and SNR = 20 (right), where the data fitting was starting to fail due to a greater amount of random noise. The plots were computed for all three IVIM parameter combinations *f*-*D** (a-b), *f*-*D* (c-d), and *D*-*D**(e-f). The contour colours describe the percentage confidence as shown by the colour bar.

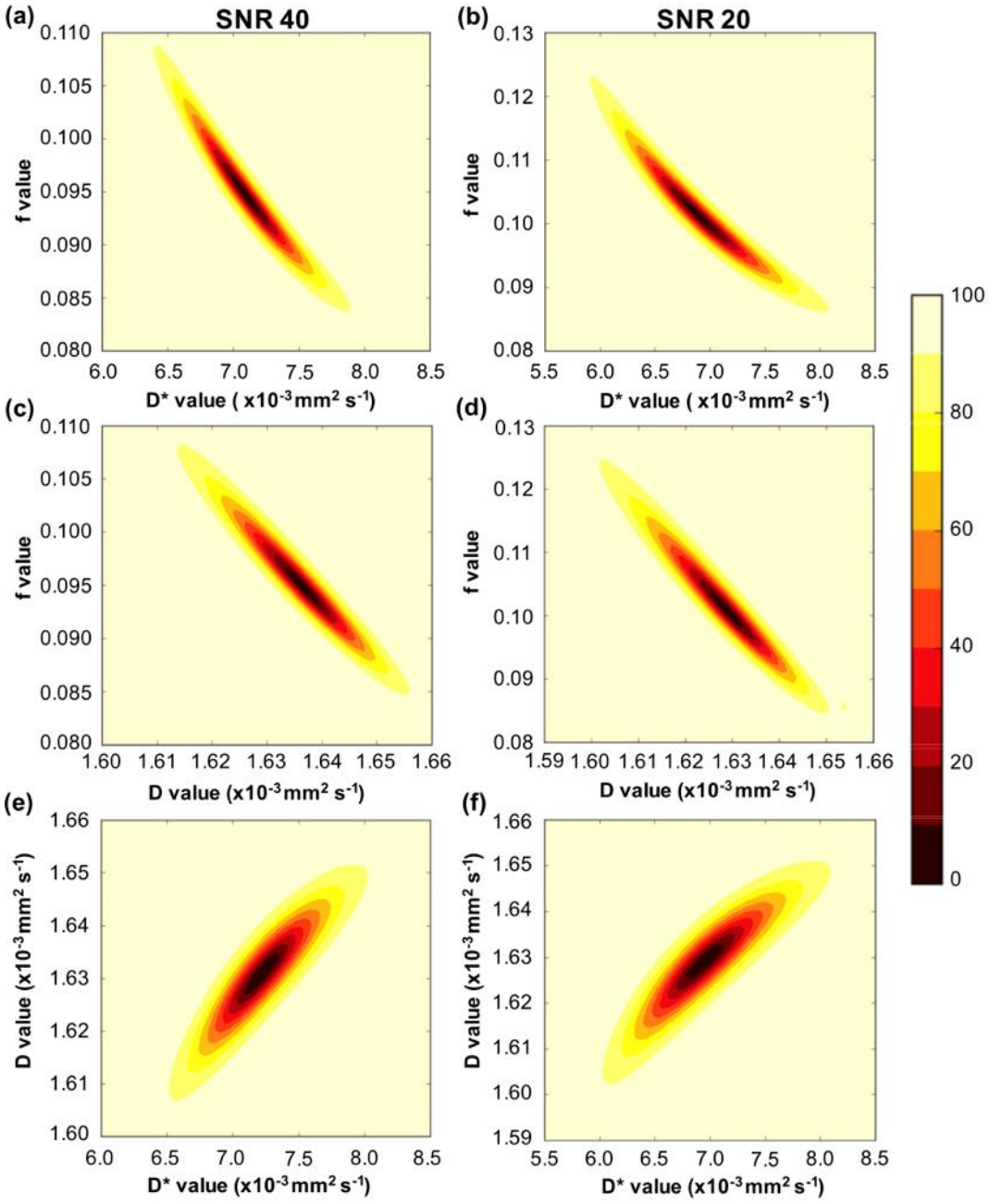

Figure 3.5 Error norm plots for the tumour model. Examples of segmented fitting and the resulting error normal plots at SNR = 40 (left) and SNR = 20 (right), where the data fitting was starting to fail due to a greater amount of random noise. The plots were computed for all three IVIM parameter combinations *f*-*D** (a-b), *f*-*D* (c-d), and *D*-*D**(e-f). The contour colours describe the percentage confidence as shown by the colour bar.

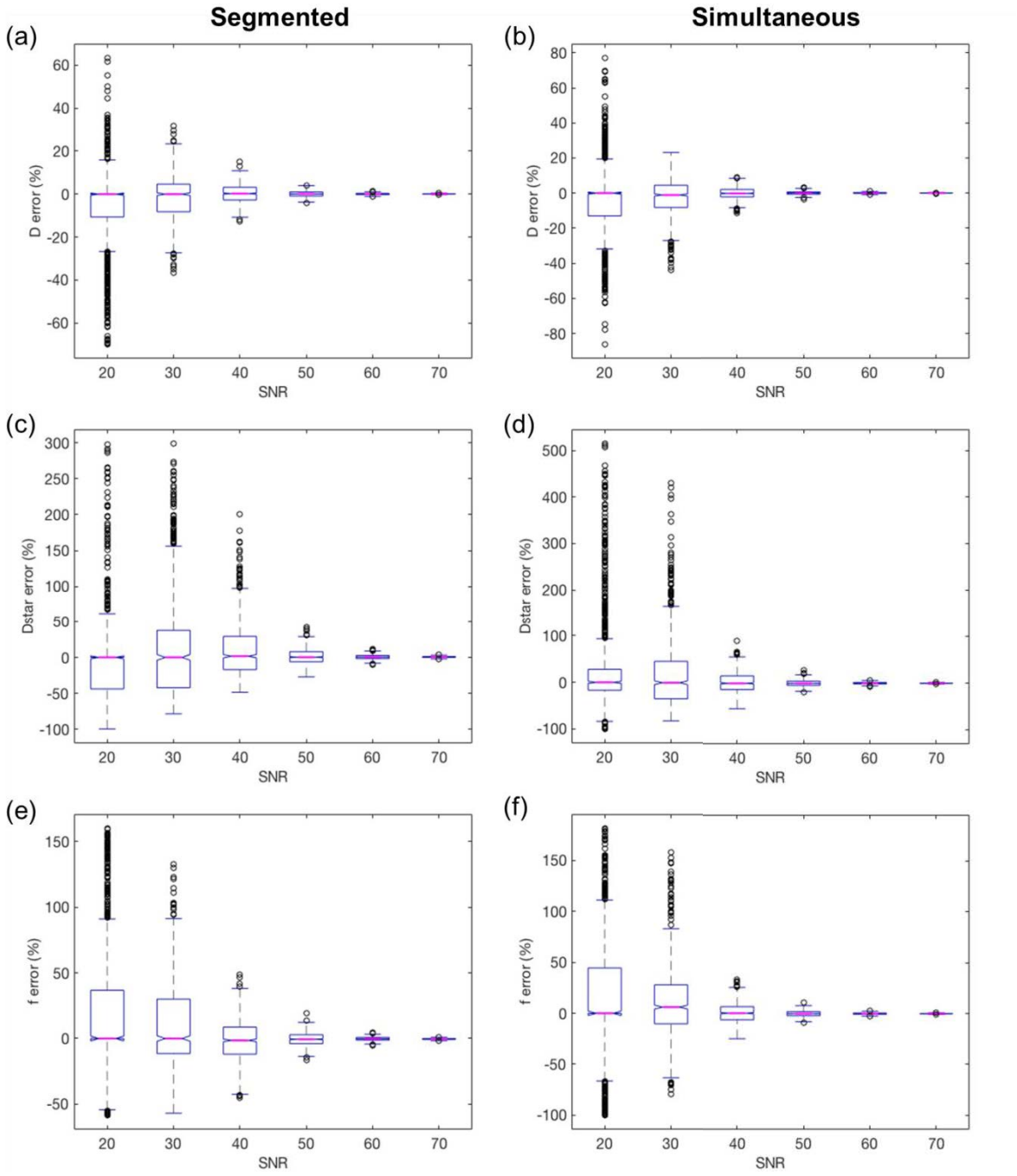

Figure 3.6 Boxplots of estimated IVIM parameters for the grey matter model. Boxplots of D (a-b), D^* (c-d) and f (e-f) value distributions with segmented (left) and simultaneous (right) fitting methods for the grey matter model. The y-axis describes the percentage error (%) to the true value, the pink lines describe the medians and notches describe the 95 % confidence levels of the median. The box edges are the first (Q1) and the third (Q3) quartiles, with whiskers showing the more extreme data points not considered outliers.

3.4 Discussion

In this Chapter, simulated multi *b*-value DW-MRI data for the determination of IVIM parameters was used to investigate the robustness of the fitting methods in low-perfused brain tissues. The model simulations suggested that the constrained segmented and two-step methods performed similarly but better than simultaneous fitting. At the lower SNR levels, the estimated parameters from the constrained methods differed significantly to the ones derived with simultaneous fitting. The use of constrained fitting methods reduced the number of outliers and provided more reproducible estimation of IVIM parameters. Overall, the more constrained approaches provided more robust results compared with the simultaneous fitting, in particular at the lower SNR level.

The segmented fitting has often been used to increase the reliability of the D^* parameter in abdominal or body IVIM studies (84, 89, 90, 111). However, the precision of D^* in the relatively low-perfused grey matter model was found similar across the three fitting methods, although better accuracy was achieved with the segmented method. In this study, the constrained fitting methods and especially the segmented fitting were found to produce more reliable results for the tumour model with the subtle bi-exponential signal data. This was observed with the estimation of D^* and to a lesser extent with f. Therefore, tissues of low perfusion can also benefit from the use of more constrained fitting methods.

The results from the data simulations showed that the estimation of D and f was more robust and reliable compared to D^*. Both f and D^* were affected by the degree of perfusion or bi-exponential behaviour, which resulted in a greater variance for the low-perfused tumour model. However, f was still estimated with good accuracy at lower SNR levels using the segmented fitting method. A similar perfusion-related influence was observed in a study by Wu et al. (87), where model simulations based on a healthy brain

showed greater variance for the less-perfused white matter compared to the grey matter. Therefore, the low-perfused tissues are likely to have a higher SNR requirement for the computation of reliable IVIM derived parameters. Overall, our simulations suggest that the use of segmented fitting is beneficial, providing more reliable results with the smallest number of outliers, followed by the two-step fitting, which has been the more commonly applied method in the brain (27, 28).

The uniqueness of the estimated IVIM parameters was investigated using error norm plots. For models such as the bi-exponential, the approximation of the standard error from the covariance matrix can begin to fail, and confidence intervals can provide a better measure of robustness of the parameters. Most of the grey matter and tumour model iterations produced symmetrical uncertainties and the standard errors derived from the covariance matrix produced sufficient approximates of the uncertainties. Therefore, the presented error norm plots of grey matter and tumour model cases did not reflect most of the data observed at the corresponding SNR levels, but rather indicated the behaviour of the models at higher random noise levels.

Previous studies, such as one by Jelescu et al. (155), have shown that multiple minima can occur in application of multi-compartmental models to diffusion-weighted data. Depending on factors such as the initial parameter value (set for the fitting algorithm), the minimisation process might converge in a local minimum and hence lead to incorrect estimation of the parameter value. However, in our study, no such cases were observed, meaning that the chosen algorithm was feasible for the convergence of the algorithm to the global minimum. This is important for the clinical reliability of the model.

The results from the grey matter model suggested that the estimation of D and f was still robust in the presence of noise. A loss in uniqueness of D^* was observed, with a range of D^* values estimated for the fixed D and f values. This was also illustrated as

the large number of outliers for the D^* parameter. In comparison to the other fitting methods, the segmented fitting provided the best estimate of D^*. With the limited robustness and loss in uniqueness of D^*, our study suggests that the fitting methods utilised here cannot provide a reliable measure of microvascular diffusion, specifically the parameter D^*, for the low-perfused brain tissue. An increase in SNR or the number of low b-values could potentially increase the robustness of D^*, which was previously shown in a liver study by Cohen et al. (84). Also, as previously mentioned, an increase in the number of averages would improve the fitting and hence the robustness of the D^* and f.

3.5 Study Limitations

A key limitation in this study was the use of fitting methods that assume the signal bi-exponential. In regions where the signal decay approaches mono-exponential behaviour, such as for the tumour model, the accuracy and precision of the estimated f and D^* parameters was decreased. The f parameter was affected to a lesser degree than the D^*, which performed poorly in the model simulations. In scenarios where the signal might be mono-exponential, the D and D^* would effectively be the same. This could be implemented into the in vivo fitting scenarios as a quality control method to improve the robustness and reliability in low-perfused regions.

3.6 Conclusion

The model simulations suggested that the best performance was achieved with the use of constrained fitting algorithms. These resulted in the most reliable IVIM parameters, and although similar accuracy was achieved with the simultaneous and constrained fitting methods, differences were observed in the precision or reproducibility, and the number of outliers. Greater variance was demonstrated in the estimation of the IVIM parameters in the low-perfused tumour model compared to the grey matter model. However, the estimation of D and f parameters was robust despite the low degree of bi-exponential behaviour. The D^* parameter was concluded to provide unreliable results in such regions with the fitting methods studied here. The simulations indicated that there is an important SNR requirement for reliable IVIM data analysis in the very low-perfused tissues. In our study, this was approximately SNR > 40. Overall, this study showed that the constrained fitting of the IVIM model and the D and f parameters can be used to assess low-perfused tissue regions.

Chapter 4

Rapid Measurement of IVIM Perfusion Fraction for Use in Clinical MR Imaging

4. Rapid Measurement of IVIM Perfusion Fraction for Use in Clinical MR Imaging

Some aspects of the work presented here were published in [**P02**] and [**P06**].

4.1 Introduction

The clinical adoption of the intravoxel incoherent motion (IVIM) model has been hindered by practical issues, such as the lack of consensus for the number and choice of *b*-values, and the requirements for sufficient signal-to-noise ratio (SNR) levels for accurate and reproducible post-processing (84, 85, 92). As a potential consequence, variability has been observed in the previously reported perfusion fraction *f* values, as summarised in Table 2.2, in both the brain and the abdomen. The variability of parameters can also be related to their reproducibility. However, previous studies have shown that the IVIM *D* and *f* are reproducible to a clinical standard, but greater variability has been observed with the pseudo-diffusion coefficient *D** (79, 85, 90, 156). Therefore, the variability resulting from the use of different *b*-value distributions should be addressed to estimate its contribution to the differences seen in previous studies.

As mentioned above, the poor precision and reproducibility of the *D** parameter has hindered its clinical value, particularly for the low-perfused brain tissues (28, 93, 156). This has meant that the IVIM brain applications have mainly focused on the *D* and *f* parameters, with clinical value demonstrated in brain tumour grading (27, 93, 137) and stroke imaging (93, 139). The application of IVIM and *D** has been more established in the abdominal organs such as the liver (84, 109, 111) and kidneys (157). However, the reproducibility of *D** is still reduced relative to the *D* and *f* parameters, and commonly produces very heterogeneous appearing maps (109). The application of IVIM in the abdomen is also subject to respiratory and cardiac motion artifacts.

While different challenges exist for the applications of IVIM in different tissues, the same practical issues related to the requirements for data quality and acquisition remain.

The translation of IVIM to clinical practice requires a DW-MRI protocol with a short acquisition time. One way to reduce the scanning time is to decrease the total number of *b*-values. Previously, the most robust IVIM parameters in many tissue types (85, 88, 156), including low-perfused tissues presented in Chapter 3, have been achieved with the use of segmented IVIM fitting. Using this methodology, the D and f parameters can be computed using the linear fit of high *b*-values and $b = 0$. Although this method does not allow the computation of the D^* parameter, the challenges with its reproducibility suggest that further evaluation is required to demonstrate its clinical reliability. Therefore, if only D and f are of clinical interest, the IVIM could be performed using a set of high *b*-values, thereby minimising the time required for data acquisition.

A series of high *b*-value combinations for brain tumour and stroke patients were used for the estimation of f with the segmented fitting in a study by Conklin et al. (93). The recommended *b*-value distribution was chosen by comparison to the more commonly used less constrained two-step fitting method in the brain. Although the similarity of the two fitting methods can indicate how many *b*-values are required for comparable results, it was unable to assess the accuracy and reliability of the estimated IVIM parameters.

In this Chapter, the aim is to evaluate the application of a rapid three *b*-value protocol for the estimation of clinically valuable D and f parameters, using tissue models accounting for diffusion in the brain and the abdomen, and to investigate the influence of different *b*-values in the parameter estimation. To relate and validate the results back to in vivo data, comparison of the model data to brain DW-MRI data is performed.

4.2 Methods

4.2.1 Data Simulations

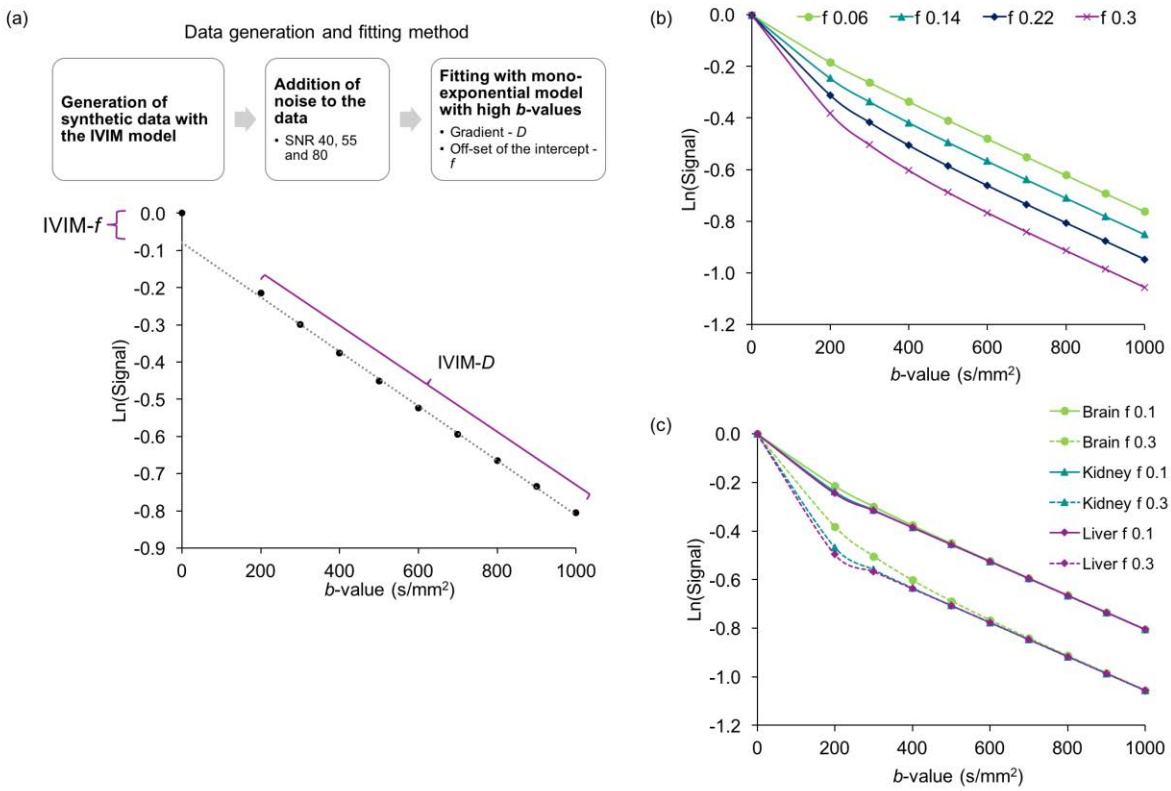

Figure 4.1 Description of the IVIM data generation and fitting method. A schematic (a) of the mono-exponential fitting of the high *b*-value diffusion signal to derive the *D* and *f* parameters from the fit gradient and off-set of the intercept to *S*(0), respectively. Plots (b) describing the data signal decay at varying *f* values for the diffusion in low-perfusion model (brain) and (c) comparison of the signal decays for the different tissue models, respectively.

All simulations and data analysis were implemented in MATLAB v.2016b (MathWorks, Natick, MA). The model data signal values were generated with the bi-exponential Eq. 2.12, using *b*-value distribution: 0, 200, 300, 400, 500, 600, 700, 800, 900, 1000 s/mm^2. The data generation and analysis are described in Figure 4.1.

Signal data sets were generated using a range of *f* values (0.06 to 0.30 in increments of 0.02) and three different *D**/*D* ratios, corresponding to previously reported ratios observed in brain, kidney and liver (10, 20 and 70, respectively (92)). The *D* parameter was fixed at 0.7 × 10^{-3} mm^2/s and *D** parameter was 7 × 10^{-3}, 14 × 10^{-3} and 49 × 10^{-3}

mm^2/s for the brain, kidney and liver models, respectively. In this chapter, these models are also referred to as low-, medium- and high-perfusion models, respectively. Signal data for the different diffusion scenarios and a series of f values is presented in Figure 4.1b and 4.1c.

Gaussian noise was introduced to the modelled data to simulate the Rician distribution of noise found in MR images using the in-built MATLAB function (Communications Systems toolbox). Signal to noise ratio (SNR) levels of 40, 55 and 80, based on Gaussian noise, were used to study the influence of noise on the estimated parameters. SNR = 40 was representative of the SNR levels measured in our volunteer cohort (b = 1000 s/mm^2) and the higher SNR levels corresponded to increasing the number of averages (NSA) from one to two and four, respectively. The data simulations were performed using N = 1,000 random data iterations for each set of IVIM parameters.

4.2.2 MR Imaging

All MR imaging was performed on a Philips Achieva 3.0 Tesla (T) TX (Philips Healthcare, Best, the Netherlands) MRI scanner with a 32-multichannel receive head coil at Birmingham Children's Hospital.

The diffusion MR protocol used a sensitivity-encoded (SENSE) approach with single-shot, spin-echo (EPI) sequence, with diffusion-weighted gradients applied in three orthogonal directions, of which a geometrical average (or trace) diffusion-weighted image was derived. The protocol used TR/TE = 4,000/91 ms, 30 contiguous 3.5 mm thick axial slices, field-of-view (FOV) 240 × 240 mm and matrix size 96 × 96, which resulted in in-plane resolution of 2.5 × 2.5 mm. The b-value distribution included values of 0, 300, 500, 1000 s/mm^2 which were used in the analysis (full b-value distribution: 0, 20, 40, 80, 110, 140, 170, 200, 300, 500, 1000 s/mm^2). The spectral presaturation with inversion recovery (SPIR) was used for fat suppression and the total scan duration was 2.12 minutes. The

T_1-weighted scan was performed with a spin-echo sequence with FOV 240 × 240 mm, matrix size 240 × 240, slice thickness 3.5 mm and TR/TE = 675/10 ms.

Additionally, four of the volunteer cases (n = 4) were scanned twice with the DW-MRI protocol to assess the IVIM parameter repeatability. The volunteers remained on the scanner bed for both of the scans. Finally, one volunteer (n = 1) had a separate scan acquired with b-values: 0, 200, 300, 400, 500, 600, 700, 800, 900 and 1000 s/mm^2 for illustrative purposes.

4.2.2.1 Volunteer Population

A cohort of healthy young adult volunteers (n = 16, age 25-30, mean age 26 years) was scanned with the above MRI protocols (DW-MRI, T_1W-MRI). The protocols for this retrospective study were approved by the research ethics committee and informed consent was gathered from all volunteers.

4.2.3 Data Analysis

IVIM data fitting was performed with the segmented method, as described in Chapter 2 (section 2.3.2.1), and demonstrated in Figure 4.1a, to estimate the IVIM D and f parameters. The fitting of generated diffusion-weighted signal was performed with b-value distributions: [200,1000], [300,1000], [400,1000], [500,1000], [600,1000], [700,1000], [800,1000] and [900,1000]. For the volunteer cohort (n = 16), due to the retrospective nature of the data, only fitting with [300,1000] and [500,1000] was performed, including the scans acquired for repeatability measurements. The IVIM D^* was estimated with the segmented fitting and the full b-value distribution was used to estimate the in vivo IVIM D^* in grey matter.

Grey matter masks were created for each volunteer case with the Brain Extraction Tool (BET) and FMRIB's Automated Segmentation Tool (FAST) in FMRIB Software Library package (Analysis Group, FMRIB, Oxford, UK, v. 5.0) using the T_1-weighted images

(158, 159). The probabilistic tissue segmentation was performed for three classes, corresponding to grey matter, white matter or cerebrospinal fluid (CSF). To assess the inclusion of only cortical grey matter and exclusion of sulcal CSF in the binary masks, partial volume tissue (PVE) segmentation was also performed for eight of the volunteer cases (n = 8). The PVE masks provided an estimation of the proportion of grey matter within the voxels (scale 0 - 1), and only voxels of value = 1 were included in the analysis, which corresponded to tissue fully representing grey matter with no partial volume of CSF or white matter (see Figure 4.13).

The T_1-weighted images were acquired using the same spatial geometry as the DWI images and no further registration was performed at post-processing. The generated masks (mask = 1, background = 0) were adjusted for the size of the acquired DWI images using bi-linear interpolation. As the interpolation of the binary masks resulted in a range of values (0 to 1) for the mask, a threshold of 0.7 was applied to remove blurring effects created around the mask edges (values > 0.7, were made to equal 1). This further minimised the number of pixels affected by partial volume effects. For the analysis, the D and f values were extracted using the grey matter masks from three slices above the lateral ventricles.

Based on the extracted grey matter values, average histograms were computed for the IVIM parameters. The number of bins was based on the square root of the maximum number of data values extracted from the regions-of-interests (ROIs). The bin widths were computed for a range of zero to the maximum IVIM value. The same number of bins was used for all the cases and b-value distributions, as well as for the IVIM values extracted with the PVE masks. The same histogram methodology was applied to the simulated IVIM parameters.

4.2.3.1 Signal-to-Noise Ratio (SNR) of DW-MRI Data

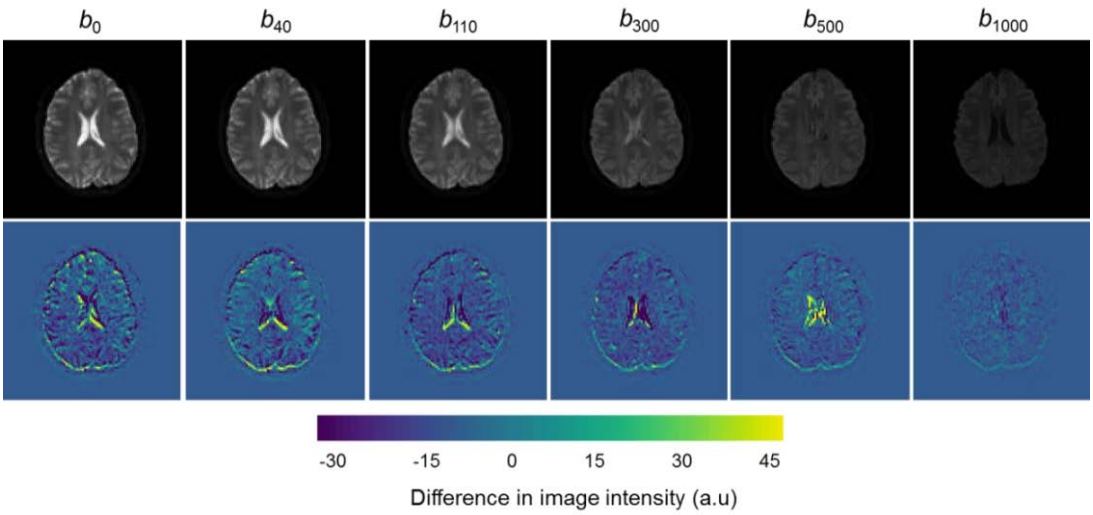

Figure 4.2 The difference images of *b*-values used for the computation of SNR. The diffusion-weighted images (top) and the difference images, [im3], (bottom) for a series of *b*-values used in the DW-MRI protocol.

SNR levels of the DWI data were determined using the standard NEMA method, which is the recommended method for computing SNR when parallel imaging such as SENSE acceleration is used (160). The method uses subtraction of two repeated signal-containing images [im_1 and im_2], providing a difference image [im_3], which gives a measure of the noise field:

$$[\mathrm{im}_3] = [\mathrm{im}_1] - [\mathrm{im}_2] \qquad [4.1]$$

Examples of the difference images for different *b*-values are shown in Figure 4.2.

The standard deviation of noise (σ) was determined from the pixel values within a region-of-interest (ROI) in [im_3]. Using the same ROI, the average signal is determined from the [im_1 and im_2]. The SNR can then be calculated using (152):

$$\mathrm{SNR}_{\mathrm{diff}}(\mathrm{im}_1, \mathrm{im}_2) = \frac{S_{diff}}{\sigma_{diff}} = \frac{\frac{1}{2}\mathrm{mean}(S_N(\mathbf{r}, \mathrm{im}_1) + S_N(\mathbf{r}, \mathrm{im}_2))}{\frac{1}{\sqrt{2}}\mathrm{stddev}((S_N(\mathbf{r}, \mathrm{im}_1) - S_N(\mathbf{r}, \mathrm{im}_2))} = \frac{\frac{1}{2}m_{\mathrm{sum}}}{\frac{1}{\sqrt{2}}s_{\mathrm{diff}}} = \frac{1}{\sqrt{2}}\frac{m_{\mathrm{sum}}}{s_{\mathrm{diff}}} \qquad [4.2]$$

where $\mathbf{r} = (x,y,z)$ is the position.

The SNR was measured for grey matter regions of five volunteers using ROI size of 3 × 3. The SNR at b = 1000 s/mm^2 was found to be in the range of 45 ± 8.

4.2.4 Statistical Analysis

Statistical analysis was performed in SPSS Statistics (IBM, Chicago, IL, v.22) and Microsoft Excel (Microsoft, Redmond, WA, v.16.0).

4.2.4.1 Simulated Model Data

The following statistics were calculated for the estimated parameters D and f. Relative bias was determined from the difference between the true parameter (used in the signal data generation) and the estimated parameter (computed from fitting of the signal data) values, which was normalised to the true parameter value:

$$\text{relative bias} = \frac{\frac{1}{N}\sum_{i=1}^{N}(x_i - X)}{X} \qquad [4.3]$$

where i = number of iterations, x_i = estimated parameter and X = true parameter. Relative error (σ) was computed as the root mean square of the distance between the true parameter to the estimated parameter:

$$\text{relative error}, \sigma = \frac{\sqrt{\frac{1}{N}\sum_{i=1}^{N}(x_i - X)^2}}{X} \qquad [4.4]$$

Both relative bias and error were determined individually for each estimated parameter (D, f) rather than for the mean values over all data iterations. The overall relative error was computed from the individual IVIM parameter errors for each b-value distribution using $\sigma_{D+f} = \sigma_D + \sigma_f$. The overall error and the σ_f were used to make recommendations for the simulated tissue regions based on the smallest overall relative error.

The reproducibility of the estimated parameters was determined as a coefficient of variation from the ratio of the standard deviation to the mean of the estimated parameters:

$$\text{coefficient of variation (\%)} = \left(\frac{\sqrt{\frac{1}{N}\sum_{i=1}^{N}(x_i - \bar{x})^2}}{\bar{x}} \right) \times 100 \qquad [4.5]$$

where $\bar{x}$ is the mean of the estimated parameter D or f.

4.2.4.2 In vivo Volunteer Data

Correlation analysis (n = 16) was performed for the mean D and f parameters of grey matter to determine how the values were related between the b-value distributions [300,1000] and [500,1000]. This was assessed using the Pearson correlation coefficient, r. An analysis of variance (ANOVA) was also performed for the mean grey matter values. This was to test if the estimated parameters differed significantly ($P < 0.05$) between the two b-value distributions. The agreement of the estimated IVIM parameters with the different b-value distributions was determined with the Bland-Altman analysis. The repeatability of the IVIM parameters was tested using within-subject coefficient of variation ($_{w}$CV%), which was the recommended statistic by the Quantitative Imaging Biomarkers Alliance (161). The methodology has been applied in previous IVIM studies (84, 88, 90). The $_{w}$CV was computed with the root mean square method (162), using the paired DW-MRI data measurements (n = 4) and 4 × 4 ROIs (two for each measurement pair) of the same grey matter regions as used in the above analysis. To assess whether the IVIM values were influenced by CSF partial volume, ANOVA was performed for IVIM histogram parameters derived with the probabilistic and PVE masks (n = 8) to determine any significant difference ($P < 0.05$).

4.3 Results

4.3.1 Model Data Simulations

The relative bias results for the estimated *f* and *D* parameters from the tissue models and the different *b*-value distributions are presented in Figure 4.3. Noise was found to influence the bias at SNR = 40, whereas results at SNR = 55 and 80 resembled one another in magnitude and behaviour for all tissue models. The direction of bias was different for *f* and *D*, with negative and positive bias shown, respectively. At the higher SNR levels (55 and 80), the magnitude of the simulated *f* value was found to not affect the bias in estimation of *f*. However, at SNR = 40, noise had a greater influence on lower *f* values and higher *b*-values. The similarity of biases at SNR = 55 and 80 suggests that these present the intrinsic magnitude of biases from the fitting of the tissue models. Higher biases were observed for the lower perfusion models, with lower *D**/*D* ratios equating to lower degrees of bi-exponential behaviour.

The choice of *b*-value had a noticeable influence on the observed bias. The intrinsic bias of the models and the estimated parameters was higher at the low *b*-value distributions, whereas noise affected the high *b*-value distributions, although only for the *f* parameter. Distributions of the estimated *f* values with different *b*-value distributions for the three models are presented in Figure 4.4 for SNR = 40. Narrower distributions were observed for the lower *b*-values, whereas the estimation of *f* with [800,1000] was largely influenced by noise. The position of the *f* value distributions, derived with [200,1000] for the lower perfusion models clearly indicated the presence of greater intrinsic negative bias.

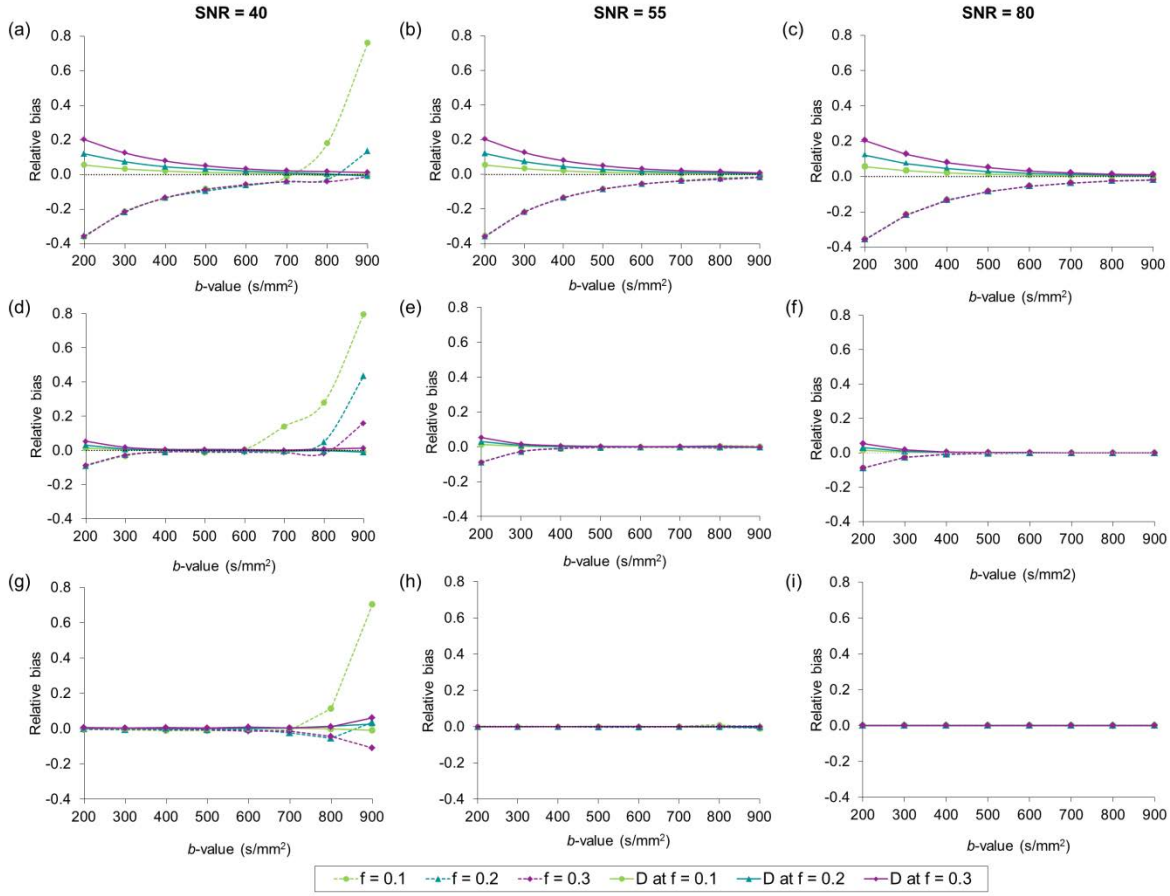

Figure 4.3 Relative bias results for the estimated IVIM parameters as a function of *b*-value. Relative bias results for the (a-c) low-, (d-f) medium- and (g-i) high-perfusion models at SNR levels 40, 55 and 80. Results are presented for simulated *f* values of 0.1, 0.2 and 0.3 for both *D* and *f*. Bias = 0 is indicated by the black dashed line.

The bias of *f* for the range of simulated values (*f* = 0.06 - 0.3) and the low-perfusion model at SNR 40 was -35.8 ± 0.3 %, -8.63 ± 0.8 % and -5.77 ± 15.0 % for [200,1000], [500,1000] and [800,1000] distributions, respectively. At SNR = 55 the biases were similar but with reduced variability: -35.7 ± 0.2 %, 8.48 ± 0.05 % and -2.62 ± 0.32 %. Similarly for the *D* parameter at SNR = 40, the bias was 11.1 ± 5.32 %, 2.72 ± 1.34 % and 0.61 ± 0.65 % for [200,1000], [500,1000] and [800,1000] distributions, respectively. For the higher perfusion models (medium and high), the bias was < 10 % for *f*, apart from the high *b*-value distributions (*b* = 700 – 900 s/mm²) at SNR = 40. The bias for the *D* parameter was < 6 % for both higher perfusion models.

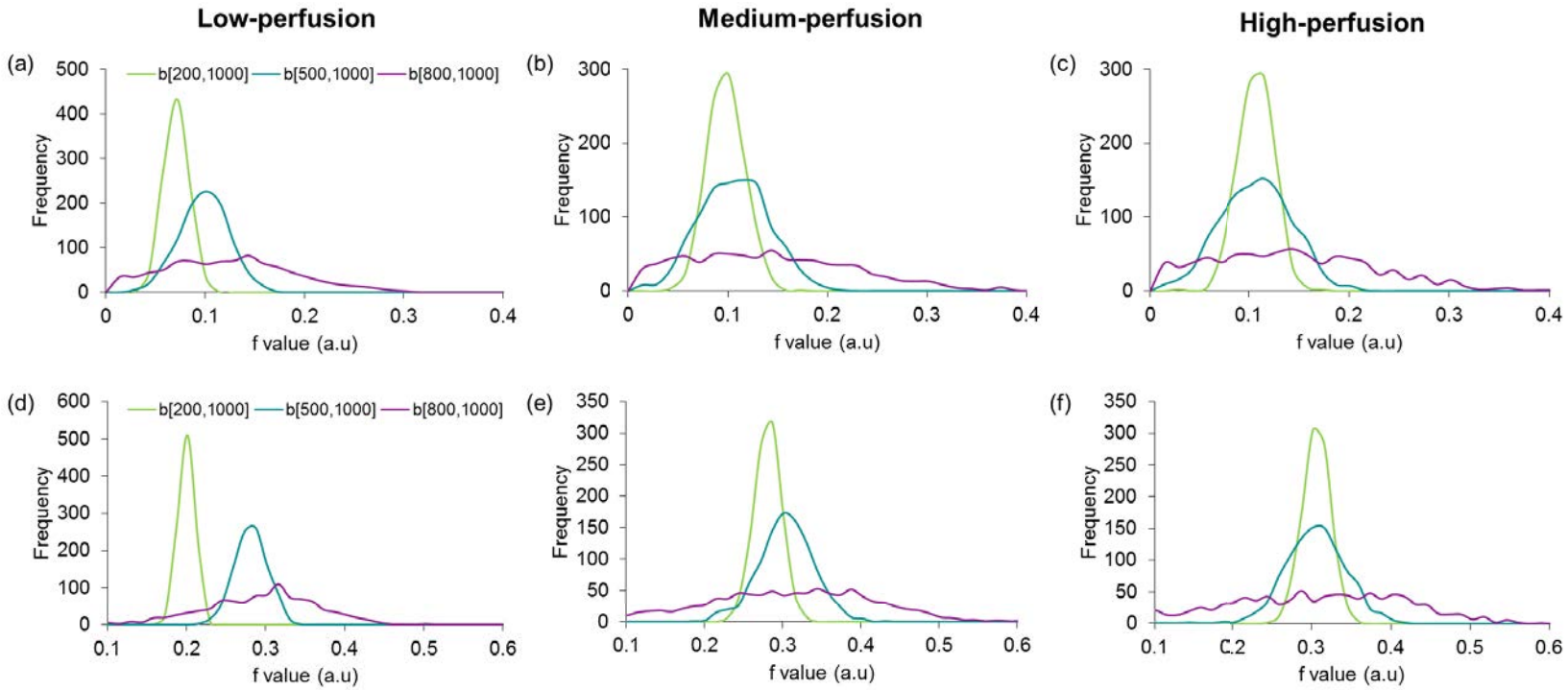

Figure 4.4 Distributions of the estimated *f* values from model simulations and *b*-value distributions at SNR = 40. Distributions based on simulations where f = 0.1 (top) and f = 0.3 (bottom) using *b*-value distributions b[200,1000], b[500,1000] and b[800,1000] for low- (a,d), medium- (b,e) and high-perfusion (c,f) tissue models.

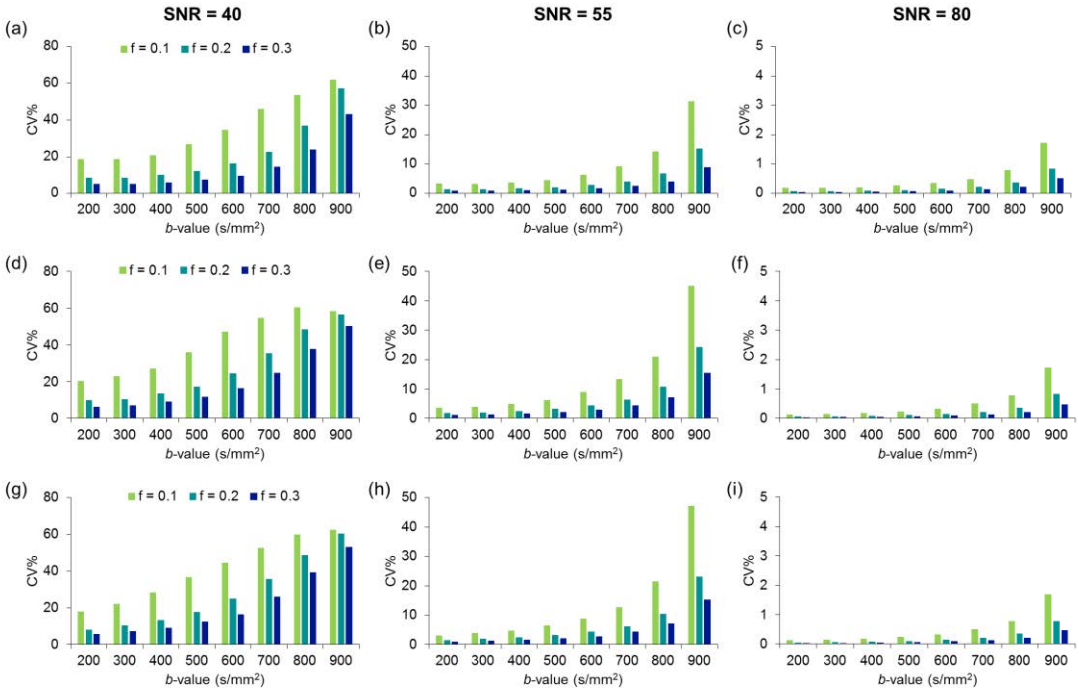

Figure 4.5 Reproducibility of perfusion fraction *f*, as a function of *b*-value. Reproducibility of *f* in low- (a-c), medium- (d-f) and high-perfusion (g-i) models at SNR levels 40, 55 and 80 for simulated *f* values 0.1, 0.2 and 0.3.

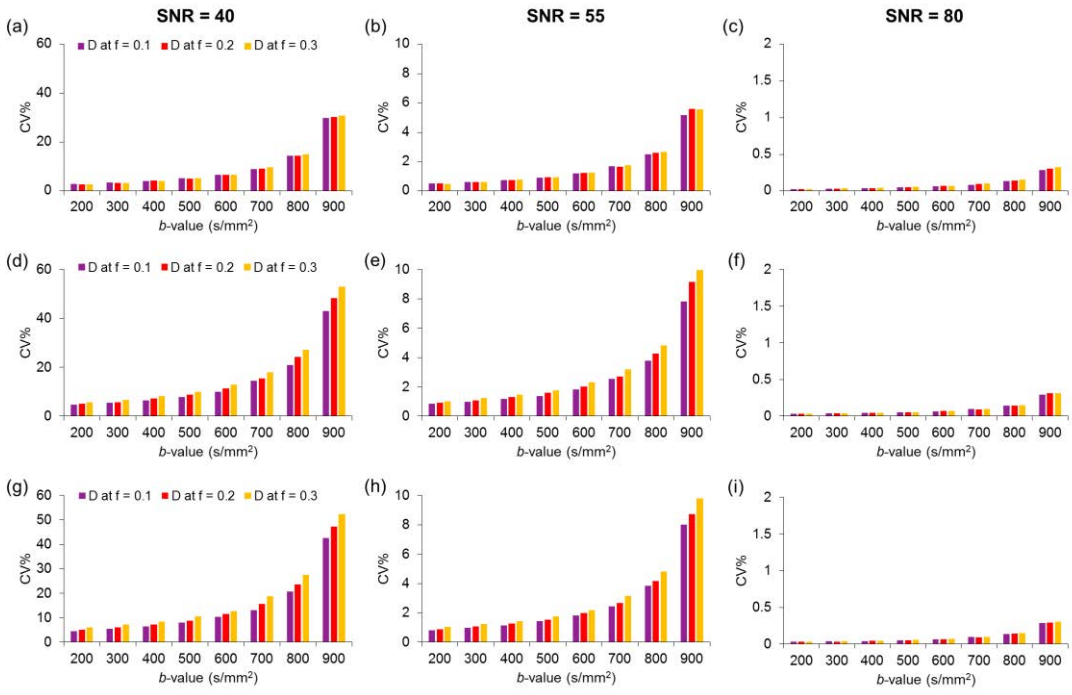

Figure 4.6 Reproducibility of diffusion coefficient *D*, as a function of b-value. Reproducibility of *D* in low- (a-c), medium- (d-f) and high-perfusion (g-i) models at SNR levels 40, 55 and 80 for simulated *f* values 0.1, 0.2 and 0.3.

The reproducibility results for *f* and *D* parameters and the different tissue models are presented in Figures 4.5 and 4.6, respectively. The variability of the estimated IVIM parameters was largely influenced by noise and dependent on the SNR level. The increase from SNR = 40 to SNR = 55 (NSA = 1 to NSA = 2) resulted in a noticeable improvement in the reproducibility of *D* and *f*, with smaller improvements observed with the increase to SNR = 80. The different tissue models did not differ to a great extent in terms of their reproducibility for the *f* parameter, but the *D* parameter was found to be more reproducible with the low-perfusion model. Lower variability of *f* and *D* was observed with the use of lower *b*-value distributions. Finally, higher *f* values had better reproducibility compared to low *f* values.

4.3.2 Optimal *b*-value distributions

The relative errors of estimating *f* and *D* individually are presented in Figures 4.7 and 4.8, respectively, for the low- and high-perfused tissue models. The relative error of *f* was greater compared to *D* in all cases. At SNR = 80, the relative errors were higher at low *b*-value distributions for the low- and medium-perfusion models because of the influence from bias. As shown previously, negligible bias was observed with the high-perfusion model. Noise had a larger influence compared to bias at SNR = 40, resulting in higher relative errors at high *b*-values. At SNR = 55 a similar magnitude of contribution from bias and noise was seen for the low-perfusion model, whereas noise was the dominant contributor for the medium- and high-perfusion models.

The overall relative errors based on both individual *f* and *D* errors are presented in Figure 4.9 for *b*-value distributions that had the lowest overall error. The overall error values for all *b*-value distributions are summarised in Table 4.1. The overall error was largely influenced by the relative error of *f*, with a small contribution from the relative error of *D*. For the low- and medium-perfusion models, a shift to a higher *b*-value distribution was observed at all SNR levels. This is seen on Figure 4.9b and 4.9d, where the relative error plots cross for the different *b*-value distributions.

Based on the minimal overall and *f* relative errors, suggestions for optimal *b*-value distributions were derived. The optimal *b*-value distributions are listed in Table 4.2 for each perfusion model. At SNR = 40, the optimal *b*-value distributions were [500,1000], [300,1000] and [200,1000] for the low-, medium, and high-perfusion models, respectively. The relative errors of the estimated *f* parameters for these *b*-value distributions were < 20 % at SNR = 40, and < 10 % for SNR = 55 and 80. For the low-perfusion model, a higher *b*-value distribution was required to minimise the influence from bias.

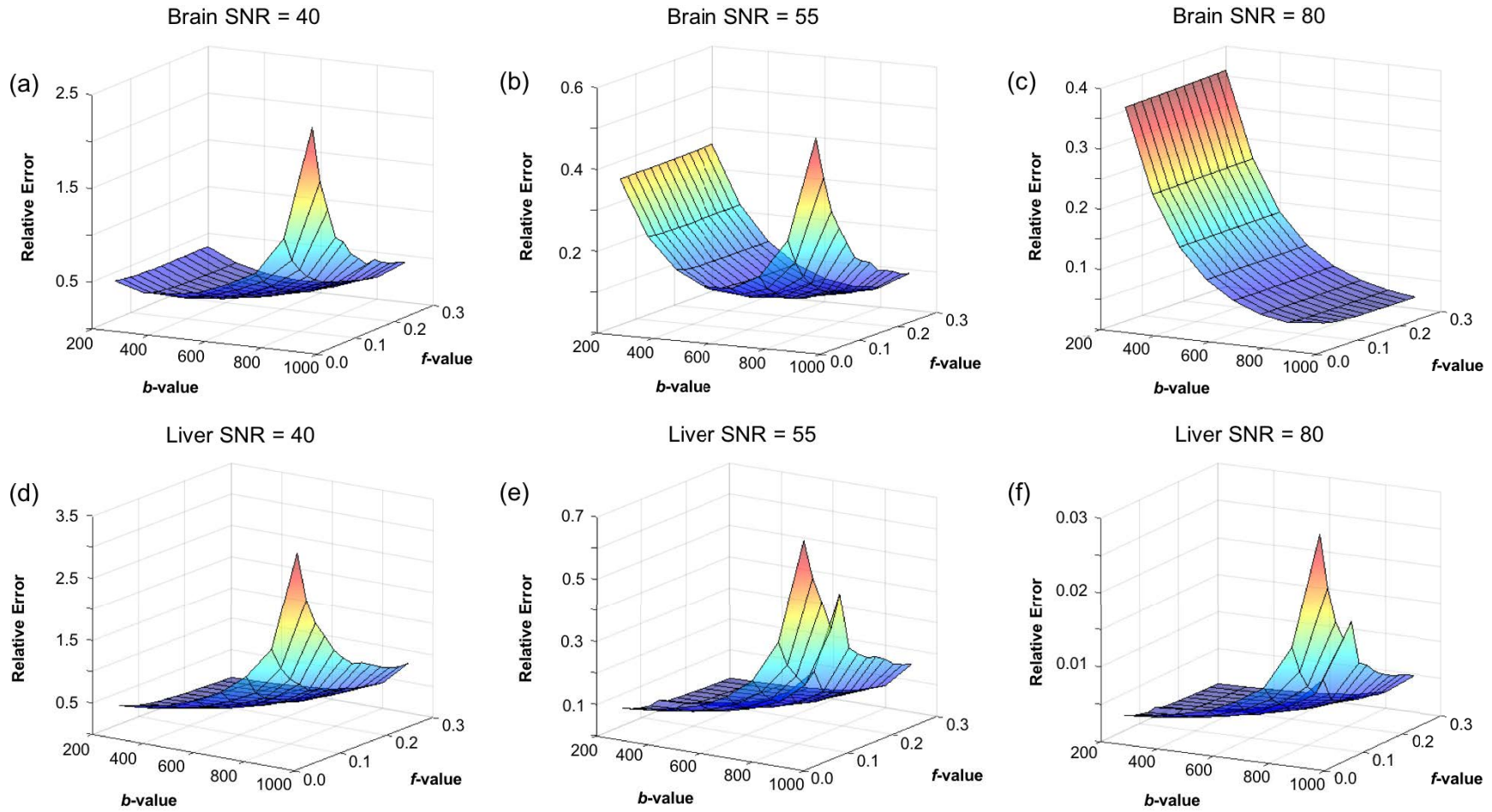

Figure 4.7 Relative error of estimating perfusion fraction *f*. Surface plots describing the relative error of f with different b-value distributions and SNR levels for (a-c) low- and (d-f) high-perfused tissue models. The b-value axis (200 to 900 s/mm^2) defines the b-value, which together with b = 1000 s/mm^2 was used to compute the f value.

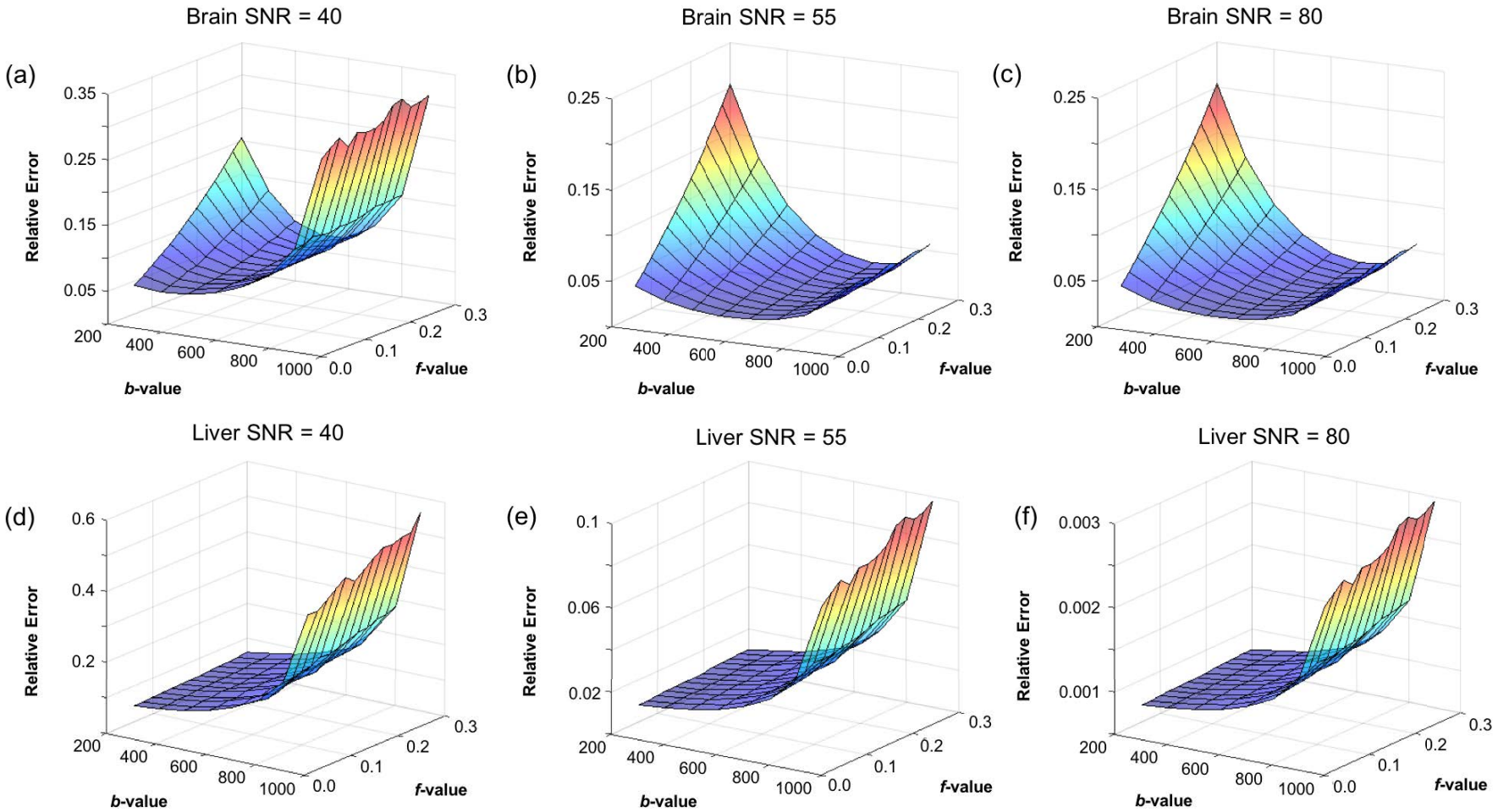

Figure 4.8 Relative error of estimating diffusion coefficient *D*. Surface plots describing the relative error of D with different b-value distributions and SNR levels for (a-c) low- and (d-f) high-perfused tissue models. The b-value axis (200 to 900 s/mm^2) defines the b-value, which together with b = 1000 s/mm^2 was used to compute the D value.

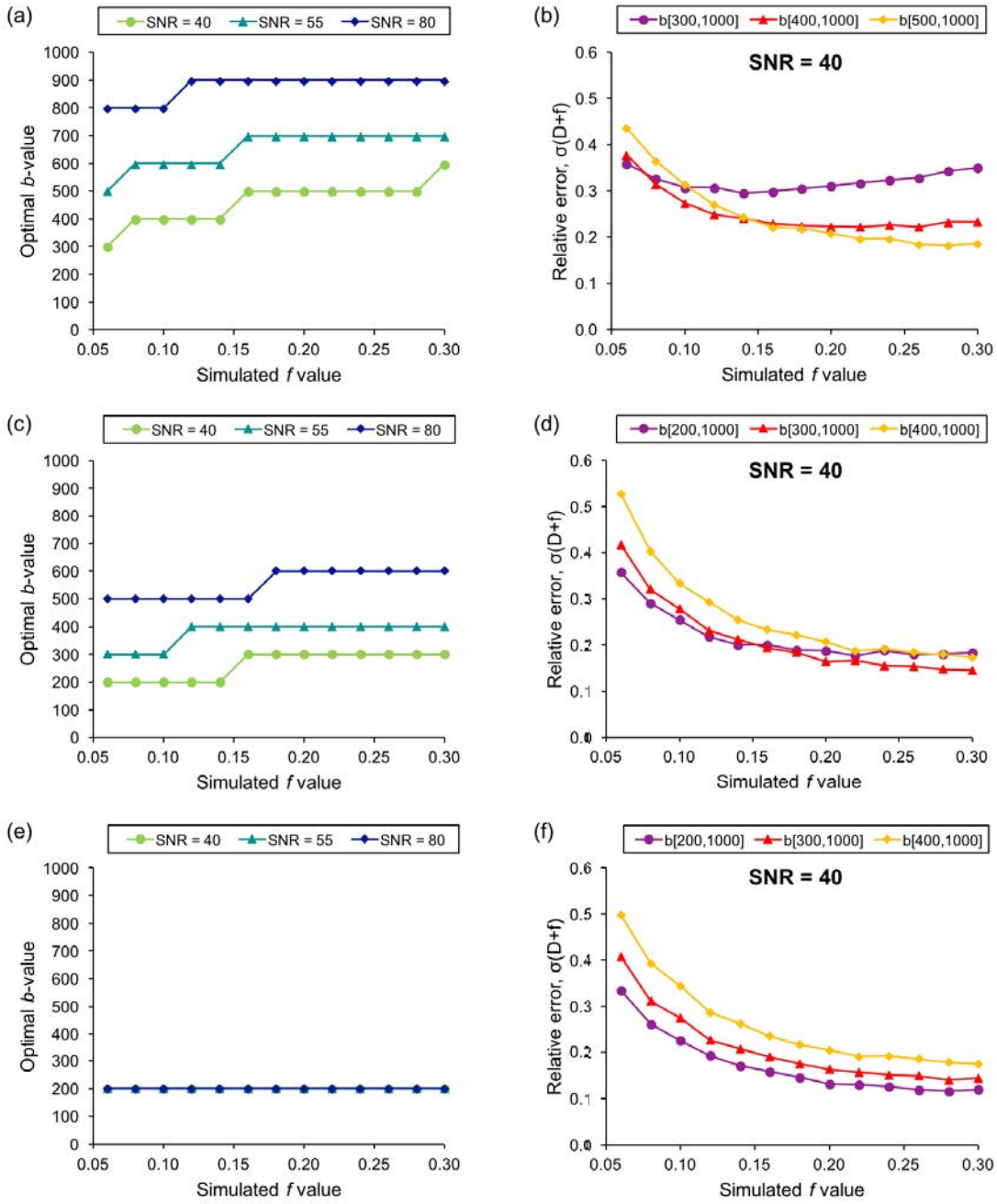

Figure 4.9 The *b*-value distributions with the lowest overall relative error in estimating *D* and *f* parameters. Plots representing the optimal *b*-value distributions with lowest overall relative errors (σ_{D+f}) for low- (a-b), medium- (c-d), and high-perfusion (e-f) models. The plots on the right-hand side represent the overall relative errors at SNR = 40, for the three best performing *b*-value distributions as a function of the simulated *f* value.

Table 4.1 Overall relative error (± standard deviation) of the estimated *D* and *f* parameters. Lowest relative errors are highlighted for each SNR level and perfusion model.

	Low-perfusion			**Medium-perfusion**			**High-perfusion**		
***b*-values**	**SNR = 40**	**SNR = 55**	**SNR = 80**	**SNR = 40**	**SNR = 55**	**SNR = 80**	**SNR = 40**	**SNR = 55**	**SNR = 80**
[200,1000]	0.49 ± 0.04	0.47 ± 0.05	0.47 ± 0.05	0.22 ± 0.05	0.12 ± 0.01	0.12 ± 0.01	**0.17 ± 0.06**	**0.03 ± 0.01**	**0.001 ± 0.0005**
[300,1000]	0.32 ± 0.02	0.29 ± 0.03	0.29 ± 0.03	**0.21 ± 0.08**	**0.05 ± 0.01**	0.04 ± 0.004	0.21 ± 0.08	0.04 ± 0.01	0.001 ± 0.0006
[400,1000]	0.26 ± 0.05	0.18 ± 0.02	0.18 ± 0.02	0.26 ± 0.10	0.05 ± 0.02	0.01 ± 0.001	0.26 ± 0.09	0.05 ± 0.02	0.002 ± 0.0007
[500,1000]	**0.25 ± 0.08**	0.12 ± 0.01	0.11 ± 0.01	0.34 ± 0.13	0.06 ± 0.02	0.004 ± 0.0004	0.34 ± 0.13	0.06 ± 0.02	0.002 ± 0.001
[600,1000]	0.30 ± 0.12	**0.09 ± 0.01**	0.07 ± 0.01	0.45 ± 0.16	0.08 ± 0.03	**0.003 ± 0.002**	0.45 ± 0.17	0.08 ± 0.3	0.003 ± 0.001
[700,1000]	0.40 ± 0.15	0.09 ± 0.03	**0.05 ± 0.01**	0.61 ± 0.19	0.12 ± 0.05	0.004 ± 0.002	0.64 ± 0.23	0.12 ± 0.05	0.004 ± 0.002
[800,1000]	0.62 ± 0.23	0.13 ± 0.06	0.03 ± 0.003	0.92 ± 0.33	0.19 ± 0.08	0.007 ± 0.003	0.99 ± 0.33	0.19 ± 0.08	0.007 ± 0.003
[900,1000]	1.20 ± 0.52	0.26 ± 0.12	0.03 ± 0.003	1.78 ± 0.74	0.40 ± 0.15	0.01 ± 0.007	1.91 ± 0.67	0.41 ± 0.16	0.01 ± 0.007

Table 4.2 Recommended *b*-value distributions for computation of IVIM perfusion fraction, based on relative error of < 10 %.

Model	**Recommended *b*-value distribution**	**Relative error of *f***	**Overall relative error**
Low-perfusion	SNR = 40; [500,1000]	18.7 ± 5.5 %*	24.8 ± 7.6 %*
	SNR = 55; [600,1000], [700,1000]	< 10 %	< 10 %
	SNR = 80; ≥ [500,1000]	< 10 %	< 10 %
Medium-perfusion	SNR = 40; [300,1000]	15.3 ± 8.3 %*	21.3 ± 7.8 %*
	SNR = 55; [300,1000] – [600,1000]	< 10 %	< 10 %
	SNR = 80; ≥ [300,1000]	< 10 %	< 10 %
High-perfusion	SNR = 40; [200,1000]	12.1 ± 6.8 %*	17.2 ± 6.4 %*
	SNR = 55; [200,1000] – [600,1000]	< 10 %	< 10 %
	SNR = 80; ≥ [200,1000]	< 10 %	< 10 %

* Lowest relative error.

4.3.3 Comparison of Grey Matter IVIM Parameters In vivo

The *b*-value distributions [300,1000] and [500,1000] were investigated retrospectively for the volunteer cohort. Average IVIM parameters for the grey matter are presented in Figure 4.10 for the *f* and *D* parameters. The average values of *f* and *D* in the grey matter were 0.141 ± 0.02 and 0.865 ± 0.05 (× 10^{-3} mm^2/s) with [500,1000], and 0.104 ± 0.01 and 0.912 ± 0.05 (× 10^{-3} mm^2/s) with [300,1000] distributions, respectively. The *f* parameters were higher and *D* parameters lower when computed using the [500,1000] distribution, agreeing with the observations made with the low-perfusion model.

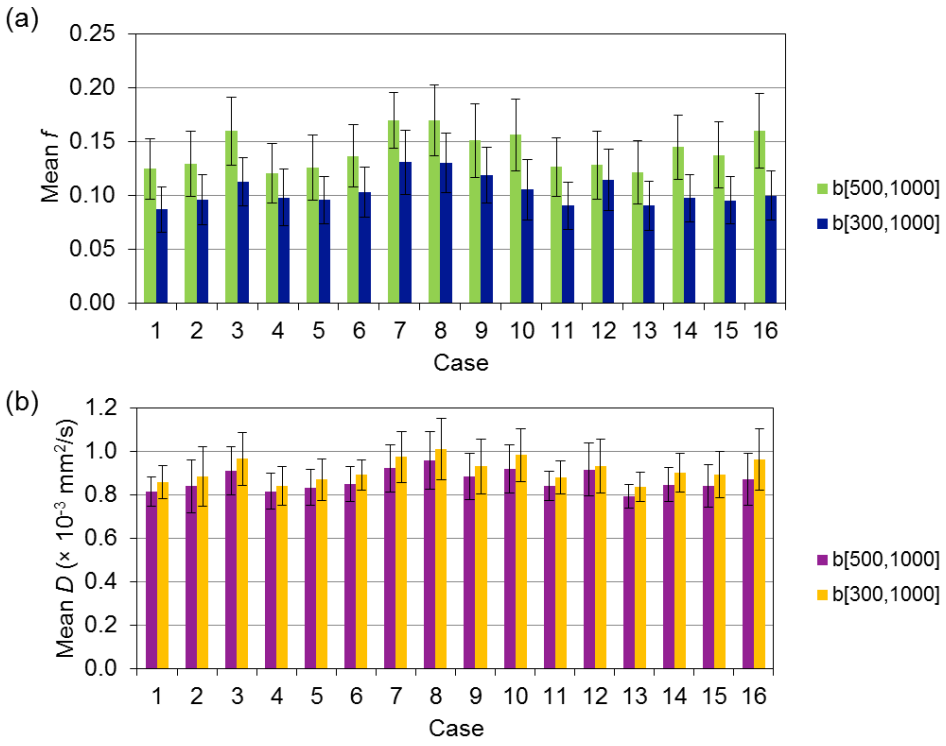

Figure 4.10 Mean IVIM parameters from in vivo grey matter. Mean *f* (a) and *D* (b) parameters derived from the volunteer cohort (n = 16).

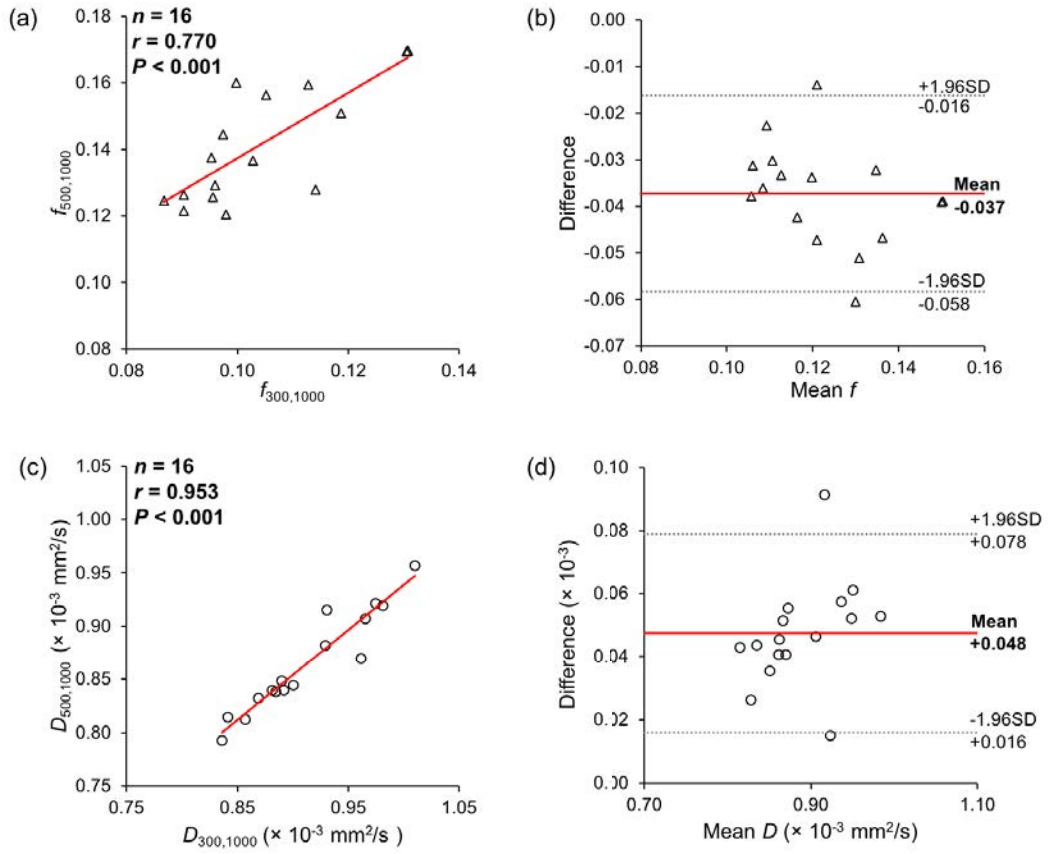

Figure 4.11 Correlation and Bland-Altman plots for *f* and *D* parameters estimated in grey matter. Results from correlation and Bland-Altman (BA) analysis for (a-b) *f* and (c-d) *D* parameters derived with [500,1000] and [300,1000] *b*-value distributions for the volunteer cohort (n = 16). The red lines in the BA plots describe the mean difference of the values and the dashed lines the agreement range (95% confidence intervals).

The estimated *f* and *D* parameters with the [500,1000] and [300,1000] distributions were analysed using correlation and Bland-Altman methods (Figure 4.11). Significant correlations were established between both IVIM parameters derived with the different *b*-value distributions, which indicated an existence of a linear relationship. Correlation of r = 0.770 (P < 0.001) was derived between the *f* parameters, and r = 0.953 (P < 0.001) between the *D* parameters. However, the estimation of *f* (P < 0.001) and *D* (P = 0.029) were significantly different between the [500,1000] and [300,1000] distributions. The agreement of methods, described by the Bland-Altman plots, showed a bias of -0.037 and 0.048 (× 10^{-3} mm^2/s) for *f* and *D* parameters respectively. However, this only indicated the bias of estimating the IVIM parameters with [500,1000] in comparison to [300,1000].

The bias was smaller at the lower *f* values and greater towards the higher *f* values. The opposite was observed for the *D* values. In comparison to the simulated *f* = 0.1 value for the low-perfusion model at SNR = 40, the differences between the mean values for [300,1000] and [500,1000] were 0.015 (× 10^{-3} mm^2/s) and -0.013 for *D* and *f* parameters, respectively. At *f* = 0.2, the differences were increased to 0.030 (× 10^{-3} mm^2/s) and -0.025, although the relative bias remained the same.

Average in vivo grey matter histograms and low-perfusion model histograms (where *f* = 0.1 at SNR = 40) were derived for the IVIM parameters (Figure 4.12). Similar behaviour was observed between the in vivo and simulated data histograms. As depicted by the simulated data histograms, the in vivo histograms based on the [300,100] distribution were narrower in shape and the histograms based on the [500,1000] distributions were shifted to higher *f* values compared to the [300,1000] distribution.

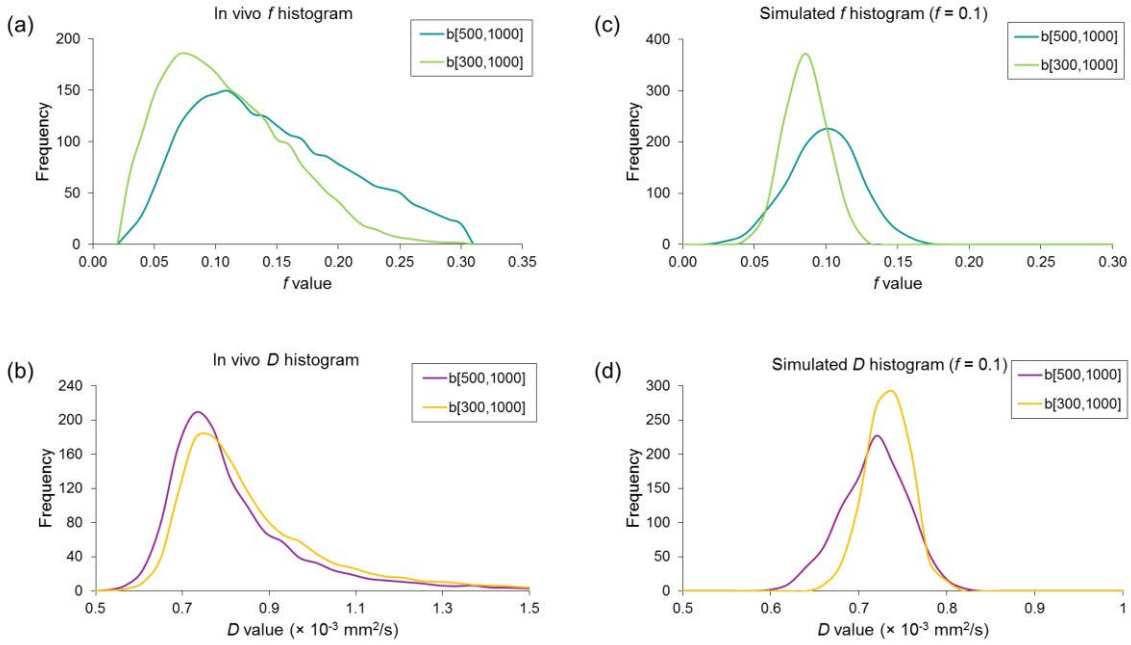

Figure 4.12 Histograms of IVIM perfusion fraction and diffusion coefficient. Histograms for in vivo (a-b) and simulated (c-d) data with *b*-value distributions [500,1000] and [300,1000]. The in-vivo histograms are the average histograms derived for the grey matter regions of the volunteer cohort (n = 16) and the simulated histograms correspond to the estimated values from the low-perfusion model at SNR = 40 and *f* = 0.1.

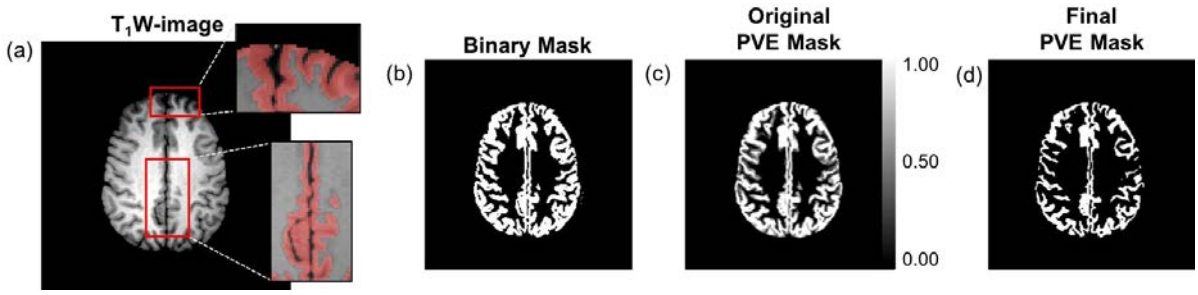

Figure 4.13 Grey matter segmentation. An example volunteer case with (a) T_1-weighted image and overlaid binary grey matter mask regions showing the exclusion of CSF, (b) the binary mask, (c) the original PVE mask (with values 0 to 1) and (d) the final (binary) PVE mask.

The $_{w}$CV was used to assess the repeatability of the in vivo IVIM parameters, which for the [500,1000] and [300,1000] distributions was 6.32 % and 3.99 % for D, and 15.3 % and 10.8 % for f, respectively. The values were similar to the ones depicted by the low-perfusion model at SNR = 40 (Figures 4.5 and 4.6), with small improvements seen with the use of [300,1000] over the [500,1000] distribution.

The IVIM parameter histograms were compared to the ones derived with PVE masks for eight volunteer cases (n = 8). No significant differences were found between the mean, median, 10^{th} and 90^{th} percentiles of the IVIM parameters derived with the different masks, for either [300,1000] or [500,1000] distributions. Example grey matter masks are presented in Figure 4.13 for a volunteer case. The overlaid mask regions showed that the sulcal CSF was successfully removed with the binary grey matter mask.

For comparing the in vivo and simulated data results, the D^* was computed for the grey matter using the full b-value distribution. The D^* was estimated to be 9.40×10^{-3} ($\pm$ 0.87×10^{-3}) mm^2/s. This agreed with the D^* used for the low-perfusion simulations, although was slightly higher than the simulated D^* (7.00×10^{-3} mm^2/s).

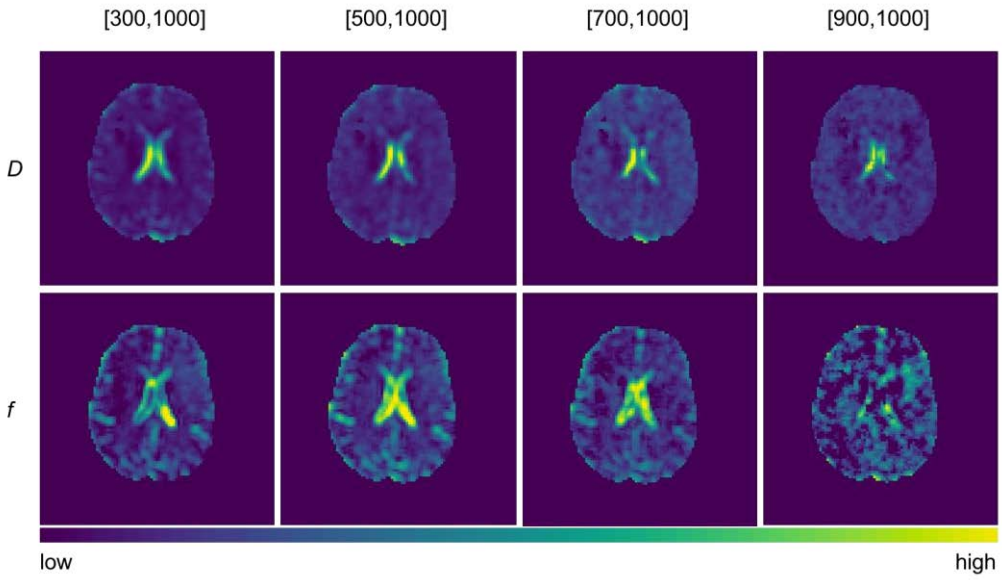

Figure 4.14 IVIM parameter maps derived with different *b*-value distributions. An example volunteer case with IVIM *D* (top) and *f* (bottom) parameter maps derived with *b*-value distributions [300,1000], [500,1000], [700,1000] and [900,1000].

Finally, IVIM parameter maps for a volunteer case are presented in Figure 4.14. The *f* maps derived with the [300,1000] and [500,1000] distributions were qualitatively similar, although differences in the magnitude of values could be observed, as depicted by the in-vivo and simulation results. The IVIM maps derived with higher *b*-values appeared increasingly noisier.

4.4 Discussion

The use of a simple fitting approach with a minimum number of *b*-values was investigated to assess the feasibility of a rapid clinical application for determination of the IVIM perfusion fraction parameter. The accuracy and reliability of the IVIM parameters from different *b*-value distributions were assessed using model simulations and confirmed using in vivo imaging. The model data simulations demonstrated that the optimal *b*-value distributions for different tissue regions are dependent on the SNR level and the degree of perfusion influencing the diffusion signal. Based on these results and the relative errors of *f* and *D*, optimal *b*-value distributions were suggested for each tissue type.

The three perfusion models were influenced by bias and noise to a different extent. Bias was found to be the dominant cause of higher relative errors for the lower perfusion models and low *b*-value distributions. The bias was found to be independent of the simulated *f* value, but dependent on the *b*-value. In a study by Conklin et al. (93), a similar effect was demonstrated with lower perfusion fraction values estimated with the use of a *b*-value distribution [300,900], compared to distributions including more intermediate *b*-values.

The other cause for the higher relative errors was noise, which affected the estimation of perfusion fraction at higher *b*-value distributions. This was likely introduced by the increased variability from extrapolating the linear fit back to the *y*-axis from the higher *b*-values. For the low-perfusion model, representing perfusion in the brain, the effects of bias and noise were found to be minimised with the use of *b*-value distribution [500,1000] at SNR = 40. This was also the case at higher SNR, due to the intrinsic bias seen with the use of low *b*-value distributions.

Similar characteristics were observed in vivo for the volunteer cohort, with regards to the estimation of the IVIM parameters. Higher f values were estimated with the [500,1000] distribution in comparison to the [300,1000] distribution, and the opposite was seen for the estimation of D. The mean f values derived in vivo were 0.141 ± 0.02 with [500,1000], and 0.104 ± 0.01 with [300,1000] distributions. For the low-perfusion model (at SNR = 40 and f = 0.14), the mean f values (error %) for [500,1000] and [300,1000] distributions were estimated to be 0.129 (-8.2 %) and 0.109 (-21.6 %), respectively.

The magnitude of differences between the b-value distributions was somewhat greater in vivo compared to the simulated data. The D^*/D ratio in vivo was estimated to be in the range of 9.31 to 12.6, which was in agreement with the ratio used in the model simulations (D^*/D = 10). However, the variability of the in vivo ratios would have influenced the magnitude of bias, and in particular for regions where $D^*/D < 10$, where the signal decay starts to approach mono-exponential behaviour. The contributions from any potential partial volume effects due to the presence of CSF were minimised with the exclusion of sulcal CSF. This was confirmed by the comparison of IVIM values derived with the binary and PVE masks, which showed no difference in the distribution of the extracted IVIM values. The PVE masks were strictly generated and no voxels presenting tissue but grey matter were included. The variability in the D^*/D ratio, together with the effect of noise, were then likely to account for the greater differences seen in vivo. Nonetheless, the observations in vivo and simulated data confirm the presence of bias in low-perfused tissues. Therefore, consideration of b-values is particularly important when analysing brain data and other low-perfused tissues, where bias is likely to have a larger influence on the estimated IVIM parameters.

The medium- and high-perfusion models, representing tissues found in the abdomen resulted in a substantial decrease in bias when estimating the perfusion fraction. Therefore, the more important factor for the optimal *b*-value distribution was the variability arising from noise. The estimation of *f* was found to be more sensitive to noise in comparison to *D*, although the increase in SNR level considerably improved the reproducibility of both parameters. The smaller contribution from bias meant that the lower *b*-value distributions had lower relative errors for estimation of the IVIM parameters in contrast to the low-perfusion model. This resulted in the optimal *b*-value distributions for the medium-and high-perfusion models to be [300,1000] and [200,1000], respectively.

The recommended *b*-values from this study can be used to inform analysis of pre-existing data of different tissue types. Previously, thresholds of b = 100 s/mm^2 (101, 103) for abdominal organs and b = 200 s/mm^2 (28, 102) for the brain have been suggested, when using the segmented fitting approach. In our study, the use of *b*-values < 500 s/mm^2 for the low-perfusion model demonstrated high biases in estimation of both the *D* and *f* parameters, resulting in higher inaccuracies for any relatively low-perfused regions. For the higher perfused regions, our results agree with the previously suggested thresholds and the use of a low *b*-value threshold should provide results with minimal influence from bias.

Previously reported IVIM parameters for different pathologies were listed in Table 2.2. For highly perfused regions, such as reported for cirrhotic liver (89, 111, 141), hepatocellular carcinomas (30, 133), prostate cancer (143, 144) and many of the pancreas related pathologies (132, 134, 135), our results suggest that the use of a low *b*-value can reduce the variability in estimating the perfusion fraction. In lower perfused tissues, such as reported for breast cancer (90, 140), a higher *b*-value is recommended to reduce

the effect of bias. A breast cancer study by Cho et al. (90) performed segmented fitting with b = 150 s/mm^2 as the threshold, which led to a negative bias in the estimation of the f values, similar to what was shown in our low-perfusion model simulations with the use of low b-values.

The other low-perfused region of clinical interest is the brain. Previous IVIM studies of brain gliomas have been inconclusive with the reported f values (27, 136-138). A range of values were reported for low- (f = 0.06 – 0.49) and high-grade (f = 0.11 – 0.40) gliomas with the use of the same threshold value b = 200 s/mm^2. Interestingly, the two studies including b-values ≥ 1500 and up to 3500 s/mm^2 (137, 138), reported relatively high f values (≥ 0.29), whereas the studies including b-values ≤ 1300 s/mm^2 (27, 136) reported much lower values (≤ 0.13). Tri-exponential fitting has been previously used for data with high b-values (> 1000 s/mm^2) in the brain (163), suggesting that using a bi-exponential fitting for higher b-value data might result in under fitting and thus potential positive bias in estimation of the IVIM parameters. On the other hand, both the IVIM model and the tri-exponential model are unable to account for the non-Gaussian diffusion and noise observed at high b-values (65). An alternative method was introduced by Iima et al. (164), who combined the IVIM and kurtosis models and investigated its use for low-perfused breast tissue up to b-values = 2500 s/mm^2. Using this methodology, the IVIM effect at low b-values and the non-Gaussian behaviour at high b-values were accounted for. Other challenges with the use of higher b-values include the lower SNR level, resulting in increased variability of the data, if not adjusted for e.g. with the use of higher NSA. In the context of these issues, the use of the standard IVIM model at b-values above 1000 s/mm^2 might not be desirable. Therefore, although the use of b = 200 s/mm^2 as a threshold in these studies was likely to have introduced

bias to the reported *f* values, the use of the high *b*-values was the more likely cause of the large differences seen between the studies.

The increase from SNR = 40 to SNR = 55, corresponding to approximately an acquisition with one and two signal averages, increased the reproducibility for all the *b*-value distributions and the resulting IVIM parameters. The improvement was less marked in going from an SNR 55 to 80. Therefore, aiming for an SNR = 55 may be a reasonable compromise between reproducibility and length of acquisition, if the biological effects being investigated are large enough, such as seen between the low- and high-grade gliomas (27, 28). Presence of small biological changes in tissue might require the use of higher SNR levels, where detection of the tissue properties can be improved with the better reproducibility of the *f* parameter.

4.5 Study Limitations

The study presented in this chapter had some limitations. First, only three separate tissue models were investigated. While this provides a general guide on the use of optimal *b*-values, variation in tissues creates a more complex scenario, as shown by the in vivo results. However, the in vivo results presented here were in agreement with the simulated data, confirming the presence of effects such as bias in low-perfused tissues.

Pathologies in the abdomen and the surrounding tissue have been found relatively high perfused, implying that the recommended *b*-value is likely to perform well for the whole imaged region. However, in abdominal MR imaging, motion effects need to be considered, and the image quality assessed to ensure sufficiently high quality for IVIM analysis. Although imaging in the brain might not be affected by motion to the same extent as in the abdomen, data quality remains an important requirement for reliable IVIM analysis. Therefore, an estimate of SNR can provide good guidance on the robustness of the results and aid in choosing the optimal *b*-values for IVIM.

4.6 Conclusion

In conclusion, this study demonstrated that IVIM parameters D and f can be estimated reliably with three b-values using the linear fitting step of the segmented IVIM approach. In this context, the fitting stability of the IVIM was therefore not of critical concern, as the pseudo-diffusion coefficient D^* was not estimated. Our results showed that the optimal b-value distribution depends on the diffusion and perfusion characteristics of the tissue and the compromise between bias and variability. The in vivo results confirmed the presence of bias in the low perfused brain tissue and underlined the importance of using high enough b-values to minimise its influence. Recommendations for b-values were made based on the model simulations, which can be used as a guide in future studies or for pre-existing data. With different clinical centres still utilising different b-value distributions, the results from this study can also aid in the interpretation of differences seen between IVIM parameters of similar tissues.

Chapter 5

Comparison Study of IVIM and DSC Perfusion Parameters in Childhood Brain Tumours

5. Comparison Study of IVIM and DSC Perfusion Parameters in Childhood Brain Tumours

5.1 Introduction

Diffusion- and perfusion-weighted MR imaging methods are becoming increasingly prevalent in clinical practice due to their ability to provide information about tissue microstructures, such as cellularity and vascularity, respectively (115, 165). Diffusion-weighted imaging (DWI) has the clinical advantage of being non-invasive, whereas the gold standard perfusion imaging method, dynamic susceptibility contrast (DSC-MRI), requires the use of an intravenous contrast agent. In paediatric patients, administering contrast can be difficult or contraindicated in such cases as renal failure and allergy. The recent reports of gadolinium deposits in the brain have also posed questions on the safety of gadolinium based contrast agents (112, 113).

A potential alternative measure to DSC derived cerebral blood volume (CBV) could be the perfusion fraction derived with the intravoxel incoherent motion (IVIM) model (119). Previous studies in the brain have suggested links between the IVIM perfusion parameters (f, D^*) and the classical perfusion parameters from DSC-MRI (Chapter 2, section 2.3.2.3). However, while f has been shown to correlate well with the DSC-CBV, comparisons of D^* to mean transit time (MTT) and fD^* to cerebral blood flow (CBF) have been rarely reported, and provided contradictory results (28, 87). This suggests that the bi-exponential behaviour in the brain might not be sufficiently pronounced for the robust computation of D^* and/or arise from the difficulties in measuring arterial input function (AIF) required for the computation of DSC-CBF and DSC-MTT (121).

The comparison of IVIM and DSC parameters has been reported for a mixture of different tumours (27, 28, 93, 122, 123). However, no studies of IVIM or its

comparison to DSC in paediatric brain tumours has been reported to date. Low-grade gliomas in children commonly have low perfusion, yet are treated with regimes aimed to be anti-angiogenic i.e. inhibit growth of new blood vessels (166). This presents a notable challenge in monitoring the pharmacodynamic effects (the biochemical or physiologic effect of a drug on an organism) of a treatment. A non-invasive measure of perfusion could therefore provide an alternative way to assess the treatment effects.

The successful use of IVIM for such a purpose was presented by Kim et al. (122), who used the IVIM perfusion fraction to differentiate recurrent tumour from treatment effects in adult glioblastomas, and reported a significant correlation between IVIM-*f* and DSC-CBV. Other previous studies have mainly focused on adult low- and high-grade gliomas, which have shown promising results in their differentiation with the IVIM-*f* (27, 28, 93, 137). However, the brain tumours in paediatrics often present histologically different and more heterogeneous than those in adults (167). In paediatrics, the most common low-grade glioma is the pilocytic astrocytoma (grade I), whereas in adults this is the diffuse astrocytoma (grade II) (168). Therefore, considering these differences, the assessment of IVIM and DSC-MRI in paediatric brain tumours could further evaluate the association of the two methods and potentially provide IVIM as a valuable alternative method for the non-invasive measurement of perfusion in childhood tumours.

This leads to the primary aim of this chapter, which is to investigate the relationship between IVIM and DSC-MRI in tumorous and healthy paediatric brain tissues. This builds on the low-perfused model simulations reported in Chapter 3, which showed that the IVIM perfusion fraction can be robustly measured in low-perfused tissues. The assessment of IVIM-*f* and DSC-CBV forms an important part of the biological validation of perfusion fraction as a potential imaging biomarker and probes the biophysical origins of the IVIM perfusion fraction.

5.2 Methods

5.2.1 MR Imaging

The data for IVIM-DSC comparison was acquired with MR imaging performed on a Philips Achieva 3.0 Tesla (T) TX (Philips Healthcare, Best, the Netherlands) MRI scanner with a 32-multichannel receive head coil at Birmingham Children's Hospital (BCH). Additional diffusion-weighted MR data (not included in the IVIM-DSC comparison) was acquired with [1] Siemens Symphony 1.5 Tesla (T) (Siemens Healthcare, Erlangen, Germany) and [2] Siemens Avanto 1.5 Tesla (T) (Siemens Healthcare, Erlangen, Germany) MRI scanners at the Great Ormond Street Hospital (GOSH).

5.2.1.1 Diffusion-weighted Imaging

The DW-MRI protocol parameters are reported in Table 5.1 for the data acquisition from the two clinical centres. For the BCH protocol, a sensitivity-encoded (SENSE) approach with a single-shot, spin echo planar imaging sequence was used. For each subject, 11 exponentially spaced *b*-values (0, 20, 40, 80, 110, 140, 170, 200, 300, 500, 1000 s/mm^2) were acquired in three orthogonal directions, of which a geometrical average diffusion-weighted image (or trace) was derived, using 30 contiguous axial slices and NSA = 1. The spectral presaturation with inversion recovery (SPIR) was used for fat suppression and the scan duration was 2.12 minutes. For the GOSH protocol, imaging was performed with 3 *b*-values (0, 500, 1000 s/mm^2) acquired in three orthogonal directions, of which a trace image was derived. For scanner [1] NSA = 2 and 20 contiguous axial slices, and scanner [2] NSA = 3 and 19 contiguous axial slices were used.

Table 5.1 The DW-MRI protocol parameters for BCH and GOSH protocols (scanners [1] and [2] specified where different parameters were used).

Centre	No. of *b*-values	TR/TE	FOV	Matrix size	Slice thickness	In-plane resolution
BCH	11	4,000/91	240 × 240	96 × 96	3.5	2.5 × 2.5
GOSH	3	3,700/108 [1] 2,700/96 [2]	230 × 230	256 × 256 [1] 128 × 128 [2]	5.0	0.90 × 0.90 [1] 1.80 × 1.80 [2]

Note: field-of-view, slice thickness and in-plane resolution reported in units of mm and TR/TE in units of ms.

5.2.1.2 Dynamic Susceptibility Contrast Imaging

The DSC protocol was acquired subsequently to the DW-MRI protocol from the same spatial location including FOV, matrix size and slice thickness. The protocol used FE-EPI sequence with TR/TE = 1,865/40 ms and a flip angle of 20°. The temporal resolution was 1.86 s, and this was repeated 60 times. The contrast agent (Dotarem, Guerbet, France) was administered in two equal doses via a power injector through a cannula inserted in an antecubital vein. The first dose was administered prior to the DSC examination to minimise T_1 effects (114), while the second dose was administered at time point 5 during the DSC examination. The total dose of contrast agent was 0.1 mmol/kg, with an injection rate of 3 mL/s. Both contrast doses were followed by injections of saline (volume of up to 10 mL, depending on patient's weight) delivered at the same rate as the contrast.

5.2.1.3 T_2-weighted Imaging

A T_2-weighted turbo spin echo (TSE) scan was acquired with the same coverage as for DWI and DSC to outline the regions-of-interest for the comparison study. The protocol was performed with a TR/TE = 4,000/100 ms, FOV 240 × 240 mm, matrix size 288 × 288, slice thickness 3.5 mm and in-plane resolution of 0.83 mm^2.

5.2.2 Patient Population

The IVIM-DSC comparison study included 11 paediatric brain tumour patients (age 1.42 to 9.26 years, mean 5.18 years) acquired at the BCH. The patient details are listed in Table 5.2. Informed parental consent was obtained for all subjects and ethical approval was granted as stated in the thesis declaration.

Table 5.2 Patient cohort demographics for the IVIM-DSC comparison study.

Case	Sex (F/M)	Age (years)	Diagnosis
1	M	9.26	Rosette-forming glioneuronal tumour
2	F	5.91	Optic pathway glioma
3	M	6.59	Optic pathway glioma
4	M	4.20	Optic pathway glioma
5	M	6.76	Optic pathway glioma
6	M	1.42	Thalamic optic pathway glioma
7	F	1.65	Optic pathway glioma
8	M	8.31	Supratentorial glioneuronal tumour
9	M	2.99	Suprasellar pilomyxoid astrocytoma
10	M	3.36	Optic pathway glioma
11	F	6.30	Optic pathway glioma

Table 5.3 Patient cohort demographics for computation of IVIM maps.

Case	Sex (F/M)	Diagnosis	Grade
1	F	Pilocytic astrocytoma	I
2	F	Pilocytic astrocytoma	I
3	F	Choroid plexus papilloma	I
4	F	Atypical choroid plexus papilloma	II
5	F	Choroid plexus carcinoma	III

Data from the GOSH (n = 5) was used for the computation of IVIM maps in paediatric low-grade gliomas and choroid plexus tumours. The patient details are listed in Table 5.3. Informed parental consent was obtained for all subjects and the same ethical approval applied as stated above.

5.2.3 Data Analysis

The image analysis was implemented using in-house Python software (Anaconda, Continuum Analytics, v. 2.7.1.0) with the LmFit library (150). For both DW-MRI and DSC-MRI images, an averaging filter of size 3 × 3 was used to smooth the images.

5.2.3.1 IVIM Model Fitting

Non-linear least-squares minimisation was performed with the Levenberg-Marquardt (153) algorithm for the IVIM fitting of the signal data. The fitting was performed on a voxel-by-voxel basis using the segmented approach, which had the best overall performance for low-perfused tissues, as described in Chapter 3.

For the GOSH image data, the segmented approach was used to define D and f from the fitting of b-values: 500 and 1000 s/mm^2, as described in Chapter 4. The fitting of diffusion signal in the brain with b-value = 500 s/mm^2 was determined previously in Chapter 4 to produce the most accurate and least biased measure of f.

The following boundaries were applied to the IVIM parameters: $0 < D < 0.1$ mm²/s, $0 < D^*$ 1 mm²/s and $0 < f < 1$. The boundaries were chosen to eliminate any non-physiological results (88).

5.2.3.2 DSC Analysis

Tracer tissue concentration-time course data was derived from the signal-time course data for each voxel using the relationship between T_2^* signal intensity and tracer tissue concentration (120). This assumes that the gadolinium contrast concentration [Gd] is approximately linearly proportional to the observed change in the T_2^* relaxation rate ($1/\Delta R_2^*$), which is proportional to the negative logarithm of the relative signal intensity:

$$[Gd] \propto \Delta R_2^* = -\frac{1}{\mathrm{TE}} \ln\left(\frac{S_t}{S_0}\right) \quad [5.1]$$

where TE is the echo time, S_t the signal at time t during passage of the contrast bolus, and S_0 the baseline signal intensity.

The relative cerebral blood volume (CBV) maps were determined using the area below the tracer concentration-time curve. The blood brain barrier breakdown and the resulting T_1-weighted leakage and T_2^*-weighted imaging (T_2/T_2^*WI) residual effects were corrected using preload-dosing (PLD) and baseline subtraction (BLS) techniques, respectively (114, 169). The reported CBV values are in arbitrary units of mL/100 mL.

5.2.4 Statistical Analysis

All statistical analysis was performed in SPSS Statistics (IBM, Chicago, IL, v.22).

The analysis workflow for the comparison study of IVIM-*f* and DSC-CBV is presented in Figure 5.1. ROIs were drawn manually on co-registered T_2-weighted images over multiple slices (3 to 5) for healthy-appearing grey matter (ROI = 596 ± 54 voxels), white matter (ROI = 545 ± 36 voxels), and tumours (ROI = 626 ± 202 voxels), with exclusion of large areas of cyst (Figure 5.2). The ROIs were transferred to the analysed IVIM-*f* and DSC-CBV perfusion maps for the correlation analysis. The correlation between the

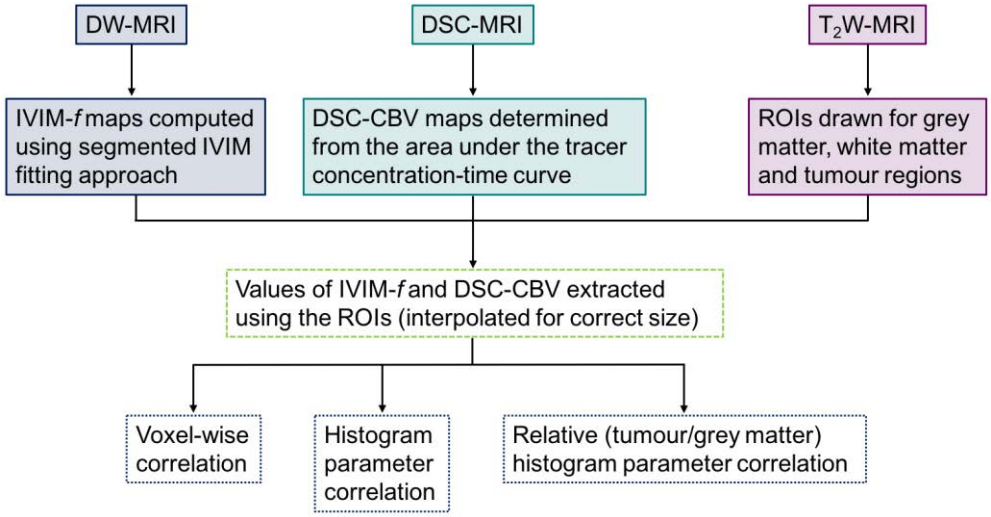

Figure 5.1 The IVIM-DSC analysis workflow. The workflow used for the analysis and comparison of IVIM-*f* and DSC-CBV parameters.

parameters was assessed using the Pearson correlation coefficient, *r*. The correlation study was performed voxel-wise and using histogram derived parameters (mean, median, 25th/75th/90th percentiles, kurtosis and skewness). The histogram parameters were also used for a relative or normalised tumour value (tumour/healthy grey matter) correlation analysis. Histograms were constructed using the same number of bins for both imaging methods. Number of bins was based on the square root rule, where the number of bins is equal to the square root of total number of data points or voxels from the ROI. The bin widths were determined between the max. value (*f* or CBV) and zero for each patient.

The correlation between the parameters was assessed using the Pearson correlation coefficient, *r*. The correlation study was performed voxel-wise and using histogram derived parameters (mean, median, 25th/75th/90th percentiles, kurtosis and skewness). The histogram parameters were also used for a relative or normalised tumour value (tumour/healthy grey matter) correlation analysis. Histograms were constructed using the same number of bins for both imaging methods. Number of bins was based on the square root rule, where the number of bins is equal to the square root of total number of

data points or voxels from the ROI. The bin widths were determined between the maximum value (*f* or CBV) and zero, for each patient case separately.

Statistical power was computed for the sample size (n = 11) to determine whether a large enough sample size was used to provide valid conclusions. Power of the study is the likelihood that the observed effect is real and is often set to be 0.8, corresponding to an 80 % chance. The sample size of 11 in this study had a power of 80 % to detect correlation of more or equal to 0.750, with a statistical significance of 0.05 using the Pearson's correlation.

For the data acquired at GOSH, ROIs were drawn manually on the IVIM parameter maps to determine representative value ranges in the different tumours and grey matter regions (ROI = 160 ± 70 voxels). The diffusion-weighted images of b = 0 were used as a guideline. Large areas of cysts were excluded and areas close to the edge of the tumours were avoided to reduce partial volume effects.

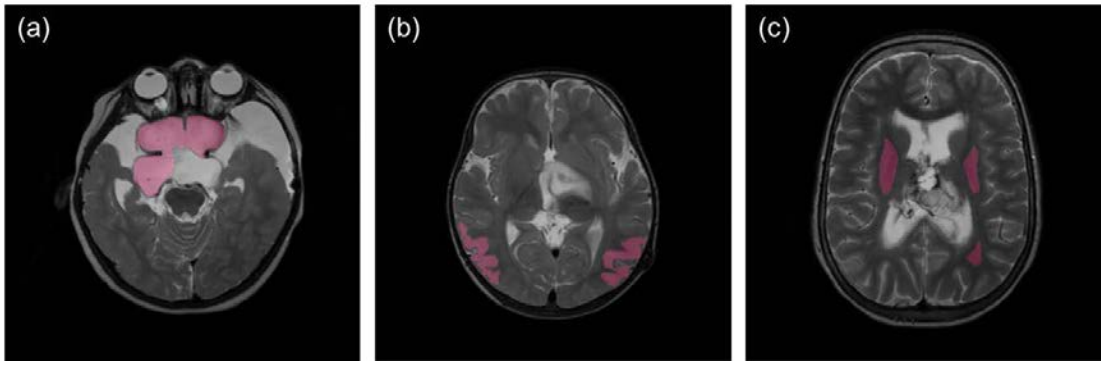

Figure 5.2 Regions-of-interests (ROIs) for the data analysis (BCH data). Examples of (a) tumour, (b) grey matter and (c) white matter ROIs used in the data analysis, shown on the T_2-weighted images. Both (a) and (b) present cases of optic pathway gliomas and (c) a case of glioneuronal tumour.

5.3 Results

5.3.1 Voxel-wise and Histogram Parameter Comparison

The median IVIM-*f* and DSC-CBV values for grey matter, white matter and tumour regions are listed in Table 5.4. Relatively lower variability was observed in the different tissue regions with the IVIM-*f* parameter compared to the DSC-CBV parameter.

Table 5.4 Median values (± standard deviation) of IVIM-*f* and DSC-CBV (n = 11).

Region	IVIM-*f*	DSC-CBV
Grey matter	0.115 ± 0.010	4.38 ± 0.96
White matter	0.090 ± 0.009	1.94 ± 0.53
Tumour	0.087 ± 0.032	1.94 ± 1.10

Voxel-wise correlations between IVIM-*f* and DSC-CBV were computed for the grey matter, white matter and tumour tissue regions. The voxel-wise correlation coefficients are listed in Table 5.5. Significant correlations were observed in all tissue regions, although not for each one of the cases. Significance was achieved in 10 out of 11 grey matter, and 8 out of 11 white matter and tumour regions. Comparison in the grey matter demonstrated the strongest correlations (r = 0.139 – 0.716, $P < 0.001$), followed by more moderate correlations in white matter (r = 0.171 – 0.298, $P < 0.001$) and tumour (r = 0.081 – 0.567, $P \leq 0.001$) regions.

Table 5.5 Voxel-wise correlations of IVIM-*f* and DSC-CBV in grey matter, white matter and tumour regions.

	White Matter		Grey Matter		Tumour	
Case	***r***	***P*-value**	***r***	***P*-value**	***r***	***P*-value**
1	0.171**	< 0.001	0.139**	< 0.001	0.033	0.292
2	0.298**	< 0.001	0.577**	< 0.001	0.329**	< 0.001
3	0.092	0.114	0.522**	< 0.001	0.193**	< 0.001
4	0.200**	< 0.001	0.364**	< 0.001	0.102**	< 0.001
5	0.180**	< 0.001	0.331**	< 0.001	0.383**	< 0.001
6	0.198**	< 0.001	0.716**	< 0.001	0.349**	< 0.001
7	0.096	0.064	0.473**	< 0.001	0.340**	< 0.001
8	0.214**	< 0.001	0.539**	< 0.001	0.016	0.791
9	0.232**	< 0.001	0.049	0.400	0.081**	0.001
10	0.199**	< 0.001	0.716**	< 0.001	0.428**	0.001
11	-0.025	0.607	0.627**	< 0.001	0.567**	< 0.001

** corresponds to a significance level of $P < 0.001$.

Low voxel-wise correlations were observed for cases 1 and 9, in both grey matter and tumour regions-of-interest. The DW-MRI data for case 1 was acquired with an increased number of slices. Although the positioning appears qualitatively similar and the IVIM-*f* and DSC-CBV maps produced comparable parameter distributions, the voxel-wise comparison might have been affected by a small shift due to the DW-MRI positioning. For case 9, the T_2 images were slightly mal-aligned to the DWI and DSC images, potentially due to patient movement between the scans. The low-correlations for the tumour cases included two cases of glioneuronal tumours and a suprasellar pilomyxoid astrocytoma. These tumours often appear heterogeneous, and are therefore more prone to mismatch between voxels due to patient movement. The other tumour regions demonstrated moderate correlations, with a more homogeneous appearance.

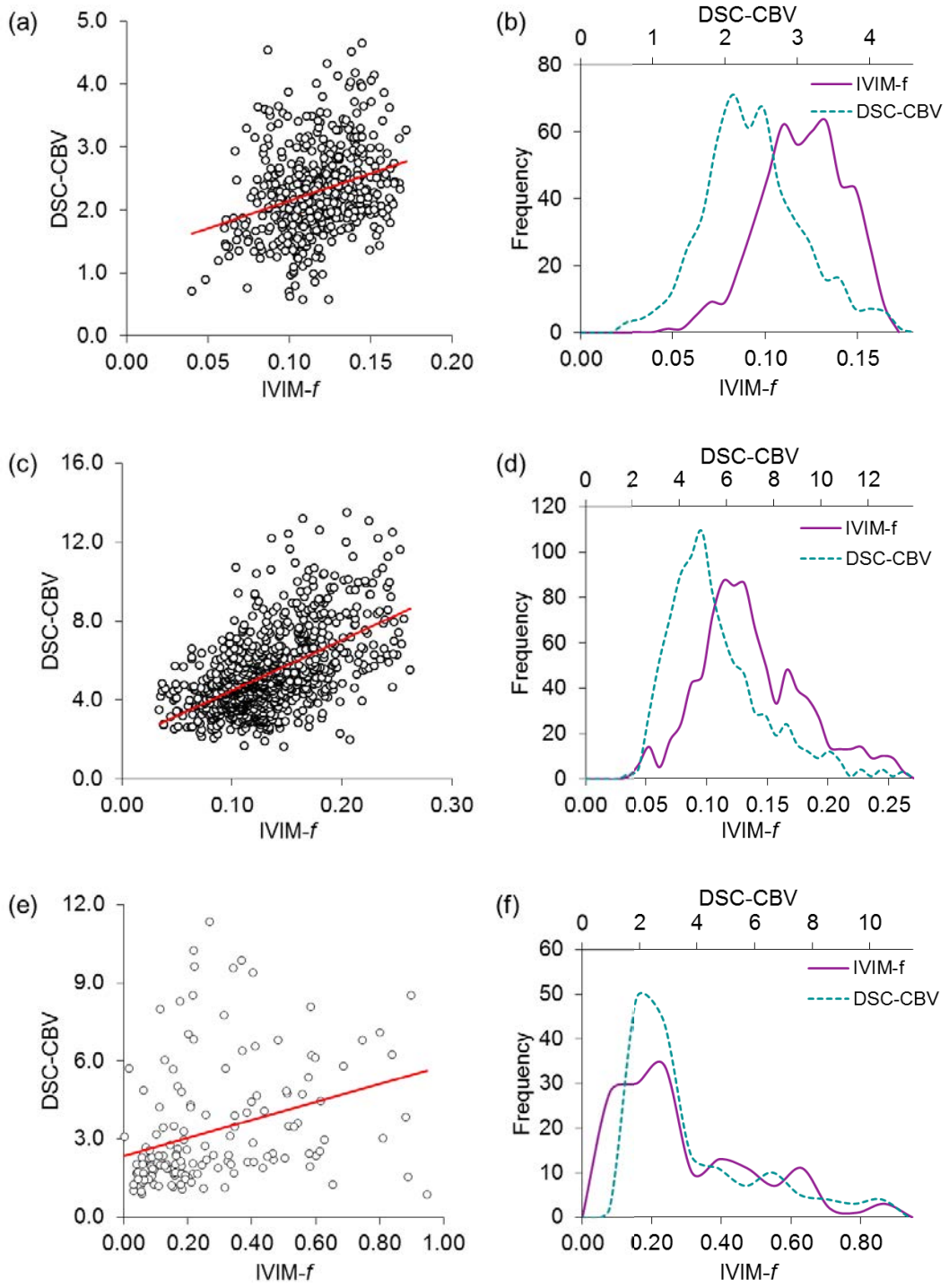

Figure 5.3 Voxel-wise comparison of IVIM-*f* and DSC-CBV parameters. Voxel-wise comparison and distributions of the perfusion parameters in white matter (a-b), grey matter (c-d), and tumour (e-f) for an example case. Each data point on the scatter plots represents a voxel.

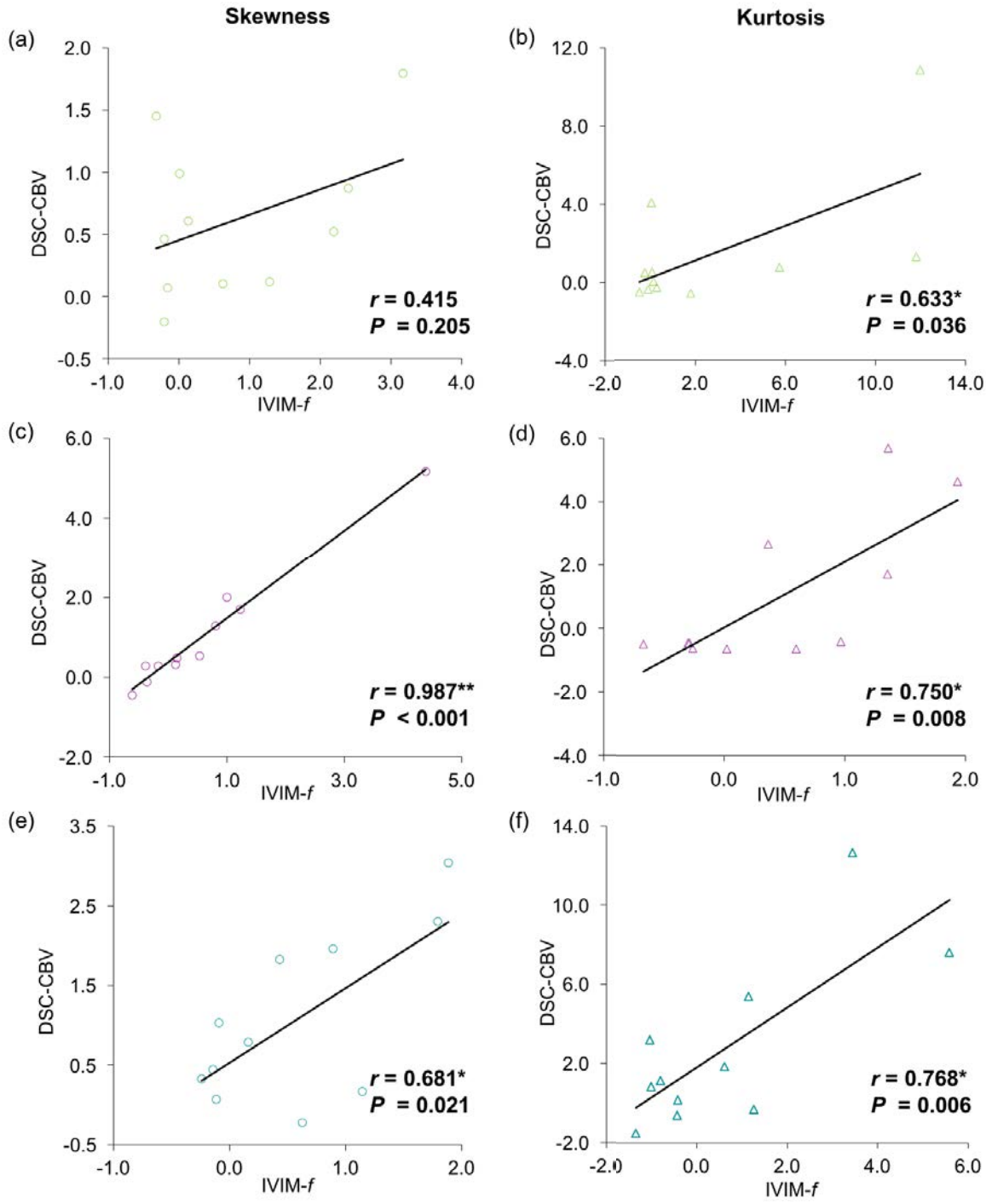

Figure 5.4 Correlation between histogram skewness and kurtosis of IVIM-*f* and DSC-CBV (*n* = 11). Plots presenting the correlation in (a-b) white matter, (c-d) grey matter, and (e-f) tumour using histogram parameters skewness (left) and kurtosis (right).

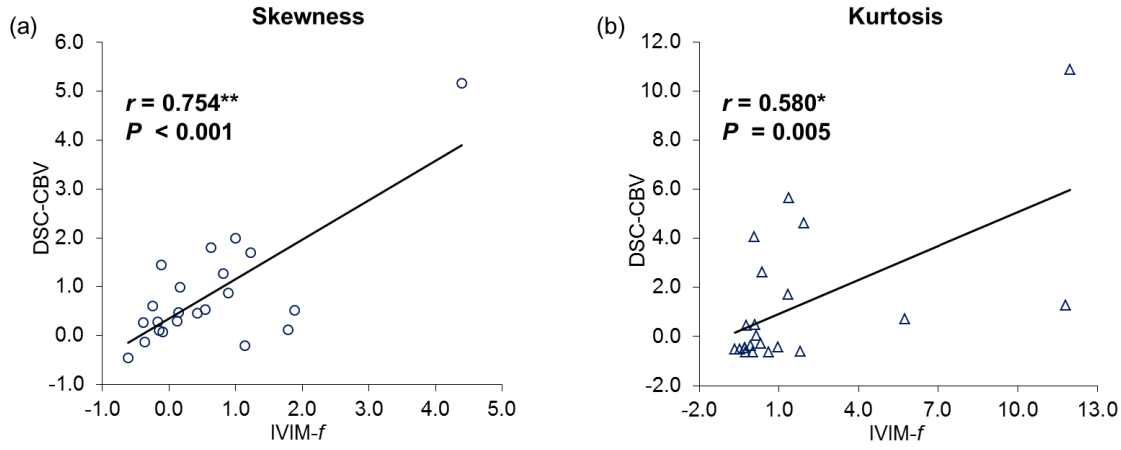

Figure 5.5 Correlation between histogram skewness and kurtosis of IVIM-*f* and DSC-CBV from combined grey and white matter regions (*n* = 22). Plots presenting the correlation for histogram (a) skewness and (b) kurtosis, with the data points corresponding to grey and white matter histogram values.

Voxel-wise correlation and distribution plots for an example patient case are presented in Figure 5.3 for white matter, grey matter and tumour regions. The white matter example (Figure 5.3a) showed a narrower range of values (f = 0.05 - 0.15) in comparison to the grey matter (f = 0.02 - 0.26). The distributions of IVIM-f and DSC-CBV parameters had similar shapes and widths, in all three tissue regions. However, a shift was observed in the distributions, which were normalised separately to the maximum values of IVIM-f and DSC-CBV. The IVIM-f values were relatively shifted towards higher values in comparison to the DSC-CBV values.

Correlation between the histogram parameters of IVIM-f and DSC-CBV was established for skewness and kurtosis (Figure 5.4). No correlation was observed for the other histogram parameters including mean, median and $25^{th}/75^{th}/90^{th}$ percentiles. However, due to the small sample size (n = 11), a correlation of more than $r \geq 0.750$ was required for a power of 80 %. Therefore, only the results for skewness and kurtosis of grey matter, and kurtosis of tumour can be considered statistically valid. The skewness of tumour demonstrated significant correlation (r = 0.681, P = 0.021), but had statistically low power of 67 %.

Due to the rather small sample size, correlation of combined grey and white matter (n = 22) was also assessed with the histogram parameters. This approach was previously used by Wirestam et al. (125). Significant correlations were established for the skewness and kurtosis parameters, which are presented in Figure 5.5. The method provided correlations of r = 0.754 (P < 0.001) and r = 0.580 (P = 0.005) for skewness and kurtosis, respectively, which both had statistical power above 80 %.

5.3.2 Relative Value Comparison

Correlations with histogram parameters were also computed using normalised tumour values. The tumour values were normalised to the healthy appearing grey matter values, which is the commonly used method in the clinical practice of DSC-MRI (28, 120, 121). Using this methodology for both DSC-CBV and IVIM-*f*, a significant correlation was observed with the histogram skewness, but not with kurtosis (Table 5.6, Figure 5.6). The mean relative values demonstrated a significant correlation, but had statistically low power of 59 %, and a larger sample size would be required to validate this observation.

Table 5.6 Correlation results of relative histogram parameters of IVIM-*f* and DSC-CBV.

Histogram parameter	*r*	*P*-value
Mean	0.628*	0.039
Median	0.294	0.380
Skewness	0.775*	0.005
Kurtosis	0.215	0.525
25th percentile	0.253	0.453
75th percentile	0.134	0.694
90th percentile	0.215	0.525

* corresponds to a significance level of P < 0.05.

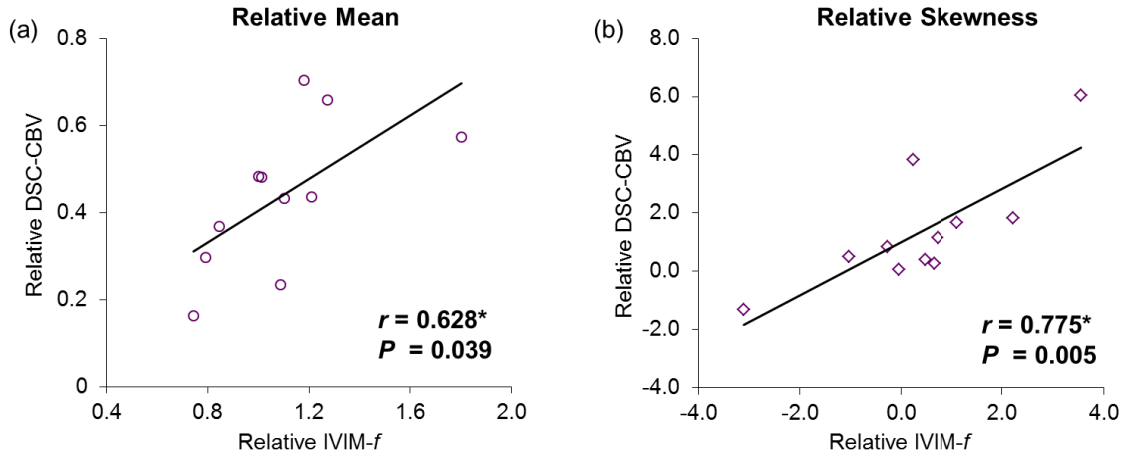

Figure 5.6 Comparison between normalised tumour values of IVIM-*f* and DSC-CBV (*n* = 11). Plots presenting the correlation for relative tumour histogram (a) mean and (b) skewness values.

Two patient cases are presented in Figure 5.7 with the derived IVIM and DSC parametric maps. The glioneuronal tumour (Figure 5.7a) appeared heterogeneous with some cystic regions, whereas the optic pathway glioma (Figure 5.7b) presented as a more homogeneous lesion. Both tumours appeared low-perfused in the parameter maps. The glioneuronal tumour case demonstrated poor voxel-wise correlation between IVIM-*f* and DSC-CBV, whereas moderate correlation was observed for the optic pathway glioma.

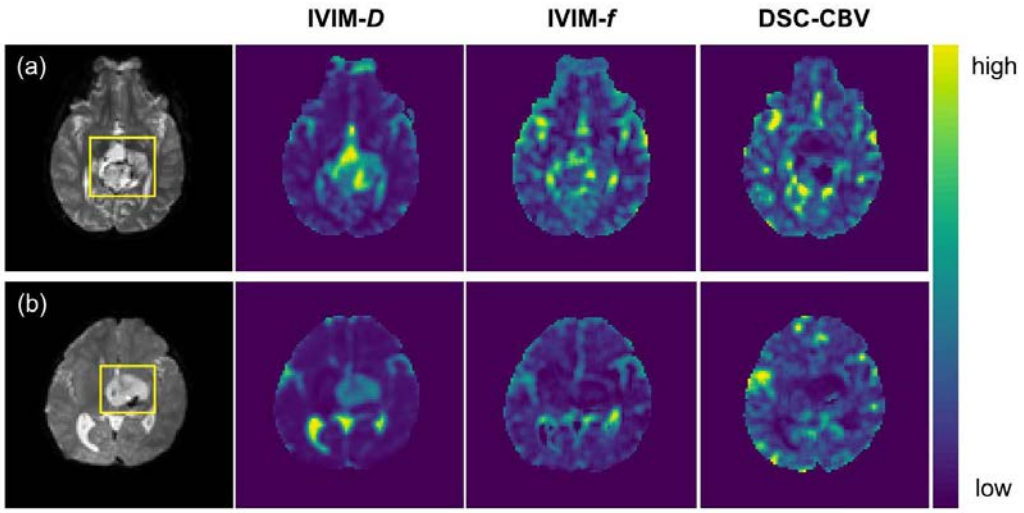

Figure 5.7 Characterisation of brain tumours with IVIM and DSC. Example cases of (a) glioneuronal tumour and (b) hypothalamic glioma shown on b_0 images and the parametric maps of IVIM-*D* and *f*, and DSC-CBV. The yellow boxes indicate the locations of the pathologies.

5.3.3 Age Effect on Perfusion

The effect of age on the level of perfusion was assessed for the median IVIM-*f* and DSC-CBV values in the healthy brain tissues (Figure 5.8). No significant correlations were observed in this cohort, but a general trend of increasing perfusion with age could be seen for the grey matter (Figure 5.8a). In white matter, the changes in perfusion with age appeared to be more modest. The median values in Figure 5.8 were derived from the same ROIs as used in the correlation analysis.

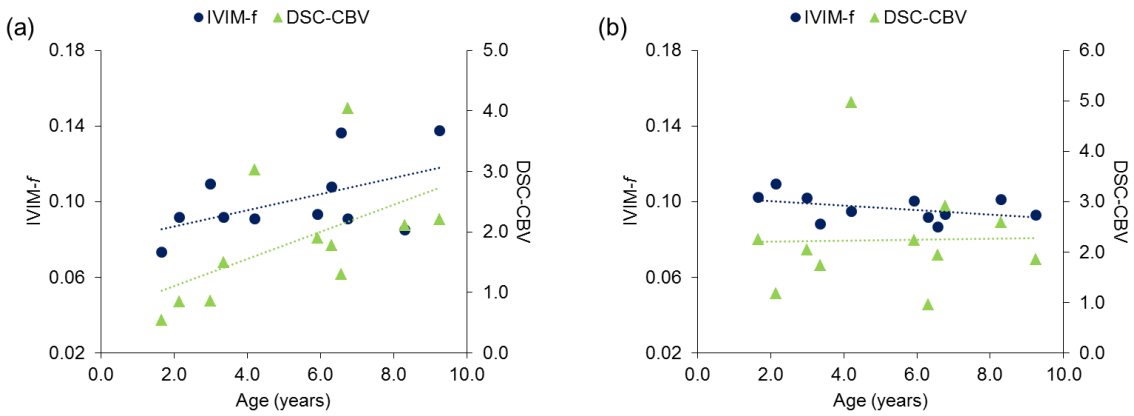

Figure 5.8 The effect of age on perfusion in paediatrics. The plots describe the median IVIM-*f* and DSC-CBV values in (a) grey matter and (b) white matter as a function of age.

5.3.4 IVIM Maps of Low-Grade Gliomas and Choroid Plexus Tumours

Data acquired from patients at GOSH was analysed with the IVIM model to inspect low-grade gliomas acquired at a different centre, and choroid plexus tumours, which have previously been reported to demonstrate elevated cerebral blood volume levels (170). The IVIM diffusion coefficient and perfusion fraction values for these tumours are reported in Table 5.7, and characteristic parameter maps are presented in Figure 5.9 and Figure 5.10 for low-grade gliomas and the choroid plexus tumours, respectively.

The low-grade gliomas appeared low-perfused on the IVIM-*f* maps relative to the grey matter, similarly to the cases acquired at the local institution. Although different sets of *b*-values were used for the two cohorts, the *f* values were found to be comparable. The choroid plexus tumours presented in Figure 5.10 showed interesting perfusion characteristics. The grade I choroid plexus tumour demonstrated slightly elevated *f* values compared to the low-grade gliomas, whereas the *D* values were similar. The higher grade (II and III) tumours showed highly increased perfusion ($f > 0.2$) with more restricted diffusion.

Table 5.7 IVIM parameters extracted from the tumour regions for the GOSH data.

Case	Diagnosis	Grade	IVIM-*D*	IVIM-*f*
1	Pilocytic astrocytoma	I	1.41 ± 0.10	0.0750 ± 0.03
2	Pilocytic astrocytoma	I	1.66 ± 0.12	0.103 ± 0.03
3	Choroid plexus papilloma	I	1.37 ± 0.08	0.192 ± 0.03
4	Atypical choroid plexus papilloma	II	1.28 ± 0.13	0.240 ± 0.04
5	Choroid plexus carcinoma	III	0.71 ± 0.01	0.252 ± 0.07

Note: *D* values are reported in units of $\times 10^{-3}$ mm^2/s.

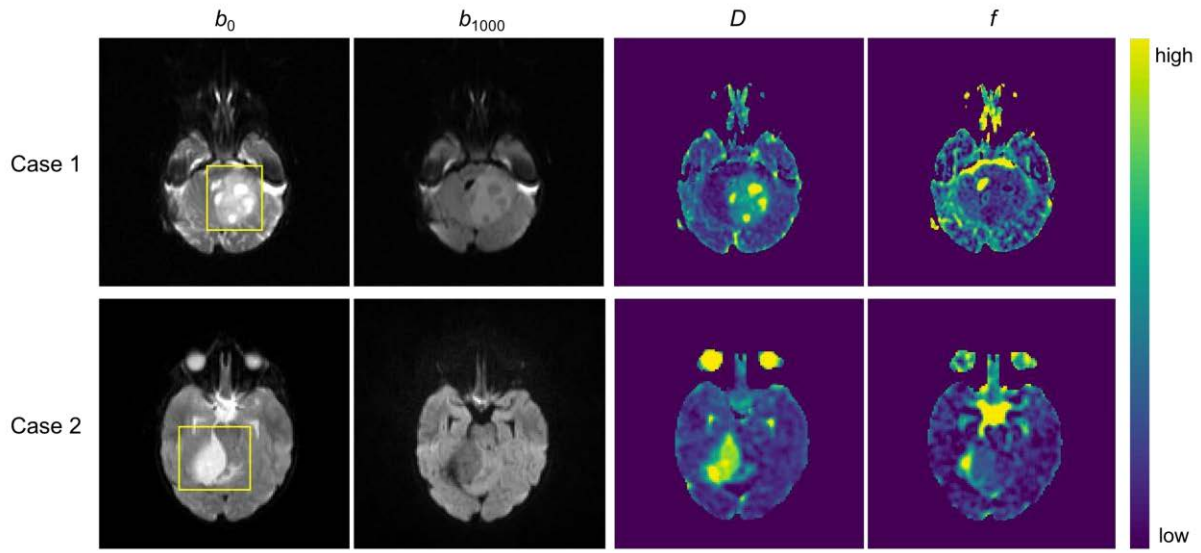

Figure 5.9 IVIM maps of low-grade gliomas. Example cases of two pilocytic astrocytoma tumours computed using the 3 *b*-value IVIM approach. The yellow boxes indicate the locations of the pathologies.

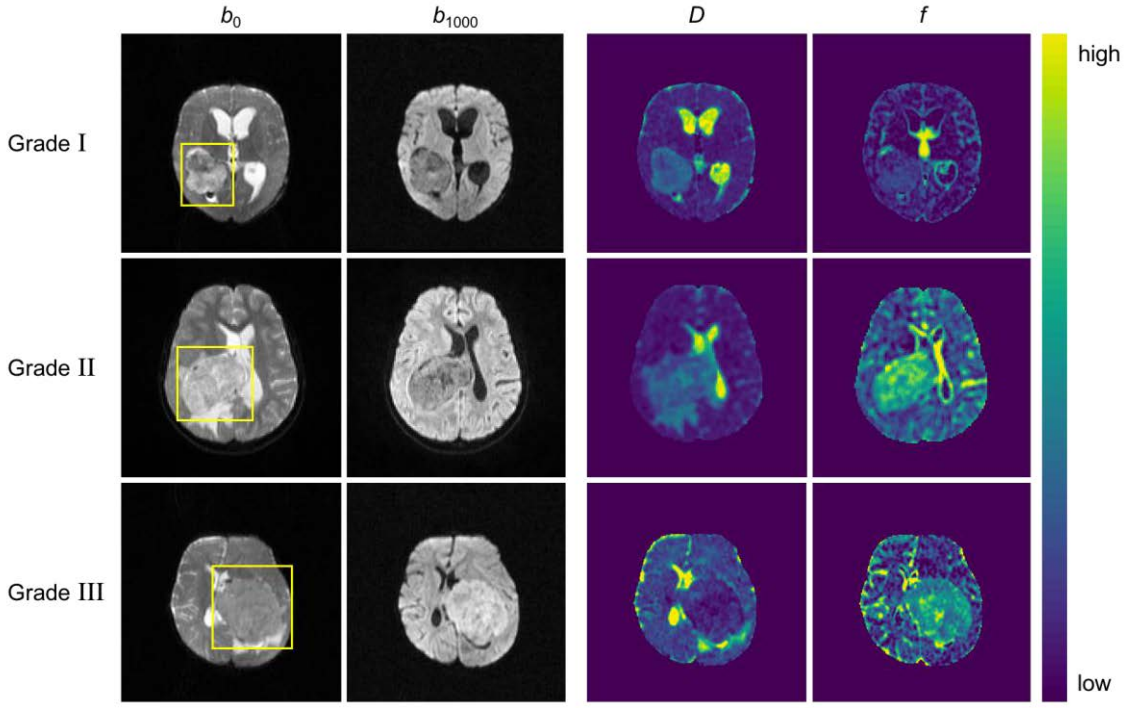

Figure 5.10 IVIM maps of choroid plexus tumours of grades I to III. Example cases of choroid plexus papilloma (I), atypical choroid plexus papilloma (II) and choroid plexus carcinoma (III) computed using the 3 b-value IVIM approach. The yellow boxes indicate the locations of the pathologies.

5.4 Discussion

Comparison of the IVIM derived *f* parameter and the DSC-MRI derived CBV parameter was performed to assess the relationship of the two parameters in low-perfused paediatric brain tissues. Significant correlations were established using a voxel-wise comparison and histogram parameters in white matter, grey matter and tumour regions. Significant correlations were also observed with the use of normalised tumour values, as commonly used in the reporting of DSC-CBV, for the mean and skewness histogram parameters.

The IVIM perfusion fraction values of healthy brain tissue were found to be higher in comparison to previous adult studies (f_{GM} = 0.115 ± 0.01; f_{WM} = 0.090 ± 0.009). Previous reports include ones by Grech-Sollars et al. (79) (f_{GM} = 0.10 ± 0.002; f_{WM} = 0.080 ± 0.002), Wu et al. (87) (f_{GM} = 0.14 ± 0.02; f_{WM} = 0.07 ± 0.01) and Bisdas et al. (136) (f_{WM} = 0.065 ± 0.037). Although some variation exists between these studies, the higher values in our study are not fully accounted for by the variability. Therefore, the more likely reason for the greater values is the elevated perfusion observed in children compared to adults (95, 171). The grey matter volume, proportional to the cerebral blood flow (95), has been found to first increase and then decrease with age in the first two decades of life (172). In white matter, the increase in volume has been found to be linear in the same period, but to a lesser extent. The cohort used in this study showed a moderate increase in perfusion with age in the grey matter, and more modest change in the white matter. Another cause of elevated perfusion in our cohort could be a result anaesthesia (173), which is often used in younger children during MR imaging. The developmental microstructural changes and the potential effect of anaesthetic make it difficult to compare the values across the cohort, and particularly with the previous adult studies.

The DSC-CBV values in our cohort were found to be CBV_{GM} = 4.38 ± 0.96 mL/100 mL and CBV_{WM} = 1.94 ± 0.53 mL/100 mL. These values were in good agreement with a study by Wu et al. (87) (CBV_{GM} = 4.4 ± 0.5 mL/100 mL and CBV_{WM} = 1.9 ± 0.2 mL/100 mL), but appeared slightly elevated compared to a study by Sourbron et al. (174) (CBV_{GM} = 2.6 ± 0.8 mL/100 mL and CBV_{WM} = 1.3 ± 0.4 mL/100 mL). Other adult studies have shown the grey matter CBV to vary between 3 to 7 mL/100 mL (175-177). Similarly to the IVIM-*f,* the differences were likely to arise due to the influence of age, but also from the differences in data analysis used in the computation of CBV values.

Discrimination of adult low- and high-grade gliomas has been possible in previous studies using IVIM-*f* (27, 28, 137) and DSC-CBV (115, 178). The low-grade tumours in our cohort appeared generally hypo-perfused compared to the grey matter with both IVIM and DSC-MRI. This agrees with the previous adult studies, apart from the studies by Hu et al. (137) and Lin et al. (138), who reported higher *f* values for the low-grade gliomas. However, these studies reported the use of IVIM including high *b*-values (> 1000 s/mm^2), producing a more challenging scenario for the accurate estimation of IVIM parameters, as discussed in Chapter 4.

The voxel-wise correlations between IVIM-*f* and DSC-CBV were significant for most of the grey matter, white matter and tumour regions. A few of the cases with lower correlations were found to be influenced by motion or misalignment of the slices, which had a direct effect on the voxel-wise comparison. In general, the correlations were more moderate in the white matter and tumour tissues, most likely due to the lower overall perfusion and small range of values seen in these regions. In a previous study by Wu et al. (87), voxel-wise correlations were only found in grey matter, but not in white matter. In our study, the range of *f*-values produced in the white matter was narrow, which would have reduced the correlation strength. Also, the measurement of both perfusion

parameters is more difficult in low-perfused tissues, with the measurements having inherently lower accuracy. This was shown for IVIM-*f* in Chapter 3 with the low-perfused tumour simulations, where the IVIM fitting was less robust compared to the grey matter model. The measurement of IVIM-*f* is also affected by higher variability at the lower *f* value region, as shown in Chapter 4. With regards to bias, the use of *b*-value = 300 s/mm^2 in the brain was likely to introduce some bias to the *f* values. However, as demonstrated previously, the bias was independent of the magnitude of *f*, but dependent on the *b*-value, and therefore the bias would have influenced the fitting performed across the brain. Therefore, this was not likely to affect the correlation between IVIM and DSC measurements.

An interesting observation was made in the previous studies by Wu et al. (87) and Conklin et al. (93), where a reduction in the correlation strength was seen when CBV > 10, which was attributed to voxels containing larger vessels. Similar behaviour was also observed in our study (Figure 5.3). Coherent flow in larger vessels does not comply with the randomly oriented microvasculature as assumed by the IVIM model. This means that the contribution from the larger vessels is likely to go towards the perfusion free diffusion component *D*, with the increase in phase accumulation rather than the signal decay. This has an important consequence for the comparison of IVIM and DSC in such regions, and indicates the inherent differences in the properties of the two measures.

To mitigate some of the motion effects likely influencing the voxel-wise correlations, histogram parameters were derived for the brain tissue regions. However, no correlations were observed between the histogram "value" parameters e.g. mean or percentiles. Instead, significant correlations were observed using skewness and kurtosis, signifying the similarities between the shapes of the perfusion parameter distributions. Although the strong correlations between the distribution shapes suggests that similar

tissue properties contribute towards both *f* and CBV, it is well known that the two measures are not comparable as exact values (102). This likely resulted in a shift between the *f* and CBV histograms in the different tissue regions and likely accounted for the poor correlations of the histogram values such as the mean and median.

The final correlations were performed using normalised tumour values, as used in the clinical practice of DSC-MRI to provide semi-quantitative CBV values (120, 121). The normalisation to a healthy tissue aims to reduce the variability of tumour CBV between patient cases by accounting for the variability in contrast bolus arrival due to microstructural differences. Using this approach, significant correlations were established between the mean and the skewness histogram parameters. The significant correlation between the histogram skewness indicated similarities in the distributions of the perfusion parameters, which suggested that a correlation should also exist between the medians. This was found to not be the case, similarly to the percentile measures. The magnitude of skewness for the IVIM-*f* and DSC-CBV were found to increase in a similar fashion in both grey matter and tumour regions, although lower skewness was observed for the IVIM-*f*. The skewness was found to be more variable between the IVIM-*f* and DSC-CBV measures in the low-perfused tissues of tumour and white matter, potentially influenced by the aforementioned issues in the measurement of both parameters. Therefore, the distributions of the parameters were not similar enough to produce agreement between the medians. However, the significant correlation between the relative mean parameters in this study and previous studies is promising and should be further confirmed in a larger cohort.

Data from GOSH was included in this Chapter to assess the applicability of the 3 *b*-value fitting (Chapter 4) and whether low-grade gliomas appeared low-perfused, similarly to the cases in our cohort. The two cases presented appeared relatively low-

perfused and further confirmed this observation in paediatric patients. No IVIM studies to date have presented the finding of low-perfusion in paediatric low-grade gliomas. This is important for the use of IVIM-*f* as a potential biomarker in tumour grading, and further studies are required for its validation in larger paediatric cohorts including high-grade gliomas.

The other cases included in this study were the choroid plexus tumours of different grades. As reported previously in the literature (170), these type of tumours have shown higher levels of perfusion. While the low-grade gliomas in this study appeared low-perfused, the IVIM-*f* values in the choroid plexus tumours were estimated relatively high as expected given their vascular origin. Interestingly, the IVIM-*f* increased with grade in the choroid plexus tumours, and differences in their appearance could be observed for the benign grade I and the more malignant grade II and III tumours.

The vasculature in tumours is known to be unevenly distributed with irregular branching of the tumour vessels and no well-defined hierarchy (179). As a result, the blood flow in tumours is not constant along a single direction, and may follow different paths and even change direction through the same vessel. In contrast, the vasculature in healthy tissues is arranged in a hierarchy of well-differentiated components. The complex nature of the underlying vasculature of these tumours and the origins of the increase seen in the IVIM perfusion fraction pose interesting questions requiring further studies to investigate the physiologic origins of the IVIM perfusion fraction.

5.5 Study Limitations

Some limitations were present in this study. The IVIM model used here did not consider differences in relaxation times, which have been shown to affect the perfusion-related parameters in the liver (180). However, while statistical support for the extended IVIM model has been shown in the liver, this was not the case for the lower perfused organs, namely spleen and kidney (181). Therefore, these effects are likely to be negligible in the low-perfused tissues investigated here.

The greatest limitation perhaps of this study was the small cohort size. However, the significant correlations observed in the voxel-wise comparison and the histogram parameters with statistically sufficient power suggest that promising results could be expected in a larger cohort. An additional limitation in our study was the influence of developing brain on the perfusion, which provided a more complex scenario compared to the previous adult studies. A larger cohort is required for the assessment of the influence of age on both the IVIM and DSC perfusion parameters.

Finally, the IVIM fitting used for the GOSH data was found to be limited by the smaller voxel size and potentially lower SNR in regions of white matter in comparison to the data from the local institution. The fitting in these cases was found to result in negative values for perfusion fraction, which were set to zero to ensure biologically valid parameters. This would however result in a positive bias to results over a region of interest containing such voxels. Therefore, as shown in the previous Chapters, the consideration of SNR level and hence the use of a sufficient voxel size are essential for the application of IVIM, particularly where this is dependent on only three *b*-values.

5.6 Conclusion

The results presented in this Chapter agree with the previous studies and support the link between the IVIM-*f* and DSC-CBV parameters. The voxel-wise correlations in the grey matter were significant, demonstrating a promising association of the parameters. However, the measurement of the parameters was technically challenging in the lower perfused tissues, i.e. the white matter. Some key differences also exist between what is measured by each parameter, which leads to scenarios where the relationship between the two parameters is likely to reduce. Such scenarios were found in both low- and high-perfused tissues. At low perfusion, the challenge was the inherently lower accuracy of both methods and higher variability of the IVIM-*f*. Also, bias was introduced in low-perfused tissues with IVIM fitting resulting in negative *f* values, and with DSC-CBV from T_1 effects in contrast enhancing tissues which are only partially allowed for. In regions of relatively high perfusion with larger vessels, a plateau was observed for the CBV values, and IVIM was hypothesised to measure only the perfusion arising from the microvascular capillary network due to the limited timescale used in DW-MRI. Differences also exist in what both parameters measure of the underlying tissue. IVIM measures the inherent perfusion influenced diffusion of water, while DSC relies on the timings and concentration of the administered contrast. Therefore, while the correlations suggested that the IVIM-*f* and DSC-CBV arise from similar tissue properties, the limitations of both methods result in differences in certain tissue regions.

Overall, the presented study suggests that the non-invasive DW-MRI could provide a contrast-free perfusion biomarker for the assessment of childhood brain tumours, which can be made more robust by the appropriate acquisition and analysis of data. Used in conjunction with the IVIM *D*, this could result in a more comprehensive investigation of the underlying tissue microenvironment in a single MRI protocol.

Chapter 6

MIROR Clinical Decision Support System: Implementation of Diffusion Module and Investigation of Childhood Solid Tumours

6. MIROR Clinical Decision Support System: Implementation of Diffusion Module and Investigation of Childhood Solid Tumours

Some aspects of the work presented here were published in [**P03**], [**P04**] and [**P07**].

This Chapter was part of a larger collaborative project, with the contributions from others detailed in the Declarations section at the beginning of this thesis. In the text, where clarity was required, the initials of the contributor were also included.

6.1 Introduction

New MRI applications are continuously developed with the aim to improve clinical decision making in scenarios such as diagnosis and treatment response. This has led to the discovery of specific imaging biomarkers, which often require computationally intensive quantitative image analysis techniques (59, 182-184). Nevertheless, the clinical interpretation remains largely qualitative and subjective by expert review. Therefore, improvements are required in the presentation and accessibility of the advanced features, and the versatile amount of quantitative information derived from different MR modalities to promote their clinical uptake.

In the past decade, clinical decision support systems (CDSSs) have gained more attention with the aim to reduce the translational gap between research and clinical use of the advanced analytical methods (185-188). The idea of a translational gap was introduced in Chapter 1 in the context of imaging biomarkers, and involves the crucial final step of integrating the new biomarker into a routine clinical practice. The CDSSs approach this challenge by providing a platform for extracting relevant features from the image data, with the aim to reduce any user prone or expertise related errors. Furthermore, the CDSSs allow the incorporation of evidence-based medicine or practice

of medicine based on the best available scientific evidence, which has been found to improve clinical outcomes (189). Therefore, the availability of a user-friendly, flexible and evidence-based CDSS could accelerate the clinical uptake of more advanced imaging methods, and allow the simultaneous assessment of modular data in a scientifically informative and convenient manner.

In this Chapter, aspects of a collaborative project in designing and developing a modular medical image region of interest analysis tool and repository (MIROR) platform are described (Figure 6.1). MIROR is currently developed and used at Birmingham Children's Hospital to determine its role in facilitating non-invasive diagnosis of childhood brain and abdominal tumours. The project involved both experts in MRI data processing and clinicians, to ensure the fit for purpose of MIROR to clinical practice. Here, the development of a diffusion MRI module for MIROR including both the ADC and IVIM analysis pathways is described, with the aim to provide a tool for integration of the analysis into routine clinical practice.

The second aim of this Chapter was to test the implemented diffusion module in a cohort of childhood abdominal lesions. Malignant abdominal tumours are usually diagnosed with a combination of conventional imaging techniques and histology (82). However, histological diagnosis requires the invasive procedure of biopsy with risks of morbidity and sampling errors in large abdominal lesions (190, 191). Conclusive diagnosis based on conventional imaging alone can be difficult with similar morphological appearances of some childhood tumours (7). Therefore, diagnosis based on an advanced MR imaging modalities would be of important clinical value.

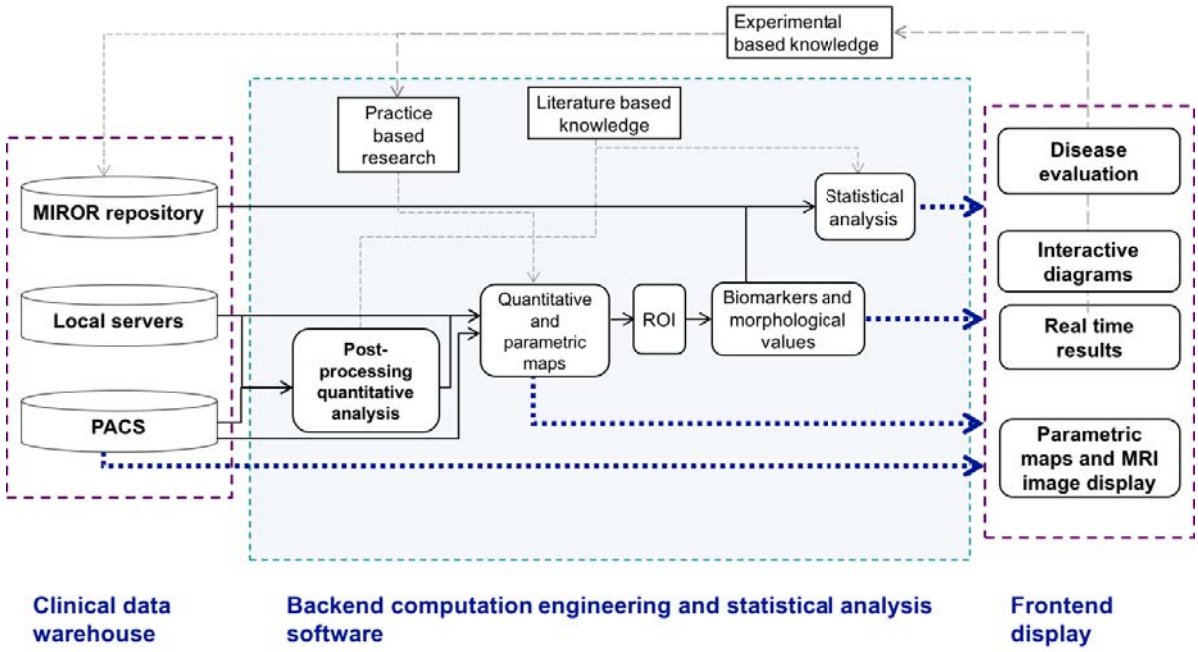

Figure 6.1 Hierarchical structure of MIROR. The workflow of clinical imaging data from storage to diagnostic evaluation, adapted from reference (192) with the permission of the author. PACS corresponds to the picture archiving and communications system, which provides storage and access to images from multiple modalities.

Promising results have been shown with the use of diffusion-weighted MR imaging and the apparent diffusion coefficient (ADC) in paediatric abdominal tumours (41, 193). ADC has been able to discriminate benign from malignant solid tumours, likely reflecting the more restricted diffusion and hence higher cellularity found in malignant lesions (14, 16). However, discrimination between individual tumour types with ADC was not possible in the previous studies. The ADC approach for heterogeneous tissues such as those found in abdominal tumours can be relatively simplistic and does not maximise the information that can be potentially extracted from the DW-MRI (11). Therefore, the use of the intravoxel incoherent motion (IVIM) model could provide additional parameters of clinical value. Previously, an adult study showed the IVIM parameters to be helpful in discriminating common malignant pancreatic tumours, as well as benign from malignant lesions (132). In another study, significantly better discrimination of low- and high-grade hepatocellular carcinoma (HCC) was achieved with the use of the

IVIM derived diffusion coefficient compared to the ADC (30). Therefore, the application of IVIM should be investigated in paediatric abdominal tumours to evaluate its diagnostic value.

The heterogeneous nature of abdominal tumours can be difficult to characterise based on imaging measures such as the mean value of a region-of-interest alone. In a previous study, the use of histograms in paediatric Wilms' tumours was able to identify distinct cellular regions based on ADC values, and to determine predominant histological cell types (194). The use of histogram parameters based on IVIM parametric values was also shown to discriminate recurrent tumours from treatment effects in adult glioblastomas (122) and showed significant differences among tumour subtypes in breast cancer (195). Therefore, in this study, histograms were derived for the whole tumour regions to allow the inspection of the distribution of parametric values.

Overall, the aim of this study was to develop a diffusion module to the MIROR platform, and to evaluate the diagnostic performance of IVIM in a cohort of childhood abdominal tumours using the implemented diffusion module.

6.2 Methods

6.2.1 Development of Diffusion Module for MIROR

6.2.1.1 MIROR Framework

A short summary of the design and development of MIROR is provided here for the completeness, with a more comprehensive study presented in ref. (192). The MIROR framework was implemented by N.Z.

The MIROR platform has a modular and open architecture (196) to ensure seamless incorporation of new workflows to facilitate the new developments made in MR data analysis. Such an approach was chosen to allow the development of independent modules in their own life cycles, before the addition to the final product. MIROR was designed to use the evidence-adaptive CDSS approach, based on the American medical informatics association (AMIA) recommendations (189). This means that the clinical knowledge base of MIROR is derived from and continually reflects the most up-to-date evidence from the research literature and practice-based sources (197). Quantitative and statistical analysis modules for MIROR were developed based on literature and local practice based research.

The MIROR repository is an evolving database, which stores the analysed diagnostic data from routine clinical practice. The experimental based knowledge and evidence from the outcomes of the MIROR repository can then inform clinical investigation, reflect on clinical practise, and develop the quantitative analysis modules further. The practice-based evidence can advise the choice of MRI protocol and parametric maps to be used for future analysis and clinical evaluations.

6.2.1.2 Implementation of Diffusion Module to MIROR

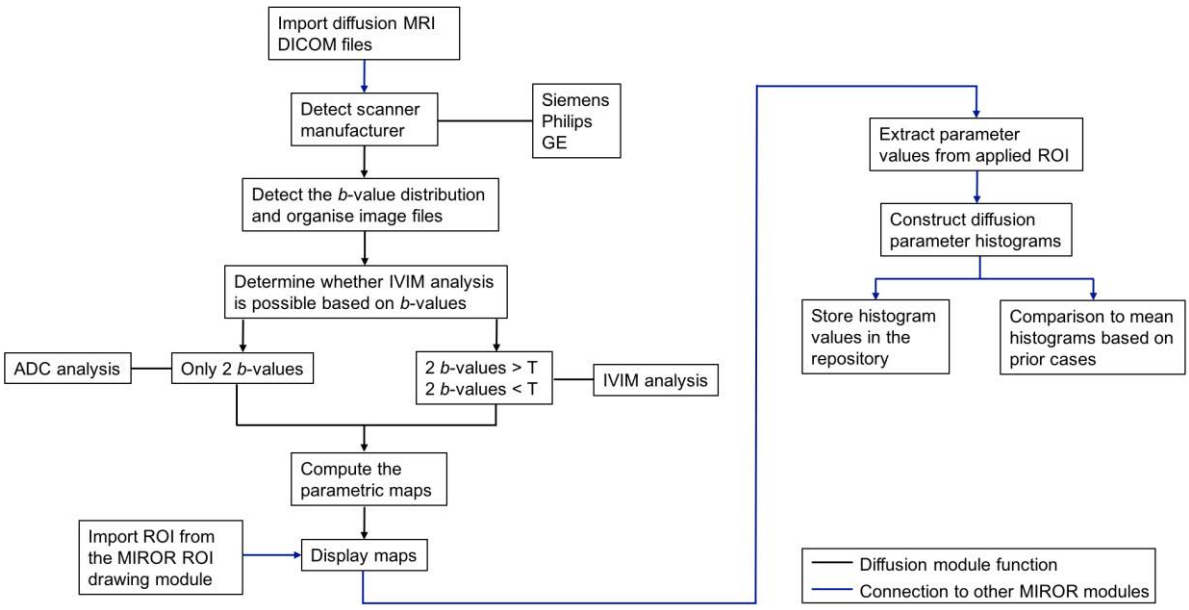

Figure 6.2 Design of the MIROR diffusion module. The workflow of the diffusion module and the connection to the MIROR ROI and statistical analysis modules. T corresponds to a chosen threshold value used in the segmented IVIM fitting.

The platform used in this study was MeVisLab (MeVis Medical Solutions AG - Fraunhofer MEVIS, v. 2.7.1) (198, 199). MeVisLab is a research based rapid prototyping platform for medical image processing. The diffusion analysis module, with IVIM and ADC fitting algorithms, was developed using Python (v.2.7), which was embedded within MeVisLab. The user interface and the connections of modules in MeVisLab were defined using an abstract module definition language (MDL).

The workflow of the diffusion module is described in Figure 6.2. In the current version, the diffusion module only accepts images in digital imaging and communications in medicine (DICOM) format. The workflow starts by converting an ML (MeVis Image Processing Library) image to a native python numerical data structure, followed by the detection of the imported DICOM files. A function then determines which manufacturer diffusion-weighted MR scans have been imported by reading the DICOM tag. Based on the manufacturer, the *b*-values are extracted from the correct DICOM tag location. If

non-enhanced DICOM files are imported, the image files are sorted based on the DICOM instance number tag. The next step involves the determination of diffusion analysis, which is feasible for the available image data.

The segmented fitting approach was chosen for the IVIM analysis to increase the stability of the bi-exponential fitting and reliability of the IVIM parameters, as reported by previous studies (84, 85, 88, 90). This approach allows the computation of IVIM diffusion coefficient (D) and perfusion fraction (f) parameters on data with limited number of b-values. Based on the set threshold (determining high b-values for the linear fitting step), if two or more b-values are available > $b_{threshold}$, the computation of D and f parameters is performed. This validity criteria for determining D and f by using two b-values was studied in Chapter 4, which showed that robust estimates for the parameters can be derived (Figure 4.9). The criteria for computation of the pseudo-diffusion parameter (D^*) requires at least two b-values < $b_{threshold}$ (excluding b_0), as well as the validity of criteria for D and f parameters. The bi-exponential fitting step was implemented using the Levenberg-Marquardt algorithm, the functionality of which needed to be developed in-house as no third-party fitting modules were available. For all diffusion data with at least 2 b-values, where one of them is b_0, computation of ADC is performed. Finally, the resulting diffusion parametric maps are stored in the MIROR repository.

The diffusion module connects to the other modules of the MIROR framework. This allows the use of previously drawn regions-of-interest (ROIs) and the extraction of the data for statistical analysis from the diffusion maps saved in the MIROR repository. The results from the statistical analysis, including histograms, are then saved in the MIROR repository, allowing the building of the database for different tumour types. This ensures that the prediction outcome for new input cases achieves the maximal statistical power.

6.2.2 Patient Study of Retroperitoneal Lesions

6.2.2.1 MR Imaging

All MR imaging was performed on a Siemens Avanto 1.5 Tesla (T) (Siemens Healthcare, Erlangen, Germany) MRI scanner with a 4-channel receive body coil at Birmingham Children's Hospital. The imaging protocol included fat-suppressed axial and coronal pre- and post-gadolinium T_1-weighted turbo spin echo (TR/TE 760 to 817/7.7 ms), axial T_2-weighted turbo spin echo (TR/TE 3000 to 5640/67 to 87 ms) and diffusion-weighted imaging.

The DW-MRI protocol used a spin-echo planar imaging (EPI) sequence with 6 *b*-values (0, 50, 100, 150, 600, 1000 s/mm^2), EPI factor = 174, three signal averages (NSA = 3), TR/TE 3,200 to 9,900/92 ms, parallel imaging (GRAPPA) with an acceleration factor = 2 and 75 % partial Fourier encoding. The fat suppression was performed with a frequency-selective preparation pulse. The diffusion weighting was applied in three orthogonal directions, of which a trace image was derived in the axial acquisition plane. Depending on the patient size, the field-of-view (FOV) was 221 to 350 × 172 to 317 mm, matrix size 122 to 192 × 128 to 192, slice thickness 5 mm with no gap between slices, number of slices from 35 to 75, and voxel size of 1 to 2.34 mm^2 × 5 mm. The DWI protocol acquisition time ranged from 4 minutes 52 seconds to 7 minutes 35 seconds.

6.2.2.2 Patient Population

A computerised search of medical records identified 55 patients who underwent abdominal MR imaging between June 2012 and September 2016, where the DW-MRI protocol was part of standard care. All cases were reviewed in the local tumour study board for suspected malignancy. Informed parental consent was obtained for all subjects. The following exclusion criteria were applied to the cohort: having received treatment prior to imaging (chemotherapy or surgery); non-solid pathology (n = 1); incomplete MRI

or small lesions (single slice largest area < 3 cm^2 or total volume < 6 cm^3, n = 12). The final population included 42 patients, and comprised of 10 benign and 32 malignant cases (Figure 6.3).

The patient cohort demographics are summarised in Table 6.1. The cohort comprised of 16 female (mean age 3.6 ± 4.2 years) and 26 male (mean age 3.3 ± 3.0 years) patients. The age range for the whole group was 0-14 years, with mean age 3.7 ± 2.8 years. The malignant tumour types are listed in Table 6.1. The benign lesions consisted of indolent abdominal mass (n = 1), ganglioneuroma (n = 3), haematocolpos (n = 1), lipoma (n = 1), haemangioma (n = 1), mesoblastic nephroma (n = 1), osteomyelitis (n = 1) and vascular malformation (n = 1). The maximum diameter of the malignant tumours was 32.1 cm (range 8.5 ± 53.1 cm) and benign lesions 16.8 cm (range 7.2 ± 47.7 cm).

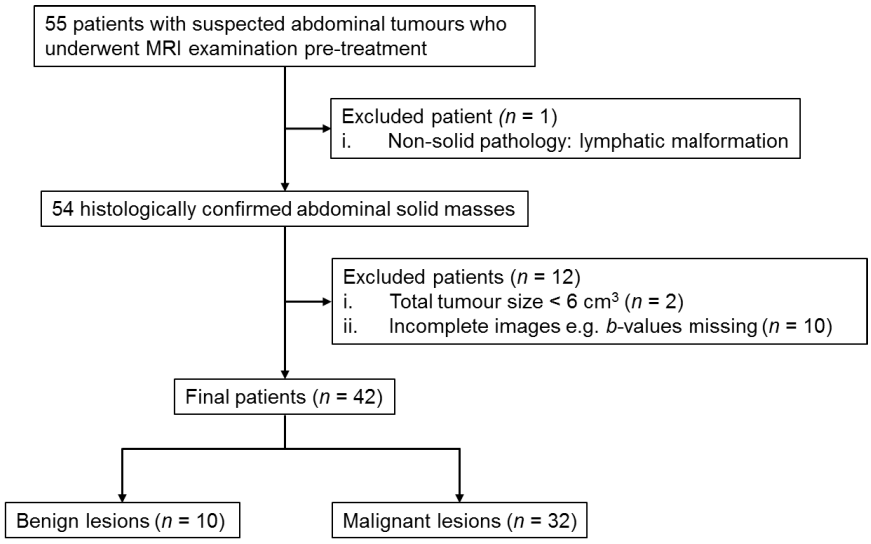

Figure 6.3 Patient selection. Flow diagram describing the patient selection process, with inclusion and exclusion criteria.

Table 6.1 Patient cohort demographics.

Lesion type	Cases	Sex (F/M)	Mean age, range (yrs)
Benign	10	3/7	4.0 (0-10)
Clear cell sarcoma	1	0/1	3.5
Ewing's sarcoma	1	0/1	9.3
Germ cell tumour	1	0/1	2.4
Hepatoblastoma	4	2/2	0.9 (0-2)
Nephroblastomatosis	1	0/1	0.1
Neuroblastoma	11	5/6	1.9 (0-6)
Ovarian immature teratoma	1	1/0	11.8
Rhabdoid tumour	2	1/1	0.9 (0-1)
Rhabdomyosarcoma	2	0/2	5.8 (5-7)
Wilms' tumour	8	4/4	6.1 (1-14)
Total	42	16/26	3.7 (0-14)

6.2.2.3 Data Analysis

Post-processing of the diffusion-weighted MR data was performed using the diffusion module developed for MIROR, as described in the previous section. This allowed the generation of ADC and IVIM D, D^* and f parameter maps. ADC parameter maps were computed using b-values 0 and 1000 s/mm^2. A threshold of b = 150 s/mm^2 was chosen for IVIM based on the local clinical abdominal MR protocol, a previously reported consensus statement (101), and the study presented in Chapter 4.

IVIM and ADC parameter values were extracted from the parameter maps using the MIROR region-of-interest (ROI) drawing module. Whole tumour areas were included in the ROIs, including cystic and necrotic areas. ROIs were drawn by a junior clinician (K.M) and inspected by an experienced radiologist (10 years of experience, K.F.). The

whole tumour approach was shown previously to result in better inter-observer reproducibility compared to single section or slice ROI analysis (200, 201). The ROIs were drawn manually on diffusion-weighted b_0 images with the aid of conventional MRI for the tumour outline at each consecutive slice, excluding peritumoural oedema. Peritumoural oedema refers to the excess fluid found around a tumour, collecting in tissues and causing swelling. On each slice, sections of tumour > 50 % of the more central adjacent slice and ≥ 3 cm were included to minimise any partial volume effects.

A MIROR histogram module was applied to the extracted data to construct histograms. For each patient case, mean, median, $5^{th}/25^{th}/75^{th}/90^{th}$ percentiles, skewness, kurtosis and entropy were calculated based on normalised histograms. Histograms were normalised to their maximum values to dissociate histogram parameters from differences in lesion sizes and to compute average histograms for individual tumour types. The histogram analysis was chosen to allow the analysis of different proportions of histological tissue types and necrosis within tumours.

6.2.2.4 Statistical Analysis

All statistical analysis was performed using SPSS Statistics (IBM, Chicago, IL, v.23). Non-parametric statistics were performed for the histogram derived data. These included the Kruskal-Wallis and Dunn's tests, which were used to compare the ADC and IVIM parameters from the malignant tumours and to determine which tumours gave rise to the difference, respectively. Mann-Whitney U test was used to establish differences between the malignant and benign lesions. Bonferroni correction was used to adjust the *P*-values for the Dunn's test, when several statistical tests were performed simultaneously. In SPSS, this is performed by multiplying the *P*-values with the number of comparisons made.

Receiver operating characteristic (ROC) curves were used to determine how well the diffusion parameters discriminated individual tumour types, and benign from malignant lesions. The area under the ROC curve (AUC) was measured to assess the diagnostic performance of the diffusion parameters. The cutoff values for the diagnostic tests and the diffusion parameters were determined using the maximum Youden index (or Youden's J statistic), estimated for all points on the ROC curves from the corresponding sensitivity and specificity values:

$$\text{Youden index} = \text{sensitivity} + \text{specificity} - 1 \quad [6.1]$$

The Youden index defines the maximum potential effectiveness of a biomarker, and determines the cutoff value that optimises the biomarkers differentiating ability, when sensitivity and specificity are given equal weight (202).

All tests performed were two-sided. P-value < 0.05 was considered to indicate significant difference.

6.3 Results

6.3.1 MIROR Diffusion Module

An example IVIM *f* parametric map computed with the implemented diffusion module is presented in Figure 6.4 in the MIROR (v. 2.0) user interface developed by N.Z. (with contributions from E.M.M.). The b_0 anatomical image was included in the interface for easier inspection of the drawn region-of-interest (ROI), which was imported separately using the MIROR ROI module. Based on the ROI, a histogram was constructed from the extracted IVIM *f* values, allowing the computation of the histogram statistics.

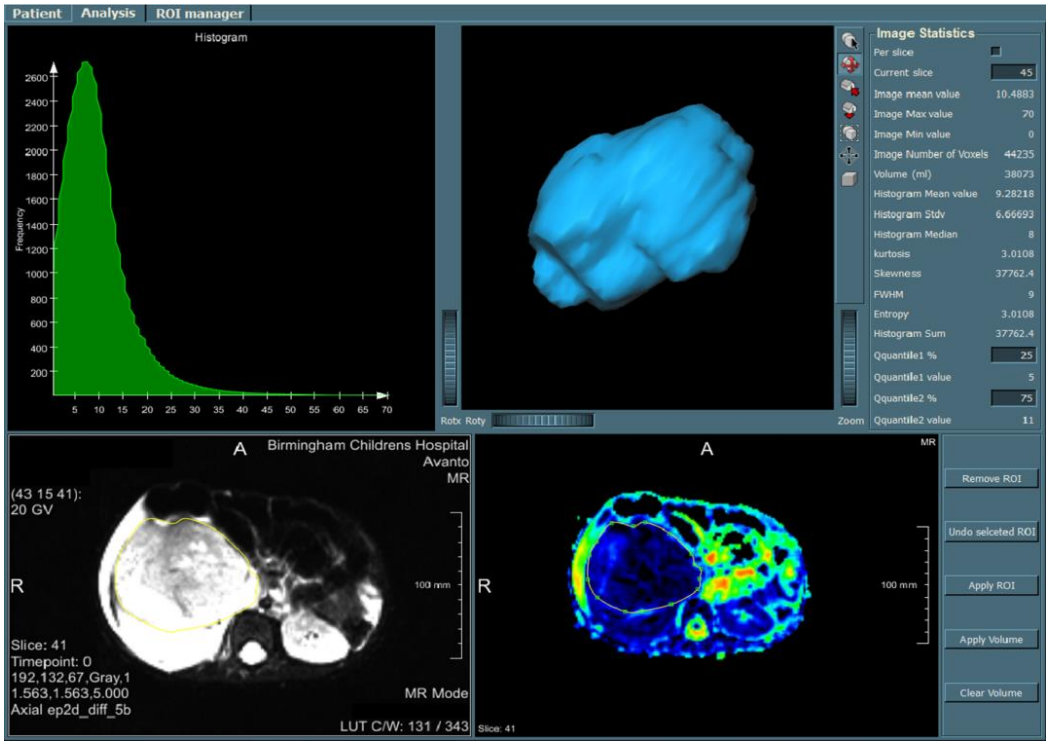

Figure 6.4 MIROR user interface patient view (v. 2.0). The figure shows a malignant tumour case, with the imported ROI (drawn in MIROR ROI module), the overlaid ROI on the IVIM *f* parametric map, the resulting *f* value histogram, a 3D presentation of the ROI or tumour surface and the image statistics based on the histogram of the whole tumour region.

The next part of the workflow involved the connection of the diffusion module to the analysis module (N.Z.), which pulls the previously stored information from the MIROR repository (Figure 6.5). This functionality was implemented in the MIROR v.2.1. This allowed the comparison of the input case histogram to mean histograms of different tumour types or benign lesions, based on a chosen diffusion parameter (IVIM or ADC)

As part of the MIROR v. 2.1.1, a more sophisticated layout of the diffusion module was implemented. This allowed the visualisation of all the diffusion maps as well as their corresponding histograms and histogram based statistics.

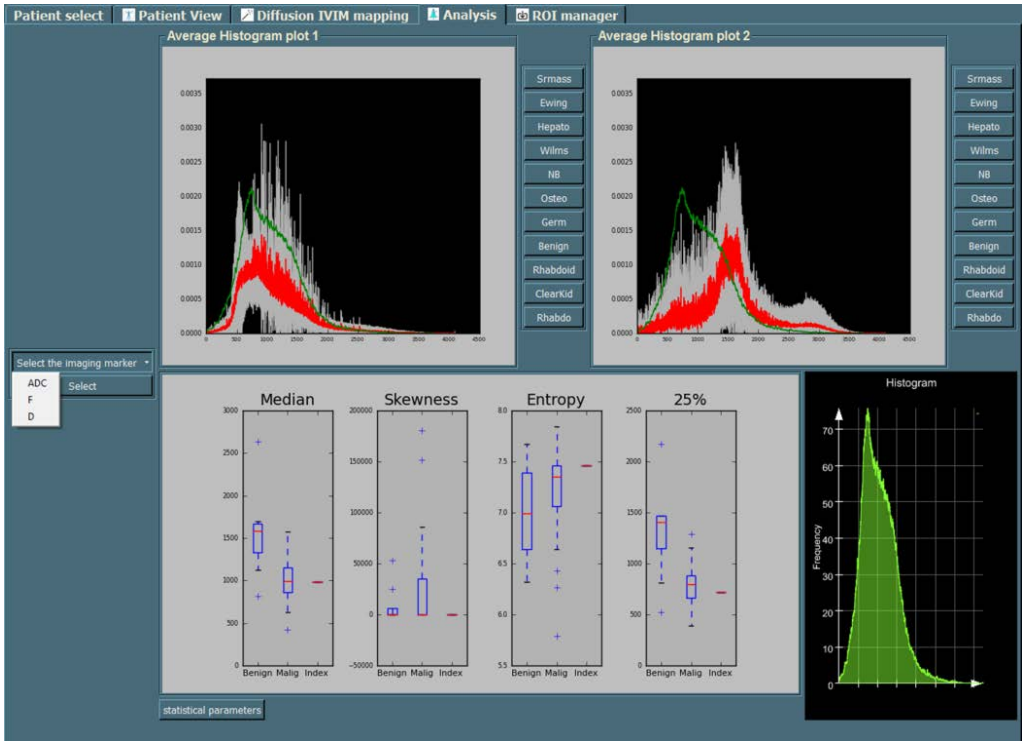

Figure 6.5 MIROR analysis interface (v. 2.1). The figure shows a malignant neuroblastoma ADC histogram (green), overlaid on a mean ADC neuroblastoma histogram (red, top left), and on a mean ADC benign lesion histogram (red, top right) with grey plots indicating the standard deviation. The boxplots describe the histogram values for malignant and benign abdominal lesions, from the MIROR repository with the index describing the statistics of the input case.

6.3.2 Diagnosis of Childhood Retroperitoneal Lesions

The implemented diffusion module for MIROR was tested and evaluated for its clinical value in a cohort of childhood retroperitoneal lesions in the renal bed. MRI data sets were imported to MIROR from the local PACS. The IVIM and ADC analyses were fully computed within MIROR.

6.3.2.1 Discrimination between Tumour Types

The median diffusion parameter values derived for each malignant and benign lesion are presented in Figure 6.6. The benign lesions were combined into one group, which had the widest distribution of values, compared to the malignant lesions. Relative to the other parameters, the widest distribution of median values for benign cases was seen with the *f* parameter (Figure 6.6d).

The comparison between tumour types included cohorts of hepatoblastoma, neuroblastoma and Wilms' tumours. Other tumour types were excluded due to their small sample sizes. The histogram values for these tumour types are summarised in Table 6.2.

The results from the comparison between the ADC, *D*, *D** and *f* histogram parameters of the malignant tumour types are listed in Table 6.3. The Kruskal-Wallis test revealed significant differences in the histogram parameters of *D** ($P = 0.007$ to 0.021) and *f* ($P <$ 0.001 to 0.008). For both *D** and *f* these included histogram parameters: mean, median and 75^{th}/90^{th} percentiles. Additionally, *D** skewness and *f* 25^{th} percentile, kurtosis and entropy showed significant differences. No differences were observed for ADC and *D* histogram parameters.

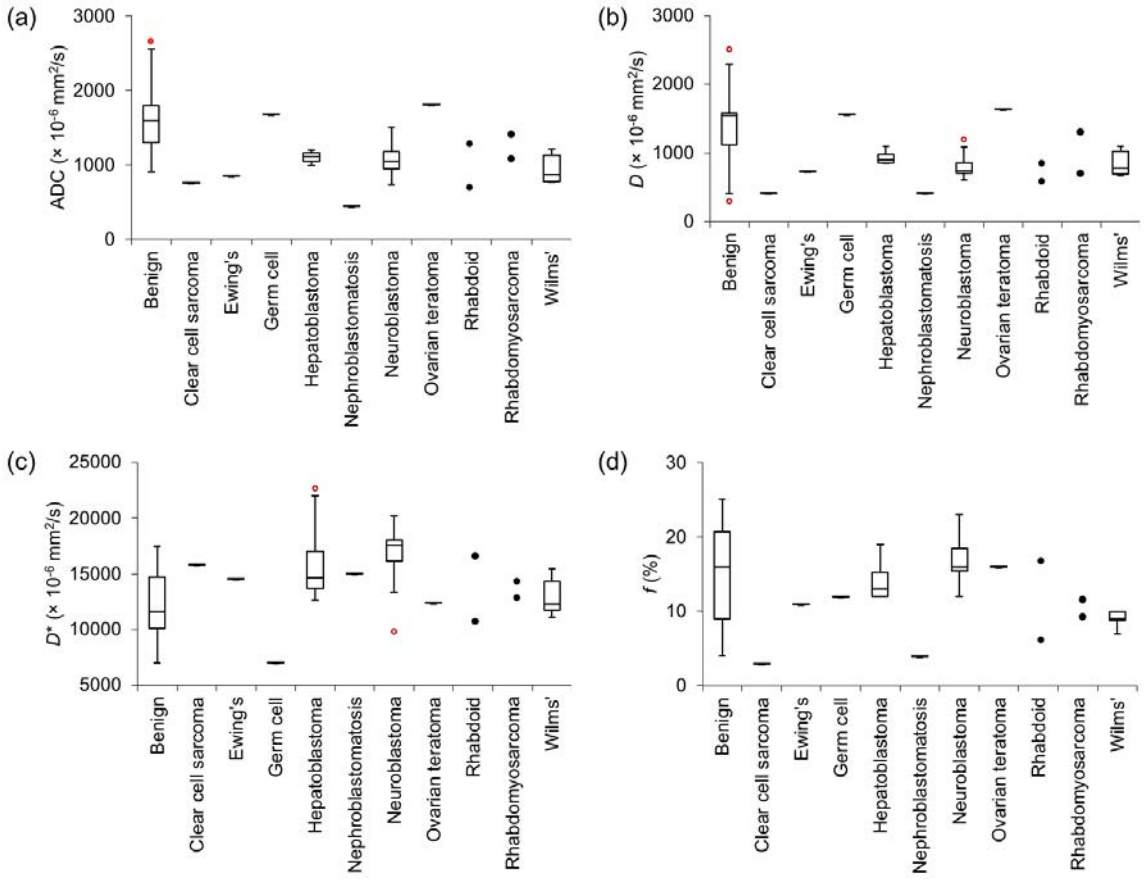

Figure 6.6 Distributions of median diffusion parameter values for different tumour types. Box plots describing the ADC (a) and IVIM D (b), D^* (c) and f (d) parameter distributions. Top and bottom of the boxes represent 25 % and 75 % percentiles of data values, respectively, and the horizontal lines in boxes represent the median. The whiskers extend to the most extreme data points not considered outliers, with outliers indicated by red circles. For data where n = 1, a dash is shown for the median value, and for n = 2, dots indicate the medians of the two cases.

Table 6.2 Histogram parameters of ADC, *D*, *D** and *f* for the individual malignant tumour types.

		Mean	**Median**	**5th %**	**25th %**	**75th %**	**90th %**	**Kurtosis**	**Skewness**	**Entropy**
HB	ADC	1181±71	1104±77	767±110	972±66	1301±96	1632±96	2.19±4.0 × 10^{-2}	3.1 × 10^{-2}±1.6 × 10^{-3}	6.91±2.2× 10^{-1}
n = 4	*D*	962±61	938±51	386±131	791±60	1096±65	1356±71	2.21±6.5 × 10^{-3}	3.4 × 10^{-2}±3.4 × 10^{-4}	7.01±8.4 × 10^{-2}
	*D**	18723±1878	16144±1933	5068±589	11042±1295	24000±2616	33940±3412	2.22±3.0 × 10^{-2}	7.3 × 10^{-3}±4.3 × 10^{-4}	9.78±1.8 × 10^{-1}
	f	16.6±1.53	14.3±1.43	4.00±0.94	9.00±1.17	20.8±1.78	31.3±2.48	2.15±2.8 × 10^{-2}	2.2 × 10^{-1}±8.4 × 10^{-3}	3.60±7.0 × 10^{-2}
NB	ADC	1164±190	1070±201	625±124	825±139	1416±271	1770±352	2.22±7.5 × 10^{-2}	3.3 × 10^{-2}±5.7 × 10^{-3}	7.09±3.9 × 10^{-1}
n = 11	*D*	885±88	817±85	374±102	616±76	1098±114	1413±157	2.15±5.7 × 10^{-2}	3.0 × 10^{-2}±6.4 × 10^{-3}	7.04±2.3 × 10^{-1}
	*D**	19348±1213	16957±1318	5120±608	10651±1457	24127±1762	35328±2118	2.22±1.6 × 10^{-2}	7.3 × 10^{-3}±1.9 × 10^{-4}	9.30±5.6 × 10^{-1}
	f	21.1±1.85	17.1±1.75	3.82±0.47	9.72±1.09	28.6± .04	43.1±4.27	2.20±1.9 × 10^{-2}	2.1 × 10^{-1}±6.4 × 10^{-3}	3.88±1.2 × 10^{-1}
W	ADC	1033±191	939±178	643±103	795±138	1180±243	1511±317	2.19±5.4 × 10^{-2}	3.5 × 10^{-2}±2.9 × 10^{-3}	6.95±3.2 × 10^{-1}
n = 8	*D*	935±94	847±85	586±42	722±63	1060±120	1368±167	2.19±3.1 × 10^{-2}	3.4 × 10^{-2}±1.7 × 10^{-3}	6.86±2.0 × 10^{-1}
	*D**	14944±791	13004±787	4762±729	9429±655	18147±1104	25530±1683	2.21±1.2 × 10^{-2}	7.8 × 10^{-3}±3.8 × 10^{-5}	9.84±7.5 × 10^{-2}
	f	11.0±0.80	9.00±0.50	2.75±0.41	6.50±0.50	13.1 ± 0.92	20.3 ± 2.69	2.07±3.6 × 10^{-2}	1.9 × 10^{-1}±2.9 × 10^{-2}	3.60±7.0 × 10^{-2}

Note: HB = hepatoblastoma, NB = neuroblastoma, W = Wilms' tumour. Data presented corresponds to mean values ± standard deviations. The units for mean, median and percentiles of ADC, *D* and *D** are in × 10^{-6} mm^2/s and *f* as a percentage (%).

Table 6.3 Comparison of malignant tumour types and their ADC, *D*, *D** and *f* histogram parameters.

	Kruskal-Wallis test (*P*-value)				**Dunn's test (*P*-value)**			
Parameter	**ADC**	***D***	***D****	***f***	**ADC**	***D***	***D****	***f***
Mean	0.470	0.277	0.013*	< 0.001*	-	-	NB-W = 0.010	NB-W < 0.001
Median	0.273	0.198	0.013*	< 0.001*	-	-	NB-W = 0.010	NB-W < 0.001
5th percentile	0.201	0.088	0.944	0.110	-	-	-	-
25th percentile	0.151	0.142	0.413	0.003*	-	-	-	NB-W = 0.002
75th percentile	0.244	0.340	0.015*	< 0.001*	-	-	NB-W = 0.012	NB-W < 0.001
90th percentile	0.392	0.405	0.007*	0.001*	-	-	NB-W = 0.005	NB-W < 0.001
Kurtosis	0.395	0.445	0.651	0.008*	-	-	-	NB-W = 0.006
Skewness	0.183	0.344	0.021*	0.651	-	-	NB-W = 0.017	-
Entropy	0.462	0.466	0.974	0.001*	-	-	-	NB-W < 0.001

Note: HB = hepatoblastoma, NB = neuroblastoma, W = Wilms'. * indicates *P* value of a significant difference. Bonferroni correction factor = 3 was applied to the Dunn's test results.

The Dunn's test revealed that the *D** values of neuroblastoma were significantly higher in comparison to Wilms' tumours (P = 0.005 to 0.012) and skewness was significantly higher for Wilms' compared to neuroblastoma (P = 0.017). Similarly, the *f* values in neuroblastoma were significantly higher in comparison to Wilms' tumours (P < 0.001 to 0.002) and higher kurtosis (P = 0.006) and entropy (P < 0.001) were seen for neuroblastoma.

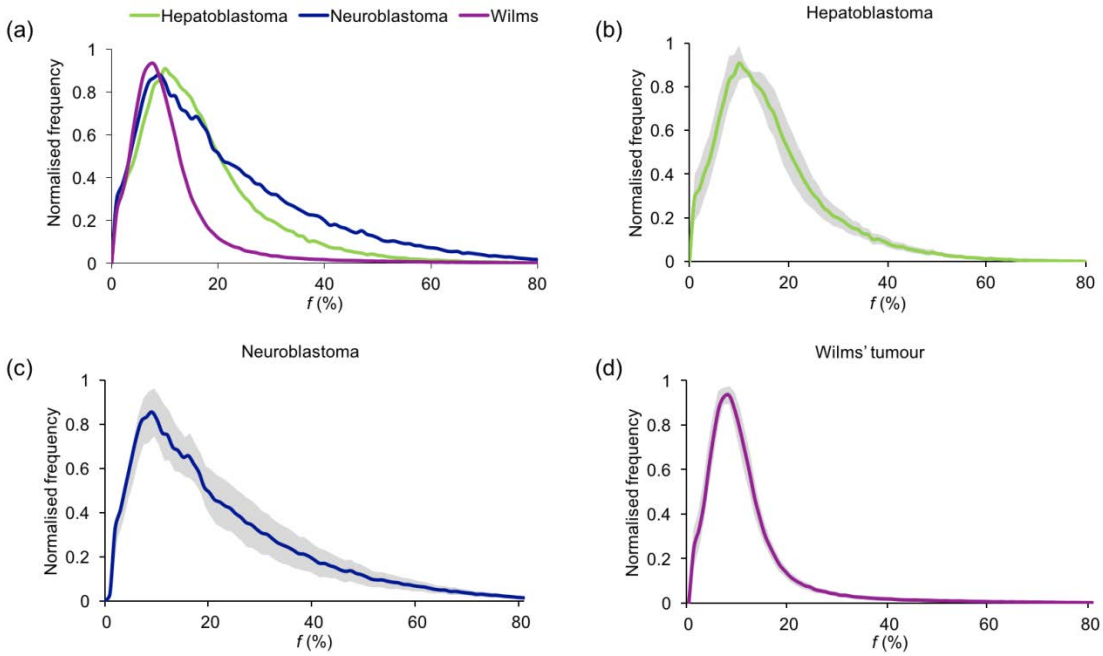

Figure 6.7 Average perfusion fraction *f* histograms. Histograms shown for (a) hepatoblastoma (n = 4), neuroblastoma (n = 11) and Wilms' tumour (n = 8). The (b-d) histograms show the major tumour types, with standard deviation between individual cases indicated by grey shading.

Normalised *f* histograms, averaged for the individual malignant tumour types are shown in Figure 6.7. The median *f* values (%) were 14.3 ± 1.43 for hepatoblastoma, 17.1 ± 1.75 for neuroblastoma and 9.00 ± 0.50 for Wilms' tumour. The Wilms' tumour and neuroblastoma histogram shapes demonstrate the differences seen in kurtosis and entropy between the tumour types. Kurtosis, which is an interpretation of tail extremity or "tailedness" (203), was found to be higher, as shown with the heavy-tailed distribution relative to normal distribution, in neuroblastoma. The higher entropy of neuroblastoma was observed as a more irregularly distributed histogram with greater deviation seen between some of the cohort cases.

ROC analysis was performed with D^* and f histogram parameters to study the diagnostic performance of discriminating Wilms' tumours from neuroblastoma. The results from ROC analysis are presented in Table 6.4. The D^* histogram parameters mean, median, $75^{th}/90^{th}$ percentiles and skewness could discriminate the two tumour types with AUC values > 0.900 (range, 0.909 – 0.935; P = 0.002 to 0.004). The f histogram parameters mean, median, $5^{th}/2th/75^{th}/90^{th}$ percentiles, kurtosis and entropy could discriminate Wilms' tumours from neuroblastoma, with mean, median $25^{th}/75^{th}/90^{th}$ and entropy demonstrating AUC values > 0.900 (range, 0.938 – 1.00; P < 0.001 to 0.029).

Representative parametric maps of Wilms' tumour and neuroblastoma are shown in Figures 6.8 and 6.9, respectively. The ADC and D maps were similar in appearance, although the D values were generally lower. For both Wilms' and neuroblastoma, the D^* maps appeared the most heterogeneous, indicating greater variability of values, which accounted for the higher histogram entropies. In reference to the healthy kidneys seen on the f maps, lower vascular character was suggested for the Wilms' case, while more variability was observed for neuroblastoma.

Table 6.4 Diagnostic performance of *D** and *f* histogram parameters in discriminating Wilms' tumour from neuroblastoma.

		Mean	**Median**	**5th %**	**25th %**	**75th %**	**90th %**	**Kurtosis**	**Skewness**	**Entropy**
*D**	AUC	0.909	0.909	0.506	0.675	0.909	0.935	0.571	0.909	0.532
	Confidence interval	0.739, 1.00	0.739, 1.00	0.177, 0.836	0.408, 0.942	0.739, 1.00	0.807, 1.00	0.285, 0.858	0.739, 1.00	0.254, 0.811
	Sensitivity %	90.9	90.9	81.8	81.8	90.9	90.9	63.6	90.9	45.5
	Specificity %	100	100	57.1	71.4	100	100	85.7	100	100
	P-value	0.004*	0.004*	0.964	0.221	0.004*	0.002*	0.618	0.004*	0.821
	Cutoff value	17826	15636	5471	9612	22044	32376	2.22	7.60×10^{-3}	9.62
f	AUC	1.00	1.00	0.784	0.938	1.00	0.966	0.886	0.523	0.977
	Confidence interval	1.00, 1.00	1.00, 1.00	0.574, 0.994	0.835, 1.00	1.00, 1.00	0.889, 1.00	0.676, 1.00	0.245, 0.801	0.920, 1.00
	Sensitivity %	100	100	50.0	75.0	100	87.5	87.5	50.0	87.5
	Specificity %	100	100	90.9	90.9	100	100	100	72.7	100
	P-value	<0.001*	<0.001*	0.039*	0.001*	<0.001*	0.001*	0.005*	0.869	0.029*
	Cutoff value	14.7	11.0	2.50	7.50	17.5	24.50	2.10	2.01×10^{-1}	3.35

Note: * indicates *P* value of a significant difference. AUC is the area under the ROC curve. The units for mean, median and percentiles of *D** cutoff values are in $\times 10^{-6}$ mm^2/s and *f* as a percentage (%). The specificity, sensitivity and cutoff values are from the Youden analysis.

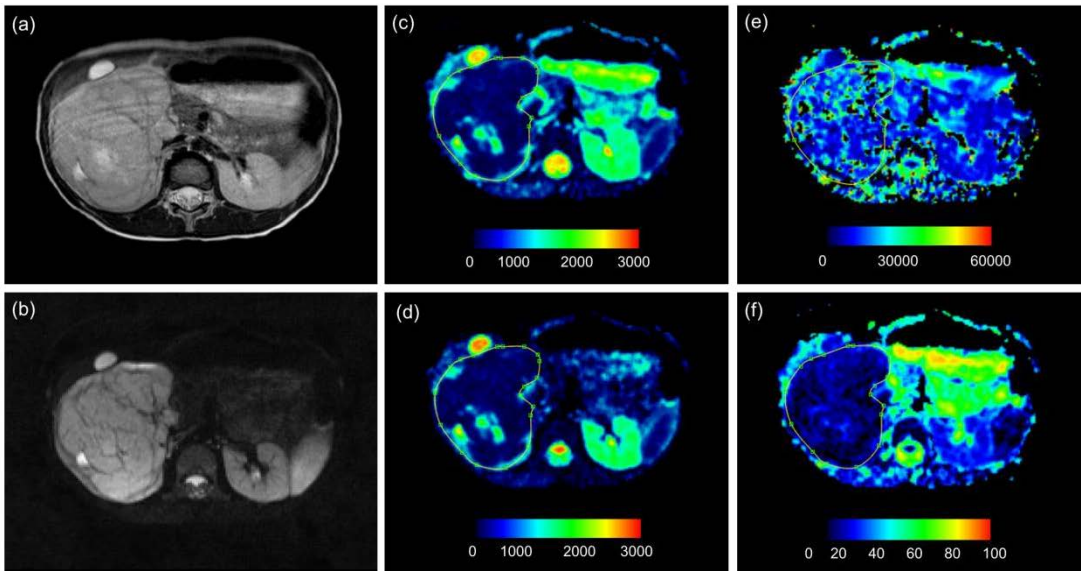

Figure 6.8 Histologically verified low risk Wilms' tumour. (a) T_2-weighted and (b) b = 150 s/mm^2 axial images, and (c-f) parametric maps (ADC, D, D^* and f, respectively). Whole tumour ROI is shown drawn on the parametric maps.

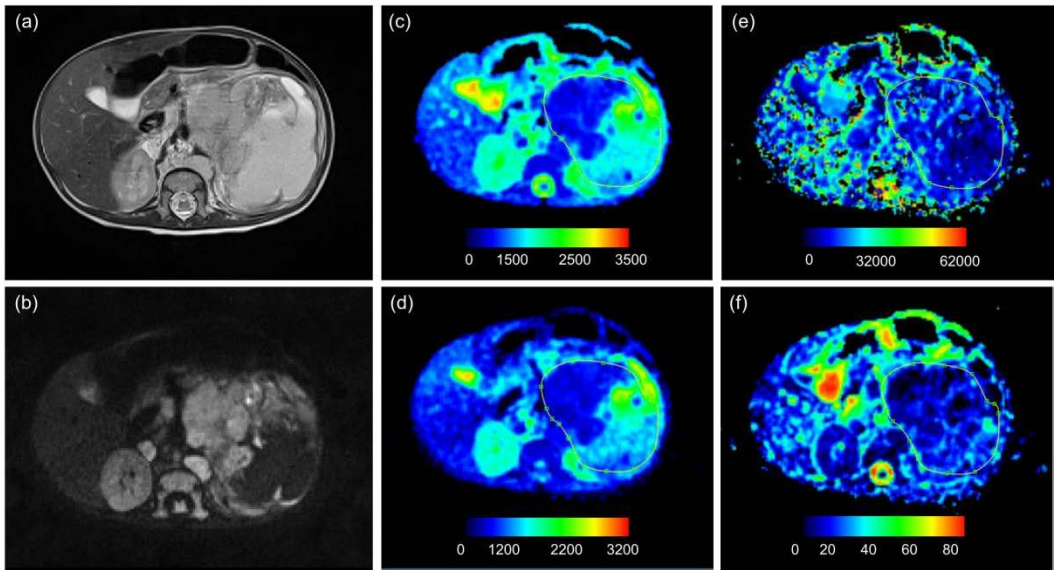

Figure 6.9 Histologically verified neuroblastoma (grade IV). (a) T_2-weighted and (b) b = 150 s/mm^2 images and (c-f) parametric maps (ADC, D, D^* and f, respectively). Whole ROI is shown drawn on the parametric maps.

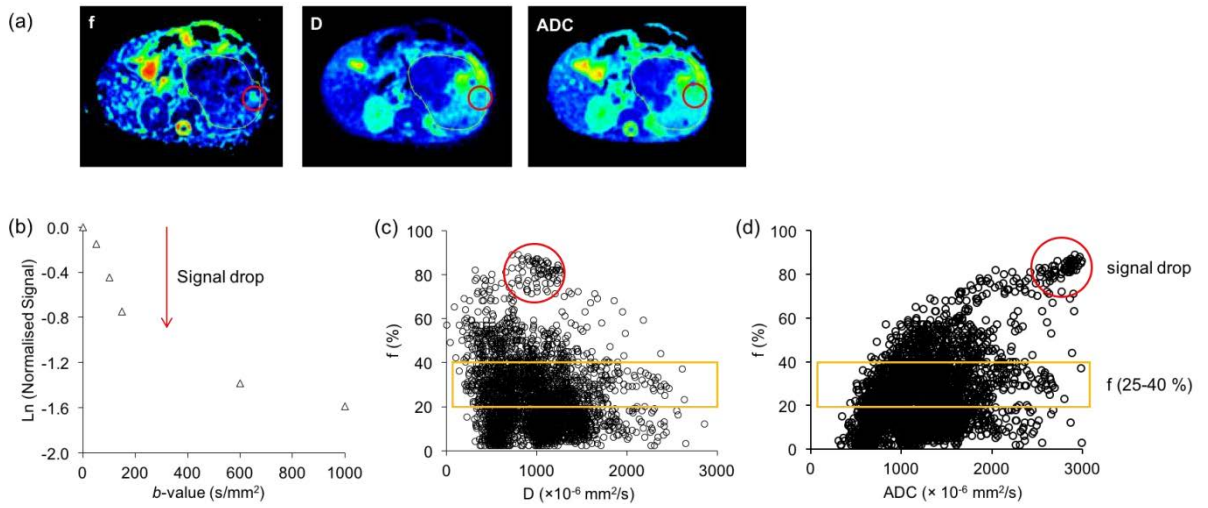

Figure 6.10 Investigation of higher *f* values observed in neuroblastoma. (a) Parametric maps of *f*, *D* and ADC, with a high *f* value (> 40 %) region indicated with a red circle, and (b) the large signal drop observed at low *b*-values for this region. The voxel-wise correlations for *f*-*D* (c) and *f*-ADC (d) for a single slice tumour ROI, with yellow box indicating the region where neuroblastoma differed the most from Wilms' (*f* = 20-40 %) and red circle indicating the parametric values resulting from the signal drop at very high *f* values.

The greatest difference in the *f* values between neuroblastoma and Wilms' tumours was observed to occur when *f* = 20 – 40 % (Figure 6.7). This region was investigated for a few example cases (n = 4), with a neuroblastoma case presented in Figure 6.10. No correlation was established between IVIM and ADC parameters in the corresponding image regions, as indicated by the yellow boxes in Figures 6.10c-d. In a region where *f* was > 40 % (Figure 6.10a-b), a large signal drop was observed at the lower *b*-values. These regions are indicated by the red circles in Figures 6.10c-d, where very high *f* values resulted in relatively low *D* and high ADC values. Voxel-wise correlations in neuroblastoma and Wilms' for the whole range of *f* values demonstrated negative correlation for *D* and *f* (r = -0.165 to -0.307; P < 0.001), while ADC and *f* (r = 0.310 to 0.487; P < 0.001) showed a positive correlation.

6.3.2.2 Discrimination between Benign and Malignant Lesions

Discrimination between benign and malignant lesions was possible with *D*, *D** and ADC parameters (Table 6.5). The ADC, *D*, *D** and *f* for benign lesions were as follows: ADC = 1597 ± 484 (× 10^{-6} mm^2/s), *D* = 1552 ± 622 (× 10^{-6} mm^2/s), *D** = 11610 ± 3385 (× 10^{-6} mm^2/s) and *f* = 16 ± 6.7 %. Both *D* and ADC were found to be significantly lower and *D** significantly higher in malignant tumours. Most ADC histogram parameters demonstrated significantly lower values in malignant tumours (*P* = 0.001 to 0.007), as well as higher kurtosis, skewness and entropy (*P* < 0.001 to 0.036). The *D* parameter could discriminate malignant tumours with lower median, 25th percentile (*P* = 0.045 to 0.049) and higher skewness (*P* = 0.018). The opposite was observed with the *D** parameter, which demonstrated higher median (*P* = 0.039) and entropy (*P* = 0.002) values in malignant tumours. The *f* histogram parameters were found to not show any significant differences between the benign and malignant lesions. The histogram parameters for the benign and malignant groups are summarised in Table 6.6.

Table 6.5 Comparison of benign (*n* = 10) and malignant (*n* = 32) lesions with ADC, *D*, *D** and *f* histogram parameters.

	Mann-Whitney test (*P*-value)			
Parameter	**ADC**	***D***	***D****	***f***
Mean	0.007*	0.070	0.127	0.390
Median	0.001*	0.049*	0.039*	0.320
5th percentile	0.005*	0.056	0.135	0.919
25th percentile	0.002*	0.045*	0.092	0.248
75th percentile	0.007*	0.052	0.127	0.494
90th percentile	0.202	0.112	0.259	0.760
Kurtosis	< 0.001*	0.740	0.247	0.631
Skewness	< 0.001*	0.018*	0.647	0.122
Entropy	0.036*	0.081	0.002*	0.965

Note: * indicates *P* value of a significant difference.

Table 6.6 Histogram parameters of ADC, *D*, *D** and *f* for the malignant and benign tumour groups.

		Mean	**Median**	**5th %**	**25th %**	**75th %**	**90th %**	**Kurtosis**	**Skewness**	**Entropy**
Malignant	ADC	1149±279	1057±285	678±202	864±243	1348±343	1694±406	$2.18\pm8.9\times10^{-2}$	$3.2\times10^{-2}\pm6.8\times10^{-3}$	$7.00\pm3.9\times10^{-1}$
$n = 32$	*D*	949±271	879±273	476±222	712±239	1124±332	1427±403	$2.15\pm1.2\times10^{-1}$	$3.1\times10^{-2}\pm1.0\times10^{-2}$	$6.96\pm5.2\times10^{-1}$
	*D**	17380±3196	15014±3287	4904±1575	9915±2723	21722±4422	31425±6177	$2.26\pm1.5\times10^{-2}$	$7.6\times10^{-3}\pm6.7\times10^{-4}$	$9.42\pm8.8\times10^{-1}$
	f	17.1±6.49	13.8±5.73	3.51±1.61	8.54±3.47	22.1±9.76	34.0±14.3	$2.13\pm9.1\times10^{-2}$	$2.0\times10^{-1}\pm3.3\times10^{-2}$	$3.55\pm4.3\times10^{-1}$
Benign	ADC	1581±442	1592±483	1044±342	1363±427	1812±507	1977±511	$1.99\pm1.4\times10^{-1}$	$-5.0\times10^{-3}\pm2.4\times10^{-3}$	$6.58\pm5.8\times10^{-1}$
$n = 10$	*D*	1361±557	1357±622	795±447	1118±571	1615±614	1820±586	$2.08\pm1.7\times10^{-1}$	$-8.6\times10^{-3}\pm3.3\times10^{-2}$	$6.76\pm4.8\times10^{-1}$
	*D**	14854±4076	12320±3384	3779±1782	8541±2137	18461±5829	27531±8919	$2.19\pm5.9\times10^{-2}$	$2.4\times10^{-3}\pm1.6\times10^{-2}$	8.47±1.0
	f	16.6±6.66	14.3±6.74	3.22±1.75	9.01±4.15	21.9±6.76	37.6±21.1	$2.11\pm8.3\times10^{-2}$	$2.2\times10^{-1}\pm1.7\times10^{-2}$	$3.46\pm5.5\times10^{-1}$

Note: Data presented corresponds to mean values ± standard deviations. The units for mean, median and percentiles of ADC, *D* and *D** are in $\times 10^{-6}$ mm^2/s and *f* as a percentage (%).

The median values of each parameter for each of the benign cases are plotted in Figure 6.11. The ADC and *D* value plots indicated how the benign and malignant lesions are separated into two distinct groups. Although the values of ADC and *D* were similar, some differences were observed. The separation of the two groups was clearer with the use of *D* values, but two benign cases (vascular malformation and lipoma) were found to have lower diffusion coefficients than the malignant group. The separation of the two groups with the *D** values was not as clear and large overlap of values with benign and malignant cases could be observed. This was also seen with the *f* values, but to a greater extent.

The performance of the histogram parameters in differentiating benign from malignant cases was evaluated using the ROC analysis. The results from the ROC analysis are reported in Table 6.7 for ADC, *D* and *D** parameters, which showed significant differences between benign and malignant lesions. ROC curves for median histogram values and histogram parameters that resulted in the highest AUC values for ADC, *D* and *D** parameters are shown in Figure 6.12. The most accurate cutoff levels based on the median histogram parameters were 1219×10^{-6} mm^2/s, 1242×10^{-6} mm^2/s and 11104×10^{-6} mm^2/s for ADC, *D* and *D** parameters, respectively. These corresponded to sensitivity and specificity of 80.0 % and 81.3 % for ADC, 66.7 % and 87.9 % for *D* and 55.6 % and 93.8 % for *D**. The median ADC parameter was found to have better diagnostic performance than *D* or *D** in discriminating benign from malignant lesions with AUC values 0.825 ($P = 0.002$), 0.717 ($P = 0.048$) and 0.736 ($P = 0.032$), respectively. The best diagnostic performance was achieved with histogram skewness for ADC (AUC = 0.919; $P < 0.001$) and *D* (AUC = 0.758; $P = 0.019$), and entropy for *D** (AUC = 0.840; $P = 0.002$). The optimal cutoff values were 3.30×10^{-2}, 3.56×10^{-2} and 9.32 for ADC skewness, *D* skewness and *D** entropy, respectively.

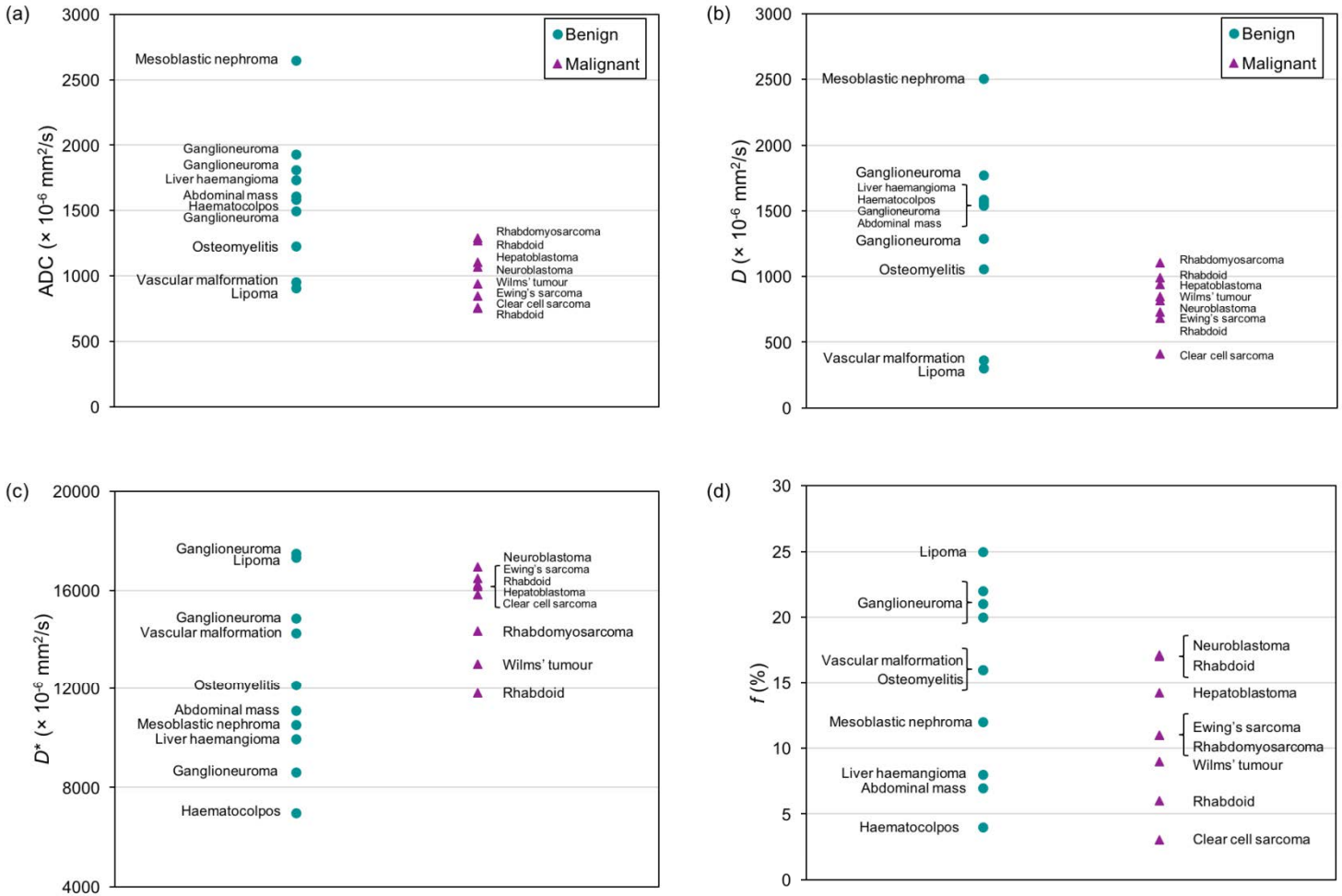

Figure 6.11 The median values of benign and malignant cases. Median values of ADC (a), *D* (b), *D** (c) and *f* (d) plotted for each of the benign case and median values of cohorts of the malignant lesions.

Table 6.7 Diagnostic performance of histogram parameters in discriminating benign from malignant lesions.

Parameters		**Mean**	**Median**	**5th %**	**25th %**	**75th %**	**90th %**	**Kurtosis**	**Skewness**	**Entropy**
ADC	AUC	0.781	0.825	0.788	0.819	0.778	0.638	0.875	0.919	0.722
	Confidence interval	0.601, 0.962	0.659, 0.991	0.488, 0.987	0.646, 0.992	0.610, 0.946	0.439, 0.836	0.738, 1.00	0.823, 1.00	0.513, 0.931
	Sensitivity %	70.0	80.0	70.0	70.0	70.0	90.0	80.0	70.0	60.0
	Specificity %	87.5	81.3	90.6	93.7	81.2	43.7	93.7	100	87.5
	P value	0.008*	0.002*	0.007*	0.003*	0.009*	0.194	<0.001*	<0.001*	0.036*
	Cutoff	1439	1219	951	1310	1565	1605	2.10	3.30×10^{-2}	6.55
D	AUC	0.700	0.717	0.710	0.721	0.714	0.677	0.539	0.758	0.694
	Confidence interval	0.451, 0.950	0.458, 0.977	0.451, 0.970	0.459, 0.983	0.487, 0.941	0.471, 0.883	0.296, 0.782	0.495, 1.00	0.493, 0.894
	Sensitivity %	66.7	66.7	77.8	66.7	66.7	88.9	33.3	77.8	77.8
	Specificity %	84.8	87.9	27.7	90.9	81.8	51.5	90.9	87.9	66.7
	P value	0.068	0.048*	0.055	0.045*	0.052	0.108	0.724	0.019*	0.078
	Cutoff	1232	1242	587	1117	1375	1421	1.93	3.56×10^{-2}	6.98
*D**	AUC	0.681	0.736	0.681	0.701	0.681	0.639	0.628	0.569	0.840
	Confidence interval	0.442, 0.919	0.528, 0.945	0.481, 0.880	0.495, 0.907	0.435, 0.926	0.387, 0.891	0.383, 0.874	0.342, 0.797	0.711, 0.969
	Sensitivity %	55.6	55.6	88.9	66.7	55.6	44.4	55.6	77.8	88.9
	Specificity %	87.5	93.8	469	81.2	87.5	90.6	90.6	46.9	75.0
	P value	0.101	0.032*	0.101	0.068	0.101	0.208	0.244	0.529	0.002*
	Cutoff	13700	11104	5206	8473	16642	23690	2.19	7.61×10^{-3}	9.32

Note: * indicates *P* value of a significant difference. AUC is the area under the ROC curve. The units for mean, median and percentiles of ADC, *D* and *D** cutoff values are in $\times 10^{-6}$ mm²/s. The specificity, sensitivity and cutoff values are from the Youden analysis.

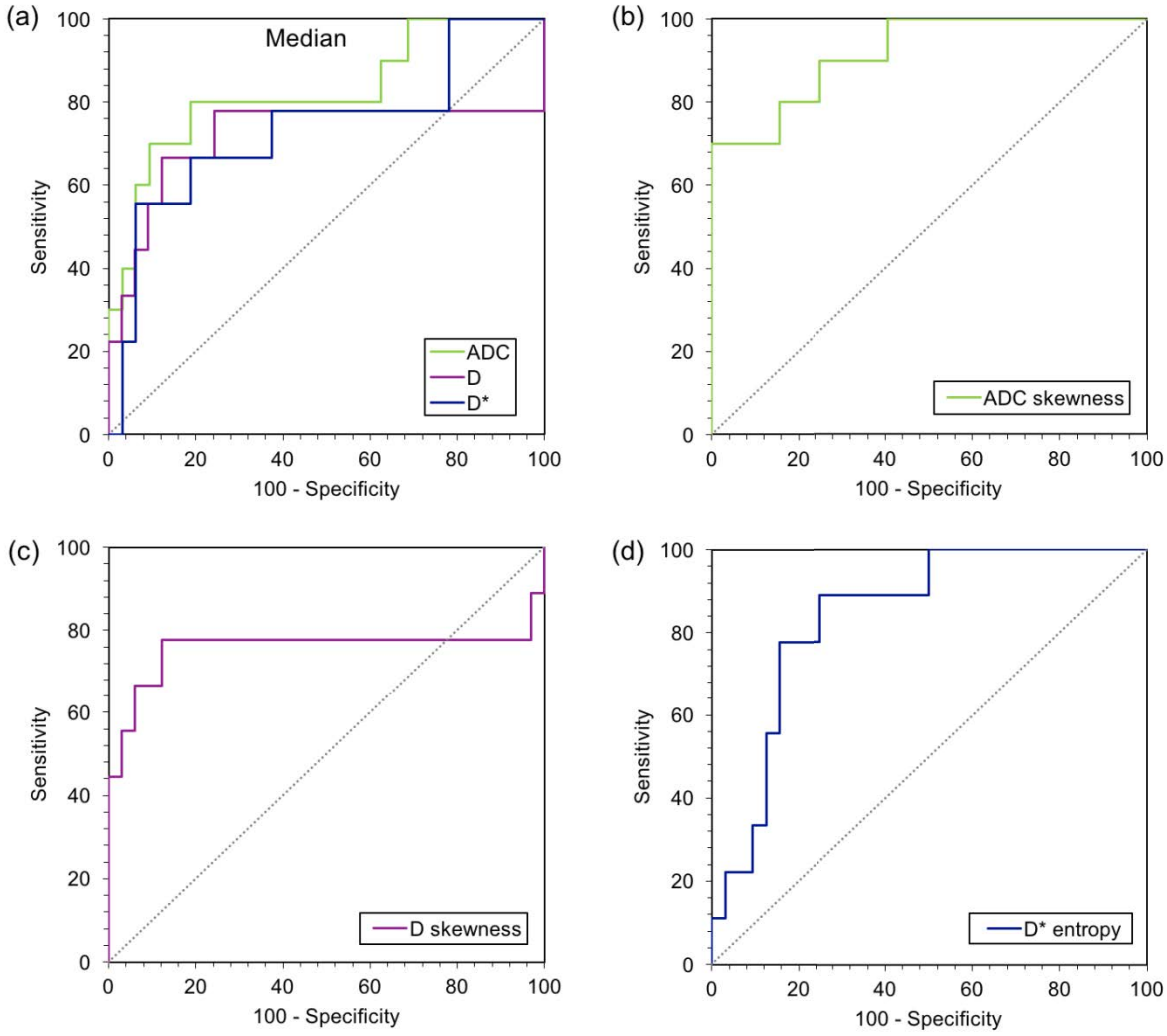

Figure 6.12 Clinical performance of diffusion parameters in discriminating benign from malignant lesions. ROC curves for median (a) ADC, *D* and *D**, and the ROC curves with the highest AUC values for each parameter: (b) ADC skewness, (c) *D* skewness and (d) *D** entropy.

6.4 Discussion

In this study, a diffusion module was implemented into a clinical decision support system, MIROR, which was tested in a cohort of childhood abdominal lesions. The module was built to allow the analysis of diffusion-weighted image data from the major MR manufacturers, and was built to be non-region specific and compatible to different data sets. The results from the diffusion analysis were stored in the MIROR repository to build a database of information, which was allowed by the connections built around the different modules of MIROR.

The application of IVIM analysis in the patient cohort revealed promising results in the use of histogram parameters for discriminating between malignant neuroblastoma and Wilms' tumours as well as differentiating benign from malignant lesions. Distinctive IVIM D^* and f parameters were revealed for Wilms' tumours and neuroblastomas, while no significant differences were observed with the use of D or ADC histogram parameters. The diffusion coefficients (D, D^* and ADC) could discriminate benign from malignant lesions. These results suggest that the complex, heterogeneous structures of retroperitoneal tumours can be characterised using histogram analysis, which has the potential to facilitate their non-invasive diagnosis.

New challenges have arisen for clinicians with the movement towards quantitative imaging methods and analysis as part of clinical practice (188, 204, 205). The complex interpretation of the vast amount of information and data resulting from the advanced imaging techniques does not often ease the diagnosis of diseases. This has promoted the role and use of CDSSs (188). MIROR, the CDSS developed in this study, was designed to guide clinicians through the analysis of advanced MR imaging techniques to allow new methodologies to receive clinical acceptance through a translational approach.

The diffusion module of MIROR was tested and validated by its application to a cohort of childhood abdominal lesions. The use of IVIM histogram analysis for this type of cohort has not been previously reported, although the histogram approach has been increasingly used for heterogeneous and complex tissue types (206). In previous paediatric abdominal studies, the mean or median ADC values have often been reported based on single section or slice, which does not address the heterogeneity seen in many of these tumours (41, 193).

The results from our study indicate that the IVIM derived histogram parameters may facilitate discrimination between malignant neuroblastoma and Wilms' tumours. Comparison of these tumours indicated significant differences in the tumour perfusion characteristics. The perfusion influenced parameters D^* and f were found to be significant predictors of tumour type, while both ADC and D parameters were unable to discriminate between them. Although these tumours generally display different characteristic features, both in terms of clinical presentation (207) and on conventional imaging (208, 209), differentiation of the tumours may cause diagnostic confusion in the case of intrarenal neuroblastoma (210, 211), or if the tumour involves the adrenal gland (212). Neuroblastomas commonly encase vascular structures (207), which could be observed as an increase in D^* and f parameters. The lack of correlation between IVIM and ADC parameters in regions where f = 20-40 %, suggested that the higher parameter values resulted from pathological origins. This finding is of clinical importance as it could potentially be applied to other tumours, which are more difficult to discriminate, such as Wilms' from renal rhabdoid tumour, clear cell sarcoma of the kidney or benign mesoblastic nephroma. This is particularly relevant given the recommendation to avoid pre-treatment biopsy in these tumours(213).

In addition to the higher values of IVIM perfusion parameters, higher skewness for D^* and higher entropy for f were observed in neuroblastoma. This is suggestive of a more irregular and heterogeneous vasculature of neuroblastoma compared to Wilms' tumours. Diagnostic performance with sensitivity and specificity above 85 % was achieved with many of the histogram parameters of both D^* and f.

Cellularity and vascularity have been hypothesised to increase in similar manner, corresponding to a decrease in ADC or D and increase in the f parameter. Interestingly, the voxel-wise correlations in neuroblastoma and Wilms cases demonstrated this to be true for D and f, with negative correlation demonstrated, whereas positive correlation was observed between ADC and f. This agrees with the IVIM model and the proposed "true" tissue diffusion coefficient D (24), and the contribution of both diffusion and vascular characteristics to the measure of ADC.

A review of our results in a clinical context revealed the interesting observations that tumours following an unusual clinical course often had f values differing from others in the same tumour group. Tumours behaving particularly aggressively tended to have higher f values, whereas those following a more indolent course had lower f values. The mean f value for Wilms' tumours in our cohort was 11.0 ± 0.8 %; the patient with the highest mean f value (14.4 %) died following a very aggressive disease process with multiple relapses. Rhabdoid tumours are typically aggressive malignancies with poor survival. The two patients in our cohort with rhabdoid tumours had mean f values of 23.2 % and 8.4 %. The former case died three months after presentation, whereas the latter remains in remission two years following the completion of treatment. This is suggestive of f being a potential prognostic biomarker, with high-risk tumours having higher f values. This is biologically plausible with increased tumour vascularity reflected through an increase in the f parameter. Although our numbers were too small to draw

firm conclusions, this interesting observation deserves further exploration in a larger cohort.

The second investigation involved the discrimination of benign from malignant lesions. This was possible with the use of *D*, *D** and ADC histogram parameters, with highest diagnostic performance observed with the ADC. It is possible that the ADC parameter performed better due to the combination of diffusion and perfusion characteristics into a single parameter. Interestingly, ADC and *D* were both lower in malignant tumours, while *D** was found to be higher. The *f* parameter failed to reach significance in discrimination of benign from malignant tumours. A wide range of *f* values were observed for the benign cohort, which may reflect differences in vasculature rather than cellularity, particularly as benign lesions evaluated included a liver haemangioma and vascular malformation. The highest *f* value was observed for lipoma (mean *f* = 26.0 %), followed by the ganglioneuroma cases (*f* = 20.3 – 22.1 %) and vascular malformation (*f* = 18.4 %). Lipomas are formed of adipose tissue (body fat) and are generally considered to be low-perfused. However, the high *f* values seen for the lipoma case indicated the presence of a vascular component. This was confirmed by the diagnostic report, which described veins running through the lesion. Therefore, although the *f* parameter may not determine benign from malignant cases, it may be useful in evaluation the vascular environment within the lesions.

6.5 Study Limitations

This study had some limitations. Firstly, the sample size of the cohort was relatively small. Further validation with a richer data set in real time and in a clinical setting will be performed as part of future studies to reinforce the credibility and efficiency of the MIROR platform. In terms of the comparison of individual tumour types, the preliminary results were promising and suggested that discrimination is possible. Secondly, no T_2 correction was applied to the perfusion fraction, and therefore the values may have been affected by the T_2 relaxation times of blood and tissue. Thirdly, the group sizes were unbalanced for discrimination of benign from malignant tumours and the group of benign tumours was very heterogeneous as reflected in their DWI characteristics. Further larger and multi-centre studies are required to confirm these results.

6.6 Conclusion

The development and implementation of a diffusion module was completed as part of the multi-modular, non-region-specific design and architecture of the MIROR platform. This aimed to reduce the translational gap between the research and clinical use of IVIM, and made the analysis available for clinical practice at the local institution. The module underwent testing and validation with the application to a cohort of childhood retroperitoneal lesions. The use of multi-*b*-value DW-MRI allowed the computation of IVIM parameters, and the whole tumour ROI approach ensured that the heterogeneity of the tumours was taken into consideration. The results suggested that IVIM parameters and their histogram analysis can provide useful insight into the complex structures of such tumours. The use of these parameters in combination could facilitate the non-invasive diagnosis of individual tumour types. Although further investigation is needed, the perfusion fraction demonstrated potential in being a diagnostic and prognostic imaging biomarker of disease.

Chapter 7

Conclusions and Future Work

7. Conclusions and Future Work

This thesis investigated the use of the intravoxel incoherent motion (IVIM) model as a potential imaging biomarker in childhood cancers. The technical validation of the IVIM model suggested that the analysis is robust in the low-perfused tissues of the brain, but highlighted the requirement for sufficient data quality and in particular signal-to-noise ratio (SNR), whilst showing that a constrained fitting model is optimal in most instances. Furthermore, the application of IVIM was successful with the use of a rapid acquisition protocol using only three *b*-values. The fitting thresholds used here emphasised the influence of bias and variability on the IVIM parameters in different tissue types, and provided guidelines for the interpretation of the differences seen in previous studies, including its use for future studies. As part of the biological validation, significant correlations between the IVIM perfusion fraction and dynamic susceptibility contrast (DSC) derived cerebral blood volume were established for the first time in a paediatric brain tumour cohort. As a final part of this thesis, the IVIM model was successfully implemented into a clinical decision support system (MIROR) platform. Using this platform, the IVIM perfusion fraction was found to discriminate between childhood abdominal tumours, thereby proposing it as a potential diagnostic imaging biomarker.

The following list presents the conclusions from this work and suggests directions for future studies:

I. The technical validation in Chapter 3 was performed to assess the reliability of using the IVIM model in the brain and low-perfused tissues observed in the childhood brain tumours. The constrained IVIM fitting improved the robustness of the estimated parameters, with higher overall accuracy and reproducibility. The investigation of IVIM parameter space revealed that an important SNR requirement exists for the application of IVIM, in both grey matter and low-perfused tissues such as white matter and low-grade gliomas. The modelling results from this Chapter warrant further investigation of the influence of SNR on the estimation of the IVIM parameters, and in particular measurements in vivo would be of interest to validate these observations.

II. Chapter 4 investigated the use of a rapid acquisition protocol to acquire the clinically relevant IVIM diffusion coefficient and perfusion fraction parameters. The optimal *b*-value varied, depending on the underlying tissue characteristics, based on both simulated and in vivo data. This had an important consequence on the threshold used in the constrained or segmented fitting of IVIM, which in many studies might have been too low to separate the perfusion influence from the diffusion coefficient. This would have led to biased estimation of the IVIM parameters, particularly in the brain. In this Chapter, suggestions for the *b*-values to be used were given for different tissue types to minimise bias and variability of the estimated IVIM parameters. Subsequently, guidelines were provided for the interpretation of studies from different centres, which often utilise different *b*-value distributions, and to aid future studies or the analysis of pre-existing data. Therefore, and going forward, more work is needed to

standardise the multi *b*-value DW-MRI protocols and hence provide consensus for their optimal use in different imaging regions. Such work is critical for the future clinical uptake of IVIM.

III. Based on the biomarker roadmap introduced in Chapter 1, the contributions from Chapters 3 & 4 are within the single centre technical validation with assessment of precision and bias (Domain 2). Protocols from these studies with regards to *b*-values were also included in the local MRI scanner, making them available for clinical research at the local institution. The single-centre study here and the current literature provide valuable contributions towards the use of IVIM as an imaging biomarker. However, the future studies should aim to extend this to multi-centre studies, of which only a few exist to date. Such studies are essential for the assessment of reproducibility across different centres, and are required to cross the first translational gap towards the use of IVIM as an imaging biomarker.

IV. The focus in Chapter 5 was moved to the biological validation of IVIM, and in particular the perfusion fraction parameter. The use of DW-MRI and IVIM-*f* has many advantages, with no requirements for tracer delivery and by providing a single acquisition protocol for measures of diffusion and perfusion. For most cases, the perfusion fraction showed significant point-wise correlations to the "gold standard" cerebral blood volume (CBV) from dynamic susceptibility contrast (DSC) imaging. However, the correlation of the two parameters decreased in regions of very low perfusion, with the inherently lower accuracy of both methods, and high perfusion, where differences exist in what the two methods are able to measure. Therefore, while the perfusion fraction appeared to provide a measure of the underlying tissue vascularity, it is unlikely to provide the same exact

measure as DSC-CBV. Further studies determining the relationship of tissue properties to IVIM perfusion fraction, potentially with a histopathological comparison, would be of great interest. Defining the limits for the aforementioned low and high perfusion regions would also be of value, to validate the range of perfusion where IVIM-*f* and DSC-CBV can provide a similar measure.

V. The implementation of IVIM on the MIROR platform was considered an important step towards making the analysis available for clinical practice at the local institution. The implementation, described in Chapter 6, filled the third requirement of technical validation of IVIM in terms of the software availability. Although the IVIM computational performance was sufficient for the generation of the parameter maps, future collaboration should focus on the optimisation of the algorithm in terms of the speed at which it can process images. Following the optimisation, the MIROR platform could be used in future multi-centre IVIM studies, with the diffusion module designed to be adaptable for the input data and by providing standardised software for analysis of data from different centres.

VI. The clinical validation of IVIM was performed using the MIROR platform and a cohort of childhood retroperitoneal lesions. The IVIM perfusion fraction discriminated between common Wilms' tumours and neuroblastomas, which was not possible using the ADC parameter. This is promising for the use of IVIM perfusion fraction as a diagnostic imaging biomarker. Studies in larger cohorts of tumours, as well as studies comparing tumours that are difficult to differentiate on conventional MR imaging, should be investigated to further evaluate its potential. This would promote the clinical value of IVIM and increase its uptake for clinical practice.

The work in this thesis provides an important contribution towards the validation of IVIM as an imaging biomarker. The findings demonstrate its technical reliability and clinical validity, and highlight the future potential of its use as a clinical tool, albeit further work is required to complete its validation.

A large number of publications to-date have focused on the reliability of IVIM post-processing, and while standardisation is still required, the focus should now move onto its clinical validation in larger clinical trials. With very promising results demonstrated in previous smaller studies of various diseases and organs, this would provide the final key requirement for IVIM as an imaging biomarker and pave its way towards clinical practice.

References

1. Cancer Resarch UK. 2017 [Available from: http://www.cancerresearchuk.org/health-professional/cancer-statistics/childrens-cancers.

2. Stiller C. Childhood Cancer in Britain: Incidence, Survival, Mortality: OUP Oxford; 2007.

3. Manias KA, Gill SK, MacPherson L, Foster K, Oates A, Peet AC. Magnetic resonance imaging based functional imaging in paediatric oncology. Eur J Cancer. 2017;72:251-65.

4. Panigrahy A, Bluml S. Neuroimaging of pediatric brain tumors: from basic to advanced magnetic resonance imaging (MRI). J Child Neurol. 2009;24(11):1343-65.

5. Gill SK, Panigrahy A, Arvanitis TN, Peet AC. Magnetic Resonance Spectroscopy of Pediatric Brain Tumors. In: Blüml S, Panigrahy A, editors. MR Spectroscopy of Pediatric Brain Disorders. New York, NY: Springer New York; 2013. p. 45-60.

6. Children's Cancer and Leukaemia Group (CCLG). 2017 [Available from: http://www.cclg.org.uk/Types-of-childhood-cancer.

7. Goo HW. Whole-Body MRI in Children: Current Imaging Techniques and Clinical Applications. Korean J Radiol. 2015;16(5):973-85.

8. Louis DN, Perry A, Reifenberger G, von Deimling A, Figarella-Branger D, Cavenee WK, et al. The 2016 World Health Organization Classification of Tumors of the Central Nervous System: a summary. Acta Neuropathol. 2016;131(6):803-20.

9. Panigrahy A, Nelson MD, Blüml S. Magnetic resonance spectroscopy in pediatric neuroradiology: clinical and research applications. Pediatr Radiol. 2009;40(1):3.

10. Shiroishi MS, Panigrahy A, Moore KR, Nelson MD, Gilles FH, Gonzalez-Gomez I, et al. Combined MRI and MRS improves pre-therapeutic diagnoses of pediatric brain tumors over MRI alone. Neuroradiology. 2015;57(9):951-6.

11. Warren KE, Poussaint TY, Vezina G, Hargrave D, Packer RJ, Goldman S, et al. Challenges with defining response to antitumor agents in pediatric neuro-oncology: a report from the response assessment in pediatric neuro-oncology (RAPNO) working group. Pediatr Blood Cancer. 2013;60(9):1397-401.

12. Guimaraes MD, Schuch A, Hochhegger B, Gross JL, Chojniak R, Marchiori E. Functional magnetic resonance imaging in oncology: state of the art. Radiologia Brasileira. 2014;47(2):101-11.

13. Moseley ME, Cohen Y, Mintorovitch J, Chileuitt L, Shimizu H, Kucharczyk J, et al. Early detection of regional cerebral ischemia in cats: comparison of diffusion- and T2-weighted MRI and spectroscopy. Magn Reson Med. 1990;14(2):330-46.

14. Chen L, Liu M, Bao J, Xia Y, Zhang J, Zhang L, et al. The Correlation between Apparent Diffusion Coefficient and Tumor Cellularity in Patients: A Meta-Analysis. PLoS One. 2013;8(11).

15. Hayashida Y, Hirai T, Morishita S, Kitajima M, Murakami R, Korogi Y, et al. Diffusion-weighted imaging of metastatic brain tumors: comparison with histologic type and tumor cellularity. AJNR Am J Neuroradiol. 2006;27(7):1419-25.

16. Humphries PD, Sebire NJ, Siegel MJ, Olsen OE. Tumors in pediatric patients at diffusion-weighted MR imaging: apparent diffusion coefficient and tumor cellularity. Radiology. 2007;245(3):848-54.

17. Liu Y, Ye Z, Sun H, Bai R. Clinical Application of Diffusion-Weighted Magnetic Resonance Imaging in Uterine Cervical Cancer. Int J Gynecol Cancer. 2015;25(6):1073-8.

18. Manenti G, Di Roma M, Mancino S, Bartolucci DA, Palmieri G, Mastrangeli R, et al. Malignant renal neoplasms: correlation between ADC values and cellularity in diffusion weighted magnetic resonance imaging at 3 T. Radiol Med. 2008;113(2):199-213.

19. Sugahara T, Korogi Y, Kochi M, Ikushima I, Shigematu Y, Hirai T, et al. Usefulness of diffusion-weighted MRI with echo-planar technique in the evaluation of cellularity in gliomas. J Magn Reson Imaging. 1999;9(1):53-60.

20. Yamashita Y, Kumabe T, Higano S, Watanabe M, Tominaga T. Minimum apparent diffusion coefficient is significantly correlated with cellularity in medulloblastomas. Neurol Res. 2009;31(9):940-6.

21. Koral K, Mathis D, Gimi B, Gargan L, Weprin B, Bowers DC, et al. Common Pediatric Cerebellar Tumors: Correlation between Cell Densities and Apparent Diffusion Coefficient Metrics. Radiology. 2013;268(2):532-7.

22. Norris DG. The effects of microscopic tissue parameters on the diffusion weighted magnetic resonance imaging experiment. NMR Biomed. 2001;14(2):77-93.

23. Yamada I, Aung W, Himeno Y, Nakagawa T, Shibuya H. Diffusion coefficients in abdominal organs and hepatic lesions: evaluation with intravoxel incoherent motion echo-planar MR imaging. Radiology. 1999;210(3):617-23.

24. Le Bihan D, Breton E, Lallemand D, Aubin ML, Vignaud J, Laval-Jeantet M. Separation of diffusion and perfusion in intravoxel incoherent motion MR imaging. Radiology. 1988;168(2):497-505.

25. Le Bihan D, Breton E, Lallemand D, Grenier P, Cabanis E, Laval-Jeantet M. MR imaging of intravoxel incoherent motions: application to diffusion and perfusion in neurologic disorders. Radiology. 1986;161(2):401-7.

26. Neil JJ, Bosch CS, Ackerman JJ. An evaluation of the sensitivity of the intravoxel incoherent motion (IVIM) method of blood flow measurement to changes in cerebral blood flow. Magn Reson Med. 1994;32(1):60-5.

27. Federau C, Meuli R, O'Brien K, Maeder P, Hagmann P. Perfusion Measurement in Brain Gliomas with Intravoxel Incoherent Motion MRI. American Journal of Neuroradiology. 2014;35(2):256-62.

28. Federau C, O'Brien K, Meuli R, Hagmann P, Maeder P. Measuring brain perfusion with intravoxel incoherent motion (IVIM): Initial clinical experience. J Magn Reson Imaging. 2014;39(3):624-32.

29. Kilickesmez O, Yirik G, Bayramoglu S, Cimilli T, Aydin S. Non-breath-hold high b-value diffusion-weighted MRI with parallel imaging technique: apparent diffusion coefficient determination in normal abdominal organs. Diagnostic and interventional radiology (Ankara, Turkey). 2008;14(2):83-7.

30. Woo S, Lee JM, Yoon JH, Joo I, Han JK, Choi BI. Intravoxel incoherent motion diffusion-weighted MR imaging of hepatocellular carcinoma: correlation with enhancement degree and histologic grade. Radiology. 2014;270(3):758-67.

31. Freiman M, Perez-Rossello JM, Callahan MJ, Bittman M, Mulkern RV, Bousvaros A, et al. Characterization of fast and slow diffusion from diffusion-weighted MRI of pediatric Crohn's disease. J Magn Reson Imaging. 2013;37(1):156-63.

32. Jerome NP, Miyazaki K, Collins DJ, Orton MR, d'Arcy JA, Wallace T, et al. Repeatability of derived parameters from histograms following non-Gaussian diffusion modelling of diffusion-weighted imaging in a paediatric oncological cohort. Eur Radiol. 2017;27(1):345-53.

33. Lee CH, Yoo KH, Je BK, Kim IS, Kiefer B, Park YS, et al. Using intravoxel incoherent motion MR imaging to evaluate cortical defects in the first episode of upper urinary tract infections: preliminary results. J Magn Reson Imaging. 2014;40(3):545-51.

34. Hilbert F, Holl-Wieden A, Sauer A, Köstler H, Neubauer H. Intravoxel incoherent motion magnetic resonance imaging of the knee joint in children with juvenile idiopathic arthritis. Pediatr Radiol. 2017;47(6):681-90.

35. Bull JG, Saunders DE, Clark CA. Discrimination of paediatric brain tumours using apparent diffusion coefficient histograms. Eur Radiol. 2012;22(2):447-57.

36. Jaremko JL, Jans LB, Coleman LT, Ditchfield MR. Value and limitations of diffusion-weighted imaging in grading and diagnosis of pediatric posterior fossa tumors. AJNR Am J Neuroradiol. 2010;31(9):1613-6.

37. Kan P, Liu JK, Hedlund G, Brockmeyer DL, Walker ML, Kestle JR. The role of diffusion-weighted magnetic resonance imaging in pediatric brain tumors. Childs Nerv Syst. 2006;22(11):1435-9.

38. Poretti A, Meoded A, Cohen KJ, Grotzer MA, Boltshauser E, Huisman TA. Apparent diffusion coefficient of pediatric cerebellar tumors: a biomarker of tumor grade? Pediatr Blood Cancer. 2013;60(12):2036-41.

39. Rodriguez Gutierrez D, Awwad A, Meijer L, Manita M, Jaspan T, Dineen RA, et al. Metrics and textural features of MRI diffusion to improve classification of pediatric posterior fossa tumors. AJNR Am J Neuroradiol. 2014;35(5):1009-15.

40. Rumboldt Z, Camacho DLA, Lake D, Welsh CT, Castillo M. Apparent Diffusion Coefficients for Differentiation of Cerebellar Tumors in Children. Am J Neuroradiol. 2006;27(6):1362-9.

41. Kocaoglu M, Bulakbasi N, Sanal HT, Kismet E, Caliskan B, Akgun V, et al. Pediatric abdominal masses: diagnostic accuracy of diffusion weighted MRI. Magn Reson Imaging. 2010;28(5):629-36.

42. Battal B, Akgun V, Kocaoglu M. Diffusion-weighted MRI beyond the central nervous system in children. Diagnostic and interventional radiology (Ankara, Turkey). 2012;18(3):288-97.

43. Uhl M, Altehoefer C, Kontny U, Il'yasov K, Buchert M, Langer M. MRI-diffusion imaging of neuroblastomas: first results and correlation to histology. Eur Radiol. 2002;12(9):2335-8.

44. Biomarkers and surrogate endpoints: preferred definitions and conceptual framework. Clin Pharmacol Ther. 2001;69(3):89-95.

45. FDA-NIH Biomarker Working Group. FDA-NIH Biomarker Working Group. BEST (Biomarkers, EndpointS, and other Tools) [Available from: https://www.ncbi.nlm.nih.gov/books/NBK326791/.

46. Micheel CM, Nass SJ, Omenn GS, Trials CROBTPPOC, Services BHC, Policy BHS, et al. Evolution of Translational Omics: Lessons Learned and the Path Forward: National Academies Press; 2012.

47. O'Connor JP, Aboagye EO, Adams JE, Aerts HJ, Barrington SF, Beer AJ, et al. Imaging biomarker roadmap for cancer studies. Nat Rev Clin Oncol. 2017;14(3):169-86.

48. Looking back on the millennium in medicine. N Engl J Med. 2000;342(1):42-9.

49. Brown RW, Cheng Y-CN, Haacke EM, Thomson MR, Venkatesan R. Magnetic Resonance Imaging: Physical Principles and Sequence Design: Wiley-Blackwell; 2014.

50. Freeman R. Magnetic Resonance in Chemistry and Medicine: Oxford University Press; 2003.

51. Hall JE. Textbook of Medical Physiology: Saunders; 2015.

52. Bloch F. Nuclear Induction. Physical Review. 1946;70(7-8):460-74.

53. Gudbjartsson H, Patz S. The Rician Distribution of Noisy MRI Data. Magn Reson Med. 1995;34(6):910-4.

54. Péreza MG, Concib A, Morenoc AB, Andaluza VH, Hernándezd JA, editors. Estimating the Rician noise level in brain MR image. ANDESCON, 2014 IEEE; 2014: IEEE.

55. Turner R, Le Bihan D, Maier J, Vavrek R, Hedges LK, Pekar J. Echo-planar imaging of intravoxel incoherent motion. Radiology. 1990;177(2):407-14.

56. Warach S, Chien D, Li W, Ronthal M, Edelman RR. Fast magnetic resonance diffusion-weighted imaging of acute human stroke. Neurology. 1992;42(9):1717-23.

57. Gonzalez RG, Schaefer PW, Buonanno FS, Schwamm LH, Budzik RF, Rordorf G, et al. Diffusion-weighted MR imaging: diagnostic accuracy in patients imaged within 6 hours of stroke symptom onset. Radiology. 1999;210(1):155-62.

58. Warach S, Dashe JF, Edelman RR. Clinical outcome in ischemic stroke predicted by early diffusion-weighted and perfusion magnetic resonance imaging: a preliminary analysis. J Cereb Blood Flow Metab. 1996;16(1):53-9.

59. Padhani AR, Liu G, Koh DM, Chenevert TL, Thoeny HC, Takahara T, et al. Diffusion-weighted magnetic resonance imaging as a cancer biomarker: consensus and recommendations. Neoplasia (New York, NY). 2009;11(2):102-25.

60. Basser PJ, Özarslan E. Chapter 1 - Introduction to Diffusion MR. Diffusion MRI (Second Edition). San Diego: Academic Press; 2014. p. 3-9.

61. Fick A. Concerns diffusion and concentration gradient. Ann Phys Lpz. 1855;170:59.

62. Brown R. A brief account of microscopical observations made in the months of June, July and August, 1827, on the particles contained in the pollen of plants; and on the general existence of active molecules in organic and inorganic bodies. 1828.

63. Einstein A. Investigations on the Theory of the Brownian Movement: Dover Publications; 1956.

64. Le Bihan D, Iima M. Diffusion Magnetic Resonance Imaging: What Water Tells Us about Biological Tissues. PLoS Biol. 2015;13(7).

65. Yablonskiy DA, Sukstanskii AL. Theoretical models of the diffusion weighted MR signal. NMR Biomed. 2010;23(7):661-81.

66. Borgnia M, Nielsen S, Engel A, Agre P. Cellular and molecular biology of the aquaporin water channels. Annu Rev Biochem. 1999;68:425-58.

67. Le Bihan D, Johansen-Berg H. Diffusion MRI at 25: exploring brain tissue structure and function. Neuroimage. 2012;61(2):324-41.

68. Stejskal EO, Tanner JE. Spin Diffusion Measurements: Spin Echoes in the Presence of a Time-Dependent Field Gradient. The Journal of Chemical Physics. 1965;42(1):288-92.

69. Mulkern RV, Haker SJ, Maier SE. On high b diffusion imaging in the human brain: ruminations and experimental insights. Magn Reson Imaging. 2009;27(8):1151-62.

70. Mulkern RV, Gudbjartsson H, Westin CF, Zengingonul HP, Gartner W, Guttmann CR, et al. Multi-component apparent diffusion coefficients in human brain. Nmr Biomed. 1999;12(1):51-62.

71. Brugieres P, Thomas P, Maraval A, Hosseini H, Combes C, Chafiq A, et al. Water diffusion compartmentation at high b values in ischemic human brain. AJNR Am J Neuroradiol. 2004;25(5):692-8.

72. Pilatus U, Shim H, Artemov D, Davis D, van Zijl PC, Glickson JD. Intracellular volume and apparent diffusion constants of perfused cancer cell cultures, as measured by NMR. Magn Reson Med. 1997;37(6):825-32.

73. van Gelderen P, de Vleeschouwer MH, DesPres D, Pekar J, van Zijl PC, Moonen CT. Water diffusion and acute stroke. Magn Reson Med. 1994;31(2):154-63.

74. Nicholson C, Sykova E. Extracellular space structure revealed by diffusion analysis. Trends Neurosci. 1998;21(5):207-15.

75. MacKay A, Whittall K, Adler J, Li D, Paty D, Graeb D. In vivo visualization of myelin water in brain by magnetic resonance. Magn Reson Med. 1994;31(6):673-7.

76. MacKay A, Laule C, Vavasour I, Bjarnason T, Kolind S, Madler B. Insights into brain microstructure from the T2 distribution. Magn Reson Imaging. 2006;24(4):515-25.

77. Jespersen SN, Kroenke CD, Ostergaard L, Ackerman JJ, Yablonskiy DA. Modeling dendrite density from magnetic resonance diffusion measurements. Neuroimage. 2007;34(4):1473-86.

78. Le Bihan D. Diffusion MRI: what water tells us about the brain. EMBO Mol Med. 2014;6(5):569-73.

79. Grech-Sollars M, Hales PW, Miyazaki K, Raschke F, Rodriguez D, Wilson M, et al. Multi-centre reproducibility of diffusion MRI parameters for clinical sequences in the brain. NMR Biomed. 2015;28(4):468-85.

80. Helenius J, Soinne L, Perkio J, Salonen O, Kangasmaki A, Kaste M, et al. Diffusion-weighted MR imaging in normal human brains in various age groups. AJNR Am J Neuroradiol. 2002;23(2):194-9.

81. Le Bihan D. Intravoxel incoherent motion perfusion MR imaging: a wake-up call. Radiology. 2008;249(3):748-52.

82. Koh DM, Collins DJ, Orton MR. Intravoxel Incoherent Motion in Body Diffusion-Weighted MRI: Reality and Challenges. American Journal of Roentgenology. 2011;196(6):1351-61.

83. Jambor I, Merisaari H, Aronen HJ, Jarvinen J, Saunavaara J, Kauko T, et al. Optimization of b-value distribution for biexponential diffusion-weighted MR imaging of normal prostate. J Magn Reson Imaging. 2014;39(5):1213-22.

84. Cohen AD, Schieke MC, Hohenwalter MD, Schmainda KM. The Effect of Low b-Values on the Intravoxel Incoherent Motion Derived Pseudodiffusion Parameter in Liver. Magn Reson Med. 2015;73(1):306-11.

85. Barbieri S, Donati OF, Froehlich JM, Thoeny HC. Impact of the calculation algorithm on biexponential fitting of diffusion-weighted MRI in upper abdominal organs. Magn Reson Med. 2016;75(5):2175-84.

86. Pang Y, Turkbey B, Bernardo M, Kruecker J, Kadoury S, Merino MJ, et al. Intravoxel incoherent motion MR imaging for prostate cancer: an evaluation of perfusion fraction and diffusion coefficient derived from different b-value combinations. Magn Reson Med. 2013;69(2):553-62.

87. Wu WC, Chen YF, Tseng HM, Yang SC, My PC. Caveat of measuring perfusion indexes using intravoxel incoherent motion magnetic resonance imaging in the human brain. Eur Radiol. 2015;25(8):2485-92.

88. Park HJ, Sung YS, Lee SS, Lee Y, Cheong H, Kim YJ, et al. Intravoxel incoherent motion diffusion-weighted MRI of the abdomen: The effect of fitting algorithms on the accuracy and reliability of the parameters. J Magn Reson Imaging. 2016.

89. Patel J, Sigmund EE, Rusinek H, Oei M, Babb JS, Taouli B. Diagnosis of Cirrhosis With Intravoxel Incoherent Motion Diffusion MRI and Dynamic Contrast-

Enhanced MRI Alone and in Combination: Preliminary Experience. J Magn Reson Imaging. 2010;31(3):589-600.

90. Cho GY, Moy L, Zhang JL, Baete S, Lattanzi R, Moccaldi M, et al. Comparison of Fitting Methods and b-Value Sampling Strategies for Intravoxel Incoherent Motion in Breast Cancer. Magn Reson Med. 2015;74(4):1077-85.

91. Lee JH, Cheong H, Lee SS, Lee CK, Sung YS, Huh JW, et al. Perfusion Assessment Using Intravoxel Incoherent Motion-Based Analysis of Diffusion-Weighted Magnetic Resonance Imaging: Validation Through Phantom Experiments. Invest Radiol. 2016;51(8):520-8.

92. Lemke A, Stieltjes B, Schad LR, Laun FB. Toward an optimal distribution of b values for intravoxel incoherent motion imaging. Magn Reson Imaging. 2011;29(6):766-76.

93. Conklin J, Heyn C, Roux M, Cerny M, Wintermark M, Federau C. A Simplified Model for Intravoxel Incoherent Motion Perfusion Imaging of the Brain. AJNR Am J Neuroradiol. 2016;37(12):2251-7.

94. Liu W, Wang B, Wolfowitz R, Yeh PH, Nathan DE, Graner J, et al. Perfusion deficits in patients with mild traumatic brain injury characterized by dynamic susceptibility contrast MRI. Nmr Biomed. 2013;26(6):651-63.

95. Biagi L, Abbruzzese A, Bianchi MC, Alsop DC, Del Guerra A, Tosetti M. Age dependence of cerebral perfusion assessed by magnetic resonance continuous arterial spin labeling. J Magn Reson Imaging. 2007;25(4):696-702.

96. Orton MR, Collins DJ, Koh DM, Leach MO. Improved intravoxel incoherent motion analysis of diffusion weighted imaging by data driven Bayesian modeling. Magn Reson Med. 2014;71(1):411-20.

97. While PT. A comparative simulation study of bayesian fitting approaches to intravoxel incoherent motion modeling in diffusion-weighted MRI. Magn Reson Med. 2017.

98. Taouli B, Beer AJ, Chenevert T, Collins D, Lehman C, Matos C, et al. Diffusion-weighted imaging outside the brain: Consensus statement from an ISMRM-sponsored workshop. J Magn Reson Imaging. 2016.

99. Dyvorne H, Jajamovich G, Kakite S, Kuehn B, Taouli B. Intravoxel incoherent motion diffusion imaging of the liver: optimal b-value subsampling and impact on parameter precision and reproducibility. Eur J Radiol. 2014;83(12):2109-13.

100. Zhang JL, Sigmund EE, Rusinek H, Chandarana H, Storey P, Chen Q, et al. Optimization of b-value sampling for diffusion-weighted imaging of the kidney. Magn Reson Med. 2012;67(1):89-97.

101. Taouli B, Beer AJ, Chenevert T, Collins D, Lehman C, Matos C, et al. Diffusion-weighted imaging outside the brain: Consensus statement from an ISMRM-sponsored workshop. J Magn Reson Imaging. 2016;44(3):521-40.

102. Le Bihan D, Turner R, MacFall JR. Effects of intravoxel incoherent motions (IVIM) in steady-state free precession (SSFP) imaging: application to molecular diffusion imaging. Magn Reson Med. 1989;10(3):324-37.

103. Wurnig MC, Donati OF, Ulbrich E, Filli L, Kenkel D, Thoeny HC, et al. Systematic analysis of the intravoxel incoherent motion threshold separating perfusion and diffusion effects: Proposal of a standardized algorithm. Magn Reson Med. 2015;74(5):1414-22.

104. Sasaki M, Yamada K, Watanabe Y, Matsui M, Ida M, Fujiwara S, et al. Variability in absolute apparent diffusion coefficient values across different platforms may be substantial: a multivendor, multi-institutional comparison study. Radiology. 2008;249(2):624-30.

105. Pfefferbaum A, Adalsteinsson E, Sullivan EV. Replicability of diffusion tensor imaging measurements of fractional anisotropy and trace in brain. J Magn Reson Imaging. 2003;18(4):427-33.

106. Vollmar C, O'Muircheartaigh J, Barker GJ, Symms MR, Thompson P, Kumari V, et al. Identical, but not the same: intra-site and inter-site reproducibility of fractional anisotropy measures on two 3.0T scanners. Neuroimage. 2010;51(4):1384-94.

107. Magnotta VA, Matsui JT, Liu D, Johnson HJ, Long JD, Bolster BD, Jr., et al. Multicenter reliability of diffusion tensor imaging. Brain connectivity. 2012;2(6):345-55.

108. Andreou A, Koh DM, Collins DJ, Blackledge M, Wallace T, Leach MO, et al. Measurement reproducibility of perfusion fraction and pseudodiffusion coefficient derived by intravoxel incoherent motion diffusion-weighted MR imaging in normal liver and metastases. Eur Radiol. 2013;23(2):428-34.

109. Li YT, Cercueil JP, Yuan J, Chen W, Loffroy R, Wáng YXJ. Liver intravoxel incoherent motion (IVIM) magnetic resonance imaging: a comprehensive review of published data on normal values and applications for fibrosis and tumor evaluation. Quantitative Imaging in Medicine and Surgery. 2017;7(1):59-78.

110. Kakite S, Dyvorne H, Besa C, Cooper N, Facciuto M, Donnerhack C, et al. Hepatocellular carcinoma: short-term reproducibility of apparent diffusion coefficient and intravoxel incoherent motion parameters at 3.0T. J Magn Reson Imaging. 2015;41(1):149-56.

111. Luciani A, Vignaud A, Cavet M, Van Nhieu JT, Mallat A, Ruel L, et al. Liver Cirrhosis: Intravoxel Incoherent Motion MR Imaging-Pilot Study. Radiology. 2008;249(3):891-9.

112. Runge VM. Safety of the Gadolinium-Based Contrast Agents for Magnetic Resonance Imaging, Focusing in Part on Their Accumulation in the Brain and Especially the Dentate Nucleus. Invest Radiol. 2016;51(5):273-9.

113. Stojanov D, Aracki-Trenkic A, Benedeto-Stojanov D. Gadolinium deposition within the dentate nucleus and globus pallidus after repeated administrations of gadolinium-based contrast agents-current status. Neuroradiology. 2016;58(5):433-41.

114. Boxerman JL, Schmainda KM, Weisskoff RM. Relative cerebral blood volume maps corrected for contrast agent extravasation significantly correlate with glioma tumor grade, whereas uncorrected maps do not. American Journal of Neuroradiology. 2006;27(4):859-67.

115. Law M, Yang S, Babb JS, Knopp EA, Golfinos JG, Zagzag D, et al. Comparison of cerebral blood volume and vascular permeability from dynamic susceptibility contrast-enhanced perfusion MR imaging with glioma grade. American Journal of Neuroradiology. 2004;25(5):746-55.

116. Saito T, Yamasaki F, Kajiwara Y, Abe N, Akiyama Y, Kakuda T, et al. Role of perfusion-weighted imaging at 3T in the histopathological differentiation between astrocytic and oligodendroglial tumors. Eur J Radiol. 2012;81(8):1863-9.

117. Knopp EA, Cha S, Johnson G, Mazumdar A, Golfinos JG, Zagzag D, et al. Glial neoplasms: dynamic contrast-enhanced T2*-weighted MR imaging. Radiology. 1999;211(3):791-8.

118. Hipp SJ, Steffen-Smith E, Hammoud D, Shih JH, Bent R, Warren KE. Predicting outcome of children with diffuse intrinsic pontine gliomas using multiparametric imaging. Neuro Oncol. 2011;13(8):904-9.

119. Le Bihan D, Turner R. The capillary network: a link between IVIM and classical perfusion. Magn Reson Med. 1992;27(1):171-8.

120. Shiroishi MS, Castellazzi G, Boxerman JL, D'Amore F, Essig M, Nguyen TB, et al. Principles of T2 *-weighted dynamic susceptibility contrast MRI technique in brain tumor imaging. J Magn Reson Imaging. 2015;41(2):296-313.

121. Calamante F. Arterial input function in perfusion MRI: a comprehensive review. Progress in nuclear magnetic resonance spectroscopy. 2013;74:1-32.

122. Kim HS, Suh CH, Kim N, Choi CG, Kim SJ. Histogram Analysis of Intravoxel Incoherent Motion for Differentiating Recurrent Tumor from Treatment Effect in Patients with Glioblastoma: Initial Clinical Experience. American Journal of Neuroradiology. 2014;35(3):490-7.

123. Puig J, Sánchez-González J, Blasco G, Daunis-i-Estadella P, Federau C, Alberich-Bayarri Á, et al. Intravoxel Incoherent Motion Metrics as Potential Biomarkers for Survival in Glioblastoma. PLoS One. 2016;11(7).

124. Withey SB, Novak J, MacPherson L, Peet AC. Arterial input function and gray matter cerebral blood volume measurements in children. J Magn Reson Imaging. 2015.

125. Wirestam R, Borg M, Brockstedt S, Lindgren A, Holtas S, Stahlberg F. Perfusion-related parameters in intravoxel incoherent motion MR imaging compared with CBV and CBF measured by dynamic susceptibility-contrast MR technique. Acta Radiol. 2001;42(2):123-8.

126. Leenders KL, Perani D, Lammertsma AA, Heather JD, Buckingham P, Healy MJ, et al. Cerebral blood flow, blood volume and oxygen utilization. Normal values and effect of age. Brain. 1990;113 (Pt 1):27-47.

127. Iima M, Reynaud O, Tsurugizawa T, Ciobanu L, Li JR, Geffroy F, et al. Characterization of glioma microcirculation and tissue features using intravoxel incoherent motion magnetic resonance imaging in a rat brain model. Invest Radiol. 2014;49(7):485-90.

128. Lee HJ, Rha SY, Chung YE, Shim HS, Kim YJ, Hur J, et al. Tumor perfusion-related parameter of diffusion-weighted magnetic resonance imaging: correlation with histological microvessel density. Magn Reson Med. 2014;71(4):1554-8.

129. Port RE, Knopp MV, Brix G. Dynamic contrast-enhanced MRI using Gd-DTPA: interindividual variability of the arterial input function and consequences for the assessment of kinetics in tumors. Magn Reson Med. 2001;45(6):1030-8.

130. Cho GY, Kim S, Jensen JH, Storey P, Sodickson DK, Sigmund EE. A versatile flow phantom for intravoxel incoherent motion MRI. Magn Reson Med. 2012;67(6):1710-20.

131. Iima M, Le Bihan D. Clinical Intravoxel Incoherent Motion and Diffusion MR Imaging: Past, Present, and Future. Radiology. 2016;278(1):13-32.

132. Kang KM, Lee JM, Yoon JH, Kiefer B, Han JK, Choi BI. Intravoxel incoherent motion diffusion-weighted MR imaging for characterization of focal pancreatic lesions. Radiology. 2014;270(2):444-53.

133. Hectors SJ, Wagner M, Besa C, Bane O, Dyvorne HA, Fiel MI, et al. Intravoxel incoherent motion diffusion-weighted imaging of hepatocellular carcinoma: Is there a correlation with flow and perfusion metrics obtained with dynamic contrast-enhanced MRI? J Magn Reson Imaging. 2016.

134. Klauss M, Lemke A, Grunberg K, Simon D, Re TJ, Wente MN, et al. Intravoxel incoherent motion MRI for the differentiation between mass forming chronic pancreatitis and pancreatic carcinoma. Invest Radiol. 2011;46(1):57-63.

135. Lemke A, Laun FB, Klauss M, Re TJ, Simon D, Delorme S, et al. Differentiation of pancreas carcinoma from healthy pancreatic tissue using multiple b-values: comparison of apparent diffusion coefficient and intravoxel incoherent motion derived parameters. Invest Radiol. 2009;44(12):769-75.

136. Bisdas S, Koh TS, Roder C, Braun C, Schittenhelm J, Ernemann U, et al. Intravoxel incoherent motion diffusion-weighted MR imaging of gliomas: feasibility of the method and initial results. Neuroradiology. 2013;55(10):1189-96.

137. Hu YC, Yan LF, Wu L, Du P, Chen BY, Wang L, et al. Intravoxel incoherent motion diffusion-weighted MR imaging of gliomas: efficacy in preoperative grading. Sci Rep. 2014;4:7208.

138. Lin YK, Li JR, Zhang ZQ, Xu Q, Zhou ZY, Zhang ZP, et al. Comparison of Intravoxel Incoherent Motion Diffusion-Weighted MR Imaging and Arterial Spin Labeling MR Imaging in Gliomas. Biomed Research International. 2015.

139. Suo S, Cao M, Zhu W, Li L, Li J, Shen F, et al. Stroke assessment with intravoxel incoherent motion diffusion-weighted MRI. NMR Biomed. 2016;29(3):320-8.

140. Sigmund EE, Cho GY, Kim S, Finn M, Moccaldi M, Jensen JH, et al. Intravoxel Incoherent Motion Imaging of Tumor Microenvironment in Locally Advanced Breast Cancer. Magn Reson Med. 2011;65(5):1437-47.

141. Hayashi T, Miyati T, Takahashi J, Fukuzawa K, Sakai H, Tano M, et al. Diffusion analysis with triexponential function in liver cirrhosis. J Magn Reson Imaging. 2013;38(1):148-53.

142. Shinmoto H, Oshio K, Tanimoto A, Higuchi N, Okuda S, Kuribayashi S, et al. Biexponential apparent diffusion coefficients in prostate cancer. Magn Reson Imaging. 2009;27(3):355-9.

143. Kuru TH, Roethke MC, Stieltjes B, Maier-Hein K, Schlemmer HP, Hadaschik BA, et al. Intravoxel incoherent motion (IVIM) diffusion imaging in prostate cancer - what does it add? J Comput Assist Tomogr. 2014;38(4):558-64.

144. Ueda Y, Takahashi S, Ohno N, Kyotani K, Kawamitu H, Miyati T, et al. Triexponential function analysis of diffusion-weighted MRI for diagnosing prostate cancer. J Magn Reson Imaging. 2016;43(1):138-48.

145. Bennett KM, Schmainda KM, Bennett RT, Rowe DB, Lu H, Hyde JS. Characterization of continuously distributed cortical water diffusion rates with a stretched-exponential model. Magn Reson Med. 2003;50(4):727-34.

146. Yablonskiy DA, Bretthorst GL, Ackerman JJH. Statistical Model for Diffusion Attenuated MR Signal. Magn Reson Med. 2003;50(4):664-9.

147. Jensen JH, Helpern JA, Ramani A, Lu H, Kaczynski K. Diffusional kurtosis imaging: the quantification of non-gaussian water diffusion by means of magnetic resonance imaging. Magn Reson Med. 2005;53(6):1432-40.

148. Zhang G, Wang S, Wen D, Zhang J, Wei X, Ma W, et al. Comparison of non-Gaussian and Gaussian diffusion models of diffusion weighted imaging of rectal cancer at 3.0 T MRI. Sci Rep. 2016;6:38782.

149. Morelli JN, Runge VM, Ai F, Attenberger U, Vu L, Schmeets SH, et al. An image-based approach to understanding the physics of MR artifacts. Radiographics. 2011;31(3):849-66.

150. Newville MS, T.; Allen, D. B.; Ingargiola, A. . LMFIT: Non-Linear Least-Square Minimization and Curve-Fitting for Python. Zenodo. 2014.

151. Cihangiroglu M, Ulug AM, Firat Z, Bayram A, Kovanlikaya A, Kovanlikaya I. High b-value diffusion-weighted MR imaging of normal brain at 3 T. Eur J Radiol. 2009;69(3):454-8.

152. Dietrich O, Heiland S, Sartor K. Noise correction for the exact determination of apparent diffusion coefficients at low SNR. Magn Reson Med. 2001;45(3):448-53.

153. Moré JJ. The Levenberg-Marquardt algorithm: Implementation and theory. In: Watson GA, editor. Numerical Analysis: Proceedings of the Biennial Conference Held at Dundee, June 28–July 1, 1977. Berlin, Heidelberg: Springer Berlin Heidelberg; 1978. p. 105-16.

154. Pekar J, Moonen CTW, van Zijl PCM. On the precision of diffusion/perfusion imaging by gradient sensitization. Magn Reson Med. 1992;23(1):122-9.

155. Jelescu IO, Veraart J, Fieremans E, Novikov DS. Degeneracy in model parameter estimation for multi-compartmental diffusion in neuronal tissue. NMR Biomed. 2016;29(1):33-47.

156. Meeus EM, Novak J, Withey SB, Zarinabad N, Dehghani H, Peet AC. Evaluation of intravoxel incoherent motion fitting methods in low-perfused tissue. J Magn Reson Imaging. 2017;45(5):1325-34.

157. Schneider MJ, Dietrich O, Ingrisch M, Helck A, Winter KS, Reiser MF, et al. Intravoxel Incoherent Motion Magnetic Resonance Imaging in Partially Nephrectomized Kidneys. Invest Radiol. 2016;51(5):323-30.

158. Smith SM. Fast robust automated brain extraction. Hum Brain Mapp. 2002;17(3):143-55.

159. Zhang Y, Brady M, Smith S. Segmentation of brain MR images through a hidden Markov random field model and the expectation-maximization algorithm. IEEE Trans Med Imaging. 2001;20(1):45-57.

160. (NEMA) NEMA. Determination of Signal-to-Noise Ratio (SNR) in Diagnostic Magnetic Resonance Imaging. National Electrical Manufacturers Association. 2001.

161. Barnhart HX, Barboriak DP. Applications of the repeatability of quantitative imaging biomarkers: a review of statistical analysis of repeat data sets. Transl Oncol. 2009;2(4):231-5.

162. Hyslop NP, White WH. Estimating precision using duplicate measurements. Journal of the Air & Waste Management Association (1995). 2009;59(9):1032-9.

163. Ohno N, Miyati T, Kobayashi S, Gabata T. Modified triexponential analysis of intravoxel incoherent motion for brain perfusion and diffusion. J Magn Reson Imaging. 2016;43(4):818-23.

164. Iima M, Yano K, Kataoka M, Umehana M, Murata K, Kanao S, et al. Quantitative non-Gaussian diffusion and intravoxel incoherent motion magnetic resonance imaging: differentiation of malignant and benign breast lesions. Invest Radiol. 2015;50(4):205-11.

165. Schaefer PW, Grant PE, Gonzalez RG. Diffusion-weighted MR imaging of the brain. Radiology. 2000;217(2):331-45.

166. Avery RA, Hwang EI, Jakacki RI, Packer RJ. Marked Recovery of Vision in Children With Optic Pathway Gliomas Treated With Bevacizumab. Jama Ophthalmology. 2014;132(1):111-4.

167. Nishikawa R. Pediatric and Adult Gliomas: How Different Are They? Neuro Oncol. 2010;12(12):1203-4.

168. Stokland T, Liu J-F, Ironside JW, Ellison DW, Taylor R, Robinson KJ, et al. A multivariate analysis of factors determining tumor progression in childhood low-grade glioma: a population-based cohort study (CCLG CNS9702). Neuro Oncol. 2010;12(12):1257-68.

169. Hu LS, Baxter LC, Pinnaduwage DS, Paine TL, Karis JP, Feuerstein BG, et al. Optimized Preload Leakage-Correction Methods to Improve the Diagnostic Accuracy of Dynamic Susceptibility-Weighted Contrast-Enhanced Perfusion MR Imaging in Posttreatment Gliomas. American Journal of Neuroradiology. 2010;31(1):40-8.

170. Plaza MJ, Borja MJ, Altman N, Saigal G. Conventional and advanced MRI features of pediatric intracranial tumors: posterior fossa and suprasellar tumors. AJR Am J Roentgenol. 2013;200(5):1115-24.

171. Wintermark M, Lepori D, Cotting J, Roulet E, van Melle G, Meuli R, et al. Brain perfusion in children: evolution with age assessed by quantitative perfusion computed tomography. Pediatrics. 2004;113(6):1642-52.

172. Taki Y, Kawashima R. Brain Development in Childhood. The Open Neuroimaging Journal. 2012;6:103-10.

173. Van Aken H, Van Hemelrijck J. Influence of anesthesia on cerebral blood flow and cerebral metabolism: an overview. Agressologie. 1991;32(6-7):303-6.

174. Sourbron S, Ingrisch M, Siefert A, Reiser M, Herrmann K. Quantification of cerebral blood flow, cerebral blood volume, and blood-brain-barrier leakage with DCE-MRI. Magn Reson Med. 2009;62(1):205-17.

175. Fuss M, Wenz F, Scholdei R, Essig M, Debus J, Knopp MV, et al. Radiation-induced regional cerebral blood volume (rCBV) changes in normal brain and low-grade astrocytomas: quantification and time and dose-dependent occurrence. Int J Radiat Oncol Biol Phys. 2000;48(1):53-8.

176. Bjørnerud A, Emblem KE. A fully automated method for quantitative cerebral hemodynamic analysis using DSC–MRI. J Cereb Blood Flow Metab. 2010;30(5):1066-78.

177. Kuppusamy K, Lin W, Cizek GR, Haacke EM. In vivo regional cerebral blood volume: quantitative assessment with 3D T1-weighted pre- and postcontrast MR imaging. Radiology. 1996;201(1):106-12.

178. Thomsen H, Steffensen E, Larsson EM. Perfusion MRI (dynamic susceptibility contrast imaging) with different measurement approaches for the evaluation of blood flow and blood volume in human gliomas. Acta Radiol. 2012;53(1):95-101.

179. Nagy JA, Chang S, Dvorak AM, Dvorak HF. Why are tumour blood vessels abnormal and why is it important to know? Br J Cancer. 2009;100(6):865-9.

180. Jerome NP, d'Arcy JA, Feiweier T, Koh DM, Leach MO, Collins DJ, et al. Extended T2-IVIM model for correction of TE dependence of pseudo-diffusion volume fraction in clinical diffusion-weighted magnetic resonance imaging. Phys Med Biol. 2016;61(24):N667.

181. Orton MR, Jerome NP, Feiweier T, Koh DM, Leach MO, D.J. C, editors. Statistical assessment of a model combining IVIM and T2 decay for multi-b-value, multi-echo-time DW-MRI in abdominal organs. Annual Meeting of ISMRM; 2016; Singapore.

182. Patterson DM, Padhani AR, Collins DJ. Technology insight: water diffusion MRI--a potential new biomarker of response to cancer therapy. Nat Clin Pract Oncol. 2008;5(4):220-33.

183. O'Connor JP, Jackson A, Parker GJ, Roberts C, Jayson GC. Dynamic contrast-enhanced MRI in clinical trials of antivascular therapies. Nat Rev Clin Oncol. 2012;9(3):167-77.

184. Waldman AD, Jackson A, Price SJ, Clark CA, Booth TC, Auer DP, et al. Quantitative imaging biomarkers in neuro-oncology. Nat Rev Clin Oncol. 2009;6(8):445-54.

185. Shahmoradi L, Farzanehnejad AR, Arji G. Guideline-based Clinical Decision Support Systems as an Inseparable Tool for Better Cancer Care Management. Iran J Public Health. 2016;45(7):962-3.

186. Turgeon J, Michaud V. Clinical decision support systems: great promises for better management of patients' drug therapy. Expert Opin Drug Metab Toxicol. 2016;12(9):993-5.

187. Bates DW, Cohen M, Leape LL, Overhage JM, Shabot MM, Sheridan T. Reducing the frequency of errors in medicine using information technology. J Am Med Inform Assoc. 2001;8(4):299-308.

188. Stivaros SM, Gledson A, Nenadic G, Zeng XJ, Keane J, Jackson A. Decision support systems for clinical radiological practice -- towards the next generation. Br J Radiol. 2010;83(995):904-14.

189. Sim I, Gorman P, Greenes RA, Haynes RB, Kaplan B, Lehmann H, et al. Clinical Decision Support Systems for the Practice of Evidence-based Medicine. J Am Med Inform Assoc. 2001;8(6):527-34.

190. Dome JS, Cotton CA, Perlman EJ, Breslow NE, Kalapurakal JA, Ritchey ML, et al. Treatment of anaplastic histology Wilms' tumor: results from the fifth National Wilms' Tumor Study. J Clin Oncol. 2006;24(15):2352-8.

191. Gupta S, Seaberg K, Wallace MJ, Madoff DC, Morello FA, Jr., Ahrar K, et al. Imaging-guided percutaneous biopsy of mediastinal lesions: different approaches and anatomic considerations. Radiographics. 2005;25(3):763-86; discussion 86-8.

192. Zarinabad N, Manias KA, Meeus EM, Foster K, Peet AC. MIROR, An automated modular MRI clinical decision support system: an application in paediatric cancer diagnosis. JMIR Medical Informatics.

193. Gawande RS, Gonzalez G, Messing S, Khurana A, Daldrup-Link HE. Role of diffusion-weighted imaging in differentiating benign and malignant pediatric abdominal tumors. Pediatr Radiol. 2013;43(7):836-45.

194. Hales PW, Olsen OE, Sebire NJ, Pritchard-Jones K, Clark CA. A multi-Gaussian model for apparent diffusion coefficient histogram analysis of Wilms' tumour subtype and response to chemotherapy. NMR Biomed. 2015;28(8):948-57.

195. Cho GY, Moy L, Kim SG, Baete SH, Moccaldi M, Babb JS, et al. Evaluation of breast cancer using intravoxel incoherent motion (IVIM) histogram analysis: comparison with malignant status, histological subtype, and molecular prognostic factors. Eur Radiol. 2016;26(8):2547-58.

196. Pietka E, Kawa J, Badura P, Spinczyk D. Open architecture computer-aided diagnosis system. Expert Systems. 2010;27(1):17-39.

197. de Clercq PA, Blom JA, Korsten HH, Hasman A. Approaches for creating computer-interpretable guidelines that facilitate decision support. Artif Intell Med. 2004;31(1):1-27.

198. Egger J, Tokuda J, Chauvin L, Freisleben B, Nimsky C, Kapur T, et al. Integration of the OpenIGTLink network protocol for image-guided therapy with the medical platform MeVisLab. Int J Med Robot. 2012;8(3):282-90.

199. Heckel F, Schwier M, Peitgen H-O. Object Oriented Application Development with MeVisLab and Python. Lecture Notes in Informatics 2009;154:1338-51.

200. Nougaret S, Vargas HA, Lakhman Y, Sudre R, Do RK, Bibeau F, et al. Intravoxel Incoherent Motion-derived Histogram Metrics for Assessment of Response after Combined Chemotherapy and Radiation Therapy in Rectal Cancer: Initial Experience and Comparison between Single-Section and Volumetric Analyses. Radiology. 2016;280(2):446-54.

201. Woo S, Cho JY, Kim SY, Kim SH. Histogram analysis of apparent diffusion coefficient map of diffusion-weighted MRI in endometrial cancer: a preliminary correlation study with histological grade. Acta Radiol. 2014;55(10):1270-7.

202. Ruopp MD, Perkins NJ, Whitcomb BW, Schisterman EF. Youden Index and Optimal Cut-Point Estimated from Observations Affected by a Lower Limit of Detection. Biometrical journal Biometrische Zeitschrift. 2008;50(3):419-30.

203. Westfall PH. Kurtosis as Peakedness, 1905 – 2014. R.I.P. The American statistician. 2014;68(3):191-5.

204. Sullivan DC. Imaging as a quantitative science. Radiology. 2008;248(2):328-32.

205. Buckler AJ, Bresolin L, Dunnick NR, Sullivan DC, Aerts HJ, Bendriem B, et al. Quantitative imaging test approval and biomarker qualification: interrelated but distinct activities. Radiology. 2011;259(3):875-84.

206. Just N. Improving tumour heterogeneity MRI assessment with histograms. Br J Cancer. 2014;111(12):2205-13.

207. Dickson PV, Sims TL, Streck CJ, McCarville MB, Santana VM, McGregor LM, et al. Avoiding misdiagnosing neuroblastoma as Wilms tumor. J Pediatr Surg. 2008;43(6):1159-63.

208. Dumba M, Jawad N, McHugh K. Neuroblastoma and nephroblastoma: a radiological review. Cancer Imaging. 2015;15(1).

209. Meyer JS, Harty MP, Khademian Z. Imaging of neuroblastoma and Wilms' tumor. Magn Reson Imaging Clin N Am. 2002;10(2):275-302.

210. Faizan M, Sultana N, Anwar S, Mehmood Q, Ali AS. Intrarenal neuroblastoma: a diagnostic challenge. J Coll Physicians Surg Pak. 2015;25 Suppl 1:S41-2.

211. Farmakis SG, Siegel MJ. Intrarenal neuroblastoma with pulmonary metastases mimicking a Wilms tumor. J Pediatr Surg. 2014;49(12):1864-6.

212. Kembhavi SA, Shah S, Rangarajan V, Qureshi S, Popat P, Kurkure P. Imaging in neuroblastoma: An update. Indian J Radiol Imaging. 2015;25(2):129-36.

213. Szychot E, Apps J, Pritchard-Jones K. Wilms' tumor: biology, diagnosis and treatment. Translational Pediatrics. 2014;3(1):12-24.